LHCII-Assisted TiO_2 Photocatalysis of CO_2 to Small Organic Compounds

Rea Laila Antoniou Kourounioti

Thesis submitted to the
University of Nottingham
for the degree of
Doctor of Philosophy

JULY 2014

Abstract

The increasing concentration of CO_2 in the atmosphere is causing climate change and the increasing energy needs of the planet will aggravate this effect. Sunlight can provide the necessary energy without further impairment to the environment, but it is not always available and therefore energy needs to be stored when it is available in excess. High energy-density materials, such as conventional fuels, are an ideal storage solution, also making energy transport easy.

CO_2 photoreduction could in future be used to convert CO_2 from the emissions of fossil-fuel power plants back into fuel using solar energy, and eventually it could provide an alternative solution to fossil fuels, allowing the direct conversion of atmospheric CO_2 into hydrocarbon fuels. Photocatalysts can be used for CO_2 photoreduction, such as TiO_2. However, TiO_2 absorbs UV light which is only a small portion of the solar radiation. Plants produce a pigment-protein complex, the Light Harvesting Complex of photosystem II (LHCII), which absorbs visible light very efficiently, even under low light intensities, and the energy from this light is used by plants to convert CO_2 to sugars. The work presented in this thesis investigates the combination of the LHCII and Rh-doped TiO_2 photocatalyst, to increase the visible light absorption of the catalyst and improve its efficiency.

LHCII was extracted from spinach leaves and adsorbed on to the TiO_2:Rh catalyst surface to produce TiO_2:Rh-LHCII. The presence of LHCII on the surface was confirmed by LHCII-specific peaks in absorption and fluorescence spectra. The performance of TiO_2:Rh-LHCII was assessed in CO_2 photoreduction with simultaneous water splitting. Methane and hydrogen were detected in the gas phase and their concentrations were greatly increased for TiO_2:Rh-LHCII compared to TiO_2:Rh in visible light experiments. In the liquid phase, CO, methyl formate and acetaldehyde were detected, and the concentrations of the last two were also higher with TiO_2:Rh-LHCII. In UV light, the LHCII hindered CO_2 photoreduction. The stability of the hybrid catalyst following light treatment was explored and it was concluded that a protecting mechanism will be necessary to allow repeated use of the catalyst.

Ordinary differential equation (ODE) models were developed for CO_2 photoreduction to investigate the steady-state concentrations of the products and make predictions about their response to different experimental parameters. The light absorption was confirmed as a viable optimisation target for increasing product concentrations. Additional models investigated the rate of production of organics, hydrogen and oxygen at the early stages of the reaction. An ODE model and a stochastic discrete spatial

model were used and compared. These showed that spatial effects are important for reduction rates and that the hydrophilicity of the catalyst may lead to reaction stalling.

It was concluded that, if issues with LHCII stability and maximising light absorption without interfering with catalysis are dealt with, LHCII could be a promising method for enhancing CO_2 photoreduction with the appropriate catalyst.

List of Publications

Lee, C.-W., Antoniou Kourounioti, R., Wu, J. C. S., Murchie, E., Maroto-Valer, M., Jensen, O. E., Huang, C.-W. & Ruban, A. (2014), 'Photocatalytic conversion of CO_2 to hydrocarbons by light-harvesting complex assisted Rh-doped TiO_2 photocatalyst', *Journal of CO_2 Utilization* **5**(0), 33 – 40.

Abstract

Photocatalytic reduction of CO_2 into valuable hydrocarbons using TiO_2 serves as a promising route for mitigating the effects of global warming and meeting future energy demands. However, TiO_2 utilises UV light for photocatalysis and its hydrocarbon yields are still low. In order to enhance the light absorption and increase yields, light-harvesting complexes (LHCII) extracted from spinach were attached to the surface of Rh-doped TiO_2 (TiO_2:Rh) resulting in a hybrid catalyst, TiO_2:Rh-LHCII. The LHCII can absorb visible light in green plants, which convert CO_2 to sugars via photosynthesis. CO, acetaldehyde and methyl formate were produced from aqueous CO_2 solution in a stirred batch reactor under visible-light irradiation. The yields of acetaldehyde and methyl formate were enhanced by almost ten and four times, respectively, when using TiO_2:Rh-LHCII compared to those of TiO_2:Rh.

Acknowledgments

I would like to thank my supervisors, Dr Erik Murchie, Professor Oliver Jensen, Professor Alexander Ruban, Dr Jonathan Wattis and Professor Mercedes Maroto-Valer, for their guidance and encouragement throughout my studies. I would further like to thank the postdoctoral researchers and fellow PhD students who shared with me their experience and expertise, namely Dr Stella Edwards, Dr Dong Liu, Dr Matthew Johnson and especially Dr Erica Belgio. I am particularly grateful to the University of Nottingham, Multidisciplinary Centre for Integrative Biology (MyCIB) and the Interdisciplinary Doctoral Training Centre (IDTC) for the funding and training they provided for me; and also the people I have met through these for their continued support. I am thankful to our collaborators in Taiwan, Professor Jeffrey Wu and his lab, for their support and hospitality. To Fiona Wilkinson, Darren Hepworth, John Corrie, I am obliged for their valuable assistance.

Contents

Abbreviations

βDM	n-Dodecyl β-D-maltoside
ADP	Adenosine Di-Phosphate
APTMS	3-Aminopropyl-trimethoxy-silane
ATP	Adenosine Tri-Phosphate
BBY	PSII erchiched membrane preparation named after Berthold, Babcock and Yocum
BET	N_2 adsorption method named after Brunauer, Emmett and Teller
BSA	Bovine Serum Albumin
CCS	Carbon Capture and Storage
Chl	Chlorophyll
Chla	Chlorophyll *a*
Chlb	Chlorophyll *b*
CODH	Carbon monoxide Dehydrogenase
Cyt-b6/f	Cytochrome b6/f
EDS	Energy Dispersive Spectroscopy
EDTA	Ethylene-diamine-tetra-acetic acid
ETC	Electron Transport Chain
Fd	Ferredoxin
FDH	Formate Dehydrogenase
FID	Flame Ionization Detector
FNR	Ferredoxin NADP Reductase
FRET	Fluorescence Resonance Energy Transfer
GAP	Glyceraldehyde-3-phosphate
GC	Gas Chromatograph
HEPES	4-(2-Hydroxyethyl) piperazine-1-ethanesulfonic acid
IEF	Isoelectric Focusing
LED	Light-Emitting-Diode
LHCI	Light Harvesting Complex of photosystem I
LHCII	Light Harvesting Complex of photosystem II
MES	2-(N-morpholino)-ethanesulfonic acid

NADP	Nicotinamide Adenine Dinucleotide Phosphate
NADPH	Reduced form of NADP
NPQ	Non-Photochemical chlorophyll fluorescence Quenching
ODE	Ordinary Differential Equations
OEC	Oxygen Evolving Complex
P680	Reaction centre of PSII
PAM	Pulse-Amplitude-Modulation
PC	Plastocyanin
PDE	Partial Differential Equation
PGA	Phosphoglyceric Acids
Ph	Pheophytin
PQ	Plastoquinone
PQH_2	Plastoquinol
PSI	Photosystem I
PSII	Photosystem II
QD	Quantum Dots
Rubisco	Ribulose-1,5-bis-phosphate carboxylase/oxygenase
RuBP	Ribulose-1,5-Bis-Phosphate
RuBpy	Tris (2,2'-Bipyridyl) Ruthenium(II) chloride hexahydrate
SDE	Stochastic Differential Equations
SE	Standard Error
SEM	Scanning Electron Microscopy
SI	Sensitivity Index
TCD	Thermal Conductivity Detector
TEM	Transmission Electron Microscopy
TF	Turnover Frequency
TGA	Thermo-Gravimetric Analysis
TN	Turnover Number
TTA	Triplet-Triplet Annihilation
Tyr	Tyrosine residue
UV	Ultra Violet
UV-Vis	UV-Visible
XRD	X-Ray Diffraction

Chapter 1

Introduction

1.1 The problem

The average temperature of the earth has been increasing over the past century at a rate of 0.0065°C per year according to NCDC data (Xue et al. 2003) (figure 1.1). The cause has for a long time been accepted in the scientific community as the "greenhouse effect", the trapping of re-emitted solar radiation by so called greenhouse gases in the atmosphere. The light emitted from the earth following solar radiation has lower energy (infrared light) and can be absorbed by greenhouse gases, as opposed to the higher energy light entering the earth's atmosphere from the sun. Their concentration has greatly increased since the Industrial Revolution (18^{th} century) due to anthropogenic emissions. Carbon dioxide (CO_2) is the most common greenhouse gas and its atmospheric concentration has been monitored since 1957 (Tans & Keeling 2013), (figure 1.2). The seasonally corrected measurements of the figure show that the CO_2 levels have been increasing throughout this period. Water vapour and CH_4 are also greenhouse gases but with a shorter lifetime compared to CO_2.

As well as a long-lived greenhouse gas, CO_2 is also the main product of combustion of fossil fuels, therefore a large component of power plants' emissions. Thus it is the link between two of the major challenges of the foreseeable future, the energy crisis and climate change due to the greenhouse effect. The predicted increase in energy demand is leading to a "trilemma" with the future of energy at its centre. A solution to the problem will have to be satisfactory in all three dimensions of security, cost and carbon emissions. At the moment, security is a problem with wind and solar energy as they depend on the presence of wind/sunlight. On the other hand, fossil fuels can provide a continual source of energy when it is needed, for as long as it is possible to obtain them. Cost has a similar pattern between these two forms of energy, with fossil fuel prices being cheap, and subsidies needed to make renewables more attractive. However, on the third point, the scales are reversed. Fossil fuels have large carbon emissions, while renewable energy has relatively small emissions, coming only from the preparation of the materials required to harvest it.

Two more factors, which are not necessarily conflicting with the others and so are not discussed in terms of the "trilemma", are public opinion

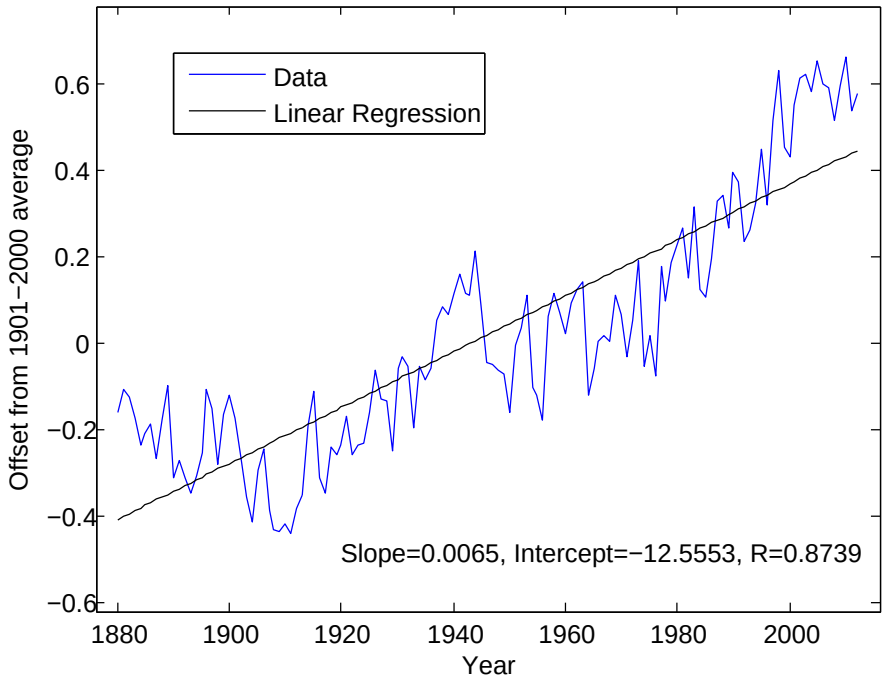

Figure 1.1: The temperature rise of the past century. The mean of the 1901-2000 is used as the zero value. Linear regression gives the slope of the increase as 0.0065°C per year. Drawn from data of the National Climatic Data Centre (NCDC) (Xue et al. 2003).

and sustainability. Public opinion is a strong issue for nuclear energy, especially since the accident at Fukushima, Japan, in 2011. It has also been an obstacle for other emerging technologies in the past, most notably genetically modified crops. Preemptive action needs to be taken to avoid this with future energy solutions. The sustainability, which is not as high a priority at the moment, will come into play indirectly through the other three factors (of the "trilemma") as fossil fuel reserves are depleted and Carbon Capture and Storage (CCS) sites are filled. CCS describes the capture of CO_2 emissions at power plants and their return to the earth in particular sites such as saline aquifers. It is a good example of a technology that is not sustainable but which could help bridge the gap between energy needs and available clean energy, until renewables can catch up. Though sustainability is not driving policy at the moment, it needs to be considered in research, otherwise the technologies will not exist when they are needed.

While electricity from renewable sources or fossil fuels with CCS is a promising source of energy for residential and industrial applications, transport is not so easy to de-carbonise. Chemical energy can be stored and transported very efficiently, so that fuel is still the best candidate for these applications and as a means to store excess electricity when this is available. At the moment, fuel is used to produce electricity, however, in the future, electricity from renewable sources is expected to be more efficient and abundant, and that will be used to produce fuel (Schindler

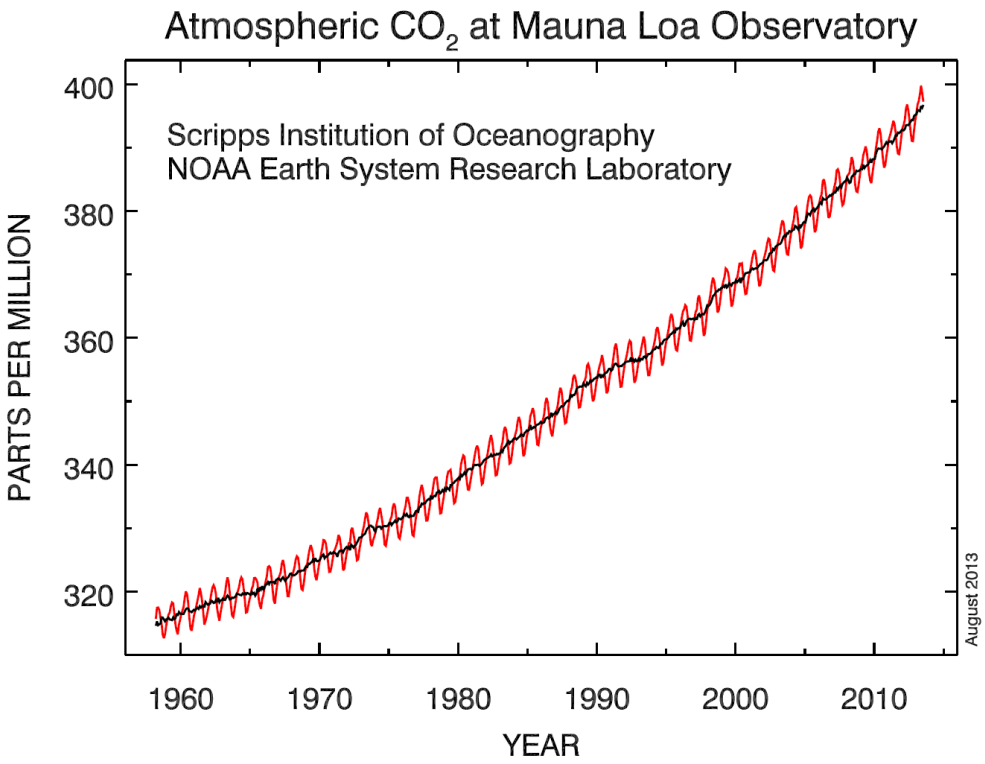

Figure 1.2: Monthly CO_2 measurements at the Mauna Loa observatory (red line). Seasonally corrected measurements are shown in black. Figure reproduced from (Tans & Keeling 2013).

et al. 2006). Hydrogen is the cleanest fuel, not producing any CO_2 during its combustion. However, it is still difficult to store and its direct use is not as well established and investigated as that of organic fuels. As technologies for its storage and use improve, hydrogen will become more attractive. Especially transport, which will rely on fuel for some time and where capture and reuse or storage of emissions are not viable options, will have to eventually become carbon-free.

1.2 Solar energy

The world is quickly turning its hopes to renewable energy to overcome the depletion of fossil fuels coupled with an increase in energy needs and to avoid further increase of the atmospheric CO_2 concentration. Many sources of renewable energy are being investigated, such as biofuel, hydropower, tidal power, geothermal, wind and solar. Wind, hydro and biomass are actually different expressions of solar energy, that have so far been easier to capture and use. In fact, fossil fuels also store solar energy, but as their name suggests, it takes a very long time for them to be formed. As they are used very quickly relative to their replenishing timescale, they are effectively not renewable.

Solar energy in the form of direct sunlight has the potential to fully cover the world's energy needs. It is estimated that, in 2010, $5.53 \cdot 10^{20}$ J of energy were used (Conti et al. 2013), which is less than the yearly total solar

energy that reaches the UK alone (Huld & Dunlop 2013). The same cannot be said for the predicted energy that will be needed in 2040, $8.65 \cdot 10^{20}$ J (Conti et al. 2013). However, the solar energy illuminating the Sahara desert, where the intensity of the radiation is higher (Huld & Dunlop 2013), could cover the predicted global energy demands for 2040 almost 100 times. Therefore, if this solar energy could be harvested, even at an efficiency of only 10%, one tenth of the Sahara desert could power the world.

1.3 Nature's solution

Plants absorb and utilise solar energy, converting it to chemical energy by photosynthesis. They use this chemical energy to grow and multiply and it is this chemical energy that chemotrophs such as animals obtain from their food as their source of energy and also the energy that is stored in biomass. Photosynthesis takes place in the chloroplast, across the thylakoid membrane and in the stroma. The leaf takes carbon dioxide from the atmosphere through the stomata and returns oxygen, which is produced from the splitting of water. Photosynthesis is separated into the "light" and "dark" reactions. Although these terms are commonly used, they are a misnomer because both happen at the same time, during daylight. Even though the "dark" reactions do not need the light directly, they rapidly use up the products of the "light" reactions and so the two need to happen in parallel. Therefore they will here be referred to as the thylakoid ("light") and Calvin cycle ("dark") reactions.

1.3.1 The Light Harvesting Complex of Photosystem II

The Light Harvesting Complex of Photosystem II (LHCII) is a hydrophobic molecule, located in the thylakoid membrane of chloroplasts. It functions by absorbing solar energy in the form of photons and passing them on to the PSII reaction centre, which is a special pair of chlorophyll *a* molecules that can perform charge separation using a red light photon. LHCII is found in plants as a trimer, which is also its most stable form (Wentworth et al. 2004, Yang et al. 2006), with the three monomers held together by hydrophobic forces (Liu et al. 2004). It is believed that the trimeric form is necessary for structural or functional reasons as mutants that are unable to prepare trimeric LHCII, compensate by forming trimers from minor antenna complexes (Ruban et al. 2003, 2006). Each monomer has three α-helices spanning the membrane (Kühlbrandt & Wang 1991) and 14 chlorophyll molecules (Liu et al. 2004) (figure 1.3), eight chlorophyll *a* (green in figure 1.3) and six chlorophyll *b* (cyan) molecules. Carotenoids are also present, which have a photosynthetic and photoprotective role. These are the xanthophylls lutein (red in figure), neoxanthin (orange) and violaxanthin (yellow).

Chlorophylls are the green pigments of plants that absorb blue and red light which is used for photosynthesis. These are packed in LHCII, giving it its colour and light absorbing properties. There are two types of chlorophylls in the LHCII, chlorophyll *a* and *b* (Chla and Chlb respectively), with overlapping absorption spectra. Chla and Chlb are positioned in an

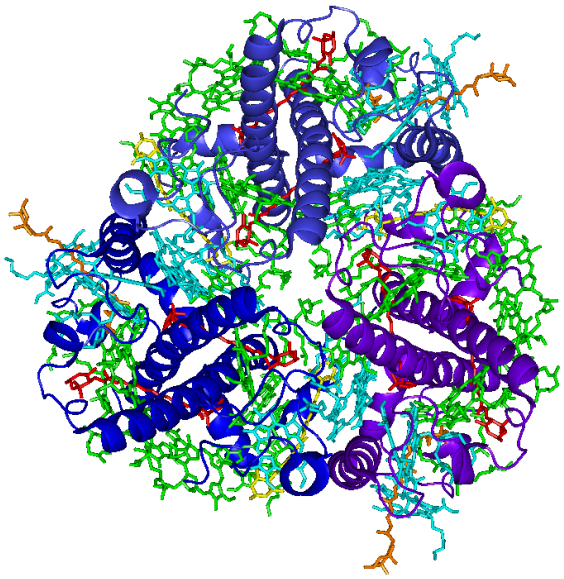

Figure 1.3: The structure of a spinach LHCII trimer seen from the stromal side created using PyMOL (Schrödinger, LLC 2010) from structure PDB ID: 1RWT (Liu et al. 2004). The figure shows the three polypeptide chains (dark blue and purple colours), the chlorophyll *a* (green), chlolophyll *b* (cyan) and the carotenoids: lutein (red), neoxanthin (orange) and violaxanthin (yellow).

ordered fashion within the complex. Indeed there are individual binding sites for each type of chlorophyll within the LHCII (Liu et al. 2004). In this way, it is possible to have the pigments at a very high concentration, so high that it would result in quenching if the chloroplyll molecules were free in solution (Beddard & Porter 1976). Chla absorbs at slightly longer wavelengths in the red and this allows the photon energy to travel "downwards" from Chlb to Chla, towards the reaction centre. To this end, the chlorophylls are positioned very close to each other, so that the energy can pass from one to the other by resonance transfer. These features were seen in the crystal structure by Liu et al. (2004), which, it was later found, shows a dissipative state of LHCII (Pascal et al. 2005).

Exposure of plants to high light leads to photodamage through the build-up of excitation energy in the LHCII antenna and photosystem II. To avoid severe damage, the photosynthetic machinery tightly controls light absorption and dissipation by gene regulation in the long-term. Non-photochemical chlorophyll fluorescence quenching (NPQ) is one of the short term mechanisms, which leads to the dissipation of the excess energy in the form of heat (Ruban et al. 2011). A mechanism for how it functions is proposed by Horton et al. (2005), Ruban et al. (2012), known as the "LHCII aggregation model". A new, non-disrupting method to investigate it has been proposed by Ruban & Murchie (2012).

In vivo, LHCII is very stable. From studies in desiccation tolerant mosses, Proctor et al. (2007) conclude that the photosynthetic machinery is largely intact following desiccation, as recovery is rapid and therefore independent of protein synthesis, while Oliver et al. (2005) say especially

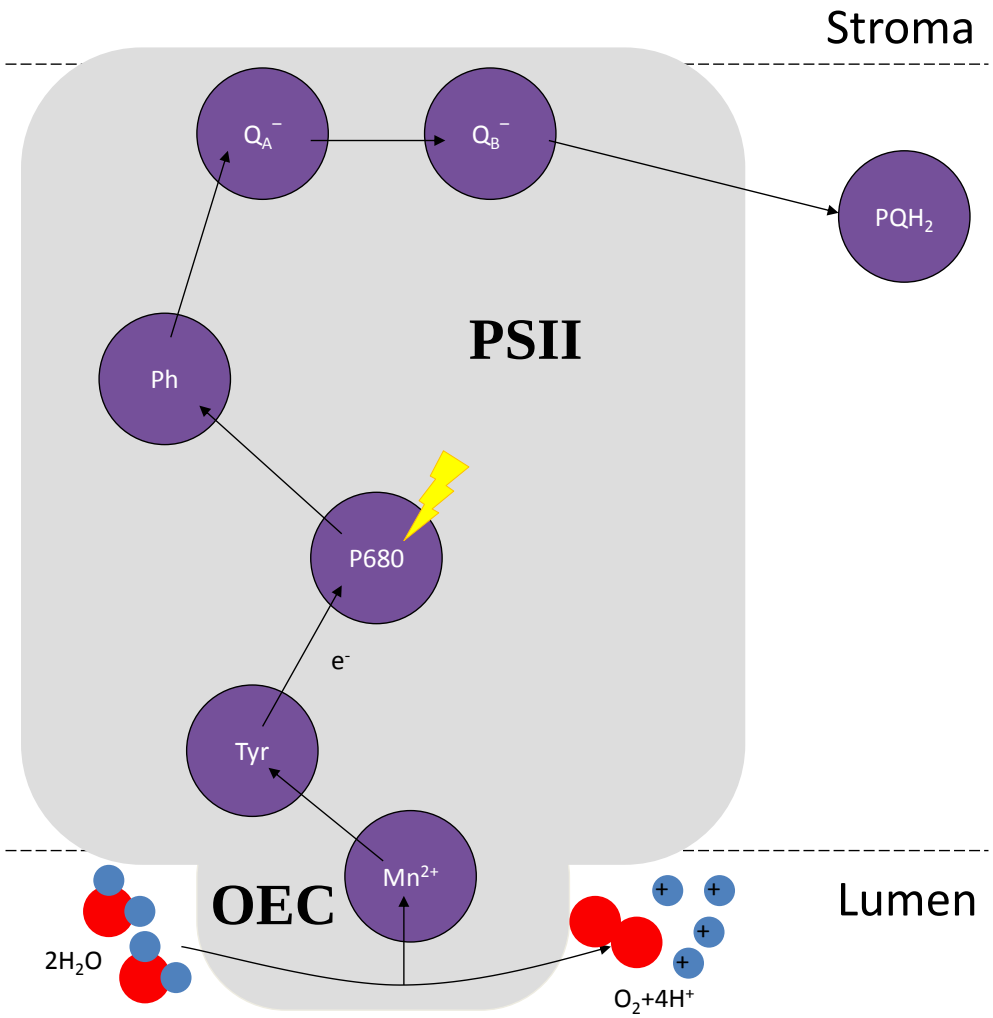

Figure 1.4: Path through electron carriers in photosystem II (PSII). Photon energy enters through P680, indicated by lightning shape. Abbreviations: Oxygen Evolving Complex (OEC), Manganese (Mn^{2+}) ions, tyrosine residue (Tyr), reaction centre (P680), pheophytin (Ph), two quinones (Q_A and Q_B), plastoquinol (PQH_2).

about PSII that it requires little repair to begin photosynthesising following rehydration. Additionally, Liu et al. (2008) showed that LHCII can be immobilised onto a metal surface and be stable for hours, providing support for its stability *in vitro*.

1.3.2 The thylakoid reactions

When a photon is absorbed by a chlorophyll molecule of the PSII antenna, LHCII, its energy passes through numerous chlorophylls to a special pair of chlorophylls, the reaction centre, P680, where an electron is released leaving a positive hole on the chlorophyll. To avoid recombination of the electron and the hole, the two are rapidly separated in space such that the electron is transported through a series of carriers inside the PSII to the stromal side of the membrane, while the hole remains on the lumenal side and is neutralised by taking an electron from water (figures 1.4, 1.5). This

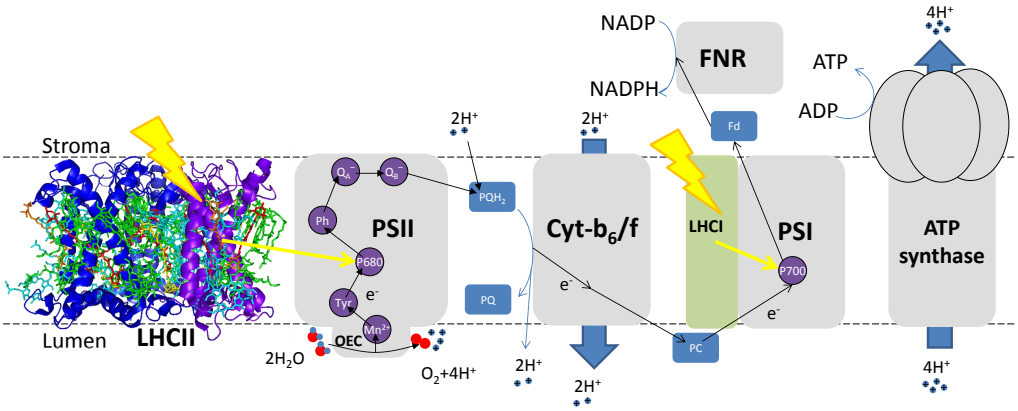

Figure 1.5: The electron transport chain (ETC). Abbreviations: Light Harvesting Complex of photosystem II (LHCII), photosystem II (PSII), plastoquinol (PQH_2), plastoquinone (PQ), cytochrome b6/f (Cyt-b6/f), plastocyanine (PC), Light Harvesting Complex of photosystem I (LHCI), photosystem I (PSI), ferredoxin (Fd), ferredoxin NADP reductase (FNR).

process is performed by the Oxygen Evolving Complex (OEC) and is called "water splitting". It results in the release of protons in the lumen and the production of oxygen gas. Two water molecules are needed for each oxygen molecule, and they provide four electrons.

The electron extracted from water by PSII is transported through various protein complexes, along and across the thylakoid membrane. This process is called the electron transport chain (ETC) and it is shown in figure 1.5. The term Z-scheme is also used to refer to this mechanism due to the shape of the energy diagram of the electron moving through the ETC, which is elevated by two photon absorbing events, one at each photosystem. A plastoquinone (PQ) takes up a pair of electrons from PSII and a pair of protons from the stroma forming plastoquinol (PQH_2). This transports the electrons to Cytochrome-b6/f where they are passed on one at a time to plastocyanin (PC), releasing the protons in the lumen. Cytochrome-b6/f pumps additional protons from the stroma to the lumen. PC carries one electron to Photosystem I (PSI) where another photon, absorbed by LHCI (the light harvesting complex of photosystem I), is used to restore the energy of the electron that was lost in the transport so far (this energy has been used to pump protons across the membrane against their concentration gradient). The PSI uses a pair of electrons and a proton from the stroma to reduce NADP to NADPH. Finally, the proton gradient that has been established by the ETC drives protons through the ATP-synthase from the lumen to the stroma, converting ADP to ATP in the process. The ETC is usually shown in figures as complexes in order, as it is in figure 1.5, but in the membrane these are actually spatially separated.

1.3.3 The Calvin cycle

The Calvin cycle reactions happen in the stroma, where both the NADPH and the ATP are released. CO_2 is fixed from the atmosphere by the enzyme Rubisco (ribulose-1,5-bis-phosphate carboxylase/oxygenase) attaching it to

RuBP (ribulose-1,5-bis-phosphate) and splitting the resulting molecule to two phosphoglyceric acids (PGA). The ATP and NADPH, that have been produced by the thylakoid reactions, convert PGA to GAP. The GAP can be used to regenerate RuBP to fix more CO_2. For every three molecules of CO_2 fixed, six GAP are generated and three RuBP are used. Five GAP can be converted to three RuBP by the Pentose Phosphate Pathway, while the sixth is the profit. Finally, two GAP can be converted to glucose without consuming any more ATP or NADPH.

Rubisco evolved in the absence of oxygen, when the CO_2 concentration of the atmosphere was very high. As a result it has a low specificity for CO_2, also fixing oxygen, which results in a process called photorespiration. To avoid losing the carbon that has been fixed, when the oxygen reacts with RuBP, the carbon from the resulting oxidised product is returned to RuBP by a complex pathway which uses up energy.

1.4 Mimicking plant photosynthesis: CO_2 photoreduction

A combined solution for the storage of renewable energy and combating atmospheric CO_2 levels, lies in the photoreduction of CO_2 to produce fuel. This is also called artificial photosynthesis and is often likened to plant photosynthesis, as the purpose and process are similar. Both reduce carbon dioxide to produce organic compounds that can later be burnt to release energy at an appropriate time. As already discussed, sunlight is the source of energy used in natural photosynthesis, and it is also the ideal source for CO_2 reduction. CO_2 photoreduction can convert solar energy to chemical energy, which can be stored, without adding new CO_2 to the atmosphere. Plants additionally use the products to make up their mass. Artificial photosynthesis can also be used to synthesise valuable organic compounds directly, or through further processing of methanol which is one of the products. This route could be used to remove CO_2 from the atmosphere, in addition to recycling it.

Artificial photosynthesis using TiO_2 has attracted a lot of scientific interest since Fujishima & Honda (1972) showed successful water splitting with TiO_2 under UV light without the use of applied electric current. TiO_2 can be used, not only for water splitting, but also for CO_2 photoreduction. Inoue et al. (1979) tested different semiconductor photocatalysts for CO_2 reduction, including TiO_2 and since then, a lot of work has focused on TiO_2 as it is relatively efficient and cheap, a very desirable property if it is to be used on a large scale commercially (Yamashita et al. 1994, Anpo et al. 1995, Kaneco et al. 1998, Tan et al. 2006, Tseng et al. 2002).

TiO_2 is commonly used to oxidise organic molecules in water treatment as well as in selective oxidation reactions (Shiraishi & Hirai 2008). As any catalyst, it will perform the reverse reaction as well as the forward reaction, meaning that it can reduce CO_2 as well as oxidise organic compounds. This material can also be used in many other applications that are being investigated, such as the development of self-cleaning surfaces or even cancer treatment. These and many others are reviewed in (Fujishima et al.

2000). The focus of this thesis is on its properties as a photocatalyst, and more specifically, its involvement in CO_2 photoreduction. Photocatalysis with TiO_2 can reduce CO_2 to CO (Anpo et al. 1995, Tan et al. 2006, Woolerton et al. 2010), formic acid, formaldehyde (Inoue et al. 1979, Kaneco et al. 1998), methanol and methane (Yamashita et al. 1994, Wu 2009), which is the primary constituent of natural gas. However, the conversion efficiency is still too low for commercial use, partly because CO_2 is a low energy molecule while methane is a much higher energy one. This is clearly demonstrated during the combustion of methane when large amounts of energy are released in the form of heat. As high to low energy reactions are favoured, the reverse reaction (methane to CO_2) is favoured over the desirable one (CO_2 to methane). TiO_2, as a catalyst, can perform the reaction in both directions, increasing only the rate of both. The energy difference between the molecules needs to be given to CO_2 in the process of the photoreaction and it is provided by the light that is absorbed by the photocatalyst.

The anatase crystal form of TiO_2 is the most reactive (Yamashita et al. 1994), but pure anatase has been shown to be a lot less efficient than metal-doped TiO_2, and doping also greatly increases the rate of reduction (Tseng et al. 2002). TiO_2 is usually doped with metals such as Cu or Pt (Varghese et al. 2009). Recent studies investigating the use of catalyst that absorbs visible light include that of Varghese et al. (2009), who used nitrogen-doped TiO_2 and performed the reaction outdoors using sunlight. They report yields 20 times higher than previous studies in the literature. However, the photocatalysis was primarily due to UV irradiation in the sunlight as using UV filters decreased the rate to 3% of that with unfiltered solar spectrum.

The mechanism of photoreduction is described in figure 1.6 and is based on (Indrakanti et al. 2009, Wu 2009) and (Dey 2007). As can be seen in box 1 of figure 1.6 the energy from a light photon that is absorbed by the catalyst can excite an electron, leaving a positive hole behind. This electron-hole pair will rapidly recombine so that the light energy is dissipated as heat. This is another factor making TiO_2 inefficient as it means that only a small fraction of the light energy is stored in chemical form in the products. The number of recombinations can be decreased by metal doping, which creates electron traps. A CO_2 molecule can be adsorbed on the surface and take up an electron, becoming more reactive. Box 2 shows the water dissociation into a proton (H^+) and a hydroxide ion (OH^-). Two adsorbed protons and another electron from the catalyst surface will react with the active CO_2 and reduce it further. Another six electrons and six protons need to be added to the carbon atom to produce methane. Parallel to the carbon reduction there is another process, the hydroxide oxidation (box 4). The hydroxide ion works as a hole scavenger, neutralising the hole on the catalyst surface and forming a hydroxyl radical. As a result the water solution inside the reactor will contain oxygen radicals and be reactive. This process leads to O_2 production.

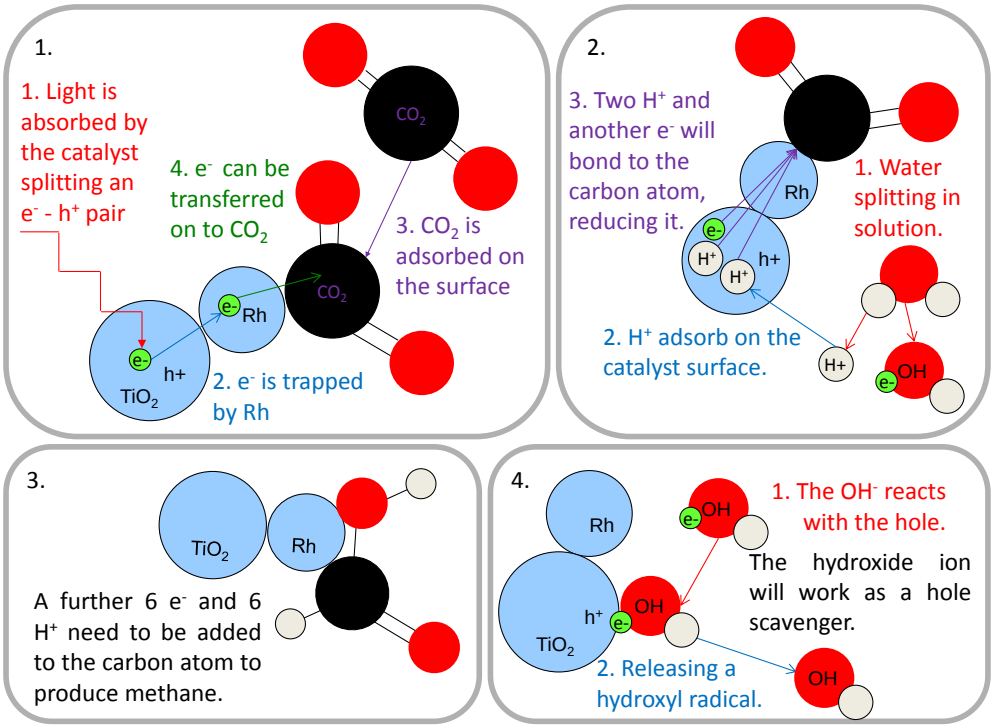

Figure 1.6: The mechanism of CO_2 photoreduction on Rh-doped TiO_2 catalyst. Box 1: Catalyst excitation and CO_2 adsorption. Box 2: Water splitting and first reduction step. Box 3: Further reduction reactions. Box 4: Hole scavenging.

1.5 Improving the existing catalyst

One of the issues with the use of TiO_2 for solar energy and solar fuel applications is that it has a large band gap which means that it absorbs UV but not visible light photons. One of the modifications that have been reported in the literature to enable visible light utilisation is dye-sensitisation of the TiO_2 catalysts. Plants also have special complexes (such as LHCII) that absorb visible light and pass on the light energy to enzymes which perform water splitting and, through the electron transport chain, are responsible for CO_2 reduction. A rather different mechanism is used in dye-sensitised TiO_2 where the light harvesters (dyes) pass on an electron directly. The dye molecules used can absorb light of longer wavelengths compared to the catalyst, but their excited state is energetically higher than the conduction band of TiO_2, which allows electron injection from the dye to the catalyst. This method, which has been used extensively in photovoltaic applications, is discussed in (Grätzel 2005).

There are also reports of its use for CO_2 photoreduction (see references in Table 1.1), where the product yield is improved by the use of dyes. However, dyes may be used up by the photocatalysis because they pass electrons on to the catalyst, instead of light, and are unable to extract them from water in order to regenerate (Indrakanti et al. 2009). Therefore, the stability of these dye-sensitised catalysts needs to be assessed together

with their efficiency.

The work of Nguyen et al. (2008) showed improved photoreduction of CO_2 to methane for catalyst samples with the ruthenium-containing N3 dye, compared to catalyst without dye, in a gas phase continuous flow reactor under concentrated natural sunlight. On the other hand they observed that when using artificial light of < 500 nm wavelength, the presence of the dye does not increase the yield of the catalyst but instead gives a small decrease. The absorption maximum of the dye, as seen in the same paper, is above 500 nm, suggesting that it does not absorb light as efficiently in the artificial light reaction. Furthermore, the presence of the dye on the catalyst surface could be blocking some reaction sites. Therefore, while in sunlight the effect of the blocked sites may be masked by the more efficient light harvesting, the same does not happen for the artificial light, where the dye is not necessary to absorb the light energy. Finally, the N3 dye is shown to be stable during the reaction by measuring UV-Vis spectra before and after reaction.

Ozcan et al. (2007*b*) describe the utilisation of visible light for CO_2 photoreduction with perylene diimide dyes as well as another Ru-dye, tris (2,2'-bipyridyl) ruthenium(II) chloride hexahydrate (RuBpy), using a gas phase reactor. One of the perylene diimide dyes, which were synthesised in their lab, gives an increase as high as the RuBpy dye (Table 1.1), while they report that there was no visible light activity in the absence of a dye. There is no evidence reported regarding the stability of the dyes in visible light but, in a second paper that year (Ozcan et al. 2007*a*), the lack of stability of the RuBpy dye under UV light is shown, with experiments re-using the same catalyst-dye sample having reduced yields.

Another group used metallophthalocyanines impregnated in TiO_2 by a range of methods and found high yield of reduced C_1 products under visible light (Zhao et al. 2007, Liu et al. 2007, Zhao et al. 2009). The main product they found was formic acid, but they also measured CH_4 production, which was higher than that in other studies discussed in this section, and other gas and liquid products. This higher yield may be partly explained by some differences in the experimental procedure between this work and others, such as the higher light intensity used in their reaction. They also do not report the use of any filters, so there may be some UV irradiation exciting the TiO_2. This is supported by the fact that some reduced molecules are also produced on unmodified TiO_2 (Table 1.1). Additionally they ran the reaction for 10 h, which is longer that the experiment times for the other catalysts. It is noteworthy that their catalyst shows a continuing increase of yield for even longer than 10 h (the next measurement is at 20 h and the product yield levels off after that). Finally they perform the reaction in an aqueous NaOH solution. OH^- ions from the NaOH can act as hole scavengers and therefore assist CO_2 reduction. Even considering these differences however, the increase in yield is still substantial.

It is interesting that, in (Liu et al. 2007), the same group report a higher yield of methane for unmodified than for the optimal sensitised catalyst. The formic acid follows a different pattern and the optimisation they carried out was based on total reduced carbon which is mainly affected by the

Photocatalyst	Product yield	Modification technique	Amount of catalyst	Photo-reactor	Light source	Time	Reference
Sol-gel TiO_2	1.0*wt*% ZnPc by *in situ* chemical synthesis	CH_4: 133.2 µmol/g (cat) HCOOH: 978.6 µmol/g (cat)	0.15 g	0.1 M NaOH aqueous solution	500 W tungsten-halogen lamp. Visible light, no filter	10 h	Zhao et al. (2007)
	Unmodified	CH_4: 16.7 µmol/g (cat) HCOOH: 321.0 µmol/g (cat)					
Sol-gel TiO_2	1.0*wt*% CoPc by *in situ* chemical synthesis	CH_4: $\sim$ 40 µmol/g (cat) HCOOH: $\sim$ 130 µmol/g (cat)	0.15 g	0.1 M NaOH aqueous solution	500 W tungsten-halogen lamp. Visible light, no filter	10 h	Liu et al. (2007)
	0.5*wt*% CoPc by *in situ* chemical synthesis	CH_4: $\sim$ 10 µmol/g (cat) HCOOH: $\sim$ 290 µmol/g (cat)					
	Unmodified	CH_4: $\sim$ 35 µmol/g (cat) HCOOH: $\sim$ 125 µmol/g (cat)					

Sol-gel TiO_2	$0.7wt\%$ CoPc by *in situ* chemical synthesis	HCOOH: 1487.6 µmol/g (cat) Total organics (HCOOH+HCHO+CH_4): 1714.9 µmol/g (cat)	0.15 g	0.1 M NaOH aqueous solution	500 W tungsten-halogen lamp. Visible light, no filter	10 h	Zhao et al. (2009)
P25 TiO_2 nanoparticles. Pt on TiO_2 surface by wet impregnation.	CdSe (2.5 nm, 6 nm diameter) Quantum Dots, Chemically prepared	CH_4: $\sim$ 1.1 µmol = 0.611 µmol/g (cat) h^{-1}, CH_3OH: 3.3 ppm/g (cat) h^{-1}	0.3 g	Gas phase reactor	300 W Xe arc lamp. Filter so that $>$ 420 nm light only used. Final intensity: $\leq$ 100 mW/cm^2	6 h	Wang et al. (2010)
TiO_2 thick films ($>$ 1 µm) (by sol-gel) on borosilicate glass. Pt on TiO_2 surface by wet impregnation.	RuBpy dye-sensitised	CH_4: $\sim$ 7.7 µmol/g (cat)	-	Gas phase reactor	75 W daylight lamp	3 h	Ozcan et al. (2007b)
	BrAsp dye-sensitised	CH_4: $\sim$ 7.6 µmol/g (cat)					

P25 Evonik Aeroxide	RuP dye-sensitised. CODH I enzyme for CO_2 to CO conversion	CO at 20°C: ~ 5 µmol $= 250$ µmol/g (cat) h^{-1} CO at 50°C: ~ 12 µmol $= 600$ µmol/g (cat) h^{-1}	5 mg	200 mM MES solution (pH 6). 2% CH_4 as standard.	Tungsten-Halogen lamp 45 mW/cm^2. Filter so that only use light > 420 nm	4 h	Woolerton et al. (2010)
P25, Degussa TiO_2, Coated on optical fibre, Cu-doped	N3 (Solaronix) dye-sensitised	CH_4: 0.847 µmol/g (cat) h^{-1} C_2H_4: 0.562 µmol/g (cat) h^{-1}	-	Optical fibre gas phase reactor.	Hg lamp 150 W, $320 - 500$ nm (225 mW/cm^2)	4 h	Nguyen et al. (2008)
	Without dye	CH_4: 0.914 µmol/g (cat) h^{-1} C_2H_4: 0.575 µmol/g (cat) h^{-1}					
	N3 (Solaronix) dye-sensitised	CH_4: 0.617 µmol/g (cat) h^{-1} Light intensity: 20 mW/cm^2	-	Optical fibre gas phase reactor.	Concentrated natural sunlight Up to ~ 800 nm		
	Without dye	CH_4: 0.281 µmol/g (cat) h^{-1} Light intensity: 60 mW/cm^2					

Table 1.1: Comparison of dye-sensitised CO_2 photoreduction work in the literature. The catalysts and dyes used are shown, as well as the experimental conditions and the products reported.

formic acid, as that is the main product. In the case of formic acid we also see that a low dye concentration is optimal ($0.7wt.\%$) (Zhao et al. 2009). These results can be related to that by Nguyen et al. (2008) who found that the presence of the dye is detrimental to the photoreduction under short wavelength light. The dye may here also be partially blocking the active sites so that too much of it is prohibitive rather than helpful. Finally, they have performed a control experiment without CO_2, confirming that the products are coming from CO_2 and not from organics left on the surface of the catalyst or dye breakdown.

Wang et al. (2010) used CdSe quantum dots instead of organic dyes to sensitise TiO_2. They report no activity for unsensitised catalyst under visible light (> 420 nm) but see significant methane production with $CdSe/Pt/TiO_2$ in a gas phase reactor (Table 1.1). However the hole accumulation on the catalyst leads to CdSe oxidation and therefore the catalyst is not active after 6 h. The yield is comparable to that of Nguyen et al. (2008) for the natural light. However, great care must be taken when making direct comparisons of yields as the reactor set up, amount/concentration of catalyst, light quality and intensity and other environmental factors may be affecting the production of reduced molecules.

A rather different approach was taken by Woolerton et al. (2010), who also attached a Ru-containing dye on TiO_2 but used an enzyme to perform the catalysis of CO_2 to CO. In this case, the TiO_2 acts as a support for the dye and enzyme and allows electrons to pass from the dye sensitiser, through itself, to the enzyme. Though it is clear that the production rate decreases after the third hour, appropriate control experiments carried out by the group, rule out photodamage of sensitiser or enzyme as the cause for this decrease.

1.6 Modelling chemical reactions

Mathematical modelling can be used to investigate chemical reaction systems, to better understand their dynamics and steady state conditions. Depending on the questions one wants to answer, the system under investigation and the data available, different types of models can be used to simulate the chemical system. The assumptions made about the system are linked to the type of model that is selected. If it is assumed that the system is well mixed, then no spatial effects are expected, and the change in concentration of chemicals can be modelled using a system of ordinary differential equations (ODEs). In this case, each variable of the model represents the concentration of each chemical, a continuous variable, and it is assumed that this concentration is the same uniformly in space (spatially homogeneous). Mitchell et al. (2010) used a system of ODEs to model the injection of CO_2 into saline aquifers for the application of CCS.

For other systems, spatial effects may be central to the progress of the model and in those cases partial differential equations (PDE) can be used for continuous variables, where it is not assumed that the system is spatially homogeneous (e.g. PDE model for CO_2 uptake in leaves (Parkhurst 1977)). ODE and PDE models, are deterministic approaches to the problem assuming a large sample where random effects are very small and the average

gives a good estimate of the whole system. On the other hand, stochastic differential equations (SDE), which are also used to model continuous variables, are a stochastic approach as they explicitly include random effects (e.g. the SDE models of aquatic ecosystems (Tiwari et al. 1978)).

If a discrete variable is under investigation, such as the absolute number of molecules instead of the concentration of a chemical, then a differential equation model would not be appropriate. Especially in cases of small samples, where stochastic effects may be important, a stochastic simulation algorithm, such as the Gillespie algorithm, could be used instead. In fact, this algorithm can be used for simulating reactions both with and without spatial effects. In the case with spatial effects, it does so by separating the space into compartments, treating space as a discrete variable. A good introduction to stochastic simulations of reaction-diffusion processes can be found in (Erban et al. 2007).

All of the methods mentioned above model systems in continuous time. Discrete time models can also be used with a fixed time step. These include difference equations (continuous variables) and cellular automata (discrete variables) amongst others. ODE models (using the mass action law) and continuous time, discrete space stochastic simulations (using the Gillespie algorithm) will be used in the current thesis to model the photoreduction of CO_2 using TiO_2 catalysts and so will be discussed further in this section.

1.6.1 ODE models with simple mass action

The law of mass action states that "the rate of an elementary reaction is proportional to the product of the concentrations of the participating molecules, raised to a power equal to the stoichiometric coefficient" (Marin & Yablonsky 2011). This is because the probability of a molecule of each reactant being in a particular position (so that they are close to one another) is proportional to its concentration. This law is often used to estimate the rates of reactions in ODE models and it was selected here for the modelling of CO_2 photoreduction.

Another common model, used for enzyme catalysed reactions in particular, is the Michaelis-Menten equation, which is a special case of a mass action-derived equation. However, this assumes no backwards reaction which is not an appropriate assumption for the photoreduction reactions. Additionally the TiO_2 has many active sites each of which can perform a few different reactions and specificity is also important for the Michaelis-Menten model making it an ill-fitting choice.

Two simple ODE models of photosynthesis and photorespiration were developed by Hahn (1991) using the law of mass action. These focused on the identification and analysis of the steady states of the models. Great insight could be gained by these simple models, which suggested that photorespiration could have a stabilising role for photosynthesis. Simple ODE models were also developed in the current thesis for CO_2 photoreduction to investigate the steady state of the reaction.

A famous photosynthesis model, that makes use of Michaelis-Menten kinetics, is that of Farquhar et al. (1980) which investigates the ETC, Calvin cycle and photorespiration. It has continued to develop over the past

30 years (von Caemmerer et al. 2009, von Caemmerer 2013). Depending on environmental conditions of photosynthesis, the ETC reactions or the carbon reactions may be the rate limiting process. This can be modelled with the following primary equation

$$A = V_c(1 - \tfrac{1}{2}\phi) - R_d, \tag{1.1}$$

where A is the CO_2 assimilation rate, V_c is the carboxylase rate, ϕ is the ratio of oxygenase to carboxylase rates and R_d is the "dark respiration". The two cases (with thylakoid reactions or carbon reactions being rate limiting) can be studied separately, using this equation as a backbone.

If the carbon reactions are rate limiting, this translates to RuBP being regenerated fast, such that Rubisco is saturated and working at its maximum activity. The carboxylase rate can be calculated in terms of the Michaelis-Menten constants (K_c, K_o) and maximal carboxylase and oxygenase rates of Rubisco (V_{cmax}, V_{omax}) and the CO_2 and O_2 partial pressures (C, O), most of which can be determined experimentally in vivo and in vitro.

If on the other hand the light reactions are rate limiting, in which case RuBP will not be regenerated fast enough, as there will not be enough NADPH and ATP, the carboxylase rate can be calculated in terms of J, an empirical variable linking potential electron transport rate to irradiance, ϕ and the CO_2 partial pressure, C.

A third case is also considered where the export of the products of the Calvin cycle limits the rate of photosynthesis. This appears to be because the rate of export of GAP from the chloroplast is equal to the rate of import of inorganic phosphate, which is necessary to perform photosynthesis. The rate constants for this model are also determined experimentally, and the authors propose an equation to make corrections for temperature effects. This gives a model which predicts the overall rate of photosynthesis under many different environmental conditions and can be used to make predictions for systems that have not yet been genetically engineered.

Plant photosynthesis is a very interesting area of research and many more models exist that take different approaches to investigate it, such as those in chapters of (Laisk et al. 2009).

1.6.2 Langmuir isotherm

The reactions in the system discussed in this work occur on the catalyst surface so adsorption of the reactants on to the catalyst is an important process. Therefore, in a detailed ODE model developed in this thesis, the Langmuir isotherm was used for adsorption and Langmuir-Hinshelwood kinetics for the reactions of CO_2 photoreduction. A central concept for both mechanisms is the coverage which is defined as

$$\text{coverage} = \frac{\text{sites occupied by reactant}}{\text{total number of sites on surface}}. \tag{1.2}$$

The Langmuir isotherm makes the following assumptions (Logan 1996):

- There is a finite number of sites on the surface, each of which can take one molecule of adsorbate, and all sites are equivalent in terms of adsorption.

- The probability of adsorption of a molecule, following a collision with an empty surface site, is independent of the total coverage of the surface.
- The probability of desorption of an adsorbed molecule is independent of the total coverage of the surface.

If θ_i is the coverage of a compound i, then

- $r_{ads} = k_i p_i \theta_E$, where r_{ads} is the rate of adsorption, k_i is the adsorption rate constant, p_i is the partial pressure of compound i and θ_E is the coverage of empty surface sites (E), and
- $r_{des} = k_{-i}\theta_i$, where r_{des} is the rate of desorption and k_{-i} is the desorption rate constant.

k_i and k_{-i} are related to the probability of adsorption and desorption respectively. At equilibrium,

$$k_i p_i \theta_E - k_{-i}\theta_i = 0. \tag{1.3}$$

Therefore

$$\theta_i = K_i p_i \theta_E \tag{1.4}$$

where

$$K_i = \frac{k_i}{k_{-i}}. \tag{1.5}$$

So, for n adsorbates, the fraction of filled sites (θ_f) is

$$\theta_f = \sum_{i=1}^{n} K_i p_i \theta_E \tag{1.6}$$

and finally, because $\theta_f = 1 - \theta_E$,

$$\theta_E = \frac{1}{1 + \sum_{i=1}^{n} K_i p_i}. \tag{1.7}$$

The Langmuir-Hinshelwood mechanism for two reacting species assumes that the two are first adsorbed on the surface and then react (Logan 1996). The rate of a reaction is then proportional to the coverage of the surface by each reactant. Therefore, in the case of gaseous reactants, the rate of a reaction can be related to the partial pressures of the reactants through the Langmuir isotherm. This mechanism has been used to model CO_2 photoreduction in gas phase reactors in the literature (Wu et al. 2005, Tan et al. 2008).

1.6.3 Discrete stochastic model

A more complex, stochastic model was also developed in this work, where the surface of the catalyst is modelled as discrete sites. This simplification was made because the catalyst surface can naturally be separated into different sites depending on the surface atom present on that site (Ti or O). Interesting patterns made up of the positions of these two atoms can thus be modelled on the surface using this method. Both continuous and discrete time approaches were tested for this model. A discrete time model was

developed first which considered all possible reactions everywhere on the surface at each time step. All reactions of a particular type were performed together, which led to a bias in the reaction order as well as averaging within each time step. It was possible to avoid both of these drawbacks by making the timestep very small, but this made the simulation very inefficient and time-consuming and so no results are presented from this model.

A more efficient, continuous time alternative is presented in Chapter 6. For continuous time stochastic simulations of discrete variables, the Gillespie algorithm is often used for its efficiency (Erban et al. 2007). An algorithm with a predetermined time step would have to carry out many cycles where no reaction takes place if it were to have a time step small enough to give accurate results. The dynamic time step of the Gillespie algorithm allows it to have one reaction at every cycle. Additionally it allows for discrete events to be modelled in continuous time.

1.7 Objectives of this thesis

The objective of this thesis is to improve CO_2 photoreduction by two approaches. The first is by immobilising the Light Harvesting Complex II (LHCII) on to the catalyst surface as this can potentially be used to pass on light energy to the catalyst, increasing the amount of light used by the catalyst, and switching the quality of the light to the more desirable, visible light wavelengths. The second is by mathematically modelling the reactions taking place on the catalyst surface to enhance the understanding of the process and to identify key areas for optimisation.

Chapters 2–3 describe the methods and results respectively used to investigate the interaction between the LHCII and the catalyst. Chapter 2 describes the methods for LHCII isolation and catalyst preparation as well as the analysis techniques of the combined material. Chapter 3 then shows the experimental results obtained from the analysis of these novel hybrid catalysts as well as the evidence for interaction between the two compounds. Various hybrid catalyst preparation methods were tested, to investigate the optimisation of the attachment for maximum photocatalytic activity and stability.

Chapter 4 shows the effect that LHCII attachment on the catalyst has on photoreduction. Three organic compounds are measured experimentally as well as CO and hydrogen production. The results presented in that chapter show that LHCII enhances the photocatalytic activity of TiO_2:Rh for most products, compared to the pure catalyst.

Chapters 5–6 describe the mathematical models that were developed for artificial photosynthesis. ODE models developed using the law of mass action are presented in Chapter 5. A simplified mechanism is used at first, and complexity is added with every subsequent model. Various products are investigated, but the focus is limited to organic compounds containing one carbon atom as well as hydrogen and oxygen. The final model presented in Chapter 5 is the ODE equivalent to the discrete model presented in Chapter 6, using the Langmuir isotherm for adsorption and the Langmuir-Hinshelwood mechanism for the reactions. Chapter 6 presents a discrete space, stochastic model simulated using the Gillespie algorithm.

Finally, Chapter 7 discusses the current systems of CO_2 photoreduction and water splitting in comparison to an ideal artificial system. Comparisons are drawn with natural systems that are often used, not only as inspiration, but also as parts of hybrid systems such as this. The mechanism of the photoreduction enhancement due to LHCII is then considered. The mathematical modelling of natural and artificial photosynthesis in the literature is briefly discussed together with the current modelling work. Finally, a conclusion is drawn about the viability of the system presented in the current thesis for applications in the near and extended future.

Chapter 2

Experimental Methods For Catalyst Preparation And Analysis

In this chapter, the experimental methods that were used to prepare and analyse the novel hybrid photocatalysts are described. Figure 2.1 shows the flow of these methods, starting from the preparation of the materials (TiO_2 and LHCII) and moving to their combination to create the hybrid catalyst and finally the analysis of this hybrid catalyst. The experiments of CO_2 photoreduction are described in Chapter 4. As well as the investigation of LHCII attachment on TiO_2, the middle column of figure 2.1 also includes the analysis of LHCII so as to compare pure LHCII to that attached to the catalyst.

2.1 The sol-gel method for TiO_2 catalyst preparation

The catalyst used in all experiments described in this thesis was prepared by a sol-gel method (Hench & West 1990) developed specifically to produce uniform TiO_2 nanoparticles (Wu et al. 2001). This method was shown to produce improved photocatalyst for CO_2 photoreduction (Tseng et al. 2002).

A sol is a liquid with colloidal particles dispersed throughout it. A gel is a liquid containing an interconnected, solid network which gives the combined material properties of both a liquid and a solid. In the sol-gel method, the colloidal particles of the sol are monomers which polymerise forming the network of the gel. In the method that will be described, the polymerisation occurs through hydrolysis and polycondensation, where water hydrolyses an alkoxide (a Ti(IV)-butoxide in this case) and then polycondensation forms a polymer and water molecules out of the hydrolysed monomers.

In the sol-gel method used for uniform TiO_2 nanoparticles, the hydrolysation needs to be slow and homogeneous to avoid formation and precipitation of large titania particles. Therefore an additional step was added to the process by Wu et al. (2001), the slow and homogeneous release of

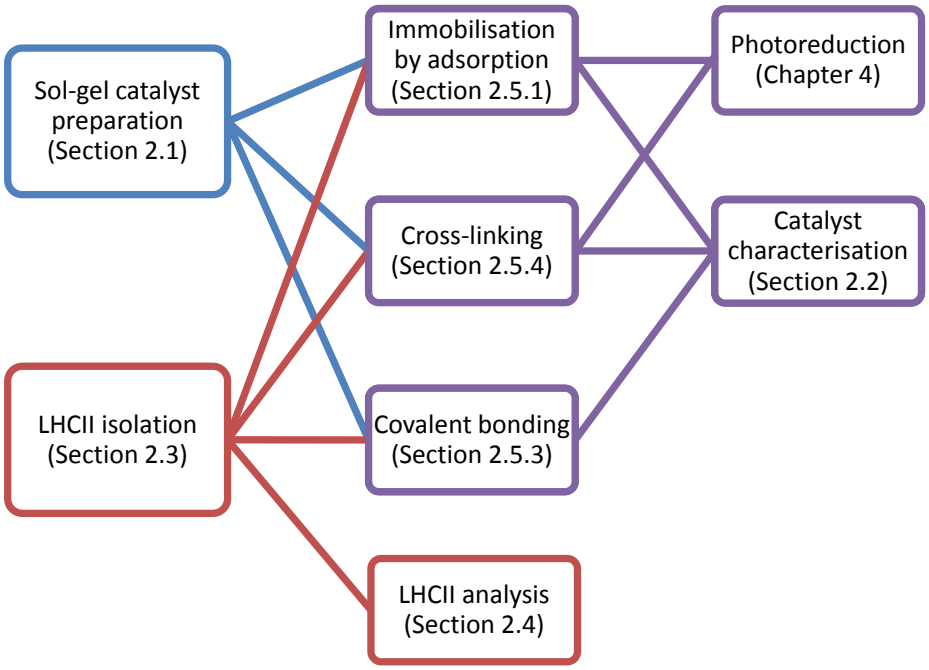

Figure 2.1: The relationship between the methods presented in this chapter. Methods on the right require input from methods on the left, as indicated by the connections.

water by esterification of the solvent components.

As the purpose of the preparation was an improved photoreduction catalyst, it was metal-doped by Rh (doping ratio of $0.02wt\%$), which enhances the catalytic activity of TiO_2 (Liu 2012). This doping metal was selected because it showed high yields using UV light in Liu (2012). Optimisation with respect to doping ratio in photoreduction with UV light was performed by Liu in the same study and the doping ratio used here gave the second highest product concentration. The absorption in visible light of this catalyst was higher than that of the optimum catalyst for UV light experiments and therefore it was used as the base for the hybrid catalyst developed in this work. For some experiments, Cu-doped TiO_2 was used instead with a doping ratio of $0.03wt\%$, which showed similarly high yield in Liu (2012). Optimisation with respect to doping metal and doping ratio in visible light experiments was not carried out in this work as the dye sensitisation was its focus.

The sol-gel method was started by adding the Ti-butoxide to the n-butanol (see table 2.1 for quantities). For the doped sample, the metal precursor (Rh-acetate 1 g/L in n-butanol for Rh-doped and $CuCl_2$ 50 g/L in n-butanol for Cu-doped) was first mixed with the n-butanol. Finally, the glacial acetic acid was added. Once the final step is completed, water will be released homogeneously throughout the solution from the esterification of the acid and the n-butanol. This water will hydrolyse the Ti-butoxide

Material	Amount
Titanium-butoxide	0.02 mol or 6.8 g
Rh-acetate (1 g/L) in n-butanol	690 µL
$CuCl_2$ (50 g/L) in butanol	25.8 µL
n-Butanol (including amount from precursor)	0.08 mol or 5.92 g
Glacial acetic acid	0.08 mol or 4.8 g

Table 2.1: Proportions of chemicals used for TiO_2 preparation

which in turn will form a polymer of Ti-O-Ti bonds that is the precursor of TiO_2. The hydrolysis will be slow so the sample was mixed with a magnetic stirrer for 6 h to achieve full hydrolysis. It was then poured into a crucible and placed in a CWF 1100 Chamber Furnace (Carbolite Ltd., Hope, UK). There were two steps carried out in the furnace. The first was the drying of the gel where the mixture was heated up to 150°C at a rate of 3°C/min and held at that temperature for 2 h. The mixture was then heated to 500°C at a rate of 5°C/min and held there for 1.5 h for the calcination step. This temperature ensured the removal of all organics (hydrocarbons were burned) and that the crystal form of the catalyst was anatase, which is the most reactive form (Yamashita et al. 1994). After the sample had cooled down, it was manually crushed into powder using a mortar and pestle for 25 min.

2.2 Catalyst characterisation methods

X-Ray Diffraction (XRD), Transmission Electron Microscopy (TEM) and UV-Vis absorption spectrometry were performed on selected catalysts at the University of Nottingham. N_2 adsorption (BET, named after Brunauer, Emmett and Teller who developed the theory this method is based on) and Scanning Electron Microscopy - Energy Dispersive Spectroscopy (SEM-EDS) were performed by Professor J.C.S. Wu's group at the National Taiwan University in Taipei.

The XRD analysis was performed by Mr David Clift using an X-ray powder diffractometer (Hiltonbrooks Ltd, Crewe, UK). Crystal structure determination by X-ray diffraction is based on the principle of interference. Two waves that are out of phase will reinforce or cancel out one another depending on the phase difference. Figure 2.2 shows two waves travelling radially from different origins and out of phase. Plot a shows them separately while plot b shows their interference pattern. Depending on where an observer stands around the sources, the intensity (amplitude) of the wave reaching them will differ. Similarly, in XRD analysis, the X-rays are scattered radially outward from each electron. For a regular crystal structure, the distance between the planes of the crystal, and therefore the atoms, is related to the angles at which the diffracted X-rays are in phase and therefore reinforced and detected. To measure these angles, an X-ray beam of a known wavelength is incident upon the sample at angle θ and the detector measures the intensity of the beam reflected at angle θ relative to the sample, and so 2θ relative to the initial beam (illustrated in figure 2.3).

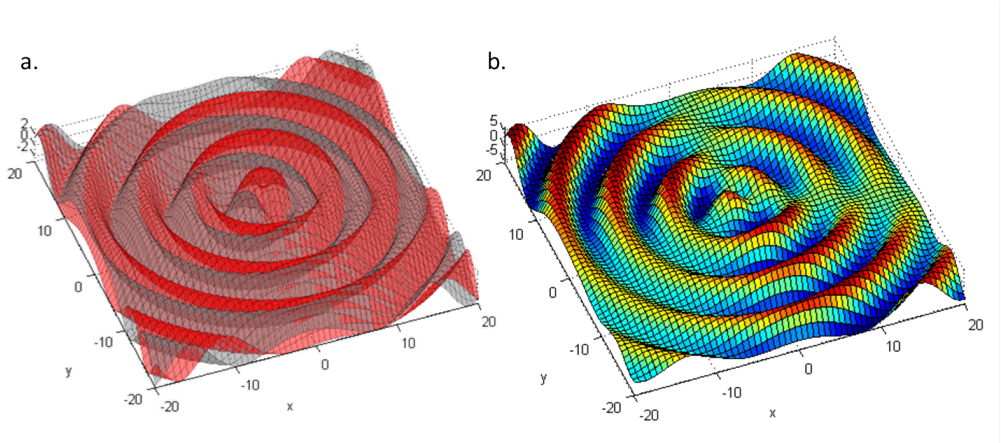

Figure 2.2: Two sinusoidal waves with origins (-1,1) (grey) and (2,3) (red) plotted separately (a) and their interference pattern (b).

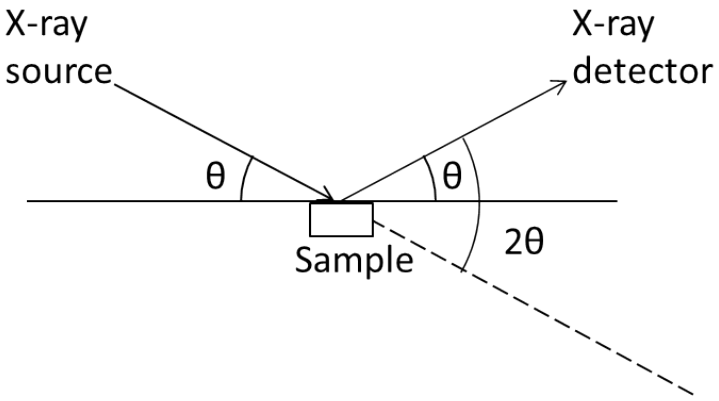

Figure 2.3: Diagram of XRD analysis.

The relationship between the angles (θ), at which the diffracted X-rays are in phase, and the interplanar distance d, is given by the "Bragg Law"

$$2d\sin(\theta) = n\lambda, \tag{2.1}$$

where n is a positive integer and λ is the wavelength of the X-ray (Waseda et al. 2011).

While the angle at the peaks gives information about the crystal structure, the width of the peaks can be used to estimate the crystallite size. Crystallites are very small crystals that make up the particles of the powder sample. Their size is related to peak width by the Scherrer equation

$$D = \frac{0.9\lambda}{B_{1/2}\cos(\theta_M)}, \tag{2.2}$$

where D is the diameter of the crystallite, λ is the wavelength of the X-ray, $B_{1/2}$ is the width of the maximum peak at half its maximum intensity and θ_M is half the angle (2θ) of the maximum peak (Waseda et al. 2011).

The TEM imaging was performed by Dr Michael Fay using a 2100F TEM, JEOL Ltd., Tokyo, Japan. The catalyst was placed on a carbon

grid and visualised at high resolution. The surface of the catalyst was visualised by SEM with a LEO 1530 Field Emission Scanning Electron Microscope (LEO Electron Microscopes, Cambridge, UK), with an energy-dispersive X-ray spectroscopy system. No fixation or staining was used for either the SEM or the TEM analyses.

For the N_2 adsorption, an ASAP 2020 (Micromeritics, Norcross, GA, U.S.A.) was used to obtain the specific surface area and pore size distribution of the catalysts.

2.3 LHCII isolation from spinach leaves

LHCII was isolated from spinach (*Spinacia oleracea*) leaves by isoelectric focusing (IEF) of PSII BBY particles as described in (Ruban et al. 1994).

2.3.1 BBY preparation

BBY particles were extracted from commercial spinach leaves bought from the supermarket (baby leaves) or a London street market (mature leaves). The leaves were dark-adapted overnight in the fridge to decrease the amount of starch present in them and their mid-ribs were removed. 80 g of the remaining leaf material were mixed with 300 mL grinding medium. This contained 0.33 M Sorbitol, 10 mM $Na_4P_2O_7.H_2O$ (pH was adjusted to 6.5), 5 mM $MgCl_2$ and 2.5 mM D-isoascorbic acid (added immediately prior to use), and had been placed in the freezer with a metal spatula to form ice crystals and obtain a "slushy" composition. The mixture of leaves and medium was homogenised using a blender and then filtered through two layers of wet muslin, followed by eight layers of muslin and one of cotton (also wet with de-ionised (DI) water prior to filtering). The muslin was used to remove the insoluble leaf material and the cotton layer to remove the starch present in the leaves. The suspension was kept on ice throughout the following procedure to minimise damage to the LHCII.

The filtered suspension was centrifuged at $4000g$ ($\sim$ 5100 rpm) for 5 min. The temperature inside the centrifuge was kept at 4°C throughout. The supernatant was discarded and the pellet was resuspended in washing medium which consisted of 0.33 M Sorbitol and 10 mM 2-(N-morpholino)-ethanesulfonic acid (MES) (pH was adjusted to 6.5). It was then again centrifuged ($4000g$) for 7.5 min (at 4°C) and the pellet was resuspended in 30 mL of resuspension medium. This consisted of 0.33 M Sorbitol, 5 mM $MgCl_2$ and 40 mM MES (pH 6.5). A squirrel tail brush was used to softly break the pellet and make the suspension homogeneous. Sorbitol was used in the previous media to ensure that the osmotic pressure is approximately equal inside and outside of the membranes to keep them intact. A medium without Sorbitol, containing only 5 mM $MgCl_2$ (pH 7.6), was used to osmotically shock the membranes in order to break the chloroplasts and release the thylakoids. 50 mL of this break medium were added to the suspended pellet for 30 s. After that time, 50 mL osmoticum medium were added to the suspension to return the osmotic potential to normal. This contained 0.66 M Sorbitol, 5 mM $MgCl_2$ and 40 mM MES (pH 6.5). The thylakoids were then centrifuged ($4000g$) for 10 min (at 4°C).

The chlorophyll content of the thylakoids was estimated at this stage using 80% acetone by the method described in Section 2.4.3. The thylakoids were then resuspended to a final chlorophyll concentration of 3 mg/mL using stacking medium to dilute the pellet. The stacking medium contained 5 mM $MgCl_2$, 15 mM NaCl and 2 mM MES (pH 6.3). They were left in the dark for 45 min without stirring to allow the membranes to stack. Triton solution was added to give a final triton concentration of 3.33% and the thylakoids were left in the dark for a further 30 min with occasional mixing. More stacking medium was then added ($3 - 6$ mL) to dilute the detergent and the suspension was centrifuged at $30,000g$ (19,000 rpm) for 30 min. The resulting pellet was resuspended in particle wash medium, containing 2 mM Ethylene-diamine-tetra-acetic acid (EDTA) (pH 7.5) and again centrifuged for 30 min at $30,000g$. The pellet was resuspended with DI H_2O to a chlorophyll concentration of 2.5 mg/mL.

2.3.2 IEF method

For the IEF, a gel ampholine slurry was prepared containing 97.5 mL DI H_2O, 2.5 mL ampholines (pH 2.5–5), 1 g glycine, 60 mg n-Dodecyl β-D-maltoside (βDM) and 4.6 g Sephadex G-75 gel. It was poured into a tray containing six electrode strips, three on each end of the tray, which were soaked in a 2% ampholine solution. The tray was placed on a balance with a fan $\sim$ 70 cm above it to help evaporate 37 g of the water in the slurry. Once the desired consistency was reached, the tray was moved to the cooling plate of the Pharmacia Multiphor II Electrophoresis system (Pharmacia Biotech, Uppsala, Sweden), with a small amount of 0.1% Triton X-100 solution placed between the tray and the plate to ensure good thermal contact. One electrode strip was soaked in anode strip solution (1 M H_3PO_4) and another in cathode strip solution (1 M NaOH) and they were placed at opposite ends of the tray, on top of the existing strips. The electrodes were then applied to the tray, matching the charges appropriately, and the power supply was turned on at 8 W, resulting in a current of $\sim$ 13 mA and a voltage of 600 V. This was to prefocus the gel and lasted for at least 45 min.

Each run of the IEF can separate a BBY sample with a chlorophyll content of 5 mg, therefore 2 mL of the BBY preparation were mixed with 1 mL of 3% βDM to prepare the sample for IEF. The sample was then kept in a sealed container for 60 min and a vortex was used to mix it every 10 min.

After the 60 min, the sample was placed in the tray at a distance of 2 cm from the cathode, using the sample applicator. This was achieved by removing the part of the gel inside the applicator and mixing it with the sample before refilling the applicator with it. The electrodes were then placed back and the system was again turned on and run overnight. The final current was $\sim$ 5.5 mA and the voltage $\sim$ 1500 V. Finally, the band corresponding to LHCII (see figure 2.4) was removed and filtered to obtain the LHCII without the gel particles. Elution buffer, containing 25 mM 4-(2-Hydroxyethyl) piperazine-1-ethanesulfonic acid (HEPES) (pH 7.6) and 0.01% βDM, was used to elute the LHCII from the gel. This was also the

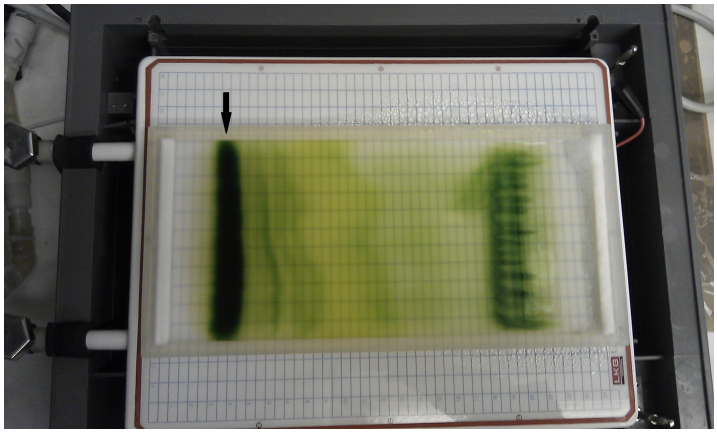

Figure 2.4: IEF bands from BBY preparation. The arrow indicates the band corresponding to LHCII. Other bands are faint as BBY is rich in LHCII compounds.

solution used to store the LHCII.

2.4 Spectrophotometry and measuring chlorophyll content

2.4.1 UV-Visible light absorption spectra of catalyst powder

UV-Visible light absorption spectra of powder samples were obtained using a UV-Vis spectrophotometer (Cary 300, Varian, Crawley, West Sussex, UK). Approximately 0.5 g of dry catalyst powder were loaded into an indented flat quartz sample holder so that the catalyst made a thick flat smooth opaque layer against the inner wall of the UV-transparent sample holder. This layer absorbed some of the light, different amounts depending on the wavelength of the light, and reflected the light that the catalyst did not absorb. The Cary WinUV software analysed the reflectance spectrum and converted it to the equivalent absorption spectrum.

2.4.2 Visible light absorption spectrum of LHCII

The absorption spectrum of LHCII was measured using a Cary 50 Spectrophotometer, Varian, Crawley, UK. LHCII was diluted in elution buffer (preparation described in Section 2.3.2), to a final chlorophyll concentration of 3.6 µg/mL, and 2 mL of the resulting solution were placed in a 1 cm-wide, glass cuvette, so that the path length was 1 cm. Measurements of the absorption were taken at wavelengths with 0.5 nm intervals.

2.4.3 Measuring chlorophyll content

The chlorophyll content of a concentrated thylakoid or LHCII suspension can be measured using the method developed by Porra et al. (1989). 20 µL of the suspension, whose chlorophyll content was to be determined, was added to 3 mL of 80% aqueous acetone solution. The mixture was vortexed and then centrifuged at $\sim 1600g$ (3000 rpm) for 5 min. The absorption of

the supernatant solution was measured by the Cary 50 Spectrophotometer at 646.6 nm, 663.6 nm and 750 nm using pure 80% acetone as a blank.

The chlorophyll a and b concentrations of the measured sample can be calculated (in µg/mL) by equations (2.3)–(2.4) according to (Porra et al. 1989).

$$[\text{Chlorophyll } a] = -2.55 \cdot \text{Abs}'_{646.6} + 12.25 \cdot \text{Abs}'_{663.6}, \quad (2.3)$$

$$[\text{Chlorophyll } b] = 20.31 \cdot \text{Abs}'_{646.6} - 4.91 \cdot \text{Abs}'_{663.6}, \quad (2.4)$$

where $\text{Abs}'_{646.6} = \text{Abs}_{646.6} - \text{Abs}_{750}$ and $\text{Abs}'_{663.6} = \text{Abs}_{663.6} - \text{Abs}_{750}$. From these concentrations, the chlorophyll concentration of the original sample can be calculated.

2.4.4 Photosynthesis yield analyser (MINI-PAM)

The chlorophyll fluorescence of samples was used as a measure of their relative LHCII content. It was measured using the MINI-PAM, Heinz Walz GmbH, Effeltrich, Germany. The MINI-PAM measures F_t, the chlorophyll fluorescence induced by low modulated measuring radiation pulses, and F_m, the maximum fluorescence following a saturating pulse of light (Rohacek & Bartak 1999). From these two values, the effective quantum yield of PSII (Rohacek & Bartak 1999) (Y) is calculated, a quantity that depends on F_t and F_m in the following way: Y=(F_m-F_t)/F_m (Heinz Walz GmbH 1999). In leaves, chlorophyll fluorescence is maximised following a saturating light pulse because the pulse leads to the closing of all reaction centres, meaning the reduction of all electron carriers in the electron transport chain, so that no further light can be used by the photochemical reactions (photochemical quenching). For pure LHCII samples, there is no electron transport chain and therefore no photochemical quenching. Therefore no difference is expected between F_t and F_m and indeed none was observed. In the case of the hybrid sample, also zero yield was measured. The catalyst is expected to function as a reaction centre but due to the large number of catalyst sites relative to the LHCII compounds on the surface, saturation is unlikely to occur and so no yield would be observed. For that reason, only the F_t was measured in experiments following these initial observations.

For the F_t measurements of catalyst pellets and solutions in translucent polypropylene 2 mL tubes, the fibreoptics was in contact with the outside of the tube and moved along it while measuring the F_t value at each point. The maximum value measured for each sample was given as its F_t. An empty tube was used to zero the MINI-PAM before the measurements.

2.4.5 Fluorescence spectroscopy - emission and excitation spectra

A Jobin Yvon FluoroMax-3 spectrophotometer (HORIBA Jobin Yvon Ltd, Stanmore, UK) was used to obtain the fluorescence spectra of LHCII and catalysts. For the room temperature fluorescence spectra, each catalyst sample was suspended in elution buffer (see Section 2.3.2) and placed in a 1 cm wide cuvette where it was mixed by a magnetic stirrer. For the 77 K fluorescence spectra, the catalyst samples were again suspended in

elution buffer, and placed in a cylindrical sample holder between two glass disks so that the sample made a thin layer between them. This holder was then placed in liquid nitrogen, and the liquid nitrogen container together with the sample were positioned inside the FluoroMax so at to obtain maximum fluorescence measurements with excitation at 435 nm and fluorescence emission at 680 nm.

The peak of chlorophyll *a* blue light absorption is at 435 nm, while that of chlorophyll *b* is at 470 nm. For the fluorescence emission spectra, the sample is excited by light of one of those two wavelengths, depending on the desired spectrum, and fluorescence is measured throughout the red light wavelengths. For excitation spectra, fluorescence is measured at 680 nm and the wavelength of the light used to excite the sample is varied through blue light wavelengths.

2.5 Hybrid catalyst preparation

2.5.1 Immobilisation by adsorption

2.5.1.a Dry sample

A simple method was devised for the preparation of hybrid catalyst (TiO_2:Rh-LHCII), based on the observation that LHCII will adsorb on to the catalyst surface when the two are mixed in acidic elution buffer, discussed in Section 3.1. LHCII was first diluted to a chlorophyll concentration of 2.11 µg/mL and then mixed with TiO_2:Rh (20 mg/mL) for 2 h at pH 5.3 in a solution of 25 mM HEPES and 0.1 mg/mL βDM (0.01%). After the 2 h, the mixture was centrifuged at $1600g$ (3000 rpm) for 10 min to form a pellet of the catalyst. Finally the supernatant liquid was removed and the catalyst was left to dry at room temperature overnight.

2.5.1.b Wet sample

The results of Section 3.4 showed that the drying step of the previous method had detrimental effects for the LHCII adsorbed on the catalyst surface. Therefore a different method was also used to prepare a wet catalyst. The required amount of LHCII was diluted in 1 mL of elution buffer (preparation described in Section 2.3.2) at a concentration selected to give 106 µg chlorophyll per g catalyst. The catalyst was mixed in detergent-free HEPES medium (25 mM), the pH of which varied depending on the experiment, and the LHCII solution was then added to the catalyst suspension. Finally the suspension was mixed using a vortex for 1 min and then centrifuged at $\sim 1600g$ (3000 rpm) for 10 min.

2.5.2 Effect of pH on adsorption

To determine the effect of the pH of the solution on the interaction of LHCII and catalyst in that solution, different pH values were tested in the adsorption preparation methods of the previous section. The pH will affect the charge on the catalyst surface as well as the state of the LHCII, as seen by the decrease in its fluorescence at low pH (Krüger et al. 2011). Four different experiments were carried out to investigate this and are described below. In all cases of centrifugation for these experiments, this was per-

formed at $\sim 1600g$ (3000 rpm) for 10 min. The results of these experiments are described in Section 3.3.2.

2.5.2.a Absorption spectra of catalysts prepared at different pH values

Four samples were first prepared by mixing the LHCII and TiO_2:Rh catalyst in one of three acidic solutions (pH 4.1, 4.5, 5.0) or a neutral (pH 7.0) solution. The preparation procedure was the same for all of these, 0.5 g TiO_2:Rh were mixed with LHCII (26.5 µg chlorophyll content) in 25 mL detergent solution (0.01% βDM), with varying buffer and pH, for 1 h and were then centrifuged. The buffer was sodium acetate for the acidic samples and HEPES for the neutral sample. To quantify the amount of LHCII absorbed on the catalyst, UV-Vis absorption spectra (method of Section 2.4.1) of the hybrid catalysts were taken. The catalyst samples were not dried prior to the UV-Vis measurement.

2.5.2.b Fluorescence spectra of catalysts prepared at different pH values

The fluorescence spectra of hybrid catalysts can be compared to the spectrum of LHCII to give information about the state of the protein complex on the catalyst. TiO_2:Rh-LHCII catalysts were prepared in media of different pH values which varied from pH 4.1 to pH 7.0 with LHCII to catalyst ratio at 376 µg chlorophyll per g catalyst. For the more acidic samples (pH 4.1, 4.5, 5.0), 25 mM sodium acetate was used as the buffer, while for the weakly acidic and neutral samples (pH 5.6, 6.0, 6.5, 7.0), 25 mM HEPES was used. The detergent solution was 0.01% βDM for all of these samples. They were mixed for 1 h, then centrifuged and dried at room temperature, and finally the fluorescence spectra of these samples were measured as described in Section 2.4.5 at 77 K.

2.5.2.c Chlorophyll content of catalysts prepared at different pH values

Hybrid catalyst was prepared with three different mixing solutions followed by chlorophyll extraction to calculate the amount of LHCII attached to the catalyst. LHCII solution with 0.021 mg/mL chlorophyll content was prepared with 0.01% βDM, 25 mM HEPES medium at pH 5.26. 0.4 g catalyst were added to 1 mL of this solution and subsequently diluted with 20 mL of one of three different media. The first was diluted with deionised H_2O, the second with detergent-free HEPES medium at pH 5.26 and the last with detergent-free HEPES medium at pH 7.61. The three samples were mixed for 15 min and then centrifuged. The pellet was treated with 80% acetone to extract the chlorophyll from the LHCII on the catalyst for 30 min with mixing every 5–10 min and the chlorophyll content was measured using the method of (Porra et al. 1989) described in Section 2.4.3.

Mixing Time	no βDM	0.003% βDM	0.01% βDM	0.06% βDM
2 min	pH 5, 7	pH 5	–	–
10 min	pH 5, 7	pH 5	–	–
30 min	–	pH 5, 7	pH 5	–
2 h	–	pH 7, 9	pH 5, 7, 9	pH 5, 9

Table 2.2: Conditions of pH, mixing time and detergent concentration for preparation of hybrid catalyst analysed according to their UV-Vis absorption spectra. The pH values, denoted as pH 5, pH 7 and pH 9 were measured as pH 5.17, 7.00, 9.04 respectively.

2.5.2.d Amount of LHCII adsorbed on the catalyst in response to different parameters

Finally, the pH, the detergent solution and the time of mixing were varied systematically to determine which affects the adsorption more strongly. A total of 16 samples were prepared using 0.4 g TiO_2 and LHCII (42.8 µg chlorophyll content) for each. The buffer used was 25 mM HEPES at different pH values (pH 5.17, 7.00, 9.04) and the volume of the solution was 25 mL. The detergent concentrations of these samples as well as the time of mixing varied as shown in table 2.2. The samples were mixed in the solution specified by the table for the respective length of time and then centrifuged. The catalyst samples were not dried prior to analysis. The visible light absorption spectra of these catalysts were measured by the method of Section 2.4.1 to compare the amounts of adsorbed LHCII.

Because results of previous experiments (Section 3.3.2) suggested that low pH assisted adsorption, while higher (neutral) did not, it was hypothesised that basic solutions would also not assist the process and so they were not tested at shorter mixing times in this experiment.The absorption spectra of samples prepared at pH 9 with short mixing times can be seen in Section 3.3.3.

2.5.3 Covalent Bonding

2.5.3.a LHCII Immobilisation on Glass Fibre Filter Disks

This initial work was aimed at investigating ways of immobilising the LHCII on the catalyst surface to produce a hybrid photocatalyst. The method described in (Taylor et al. 2005) for protein covalent immobilisation was first tested with LHCII on glass microfibre filter disks (Cat No. 1820-024, Whatman International Ltd., Maidstone, UK). The disks were refluxed for 2 h in concentrated (12 N) HCl to activate the silanol groups as explained in (Stark & Holmberg 1989). They were then refluxed overnight in 3-aminopropyl-trimethoxy-silane (APTMS) in toluene (Weetall 1969) to aminate the surface. After washing they were dipped in LHCII solution. Another disk that had not been treated with HCl and APTMS was also dipped in LHCII solution to act as the first control (referred to as "Oven-Treated"). Both the treated sample and the control were frozen with liquid nitrogen, lyophilised and oven-treated at 80°C under vacuum for 94 h. At

this stage a second untreated disk was dipped in LHCII solution and all three were lyophilised again.

2.5.3.b LHCII Immobilisation on TiO_2:Rh

The above covalent-bound attachment method was also tested for immobilisation of LHCII on the catalyst in order to obtain a more stable hybrid catalyst. This was a modified version of the immobilisation technique on glass fibre filter disks described in the previous section (2.5.3.a). The modifications allowed the same treatment to be carried out on a TiO_2:Rh powder sample which was then hybridised by mixing with LHCII in acidic detergent solution as described in section 2.5.1.a. The preparation consisted of first refluxing the powder with concentrated HCl (12 N) for 2 h, then washing it with water and drying it and finally refluxing in 10% v/v APTMS in toluene solution. The powder was then again washed, first in toluene, then in acetone and finally in deionised H_2O, and mixed for 2 h with LHCII (313.7 µg chlorophyll content) in 200 mL solution. The hybrid sample was at this stage separated into two with one part left to dry (this sample is referred to as APTMS hybrid) while the other was flash-frozen and freeze-dried. The freeze-dried sample was subsequently sealed and kept at 80°C for 4 days and then washed in 0.1 M NaCl and in deionised H_2O. Finally it was again freeze-dried giving the "Covalent hybrid catalyst".

2.5.4 Cross-linked hybrid catalyst using glutaraldehyde

Two different methods were developed for LHCII-cross-linking by treating the LHCII in 2% glutaraldehyde before (pre-treated) or after (post-treated) mixing with catalyst. This section describes the preparation of these cross-linked hybrid catalysts. In all cases of centrifugation for the cross-linked samples, this was performed at $\sim 1600g$ (3000 rpm) for 10 min.

2.5.4.a Pre-treated crosslinked TiO_2:Rh-LHCII

A solution of LHCII was diluted into 29 mL elution buffer to give a final chlorophyll concentration of 2 µg/mL. Then, 1.2 mL of 50% glutaraldehyde solution were added, giving a final glutaraldehyde concentration of $\sim 2\%$. The cross-linked LHCII solution was then separated into three samples of 10 mL and 0.2 g TiO_2:Rh catalyst were added to each. 5 mL of acidic HEPES solution were added to bring the pH to ~ 5. The suspensions were mixed using a vortex and then centrifuged. Deionised H_2O (15 mL) was used to wash the pellets by mixing with the vortex, centrifugation and removal of supernatant. The pellets were washed twice to remove the glutaraldehyde solution and the catalysts were stored wet, in the dark at room temperature. A control to this catalyst was also prepared without LHCII. For this sample, the glutaraldehyde solution was prepared without the addition of LHCII and it was used in the same way as the cross-linked LHCII suspension above.

2.5.4.b Post-treated crosslinked TiO_2:Rh-LHCII

Wet hybrid (TiO_2:Rh-LHCII) catalyst was first prepared using the method of Section 2.5.1.b. Each sample contained 0.2 g catalyst in 15 mL medium

(pH 5). The wet catalyst was then treated with 10 mL of 2% glutaraldehyde solution in H_2O. The catalyst-containing solution was mixed by vortex, centrifuged and the supernatant glutaraldehyde solution was removed. Again the resulting catalysts were washed twice with deionised H_2O, as described previously. The same process was followed without LHCII, where the catalyst was vortexed alone in detergent-free HEPES (25 mM) medium at pH 5, and the rest of the steps were carried out in the same way as for the hybrid sample. The resulting catalyst was used as a control to the post-treated crosslinked TiO_2:Rh-LHCII.

2.5.5 Cross-linked hybrid TiO_2:Cu catalyst using glutaraldehyde

Two further methods were developed for post-treated crosslinking to test whether this increased the stability of the catalyst (see Section 2.6.4 for further details). In this case TiO_2:Cu was used, prepared by the sol-gel method as described in Section 2.1 for Cu-doped TiO_2 catalyst.

2.5.5.a Dried crosslinked TiO_2:Cu-LHCII

Wet hybrid catalyst was first prepared using the method of Section 2.5.1.b. Each sample contained 1 g catalyst in 50 mL medium at pH 5. 10 mL of 2% glutaraldehyde solution was added to each wet catalyst sample. Following mixing by vortex and centrifugation, the pellet was then washed with deionised H_2O by mixing with the vortex, centrifugation and finally removal of supernatant. The same process was followed without LHCII, resulting in the crosslinked control catalyst. These catalysts were further treated as described in Section 2.6.4 and subsequently dried.

2.5.5.b Wet crosslinked TiO_2:Cu-LHCII

A similar method was used to prepare another group of crosslinked catalysts. 0.3 g TiO_2:Cu catalyst were mixed in 25 mL pH 5 buffer solution, as in Section 2.5.1.b, and then centrifuged. The resulting wet pellets were the hybrid catalyst that was used as a control for the effects of crosslinking in the experiments of Section 2.6.4. To obtain the crosslinked hybrid catalysts, the previously prepared samples were further treated with 7.5 mL glutaraldehyde solution and were then washed with deionised H_2O. Crosslinked control catalysts were also prepared following the same method but without the addition of LHCII into the buffer. Three types of catalysts were thus prepared.

2.6 Stability of hybrid catalyst

The hybrid catalyst of Section 2.5.1.a, as well as similarly prepared samples, were treated by high intensity light to test the effect this has on the photocatalyst in terms of the stability of the attached LHCII. Such experiments were also carried out on hybrid catalysts crosslinked with glutaraldehyde to test if this treatment protected the LHCII on the surface.

2.6.1 Effect of light on chlorophyll content

The stability of the hybrid catalyst in response to light was investigated by treating the hybrid catalyst in elution buffer (preparation described in Section 2.3.2, pH 5.3) with high intensity light. The results of the experiments described below are shown in Section 3.4.1.

Hybrid catalyst was prepared using dilute LHCII-detergent solution, as described in Section 2.5.1.a, where the chlorophyll to catalyst ratio was 82.5 µg/g. Following a 2 h mixing, the catalyst was centrifuged and dried at room temperature (exposed to room atmosphere and low light conditions).

The analysis was carried out after 4 days of drying. The hybrid catalyst was analysed directly as well as following treatment with elution buffer. 0.1 g hybrid catalyst was washed in 5 mL solution for 70 min under white LED light (190 µmol m^{-}2 s^{-}1) or under room light conditions (3–7 µmol m^{-}2 s^{-}1). The chlorophyll content of the treated and untreated samples was calculated as described in Section 2.4.3. To ensure all the chlorophyll was extracted, the catalyst was treated with 80% acetone solution for 30 min. This method also extracted any free chlorophyll that may have been present in the sample, though this is expected to be minimal.

An additional experiment was carried out whereby the hybrid catalyst preparation was mimicked without the drying step. This was shorter (70 min instead of 2 h) and it was carried out under the same LED light and room light conditions as the treatment of the dried sample, giving two wet hybrid samples. The chlorophyll content of those was also calculated by the same method. Finally, the chl content of the initial amount of LHCII used to prepare the hybrid catalyst was calculated. All the results were normalised relative to this amount, so that the LHCII lost by each treatment can be quantified as a percentage of the initial amount added.

2.6.2 Analysis of samples used in the reactor

To test the effect of photoreduction on the hybrid catalysts, TiO_2:Rh-LHCII samples were used in the reactor for 90 min, as in the photoreaction experiments described in Section 4.2.1. Two different light sources were used in these experiments to test the effect of each on the catalyst, the LED lamp used for the experiments of Section 4.2.1, and sunlight on a sunny day in August 2011 (average light intensity: 2300 µmol m^{-2} s^{-1}), outdoors at the Sutton Bonington Campus of the University of Nottingham.

2.6.3 TGA analysis

Thermo-Gravimetric Analysis (TGA) was performed by Professor J.C.S. Wu's group at the National Taiwan University in Taipei. The PYRIS 1 (Perkin Elmer, Waltham, MA, U.S.A.) thermogravimetric analyser was used, operated at temperatures from 30°C to 800°C with approximately 0.5 g catalyst. The catalysts were analysed by TGA to check the stability of LHCII on TiO_2:Rh and to estimate the amount of LHCII present in TiO_2:Rh-LHCII. As LHCII is made up of organic compounds, it will be burned off during the temperature rise and thus the catalyst weight will decrease. From this weight difference, its amount in the original sample

can be calculated. The results of this analysis are shown in Section 3.4.3.

2.6.4 Stability of cross-linked hybrid catalysts in response to light

One sample of the crosslinked hybrid and one of the crosslinked control prepared as described in Section 2.5.5.a (1 g of each) were treated in 50 mL deionised H_2O for 2 h with light irradiation from a Schott KL 1500 LCD (SCHOTT UK Ltd., Stafford, UK), with a light intensity of $\sim$ 1000 µmol m^{-2} s^{-1}. These two, and one more of each that were not light-treated, were then dried overnight at room temperature. These samples were subsequently analysed by UV-Vis spectrophotometry and the results are shown in Section 3.4.4.

One of each of the sample types described in Section 2.5.5.b (hybrid, crosslinked hybrid, crosslinked control), as well as a 0.3 g sample of pure TiO_2:Cu, were treated in high light conditions as above. One more of each sample type, as well as another pure TiO_2:Cu sample, were dark-treated, meaning they were mixed in 50 mL deionised H_2O as the light-treated samples but no light source was used and they were covered to protect from room light irradiation. These eight samples were analysed by UV-Vis spectrophotometry and the results are shown in Section 3.4.4.

Chapter 3

Preparation and Characterisation of the Hybrid Catalyst

This chapter describes the development of the hybrid preparation methods through the investigation of the interaction of LHCII and catalyst in solution. It also presents the results of the analysis of the TiO_2:Rh and TiO_2:Rh-LHCII by standard catalyst analysis methods used commonly in chemical engineering and by further experiments designed to test the stability of the hybrid catalyst in reactor conditions.

3.1 LHCII adsorbs on to the catalyst surface when the two are mixed in solution in acidic pH

For the purpose of functionally immobilising LHCII on to TiO_2 catalysts, work was carried out to investigate the interaction of the two substances in solution. The catalyst and the LHCII were mixed in elution buffer (prepared as in Section 2.3.2 but with pH $\sim$ 5.3) using a magnetic stirrer for 30 min, at room light conditions (3–7 µmol $m^{-2}s^{-1}$). Following the mixing, the suspension was centrifuged at $13,400g$ (13×1000 rpm) for 5 min to precipitate the catalyst. The pellet and supernatant were then separated and the MINI-PAM was used to measure the fluorescence emission of the two, as described in Section 2.4.4. Pure TiO_2:Rh catalyst was also tested with the MINI-PAM and no fluorescence was detected.

It was observed that the catalyst does not remain suspended in solution and the LHCII does not precipitate when centrifuged. The fluorescence of the supernatant was greatly decreased following the centrifugation while the pellet fluoresced strongly. These two observations demonstrate that when catalyst and LHCII are present together in the medium, the LHCII co-precipitates with the catalyst, suggesting that the two are attached. The pellet fluorescence was affected by the LHCII and catalyst concentrations. A pellet with a smaller amount of catalyst fluoresced more strongly than one prepared with the same concentration of LHCII but a larger amount of catalyst. The equivalent supernatant also had higher fluorescence, suggest-

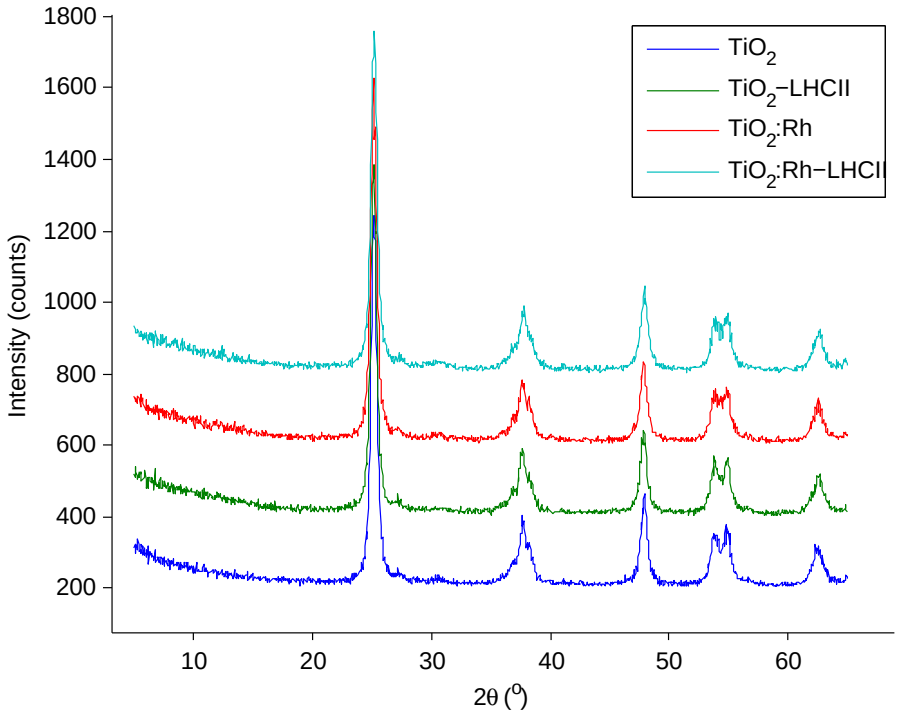

Figure 3.1: XRD patterns of catalysts, showing undoped and Rh-doped TiO_2. Equivalent hybrid catalysts are shown for both to see effect of doping metal as well as presence of LHCII on the catalyst surface. The XRD spectra are drawn with 200 counts distance between them to allow for easy comparison of the peaks.

ing that less total LHCII was attached to the catalyst, but more relative to the catalyst's amount. Therefore the LHCII was more concentrated on the surface of the catalyst in the first case. High LHCII concentration led to low pellet fluorescence, suggesting that, at high concentrations, LHCII, which is a hydrophobic complex, may preferentially bind to itself rather than the catalyst. These observations led to a method for the preparation of hybrid catalyst by adsorption (Section 2.5.1) and the parameters of this interaction are further investigated in the following sections of this chapter.

3.2 Catalyst characterisation

The methods to the following analyses are described in Section 2.2.

3.2.1 Analysis of the crystalline phase of the catalyst by XRD

Figure 3.1 shows the X-Ray diffraction (XRD) spectra of doped and undoped TiO_2 catalysts, with and without LHCII. All the catalysts tested show the same peaks that correspond to the anatase crystal form of TiO_2 which is the desired crystal structure for maximum photocatalytic activity (Yamashita et al. 1994). No evidence of the Rh or the LHCII is seen in the spectrum, suggesting that their amounts are not large enough to affect

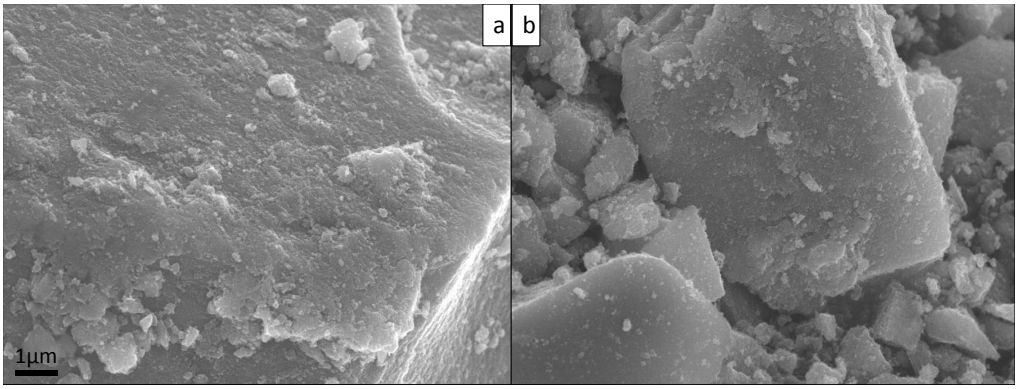

Figure 3.2: SEM image of (a) TiO_2:Rh-LHCII (prepared as in section 2.5.1.a) and (b) TiO_2:Rh.

it. Crystallite sizes were calculated from the spectra using the Scherrer equation (2.2) and were found to range from 20.10 nm to 23.26 nm.

3.2.2 BET analysis

BET analysis showed only small differences in the surface area of the two catalysts with TiO_2:Rh having 47.5 m^2/g and TiO_2:Rh-LHCII 46.2 m^2/g. This could be explained by part of the surface covered by the LHCII and thus not being available for N_2 adsorption. In fact it has been shown that in cases of organic-inorganic hybrid materials, the pressure of the N_2 during the analysis is significant as it determines whether the N_2 will penetrate the organic layer and reach the inorganic surface (Boutin et al. 2012). As only a small coverage of the surface by organics is expected in the case of the hybrid catalyst, this would only have a small effect for the surface area estimation.

3.2.3 SEM-EDS imaging

The SEM images are shown in figure 3.2. The TiO_2:Rh and TiO_2:Rh-LHCII catalysts look quite similar, as expected, since the LHCII should not affect the catalyst at this level of organisation. The LHCII itself was not observed by this method as no preparation was carried out for its fixation or staining. Imaging following such preparation was not attempted in this study but may provide interesting information relating to the localisation of the LHCII and whether the complexes have aggregated or are adsorbed separately on the surface.

The elemental composition from the SEM-EDS analysis is shown in table 3.1. As expected, the C content of the catalyst is higher with the addition of LHCII, as this is itself a source of carbon. On the other hand, the relative decrease in O could be due to the coverage of the surface by the LHCII hiding part of the oxygen atoms. The Rh content appears higher than the predicted $0.02wt\%$ but this could be because the Rh is preferentially located on the surface of the catalyst, thus giving an overestimation of the Rh content by this method which analyses the surface elements (Liu 2012). As the surface is the part of the catalyst used in the reaction, this method is most appropriate and it gives the Rh content met by the

Element	Weight%		Atomic%	
	TiO_2:Rh	TiO_2:Rh-LHCII	TiO_2:Rh	TiO_2:Rh-LHCII
C K	1.87	3.05	4.07	7.91
O K	38.77	22.41	63.41	43.63
Ti K	59.71	74.50	32.62	48.45
Rh L	BDL	0.04	BDL	0.01

Table 3.1: Elemental analysis of TiO_2:Rh and TiO_2:Rh-LHCII catalysts. Abbreviation: Below detection limit (BDL).

reactants.

3.2.4 TEM imaging

The TEM image of TiO_2:Rh is shown in figure 3.3. TiO_2:Rh-LHCII was also analysed by this method and no differences could be observed between the two images confirming that the LHCII treatment has no effect on the arrangement of the particles of TiO_2:Rh. Again the LHCII itself was not observed by this method.

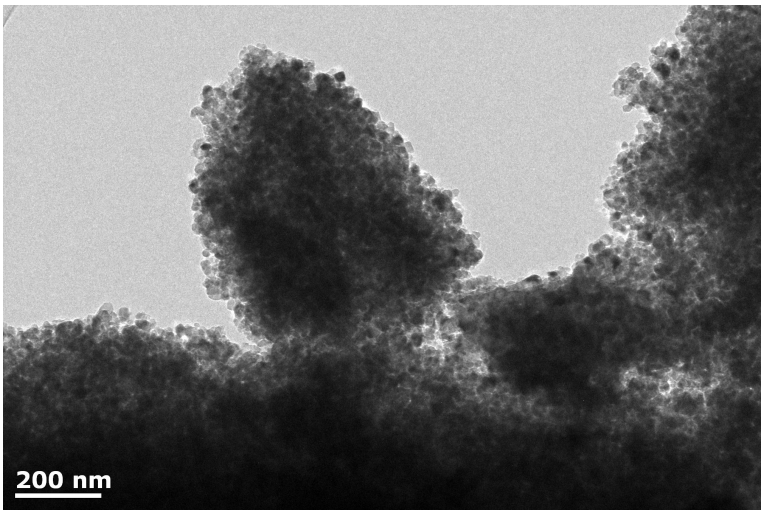

Figure 3.3: TEM image of TiO_2:Rh.

3.3 Analysis of hybrid catalysts

3.3.1 Immobilisation by adsorption

3.3.1.a UV-Visible light absorption spectra of hybrid catalyst

UV-Visible light absorption spectrum of the hybrid catalyst prepared in 2.5.1.a was obtained by the method described in Section 2.4.1, and is shown in figure 3.4. The figure also shows the spectra of pure TiO_2:Rh, pure undoped TiO_2 and hybrid TiO_2 (TiO_2-LHCII) prepared as described in Section 2.5.1.a but using undoped TiO_2 instead of Rh-doped catalyst. The absorption spectrum of LHCII, measured as described in Section 2.4.2, is shown for comparison in figure 3.5. It can be observed that the peaks of the

hybrid catalyst that are not present in the pure catalyst match the LHCII peaks, confirming that it is the source of the increased absorption in those areas of the spectrum.

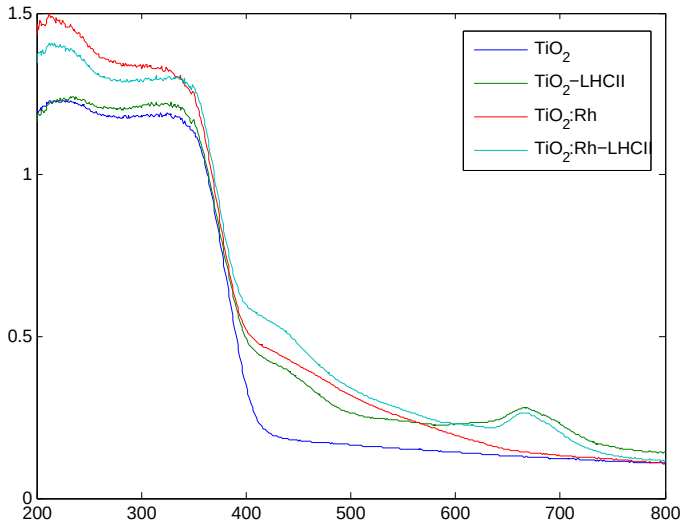

Figure 3.4: Absorption spectra of catalysts (prepared as in Section 2.5.1.a, measured as in Section 2.4.1), showing undoped and Rh-doped TiO_2. Equivalent hybrid catalysts are shown for both to see effect of doping metal as well as presence of LHCII on the catalyst surface.

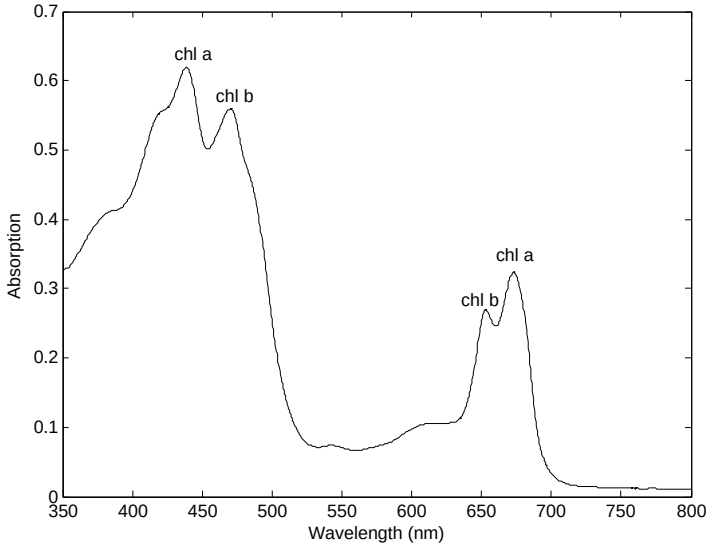

Figure 3.5: Absorption spectrum of LHCII in elution buffer (measured as in Section 2.4.2) showing the absorption peaks of chlorophyll *a* and chlorophyll *b*.

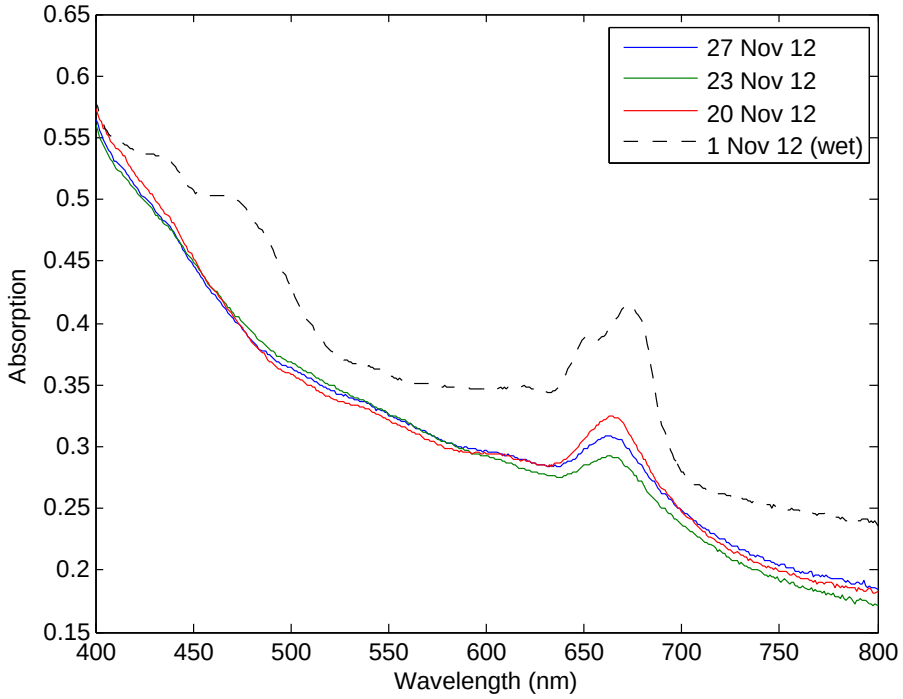

Figure 3.6: A TiO_2:Cu-LHCII catalyst sample is measured before drying ("1 Nov 12(wet)" sample) and at different times after drying (samples "20 Nov 12", "23 Nov 12" and "27 Nov 12"). The names of the samples correspond to the date the measurement was made.

To show the error in measurements of absorption spectra, a hybrid catalyst sample is shown in figure 3.6, measured at different times. This was a TiO_2:Cu-LHCII catalyst prepared by the method of Section 2.5.1.b with 1.5 g catalyst in 20 mL pH 5 medium. The spectrum of the sample was measured before and after drying. The differences in the spectra of the dried catalyst in figure 3.6 are due to limitations of the equipment and not aging of the sample as one of the later measurements shows higher absorption than an earlier one. The measurement of the same sample before drying is not directly comparable to the others because it was measured wet and thus the absorption is overestimated and damage due to drying has not occurred. The pattern of the LHCII is clearly visible in this wet sample.

3.3.1.b Fluorescence emission spectra of hybrid catalyst

Figure 3.7 shows the fluorencence spectra of hybrid catalyst prepared as described in Section 2.5.1.a measured as described in Section 2.4.5, at 77 K, with excitation at 435 nm (plot a) and 470 nm (plot b). The hybrid catalyst (TiO_2:Rh-LHCII) has a very high vibronic satellite, which refers to the broad peak at higher wavelengths (700–720 nm) compared to the chlorophyll *a* 680 nm peak. This may be caused by electrons falling to lower vibrational states and fluorescence being emitted during their return from those states to the ground state. LHCII aggregation could be causing this fluorescence, which is normally present at a low level, to become prominent

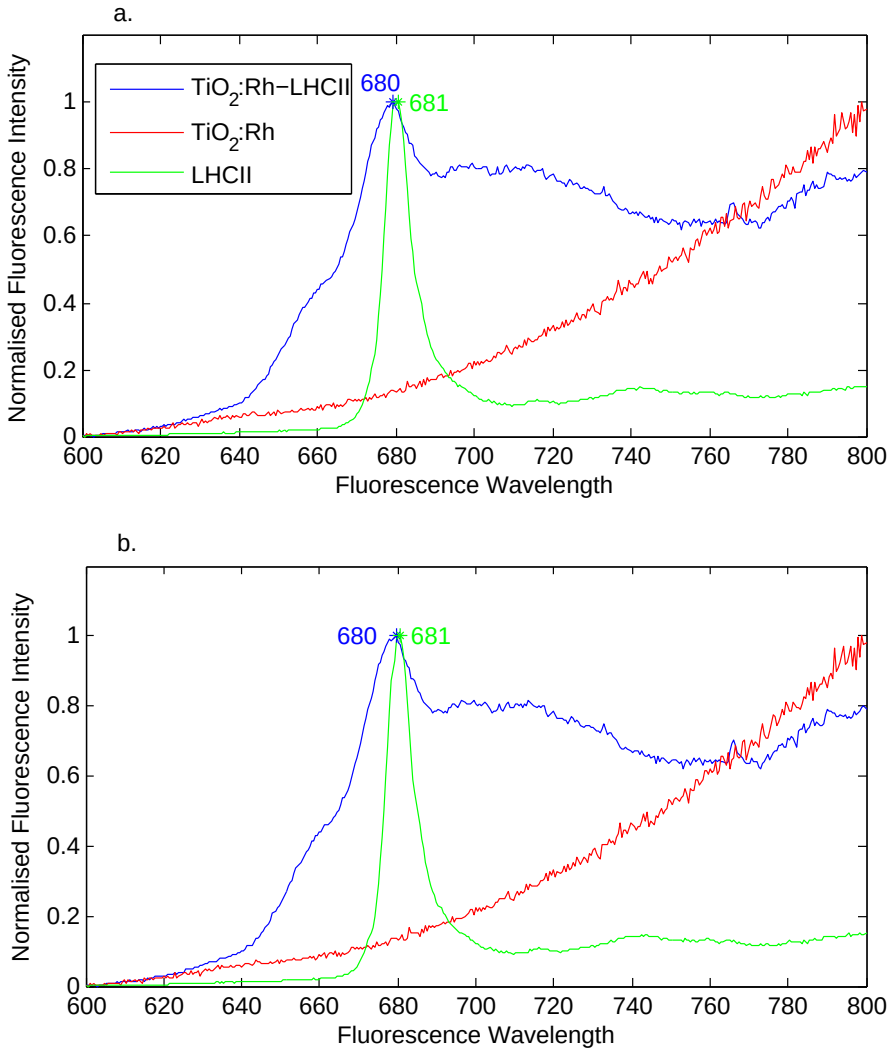

Figure 3.7: The fluorescence spectra, measured as described in Section 2.4.5, at 77 K, with excitation at 435 nm (a) and at 470 nm (b), of pure LHCII (green line), pure TiO_2:Rh (red line) and hybrid catalyst (TiO_2:Rh-LHCII, blue line) are shown in the figure. The fluorescence intensity of each spectrum has been divided by its maximum intensity to compensate for effects due to the difference in overall intensity of fluorescence and compare the shapes of the spectra.

(Ruban et al. 1999). Alternatively, the exceptionally high vibronic satellite could be evidence of charge transfer between LHCII and catalyst (Krüger et al. 2010). The increased fluorescence around 650 nm may be due to free chlorophyll *b*, indicating some damage to the LHCII on the surface, which, however, is minimal.

3.3.2 Effect of pH on adsorption

The pH of the mixing solution as well as the mixing time and the detergent concentration were varied in the experiments described in Section 2.5.2 and

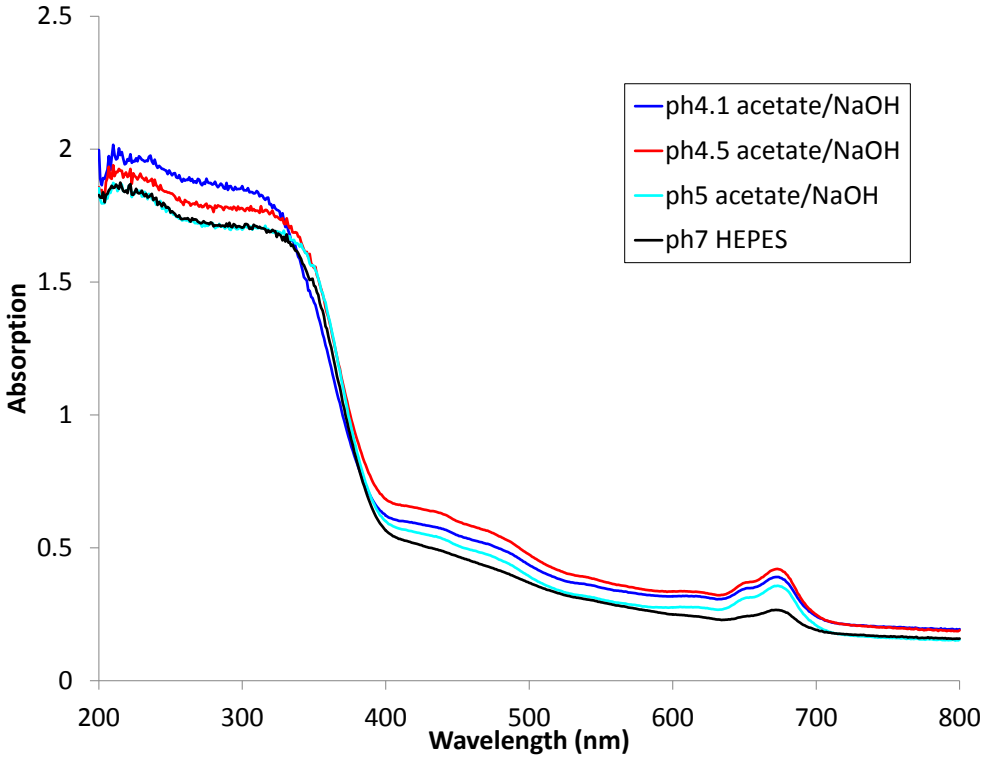

Figure 3.8: Effect of pH of the βDM medium on hybrid catalyst visible light absorption. The same amount of catalyst and LHCII were mixed, varying the pH of the mixing medium. The pH values varied between 4.1 and 7.0, as seen in the figure legend. HEPES was used as the buffer for pH 7.0, while sodium acetate was the buffer for the pH 4.1, 4.5 and 5.0 solutions.

the results are shown in figures 3.8-3.10. The purpose of these experiments was to identify which of the varied factors affects the adsorption of LHCII on to the catalyst surface most strongly.

3.3.2.a Absorption spectra of catalysts prepared at different pH values

Absorption spectra of three hybrid catalysts prepared in acidic solutions (pH 4.1, 4.5, 5.0) and one prepared in a neutral solution (pH 7.0) are shown in figure 3.8. The results show that in the acidic solutions, more LHCII was adsorbed on to the catalyst surface relative to the neutral sample. This is deduced from the LHCII absorption peaks (around $\sim$ 670 nm and $\sim$ 470 nm) which are more pronounced in the acidic samples. In particular, the sample prepared at pH 4.5 has the highest absorption relative to the background absorption ($\text{Abs}_{673} - \text{Abs}_{750}$), which is 0.220 compared to 0.188, 0.194 and 0.100 for samples with pH 4.1, 5.0 and 7.0 respectively. Absorption at 673 nm was used because that was the wavelength at the red chlorophyll *a* peak of the pure LHCII solution (figure 3.5).

3.3.2.b Fluorescence spectra of catalysts prepared at different pH values

The fluorescence emission spectra (with chlorophyll *a* excitation) of hybrid catalysts prepared in media of acidic and neutral pH values were also

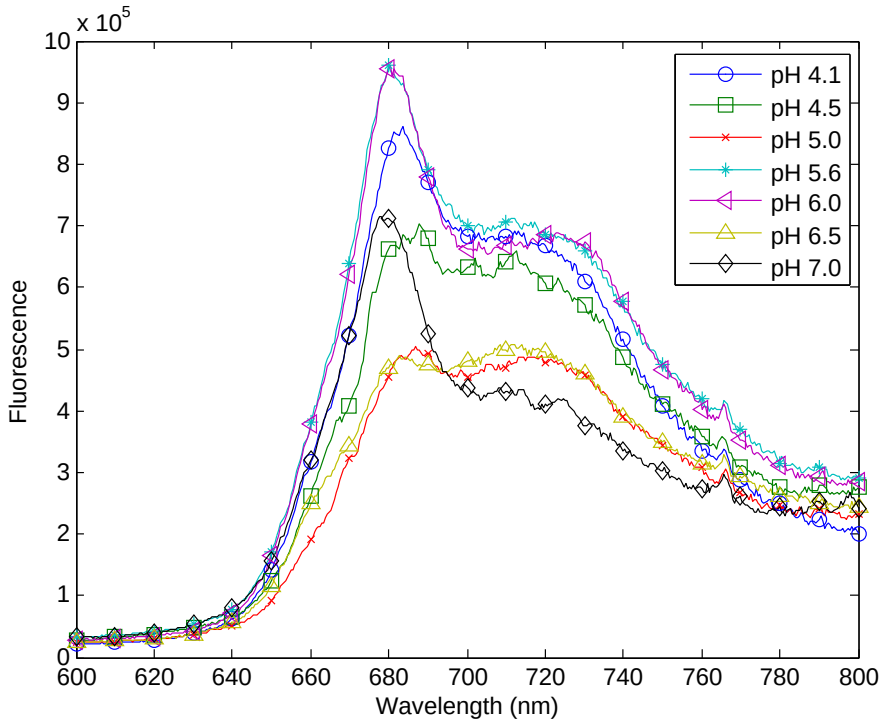

Figure 3.9: Effect of pH of the βDM medium on hybrid catalyst fluorescence at 77 K. Catalyst and LHCII were mixed as described in Section 2.5.2.b, varying the pH of the mixing medium. The pH values varied between 4.1 and 7.0, as seen in the figure legend. HEPES was used as the buffer for pH 5.6 to pH 7.0, while sodium acetate was the buffer for the more acidic pH values.

measured (method described in Section 2.4.5, at 77 K) and are shown in figure 3.9. The lowest pH values do not give the highest fluorescence, but instead there is an optimum pH for this process. Intermediate values give the highest fluorescence peak, supporting the previous choice of pH for the attachment of LHCII on the catalyst of approximately pH 5.3 (Section 2.5.1.a). The neutral solution shows low fluorescence but also a low vibrational satellite, a feature indicative of aggregation which is very high for the more acidic solutions.

Additionally, the fluorescence spectrum of a wet hybrid catalyst sample prepared by the method of Section 2.5.1.b using TiO_2:Cu in pH 9 solution is compared to an equivalent pH 5 sample in figure 3.10. The spectra were measured using the method of Section 2.4.5, at room temperature, with excitation at 435 nm. In this figure, the fluorescence of the hybrid catalyst prepared at pH 9 is higher than that of the pH 5 sample, suggesting that there is a higher amount of LHCII on the catalyst or that this LHCII is less quenched.

3.3.2.c Chlorophyll content of catalysts prepared at different pH values

The chlorophyll content of three hybrid catalyst prepared with different mixing solutions was measured by the method described in Section 2.4.3.

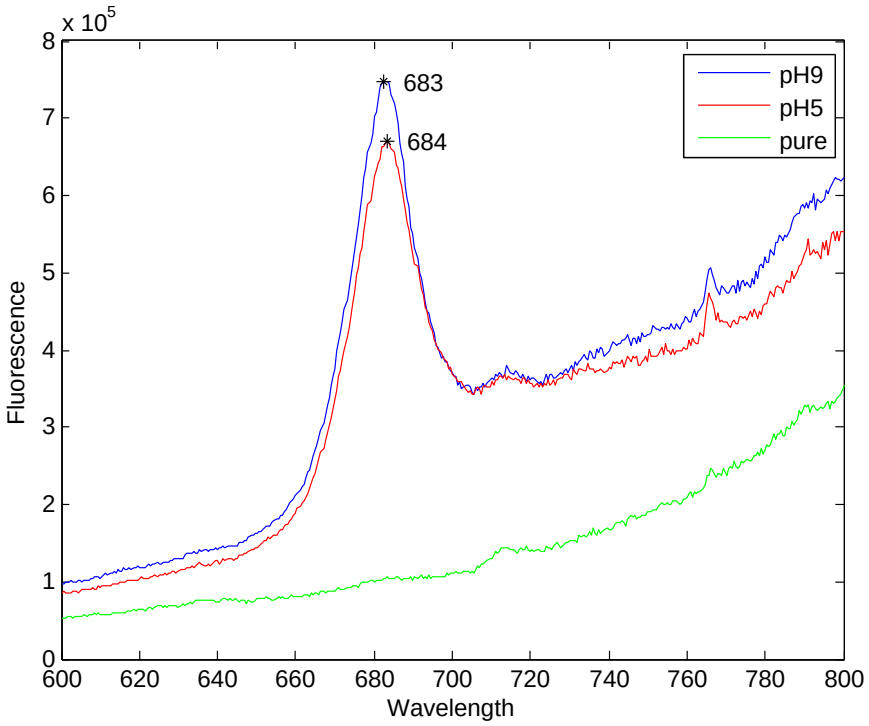

Figure 3.10: Fluorescence spectra of hybrid catalysts prepared as in Section 2.5.1.b using TiO_2:Cu in pH 9 (blue line) and pH 5 (red line) solution and pure TiO_2:Cu catalyst (green line), measured as in Section 2.4.5, at room temperature, with excitation at 435 nm.

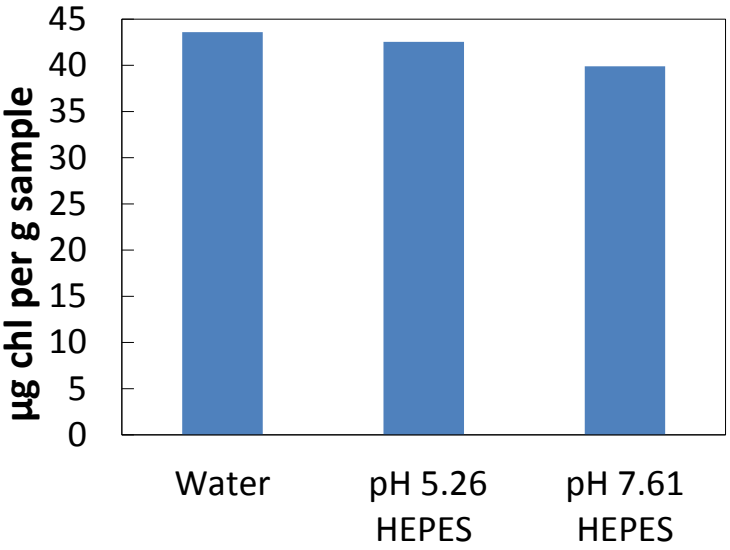

Figure 3.11: Effect of pH and presence of buffer in attachment medium on LHCII adsorption. The hybrid preparation solution was different for the three samples. Water, HEPES medium with pH 5.26 and HEPES medium with pH 7.61 were tested and the chlorophyll content of the resulting hybrid catalyst is shown.

The mixing solutions were pure deionised H_2O, detergent-free buffer solution (pH 5.26) and detergent-free buffer solution (pH 7.61). The chlorophyll contents of the catalysts are shown in figure 3.11. The acidic sample gives higher chlorophyll content compared to the slightly basic solution, in agreement with the previous results. However, the sample mixed in deionised H_2O shows a slightly higher chlorophyll content. The pH of the water will be at pH 5.6 due to CO_2 from the air dissolving into it, therefore the absence of HEPES is not thought to be the cause for this small increase.

3.3.2.d Amount of LHCII adsorbed on the catalyst in response to different parameters

Figure 3.12 shows the visible light absorption spectra of different hybrid catalysts using pure TiO_2 as the baseline. From the results it can be seen that pH is the most important factor for the adsorption of LHCII on to TiO_2, with neutral pH giving much lower LHCII adsorption and both acidic and basic solutions assisting the process (plot a). In particular, acidic solution gives the highest LHCII concentration on the catalyst but, as seen from earlier experiments, it may be damaging the LHCII. The basic pH was shown in figure 3.10 to give a higher fluorescence spectrum which may suggest less damage to the LHCII and therefore a more appropriate parameter for hybrid catalyst preparation. Another observation that can be made from the figure is that longer times reduce the amount of adsorbed LHCII for acidic pH, possibly due to damage caused to LHCII by the acidic solution, but increase it for neutral pH (plot c).

The detergent appears to have little effect on the adsorption efficiency in figure 3.12, plot b. However, for later samples prepared by the same method as the 2 min mixing samples (preparation described in Section 2.5.2) but with pH 9 buffer, it was observed that the supernatant was not clear after centrifugation if the buffer contained detergent (0.01% βDM). On the other hand, all the supernatants resulting after centrifugation from the pH 9 samples of the previous experiment, which had longer mixing times, were clear, as was the supernatant left after centrifugation of a pH 9 sample mixed for 2 min that did not contain βDM. This effect was not quantified and is reported as an observation which suggests that detergent concentration is important in some cases.

3.3.3 Excitation and absorption spectra differences

Figure 3.13 compares the absorption (method 2.4.1) and excitation (method 2.4.5) spectra of different catalysts. The former show how much light is absorbed by the catalyst at different wavelengths while the latter show the intensity of fluorescence following absorption at different wavelengths. The same spectra are also shown for pure LHCII in the same figure for comparison (plot e). These two spectra are expected to overlap and indeed for pure LHCII they do. However, in all the catalyst cases, the excitation spectrum peaks at a lower wavelength (415–421 nm) than the absorption spectrum (432–438 nm).

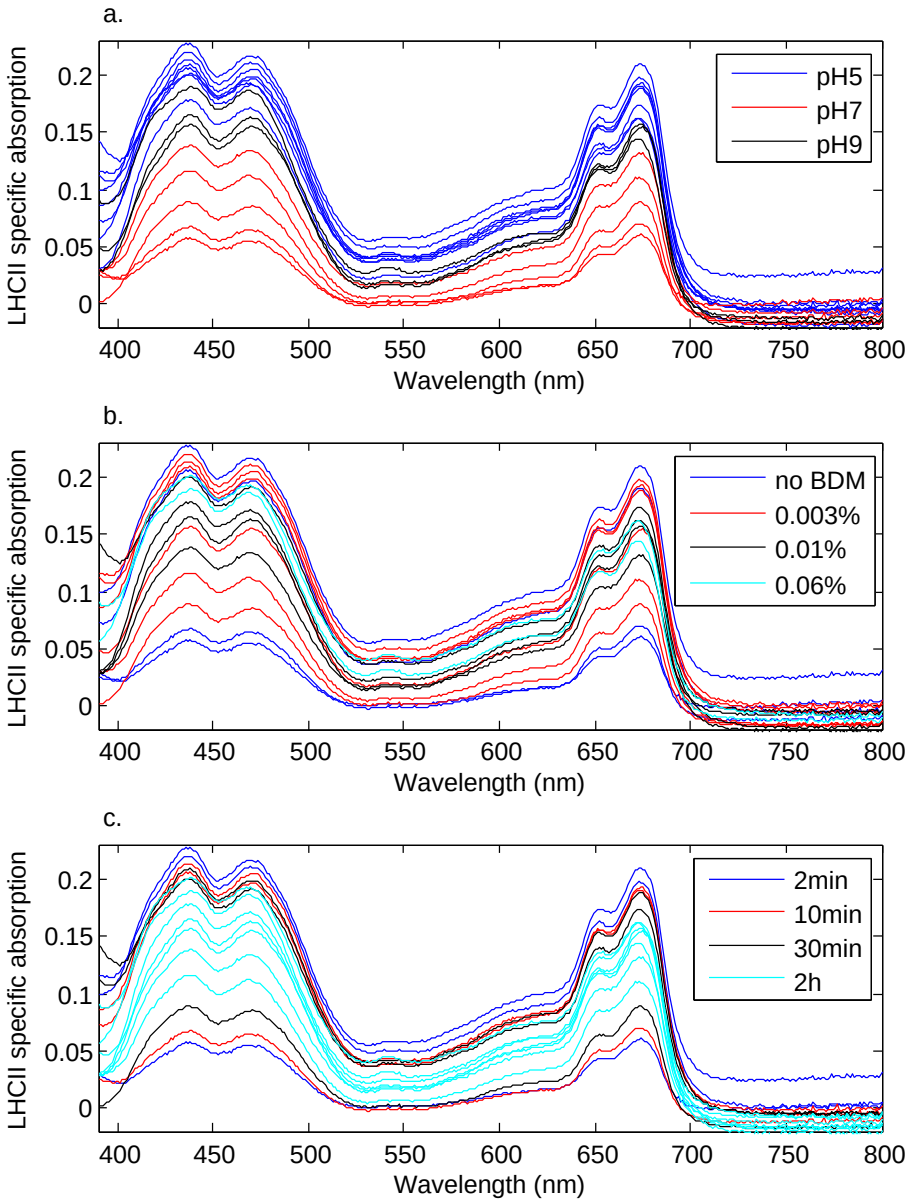

Figure 3.12: Effect of pH (a), detergent concentration (b) and time of mixing (c) on amount of LHCII attached on catalyst surface. The lines of the figures show the absorption spectrum of the hybrid catalysts measured by UV-Vis using the pure TiO_2 catalyst as the baseline. For the preparation of the different hybrid catalysts, the same amount of catalyst and LHCII were mixed in each case, varying the pH of the mixing medium, its βDM concentration and the mixing time. The samples analysed are shown in table 2.2.

3.3.4 LHCII immobilisation on glass fibre filter disks by covalent bond

To test the stability of the attachment of LHCII on glass fibre filter disks (method described in Section 2.5.3.a), a sample from the treated and each

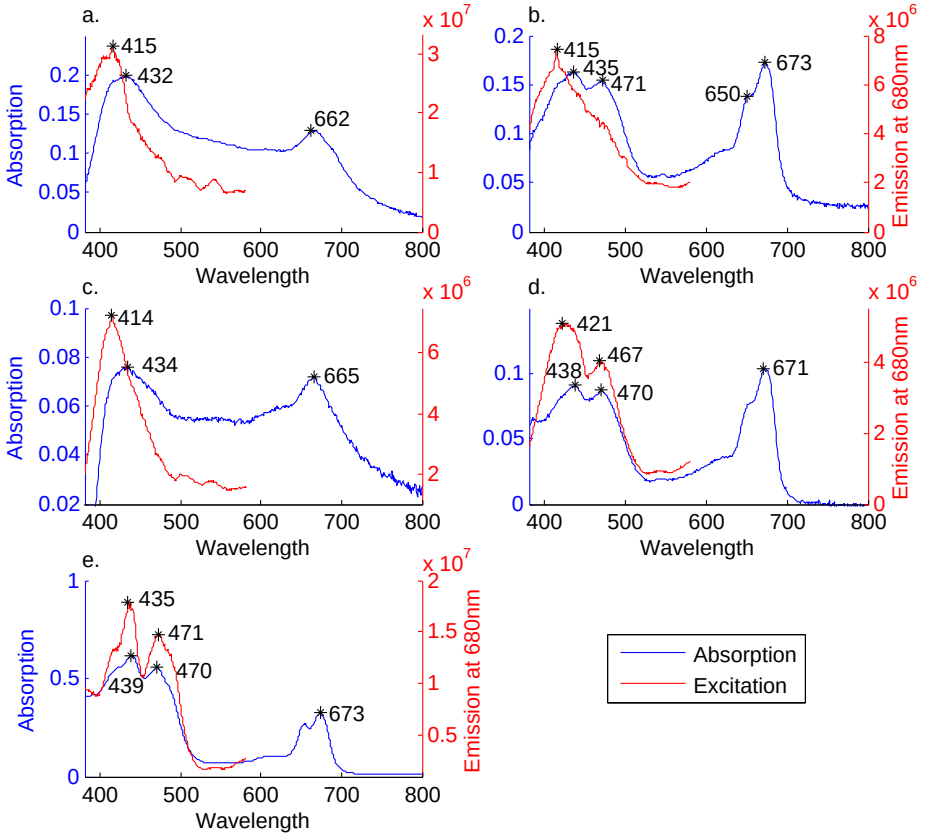

Figure 3.13: Absorption spectra (method 2.4.1) in blue and excitation spectra (method 2.4.5) in red of TiO_2:Cu-LHCII catalysts prepared in pH 5 or pH 9, before and after drying. a. Dry sample prepared at pH 5 using TiO_2:Cu by the method described in Section 2.5.1.a. Pure TiO_2:Cu was used as the baseline for the absorption spectrum. b. Wet sample prepared at pH 5 using TiO_2:Cu by the method described in Section 2.5.1.b. Pure TiO_2:Cu wet with high purity H_2O was used as the baseline for the absorption spectrum. c. Dry sample prepared at pH 9 using TiO_2:Cu by the method described in Section 2.5.1.b and then dried. Dried TiO_2:Cu that had been treated with pH 9 elution buffer was used as the baseline for the absorption spectrum. d. Wet sample prepared at pH 9 using TiO_2:Cu by the method described in Section 2.5.1.b. TiO_2:Cu that had been treated with pH 9 elution buffer was used as the baseline for the absorption spectrum. A red long pass filter was used for the excitation measurements of this sample. e. Pure LHCII in elution buffer (pH 7.6).

of the controls were washed with detergent solution for 30 min. A sample of each of the three was also collected to be used as unwashed controls. The chlorophyll content of each was measured as described in Section 2.4.3 and is shown in table 3.2.

The amount of chlorophyll removed by washing should inversely correlate to the stability of binding. In the cases of the two control samples, table 3.2 shows that the chlorophyll content of the disks is decreased after

Sample	Unwashed	Washed
Covalent-bound	39.5 µg/g	100 µg/g
Control: Oven-treated	826 µg/g	235 µg/g
Control: Dried	617 µg/g	305 µg/g

Table 3.2: Amount of chlorophyll extracted from glass fibre disks in µg chlorophyll per g disk. The washed samples were mixed in detergent solution for 30 min while untreated samples (unwashed) were used as controls. The chlorophyll content was calculated as in Section 2.4.3.

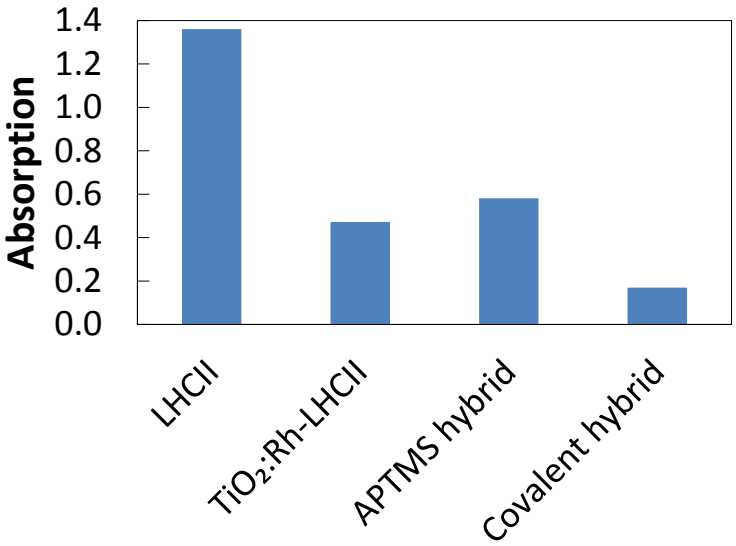

Figure 3.14: Chlorophyll extracted from covalent hybrid catalyst and controls. The first bar shows the chlorophyll content of the LHCII that was used for the preparation of each of the catalyst samples. TiO_2:Rh-LHCII is the Rh-doped hybrid catalyst prepared as described in section 2.5.1.a. Covalent hybrid is the sample prepared using the modified (Taylor et al. 2005) method described in Section 2.5.3.b, while APTMS hybrid refers to the sample described in the same section that underwent only the early steps of the method, up to the LHCII mixing.

washing. However, the results for the covalent bound sample show an increase after washing. This can be attributed to the fact that the washing process partially breaks down the disk and floating fragments with LHCII attached to them are measured as extracted chlorophyll in the case of the washed covalent sample. Therefore the washing is not seen to decrease the chlorophyll content of the disks. Furthermore, the disk remains green even after the acetone treatment, which also explains why the chlorophyll content of these samples is so low. Acetone is a standard method for extracting pigments from LHCII (Porra et al. 1989) and the fact that it fails to do this for the covalent bound sample is evidence of a very strong stabilising binding.

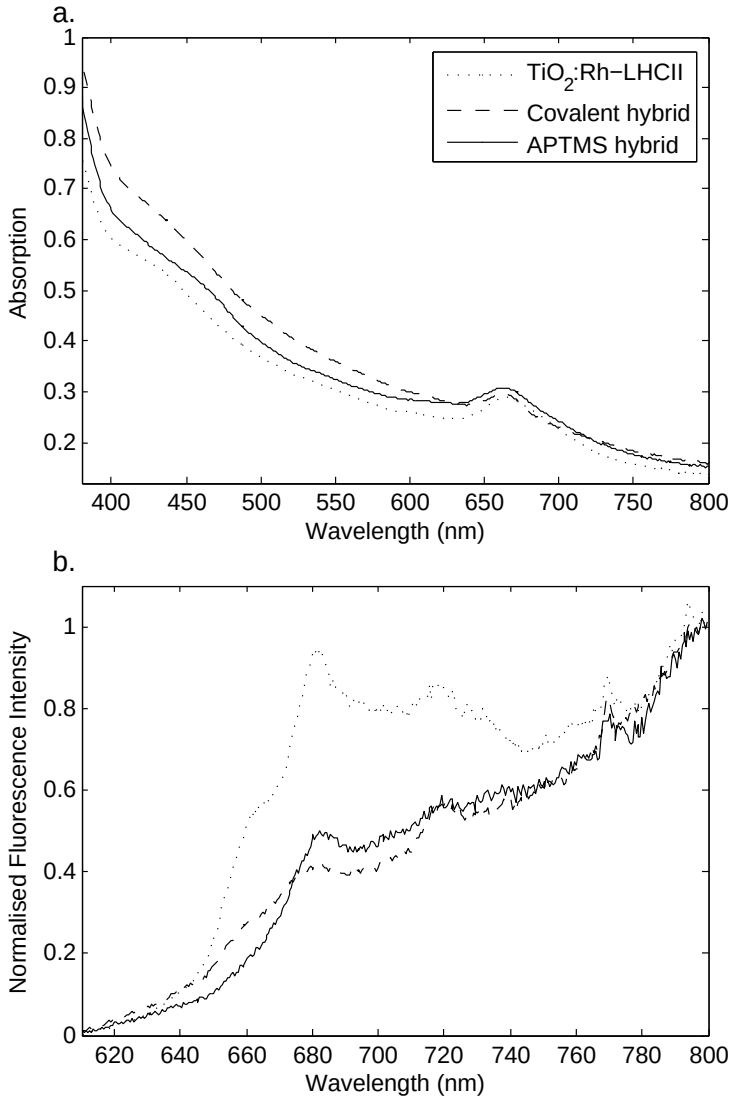

Figure 3.15: a. UV-Vis absorption spectra of covalent hybrid catalyst and controls, measured as described in Section 2.4.1. b. Fluorescence spectra of covalent hybrid catalyst and controls, measured as described in Section 2.4.5 with excitation of chlorophyll *a* (435 nm). The dotted line spectrum shows TiO_2:Rh-LHCII, the Rh-doped hybrid catalyst prepared as described in section 2.5.1.a. Covalent hybrid (dashed line) is the sample prepared using the full method described in Section 2.5.3.b, while APTMS hybrid (solid line) refers to the sample that underwent only the early steps of the same method, up to the LHCII mixing.

3.3.5 LHCII immobilisation on TiO_2:Rh by covalent bond

To test if the samples prepared by the method described in Section 2.5.3.b were as stable as the glass fibre filter disks, they were treated with 80% acetone to extract the chlorophyll. The results are shown in figure 3.14 and demonstrate that acetone can extract pigments from these samples.

Additionally the covalent hybrid has a lower chlorophyll content than either the APTMS hybrid or the TiO_2:Rh-LHCII samples. This could be due to damage during the treatment at high temperature, which neither of the other two samples underwent. On the other hand, the APTMS hybrid demonstrated high chlorophyll content. The same can be seen from the UV-Vis spectra in figure 3.15 plot a where the APTMS hybrid has the highest absorption at 664 nm. In this figure, the covalent hybrid appears to have higher absorption than the hybrid catalyst. However, the absorption over the entire spectrum is increased for both this sample and the APTMS hybrid. Therefore, if the absorption at 750 nm of each spectrum, where no LHCII absorption should be occurring, is used as the zero absorption point for that spectrum, three new values for absorption at 664 nm arise (TiO_2:Rh-LHCII 0.134, covalent hybrid 0.113, APTMS hybrid 0.133), so that APTMS hybrid and TiO_2:Rh-LHCII show approximately the same and the covalent again shows the lowest absorption.

Finally, the fluorescence spectra of these three samples were measured and are shown in figure 3.15 plot b. Here it can be seen that the LHCII present on both the APTMS hybrid and the covalent hybrid is strongly quenched, giving hardly any fluorescence.

3.4 Stability of hybrid catalyst

3.4.1 Effect of light on chlorophyll content

The effect of high intensity light on hybrid catalysts in solution was tested by the method described in Section 2.6.1. The chlorophyll content of five samples was measured, an untreated TiO_2:Rh-LHCII catalyst ("Untreated - Dried"), another washed in elution buffer without light treatment ("Dark-treated - Dried") and a third washed with simultaneous light treatment ("Light-treated - Dried"). TiO_2:Rh and LHCII were also mixed in elution buffer with ("Light-treated - Wet") and without ("Dark-treated - Wet") light treatment leading to the adsorption of the LHCII on to the TiO_2:Rh surface. Figure 3.16 shows the effects of each of the five treatments as well as the chlorophyll content of the same amount of LHCII as used in the preparation of each catalyst sample ("Untreated - Wet").

Most of the LHCII is absorbed by the hybrid preparation method (only 4% is lost) as can be seen from samples "Untreated - Wet" and "Dark-treated - Wet" in the plot of figure 3.16. However, if the preparation is carried out under high light conditions, more than 60% of the LHCII is lost. Another point raised from these results is the effect of drying on the sample. The hybrid catalyst, which was prepared similarly to the dark-treated wet sample but was additionally left to dry, has lost almost 50% of the LHCII initially added to it, even before washing. After washing, the results follow a similar pattern to the wet samples, with greatly decreased chlorophyll content following light treatment (as little as 5% of the original is left on the catalyst).

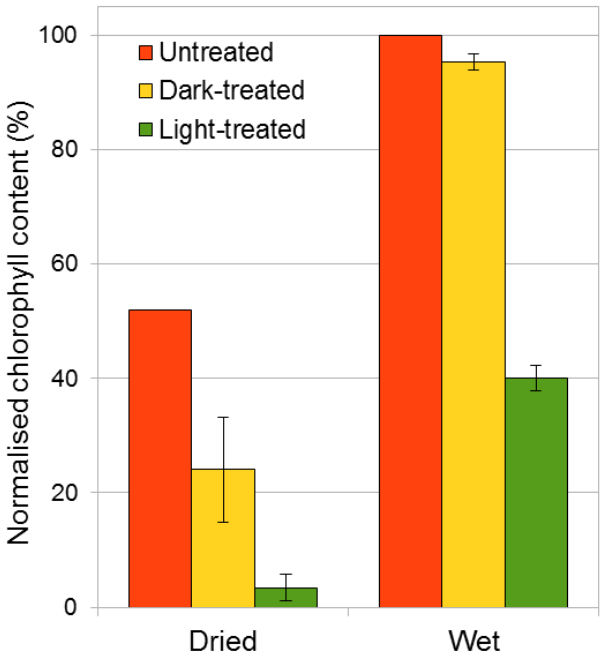

Figure 3.16: Effect of high intensity light treatment, washing and drying on hybrid catalyst. Methods described in Section 2.6.1. Dried: Hybrid catalyst, prepared 4 days prior to testing. Wet: LHCII untreated and treated with catalyst in solution in the dark and in the light (no drying). Dark-treated: Washed in detergent solution under room light/temperature conditions without additional light irradiation. Light-treated: Washed in detergent solution under high intensity light conditions with LED light source. Two repeats were made for all the treated samples and error bars of one standard deviation are shown. Chlorophyll content (y-axis) is normalised to the amount of chlorophyll present in the LHCII that was used for each sample preparation.

3.4.2 UV-Vis analysis of used samples

The damage to the hybrid catalyst from the conditions of the photoreduction experiment (described in Section 4.1.1) were also investigated by the analysis of the samples prepared in Section 2.6.2. An LED lamp and natural sunlight were used as the light sources. The samples were collected and centrifuged following the photoreaction, and their UV-Vis absorption spectra were measured by the method described in Section 2.4.1 (figure 3.17, plot a). They were also analysed by fluorescence spectroscopy at 77 K using liquid N_2 as described in Section 2.4.5 (figure 3.17, plot b). The results show severe photodamage during reaction using both sunlight and LED. The LHCII specific fluorescence and absorption peaks are almost completely lost. The "Old TiO_2:Rh-LHCII" of the same figure, which was prepared approximately a year before the others and stored in room temperature away from direct light, shows fluorescence and absorption peaks

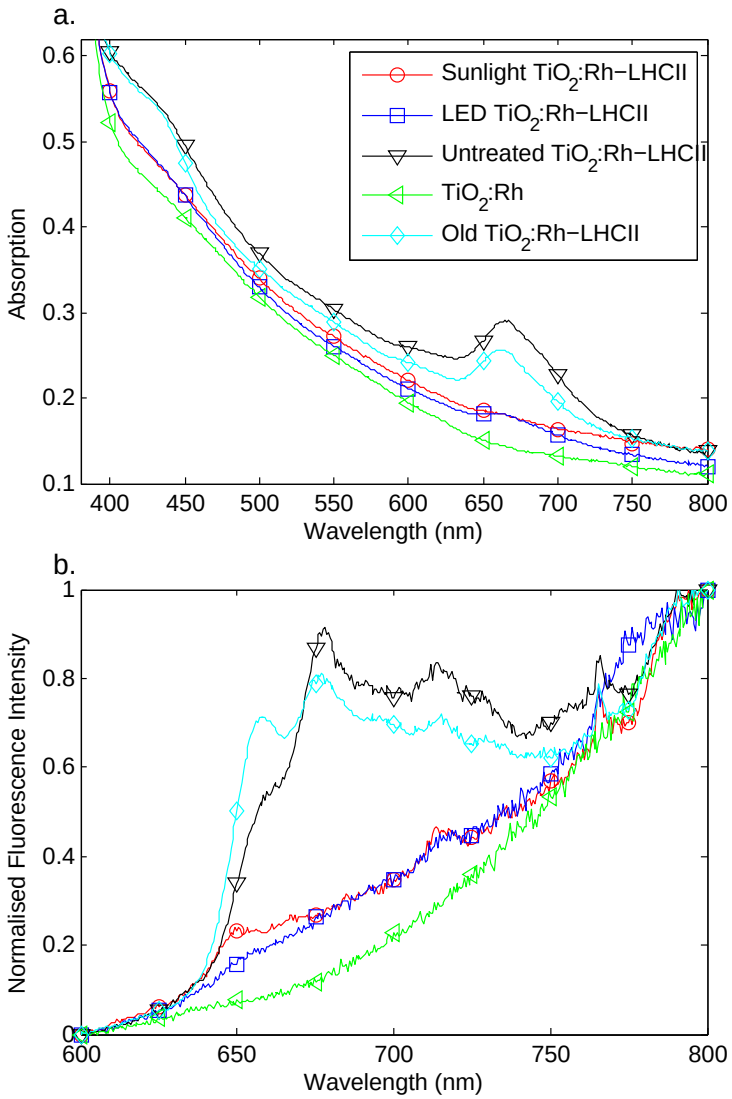

Figure 3.17: Analysis of hybrid catalysts used in photoreduction experiments described in Section 2.6.2. Plot a: UV-Vis absorption spectra of the hybrid catalysts. Plot b: Fluorescence spectra of the hybrid catalysts with chlorophyll *a* excitation (at 435 nm). Control catalyst, TiO_2:Rh, is also shown for comparison (green spectra). The hybrid catalysts are analysed before treatment (black spectra) and following sunlight (red spectra) or LED light (blue spectra) treatment in the reactor. The spectrum of an old hybrid catalyst sample, TiO_2:Rh-LHCII, is also shown, which was prepared a year earlier than the other samples by the method of Section 2.5.1.a.

only a little lower than those of the fresher sample.

3.4.3 TGA analysis

From the results of the TGA analysis (method described in Section 2.6.3), it is possible to estimate the amount of LHCII present on the catalyst surface. Figure 3.18 shows the weight variation with temperature increase for three catalyst samples, TiO_2:Rh, TiO_2:Rh-LHCII (prepared as described in

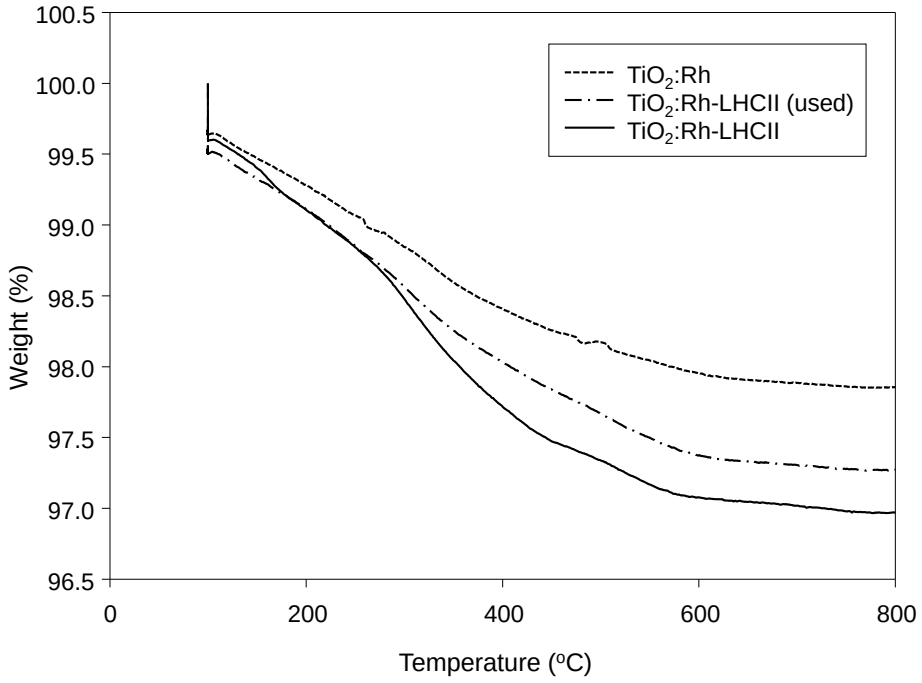

Figure 3.18: TGA analysis of TiO_2:Rh (dashed line), TiO_2:Rh-LHCII (solid line) and TiO_2:Rh-LHCII used in the reactor as described in Section 4.1.2 and then collected and dried (dash-dotted line).

Section 2.5.1.a) and used TiO_2:Rh-LHCII, meaning catalyst that had been used in the reactor. TiO_2:Rh was analysed as a control for the other two samples, showing the weight loss features that were not related to the presence of LHCII. Water loss from the catalyst surface led to the weight loss of the catalyst at ~ 100°C. The weight loss at 200–500°C might be attributed to the decomposition of organic compounds. As the temperature increased in the range of 200–400°C , and especially between 300–400°C, there was a significant weight loss in TiO_2:Rh-LHCII compared to TiO_2:Rh, suggesting this was the loss due to LHCII degradation. From this weight loss difference, the LHCII was estimated as $0.9wt\%$ of the weight of TiO_2:Rh-LHCII.

The used TiO_2:Rh-LHCII sample was collected from the reactor after the photoreduction experiments described in Section 4.1.2, which used TiO_2:Rh-LHCII prepared as in Section 2.5.1.a. It was analysed by TGA to detect any changes due to the reaction, to check the stability of LHCII in the TiO_2:Rh-LHCII catalyst. The weight loss of the used catalyst was less than that of the fresh catalyst, indicating that some components of LHCII may have been degraded or leached during the photoreaction in aqueous solution.

3.4.4 Stability of cross-linked hybrid catalysts in response to light

The crosslinked samples of Section 2.6.4 were analysed to obtain their absorption spectra and these are shown in figures 3.19 and 3.20. The

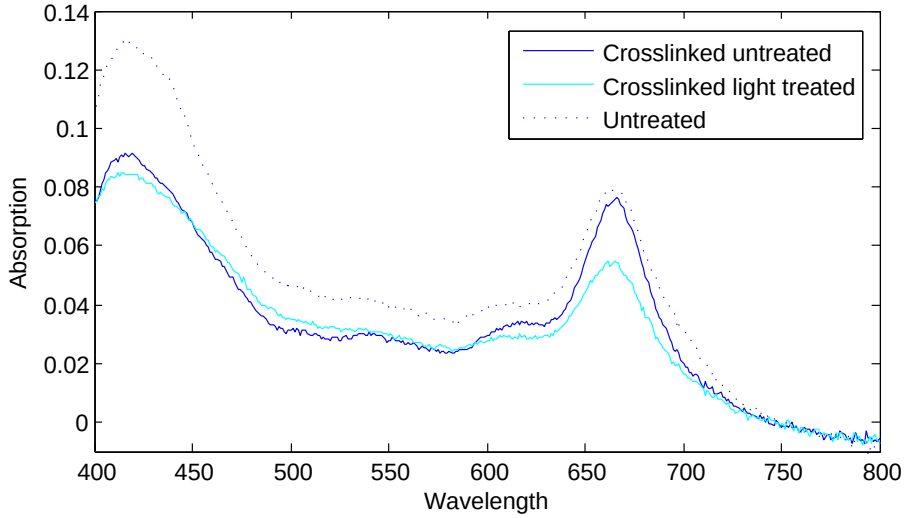

Figure 3.19: The samples prepared in Section 2.5.5.a were treated as described in Section 2.6.4 and their absorption spectra (measured as in 2.4.1) are shown. Pure catalyst samples treated in the same way as the hybrid catalyst (control samples of Section 2.6.4) were used as a baseline for the equivalent hybrid to obtain only absorption due to LHCII. Pure TiO_2:Cu catalyst was used as the baseline of the untreated hybrid catalyst.

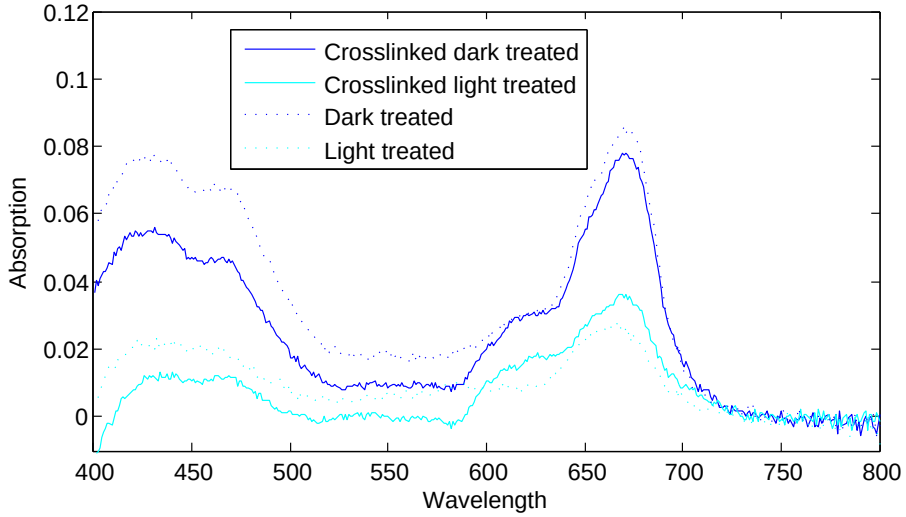

Figure 3.20: The samples prepared in Section 2.5.5.b were treated as described in Section 2.6.4 and their absorption spectra (measured as in 2.4.1) are shown. Pure catalyst samples treated in the same way as the hybrid catalyst (control samples of Section 2.6.4) were used as a baseline for the equivalent hybrid to obtain only absorption due to LHCII.

untreated dry sample (figure 3.19) shows higher LHCII peaks than the crosslinked samples, both light treated and untreated. Furthermore, the light treated sample shows lower absorption at the red light peak position than the untreated sample in the same figure. In figure 3.20, the light treated samples again show lower absorption. In this case it is possible to

compare a sample that was crosslinked to one that was not and see their response to light treatment and dark treatment (washed in deionised H_2O). The crosslinked light treated sample does not show higher LHCII content than the non-crosslinked equivalent, and for the dark treatment the opposite is seen. These results suggest that the crosslinking does not protect the catalyst from LHCII loss due to light, washing or drying.

3.4.5 Discussion

Standard catalyst characterisation methods confirmed the successful preparation of anatase by the sol-gel method. In experiments using this catalyst, LHCII spontaneously adsorbed on the catalyst surface when the two were mixed in acidic or basic solution. Most of the LHCII is taken up by the catalyst during mixing in those conditions ($> 95\%$ at pH 5.3) and the pH of the preparation solution strongly affected the success of the LHCII adsorption, with very little LHCII adsorbing on the catalyst surface in near neutral solutions. An intermediate LHCII concentration was selected for the hybrid catalyst preparation methods following results that suggested a high LHCII concentration inhibits adsorption.

The LHCII on the catalyst was observed in the absorption spectra of the hybrid catalysts, which showed LHCII specific absorption peaks. The state of the LHCII on the surface was investigated by the fluorescence spectrum and shows possible signs of charge transfer. Fluorescence spectra also indicated some damage to the LHCII on the surface. However, the spectrum with excitation at 470 nm shows that the chlorophyll *b* is passing on the the excitation energy to chlorophyll *a* since the fluorescence peak is at ~ 680 nm. This suggests that the LHCII is not broken down and there is also intact LHCII on the surface, because chlorophylls *a* and *b* are still coupled. If only chlorophyll was present on the surface, it is expected that this would be quenched and no fluorescence would be visible.

The LHCII adsorbed on the catalyst surface was relatively quantified in response to the pH of the solution in which the two interact. The fluorescence spectra together with the UV-Vis absorption results, suggest that little LHCII is adsorbed in neutral pH, but from the fluorescence spectrum it can additionally be concluded that the LHCII is less deformed in this case, as the spectrum is closer to that of pure LHCII. The ideal pH conditions for storing LHCII are at pH 7.6, which may explain the more intact state of the LHCII in this catalyst. Furthermore, the sample prepared at pH 9 has a higher fluorescence than that at pH 5. As shown in the absorption spectra of the same samples (figure 3.13), the amount of the LHCII adsorbed on the catalyst is approximately the same. Therefore the state of the LHCII may be what differs in this case.

LHCII attachment to the catalyst was also tested by a different method, whereby APTMS was used to covalently bind the LHCII on the surface. This was first tested on glass fibre filter disks where it had been shown to bind alkaline phosphatase in the work of Taylor et al. (2005). In this case a very strong attachment was shown that did not allow the extraction of chlorophyll by acetone. On the other hand, when the method was tested on the catalyst, the same result was not observed. It was seen that both

the covalent bound sample and the APTMS control had a clear LHCII absorption peak in their spectra but not a fluorescence peak. If the method is binding chlorophyll instead of the LHCII, which would also explain why this is not extracted by acetone from the glass fibre disks (if in that case the binding is covalent), this could cause the lack of fluorescence as it would be quenched. Alternatively, the LHCII may be deformed and bound in such a shape so that fluorescence is quenched.

For the catalyst to be used in CO_2 photoreduction, it needs to be stable in response to light. Otherwise, new catalyst would have to be prepared for each reaction and the energy used in its preparation is likely to exceed that of the fuel created by the photocatalysis. Light treatment of the hybrid catalyst led to a decrease in the amount of LHCII present on the catalyst. The weight of the LHCII as well as its chlorophyll content decreased following photoreaction. Crosslinking was tested as a method to stabilise the hybrid catalyst against damage by light irradiation but the results showed that this was not sufficient to protect the LHCII. Therefore, another stabilising method needs to be investigated for the hybrid catalyst to be a sustainable method of CO_2 photoreduction.

Absorption spectra, fluorescence spectra and the chlorophyll content of hybrid catalysts all show that drying has a severe effect on LHCII present on the catalyst surface. The LHCII specific absorption peaks as well as the chlorophyll content are decreased after drying, while wet samples give a fluorescence pattern much closer to that of pure LHCII (figure 3.10). Crosslinking also does not stabilise the hybrid catalyst against drying. However, the dry hybrid catalyst is relatively stable in storage at room temperature for long periods of time, a property not shared by pure LHCII.

The absorption spectra of hybrid catalysts have peaks that correspond to chlorophyll absorption. However, as shown in Section 3.3.3, the excitation spectra of the same catalysts do not match the absorption spectra. The excitation maximum (measuring emission at 680 nm) is around 415 nm, instead of the chlorophyll peak at 435 nm. The difference in the peaks of the two may indicate a functional relationship between the materials that is using the light absorbed at 435 nm for the photochemistry of the catalyst reactions instead of dissipating it as fluorescence.

Chapter 4

CO_2 Photoreduction Using Hybrid Catalyst

A novel hybrid catalyst was designed to perform CO_2 photoreduction under visible light. As discussed in Section 2.5, different techniques were tested for the preparation of this hybrid catalyst revolving around different attachment methods for the TiO_2:Rh catalyst, which was used as the base, and the LHCII, the "visible light dye". The photocatalytic activity of some of the prepared catalysts was assessed by the concentration of organics produced from the photoreduction of CO_2 in an aqueous-phase reaction. A variety of compounds were produced by the reaction; different detection systems were used, each of which measured the concentration of a subset of these products. The products detected were methane (Section 4.2.1), carbon monoxide, methyl formate and acetaldehyde (Section 4.2.2). As well as organic compounds and CO, photocatalysis in aqueous solution also produces hydrogen gas from water splitting. This was confirmed and the produced H_2 was quantified (Section 4.2.3).

4.1 Methods

4.1.1 CO_2 photoreduction detecting C-products in the gas phase

The photoactivity of the hybrid catalyst (TiO_2:Rh-LHCII), which was prepared as described in section 2.5.1.a, was measured experimentally through the concentration of organics produced during photocatalysis. These experiments were carried out at the University of Nottingham using the system shown in figures 4.1 and 4.2. 0.5 g catalyst were suspended in 200 mL deionised water inside the reactor and a magnetic stirrer was used at 200 rpm to keep it well mixed. The reactor was custom made at the National Taiwan University for the purpose of CO_2 photoreduction experiments (Liu 2012). It consists of a quartz vessel (to allow use of UV light as well as visible) of capacity 316.93 mL and a Teflon lid with a quartz tube running through its centre, to allow illumination through the centre as well as the sides of the vessel. However, this feature was not used for the work described in this thesis. The vessel was placed on a base made of hard plastic with soft silicone between base and vessel. The lid had a groove

that matched the top of the vessel, in which a silicone O-ring was placed to make the seal between vessel and lid. The lid was placed over the vessel so that the O-ring covered the opening of the vessel and it was screwed tightly to the base. There were four openings on the lid, one to introduce the CO_2 gas, one connected to a pressure meter to monitor the pressure, and two sealed with silicon septa to allow measurements to be made through them by injection of a gas tight syringe.

For the photoreduction experiment, first high purity CO_2 (< 0.1 ppm total hydrocarbon) was bubbled through the reactor for 20 min to remove any other gases and then the reactor was sealed and the pressure adjusted to 1 bar using the digital pressure gauge. The reactor was kept at this pressure to stabilise for 10 min before it was sealed completely. This is necessary for the CO_2 to reach equilibrium between the dissolved and gas phases and, in the cases when it was omitted, the reactor pressure quickly decreased after sealing. The light source was turned on, applying UV (four T5 fluorescent blacklight blue, 8 W lamps, primary wavelength at 365 nm) or visible light (LED lamp, spectrum shown in figure 4.3) on the reactor, depending on the experiment. The light intensity in front of the catalyst for the visible light was 1110 µmol $m^{-2}s^{-1}$ while the intensity of the UV light inside the reactor was 3.25 mW/cm^2 (Liu 2012). After 1.5 h, three gas samples of volume 400 µL were removed from the sealed reactor using a gas-tight sampling syringe and injected into the Gas Chromatograph (GC) for analysis (as shown in figure 4.1).

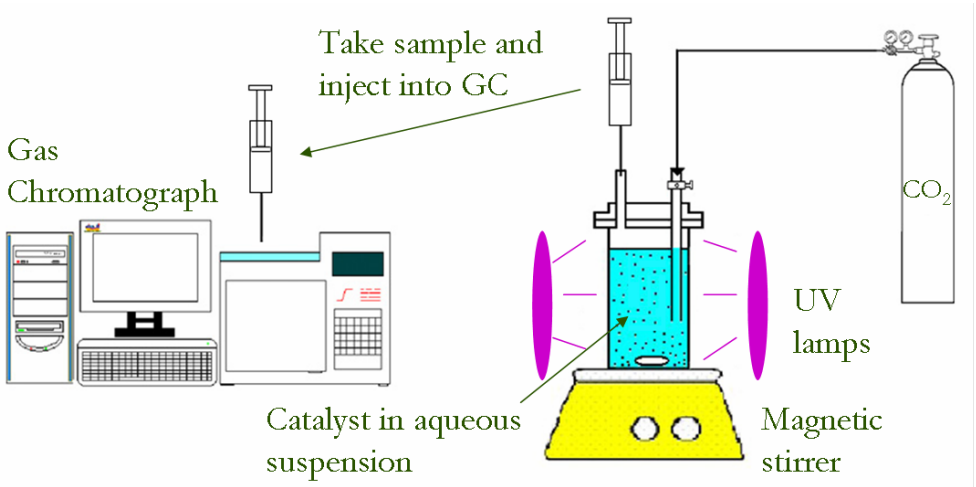

Figure 4.1: The process of photocatalysis. CO_2 is pumped from a cylinder to the photoreactor, which consists of a sealed system with water and catalyst suspended by mixing on a magnetic stirrer. UV or Visible light lamps face the reactor. A GC is used to take methane measurements. Modified from (Chiou et al. 2009) with permission from Elsevier.

The GC used was the Trace GC Ultra, Thermo Scientific (Waltham, MA, U.S.A.) with a flame ionisation detector (FID). The column used for the separation was a 30 m-long RT-Molecular sieve 5A porous layer open tubular capillary column by Restek (Bellefonte, PA, U.S.A.) with inside diameter of 0.53 mm. The inlet temperature used was 60°C, the detector

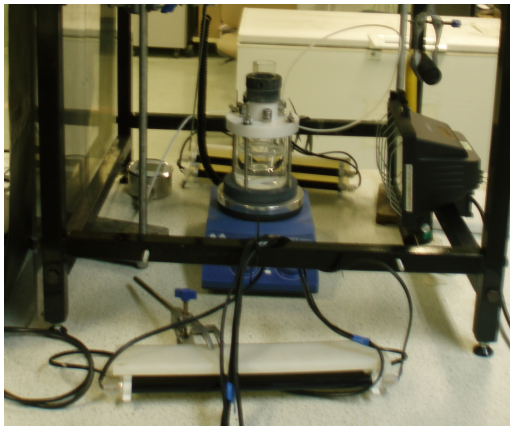

Figure 4.2: Photoreactor used in experiments at the University of Nottingham.

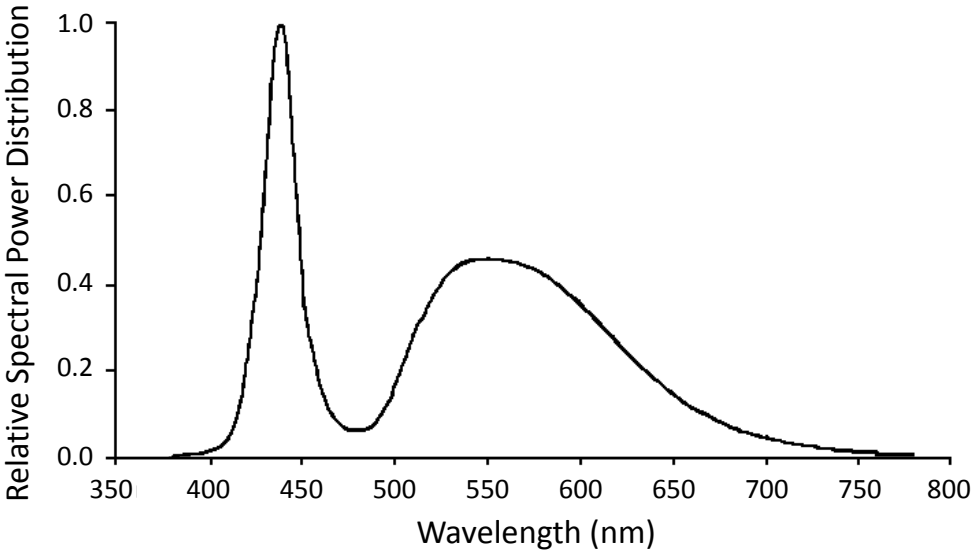

Figure 4.3: Emission spectrum of visible light source used in experiments of Section 4.1.1.

temperature was 180°C and the oven temperature was 50°C. He was used as the carrier gas and the flow rate through the column was 20 mL/min. This method was developed by Liu (2012).

There was a single peak in the chromatogram at retention time 1.34 min which had been shown with this setup to correspond to methane (Liu 2012). The retention time of this peak decreased with repeated injections due to CO_2 remaining adsorbed on the inner surface of the column and interfering with CH_4 adsorption. To prevent CO_2 build-up, a clean up method was developed by Liu (2012), where the oven temperature was increased to 185°C for 20 min, and it was performed daily.

4.1.1.a Control Experiments

As well as the hybrid catalyst (TiO_2:Rh-LHCII), a number of selected control catalysts were also used in the reactor to test whether the expected

increase in production was due to an LHCII-catalyst cooperation. Pure TiO_2:Rh ("control catalyst") was tested to measure the photoactivity of the catalyst without LHCII in order to ascertain the effect of LHCII. Pure LHCII was tested to ensure that the increase in methane was not due to LHCII breakdown unrelated to the catalyst. A TiO_2:Rh sample treated only with the detergent medium of section 2.5.1.a, the preparation medium of TiO_2:Rh-LHCII, was also tested ("Detergent-catalyst"). Finally, Bovine Serum Albumin (BSA) was attached to the catalyst in an indirect test to confirm that the increase was LHCII-specific and not due to the catalyst breaking down a generic organic compound to produce methane. The same amount, in mol, of BSA was used for the catalyst treatment, as for the LHCII. A background value was also measured from pure CO_2 taken at the start of the experiment from the reactor before the light source was turned on.

4.1.2 CO_2 photoreduction detecting C-products in the liquid phase

Further CO_2 photoreduction experiments were performed by Professor J.C.S. Wu's group at the National Taiwan University in Taipei, using the hybrid catalyst prepared by adsorption (Section 2.5.1.a). The work of this section has been submitted for publication (Lee et al. 2014).

In this case, a 2 m Parapak Q column, (China Chromatography Co., LTD, Taipei, Taiwan), was used in the GC (China Chromatography 9800, China Chromatography Co., LTD, Taipei, Taiwan) for the separation of the products which allowed the analysis of liquid samples and therefore the detection of different compounds.

The experimental setup was similar to that described in the previous section. The reactor was also manufactured at the National Taiwan University and followed the same design, excluding the lid which was made of stainless steel (figure 4.4). A smaller amount of catalyst was used in these experiments, 0.2 g of catalyst in 180 mL deionised water. Furthermore, prior to the addition of CO_2, the reactor was purged with He gas for 1 h to remove air from the solution. A GC measurement of the liquid phase was made after the He purge to confirm that the concentrations of the C-containing compounds were below detection levels at the start of the experiment. CO_2 was then bubbled through the reactor for 30 min, after which the CO_2 pressure was adjusted to 1.1 bar, the reactor was sealed and the light source was switched on.

The light source used in these experiments contained a 300 W xenon lamp. The spectrum of light produced by it is shown in figure 4.5 and ranges from 300 nm to 1000 nm meaning that it contains, as well as visible light, also a small amount of UV and some infrared light. No filter was used to prevent the UV light from reaching the catalyst in the reactor. The light intensity was 362 mW/cm^2 in front of the reactor. The distance between the light source and the reactor was 30 cm to avoid heat from the lamp reaching the reactor. Additionally, as the reactor was not insulated, there was heat exchange between it and the environment, which also slowed down the temperature increase inside the reactor.

Figure 4.4: Photoreactor used in experiments at the National Taiwan University.

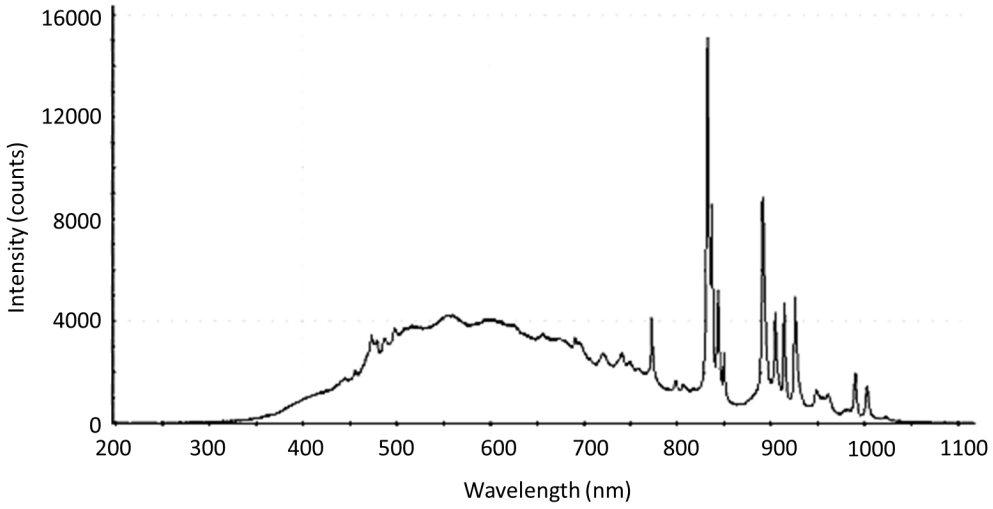

Figure 4.5: Emission spectrum of visible light source used in experiments of Section 4.1.2.

During the experiment, a 3 µL liquid sample was collected by syringe for GC analysis every hour. The reaction lasted 6 h and, after this, the catalyst was collected and analysed by TGA to detect any changes to its properties, particularly those relating to LHCII (results in Section 3.4.3). To prevent the catalyst powder from entering the GC and blocking the column, the sample was centrifuged before analysis. The carrier gas of the GC was nitrogen and the reaction products were quantified with a FID. The products that were detected were carbon monoxide, methyl formate and acetaldehyde.

For the detection of CO in particular, the GC was also connected to a methaniser which selectively transformed CO to CH_4 with H_2 at 360°C using a Ni catalyst, thus increasing the sensitivity of the GC to CO. The methaniser was connected to the GC between the column and the detector so that the sample was separated into the products before being carried into the methaniser. CO has a low retention time and therefore exits the column first. Once the peak corresponding to it appeared on the GC spectrum,

Experiment	Material	Gas	Light source
CO_2 Photoreduction with TiO_2:Rh-LHCII	TiO_2:Rh-LHCII	CO_2	On
CO_2 Photoreduction with TiO_2:Rh	TiO_2:Rh	CO_2	On
Control 1	LHCII	He	On
Control 2	LHCII	CO_2	On
Control 3	TiO_2:Rh-LHCII	He	On
Control 4	TiO_2:Rh-HEPES+βDM	He	On
Control 5	TiO_2:Rh-LHCII	CO_2	Off

Table 4.1: Control tests of CO_2 photoreduction.

the sample stream was switched to another exit to purge out CO_2, which is expected to follow it, and avoid high concentrations of CO_2 being carried into the methaniser. The sample stream was then switched back to analyse other products.

4.1.2.a Control Experiments

Additional experiments were run to confirm that the detected products resulted from the photoreduction of CO_2 and not the degradation of LHCII. The variables for these experiments were the type of material used as the catalyst, the gas in the reactor and the light conditions. Table 1 shows the conditions of each of these control experiments as well as the conditions of the original photoreduction experiments for comparison. Control 1 was performed to test whether LHCII is degraded by the light and produces small C-containing compounds. Therefore LHCII solution, without TiO_2:Rh, was illuminated in the reactor. He gas was used to purge the reactor as in the original experiment, but no CO_2 was added, to ensure that LHCII would be the only source of any products if these were detected. Control 2 tested if LHCII alone can function as a catalyst to produce C-species from CO_2. In this case also no TiO_2:Rh was added but, in contrast to Control 1, the reactor was filled with CO_2 after purging with He. It was suspected that TiO_2:Rh might actively degrade the LHCII during the reaction. To test this, Control 3 was designed and performed. In this experiment TiO_2:Rh-LHCII was suspended in deionised water, as in the original, but the reactor was not filled with CO_2 following the He purging. Consequently, any C-species detected in this experiment could only come from the LHCII treatment solution. This included LHCII as well as HEPES and βDM. Control 4 was performed to ensure the latter were not the source of the products. TiO_2:Rh-HEPES+βDM was used as the catalyst and no CO_2 was added to the reactor. Finally, a dark control (Control 5) with TiO_2:Rh-LHCII and CO_2 was performed, where the reactor was not illuminated by the light source, to confirm that the process producing the hydrocarbons is photoreduction, meaning that light is necessary.

4.1.3 Monitoring hydrogen production during CO_2 photoreduction

CO_2 photoreduction experiments were also performed during a visit to the laboratory of Professor J.C.S. Wu at the National Taiwan University. In these experiments, the hydrogen production was monitored using a GC (China Chromatography 2000, China Chromatography Co., LTD, Taipei) with a thermal conductivity detector (TCD). A 3.5 m long molecular sieve 5A (MS-5A) column was used and the carrier gas was argon. A gas sample of 0.25 mL was injected into the GC for analysis.

The experimental method was similar to that of Section 4.1.2 with the same reactor used and the same amounts of deionised water and catalyst. However, in this method, the reactor was not purged with He because the H_2 and He peaks overlapped when detected with the GC-TCD and therefore any remaining He would interfere with H_2 measurements. Instead, CO_2 was bubbled directly through the aqueous catalyst suspension for 30 min before the reactor was sealed.The light source and intensity were the same as previously given. Gas samples were taken at 2 h and 3 h and analysed by the GC. Measurements were also made before the light source was turned on (time 0) for comparison.

4.2 Results

4.2.1 CO_2 photoreduction detecting C-products in the gas phase

Photoreduction experiments were carried out as described in section 4.1.1 using different catalysts to test the hypothesis that LHCII will assist the TiO_2 catalyst in CO_2 photoreduction, and their results are shown in figure 4.6. The figure shows the relative production of CH_4 for each of the catalysts calculated as the mean over all the measurements that were taken by the GC during one or more experiments. The error bars show the 95% confidence intervals of the mean ($\pm$ 2 Standard Errors). The GC measurement error was estimated using the measurements of all the experiments. The error values were calculated by the difference between a measurement and the mean value of all the measurements of an experiment. All measurements in each experiment come from samples of the same gas and therefore any variation should only be due to GC measurement error (either from the equipment or the sampling). The standard deviation of these values from 0 was calculated as a measure of the error and its value was 0.12 ppm (or 0.56 times the hybrid catalyst's mean production). The degrees of freedom used to calculate the standard deviation were (number of measurements)-(number of experiments). Due to technical difficulties it was not possible to perform a calibration of the GC, and so the absolute amounts measured by the GC may not be accurate. Therefore, figure 4.6 shows the product concentrations of all experiments normalised to the mean product concentration of the hybrid catalyst (TiO_2:Rh-LHCII), which was measured as ~ 0.21 ppm.

It is clear that the hybrid catalyst greatly increased the methane pro-

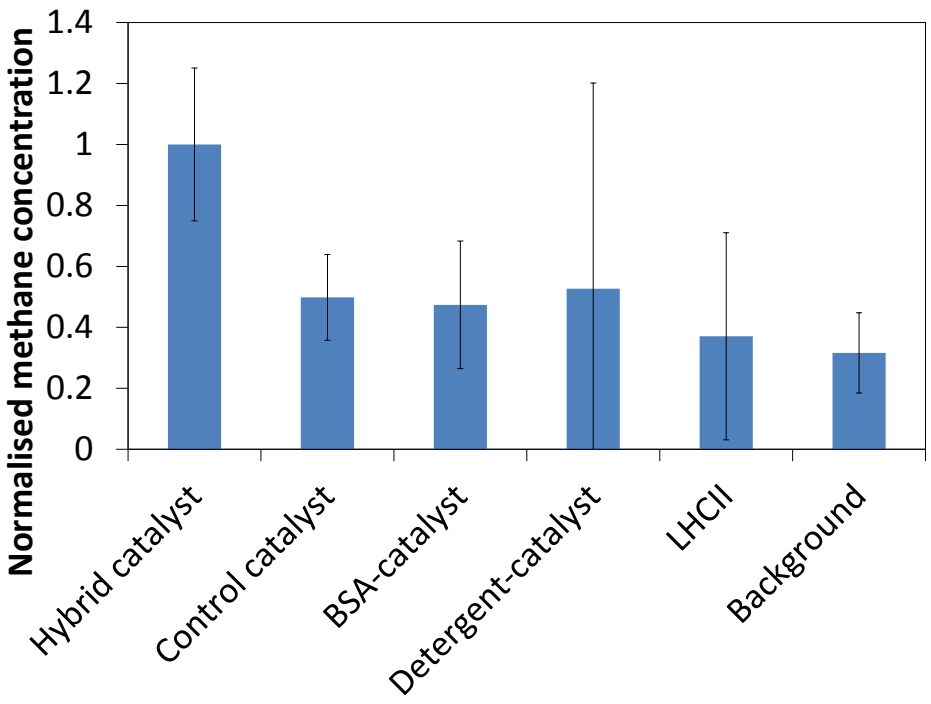

Figure 4.6: Average methane production in visible light for each catalyst sample normalised to the amount produced by the hybrid catalyst, TiO_2:Rh-LHCII (error bars of $\pm$ 2 Standard Errors). A different number of experiments was performed for each case: five with the hybrid catalyst, three with the control catalyst, two with the BSA-catalyst, one with the detergent-catalyst, one with the LHCII, six measurements were taken of pure CO_2.

duction in visible light. A one-tail T-test was performed for each of the controls against the hybrid to test whether the production by the control was significantly lower than that of the hybrid (null hypothesis: the hybrid does not produce more methane than the control). The measurements of the GC were used for this test, and not the fractions that are plotted in figure 4.6. The p values were 0.003 for the control catalyst, 0.007 for the BSA-catalyst, 0.074 for the Detergent-catalyst, 0.009 for the LHCII and 0.004 for the background measurements. This means that, other than the "Detergent-catalyst" experiment, all others produced significantly lower amounts of methane compared to the hybrid catalyst, even when using the conservative Bonferroni comparison (so that for significance it is required that $p < \frac{0.05}{5}$). The "Detergent-catalyst" experiment was only performed once due to the difficulties mentioned earlier and this partly accounts for the large standard error.

Experiments were also carried out with UV instead of visible light for the hybrid and control catalysts, and the results are shown in figure 4.7, again normalised to the visible light production of the hybrid catalyst. In this case, a two-tailed T-test was used because it is immediately obvious that the null hypothesis of the previous test (the hybrid does not produce more methane than the control) cannot be rejected. The two-tailed T-test

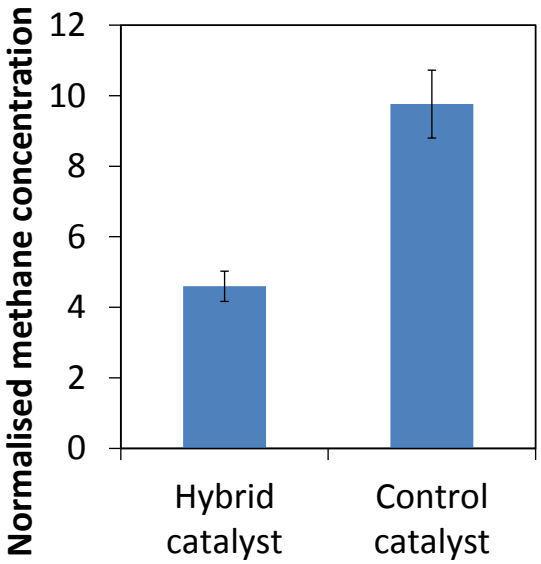

Figure 4.7: Average methane production using UV light with the hybrid catalyst and control catalyst, normalised to the amount produced by the hybrid catalyst under visible light. A single experiment was performed for each.

showed that the difference between the hybrid and the control is significant ($p=6.08 \cdot 10^{-4}$) so it was concluded that in UV light the hybrid catalyst is less efficient.

4.2.2 CO_2 photoreduction detecting C-products in the liquid phase

Carbon monoxide, methyl formate and acetaldehyde were detected in the aqueous phase of the photoreactor during the photoreduction experiment. Figure 4.8 shows the concentrations of the three products at 1 h time intervals for experiments using TiO_2:Rh and experiments using TiO_2:Rh-LHCII as the catalyst. Within the first hour of the reaction CO was produced and its concentration did not increase significantly in the later measurements suggesting that it had reached its steady state value. Its concentration decreased towards the end of the experiment but this can be attributed to the predicted temperature rise which will decrease the solubility of CO in the aqueous suspension. The catalyst used for the experiment (TiO_2:Rh or TiO_2:Rh-LHCII) does not appear to have a strong effect on the CO concentration and at the end of the experiment the concentrations were the same in the two experiments. On the other hand, the concentration of acetaldehyde at the end of the experiment is approximately ten times higher in the TiO_2:Rh-LHCII experiment than that with TiO_2:Rh. TiO_2:Rh-LHCII also increased the methyl formate production compared to TiO_2:Rh, so that the final concentration was four times higher with the hybrid catalyst. Methyl formate is believed to be formed by esterification of the formic acid and the methanol produced by the photoreduction of CO_2. However, neither of these was detected in the experiments, possibly because they primarily reacted to form the methyl formate before desorption while their concen-

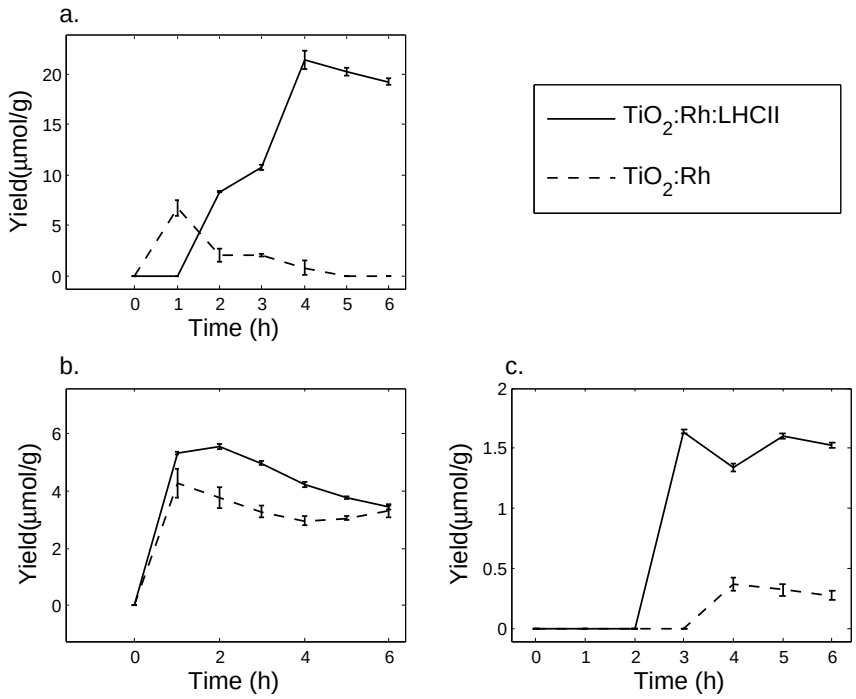

Figure 4.8: Production of C-containing compounds by TiO_2:Rh and TiO_2:Rh-LHCII catalyst. Plot a shows the concentrations of acetaldehyde for catalyst TiO_2:Rh-LHCII (solid line) and control catalyst TiO_2:Rh (dashed line). Plot b shows the concentrations of CO and plot c the concentrations of methyl formate, from the same experiments. Error bars of a single standard deviation are shown in the figure.

trations in the solution were below the detection limit.

The concentrations do not continue to increase throughout the experiment but instead plateau and in some cases decrease towards the end of the 6 h. As mentioned in Section 1.4, TiO_2 can perform both oxidation of organics to CO_2 and reduction of CO_2 to organics. Therefore this concentration pattern could be due to oxidation of the reduced products.

4.2.2.a Control experiments

Control experiments were performed to confirm the source of the C-containing compounds produced during the photoreaction (table 4.1). All control photoreactions found no products within the detection limit of the GC. The UV-Vis spectra of the catalysts (Section 3.4, figure 3.17) indicated that the absorption at 670nm diminished after the photoreaction. The same phenomenon could be observed from the TGA (figure 3.18), where the weight loss of LHCII on the catalyst decreased after the photoreaction. One explanation is that the LHCII was degraded by TiO_2:Rh during the photoreaction. Another is that part of the LHCII desorbed from the catalyst surface because of the weak adhesion. If the first explanation is correct, it could be hypothesised that some products detected by the GC might originate from LHCII degradation instead of CO_2 reduction. The results of the control experiments, which are described in Section 4.1.2.a, show that

this is not the case, since no products could be detected when CO_2 was not added to the reactor. This means that the yields shown in figure 4.8 were the result of CO_2 reduction and not due to the degradation of LHCII due to illumination (Control 1), (Control 2) or by the catalyst (Control 3). The TiO_2:Rh-HEPES+βDM catalyst also produced no detectable reduced C-species (Control 4), confirming that these are not the source of the products. Finally, (Control 5) showed that light is necessary for CO_2 reduction. The above confirm that CO_2 photoreduction is indeed occurring in the reactor and it is the only source of detectable products.

4.2.3 Monitoring hydrogen production during CO_2 photoreduction

As well as CO_2 reduction, the TiO_2 catalyst is also capable of water splitting as discussed in Section 1.4, producing hydrogen and oxygen gas at a molar ratio of 2:1. In fact, water splitting is necessary for CO_2 reduction, as it is the source of the hydrogen atoms in the organic products. H_2 measurements were made from CO_2 photoreduction experiments in visible light, as described in Section 4.1.3, using TiO_2 catalysts with and without LHCII, prepared in different ways. Figure 4.9 shows the results of these experiments. Only H_2 measurements are shown because high O_2 concentration in the air makes it impossible to distinguish between O_2 production and a small contamination (from residual air in the reactor or during injection). As H_2 is not present in the air, small amounts of air will not interfere with the measurement. Air contamination was confirmed during the measurements by the presence of a N_2 peak in the chromatogram.

Figure 4.9 shows the hydrogen concentration after 3 h of each experiment. Catalysts prepared using different methods were tested in these photocatalysis experiments. The "Control catalyst" refers to an experiment using untreated TiO_2:Rh. Only a very small amount of H_2 was produced in this case. The "Hybrid catalyst" is the TiO_2:Rh-LHCII, prepared as described in Section 2.5.1.a. The "Pre-treated" hybrid and control catalysts were treated with glutaraldehyde detergent solution with and without LHCII respectively, as described in Section 2.5.4.a. "Post-treated" hybrid and control catalysts were treated with glutaraldehyde after treatment with detergent solution with and without LHCII respectively, as described in Section 2.5.4.b.

The amount of H_2 produced using TiO_2:Rh-LHCII appears much higher than for TiO_2:Rh. Each measurement was only performed once so their uncertainty cannot be estimated. However, this observation is supported by the results of the experiments with pre-treated and post-treated catalysts which consistently show a higher H_2 production for hybrid catalysts compared to the controls. A paired t-test was used to compare the means of the catalysts with and those without LHCII and the results showed a significant difference between the two types ($p = 0.012$).

For all these experiments, a measurement was also made at time 0 h and no H_2 peak is present in the chromatograms of those measurements, confirming that no H_2 is present in the reactor before the light is turned on. The exception is the experiment using the pre-treated control sample.

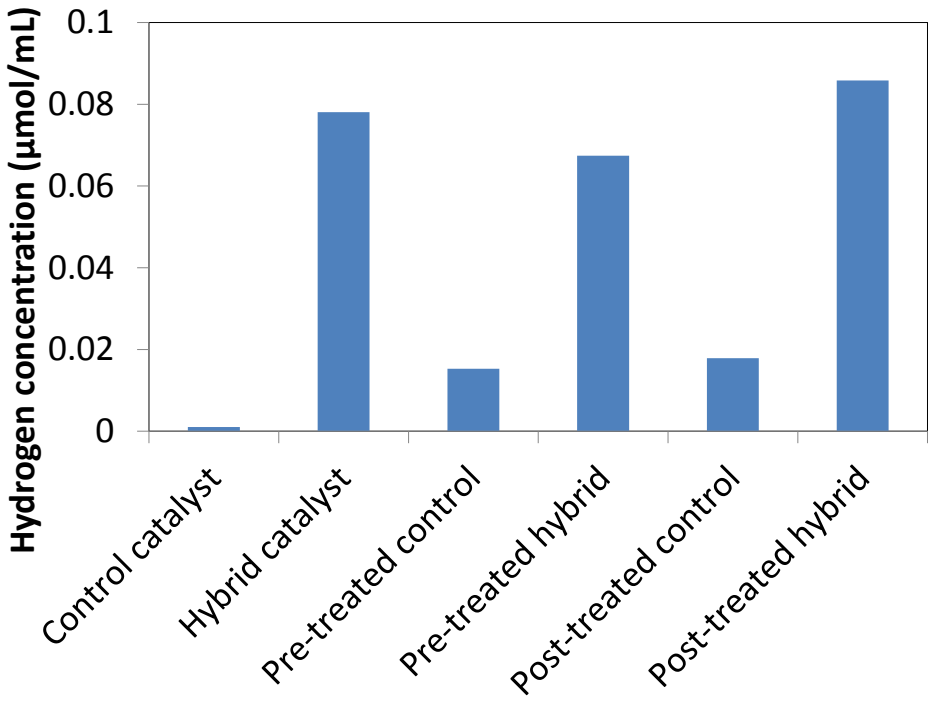

Figure 4.9: Hydrogen measurements after 3 h of photocatalysis experiments using catalysts with LHCII (hybrid) and without (control). Different preparation methods were tested. The "Control catalyst" refers to untreated TiO_2:Rh, while the "Hybrid catalyst" refers to TiO_2:Rh-LHCII prepared as described in Section 2.5.1.a. The preparation method of the "Pre-treated" samples is described in Section 2.5.4.a. Finally, the preparation method of the "Post-treated" samples is described in Section 2.5.4.b. A single experiment was performed for each catalyst.

In this case, the experiment was run for longer and to avoid significant loss in pressure, a measurement was not made at time 0 h, though there is no reason why the results of such a measurement should have been different if it had been made. Measurements were instead made every hour between 2 h and 6 h. The results are shown in figure 4.10 and indicate that the concentration of H_2 continues to increase but its production slows down with time.

4.3 Discussion

The LHCII on the catalyst enhances its visible light absorption, evident from the UV-Vis absorption spectra in Section 3.3.1.a. Additionally, in all experiments using visible light presented in this chapter, hybrid catalysts are consistently better than their undyed counterparts (by approximately two, four, seven and ten times for methane, methyl formate, hydrogen and acetaldehyle respectively), supporting the hypothesis that LHCII transfers the light energy it absorbs to the catalyst in a productive way. Controls to test alternative explanations as to how the LHCII enhances photocatalysis concluded that this result was LHCII specific, as a control organic compound does not give a higher production than the catalyst alone and

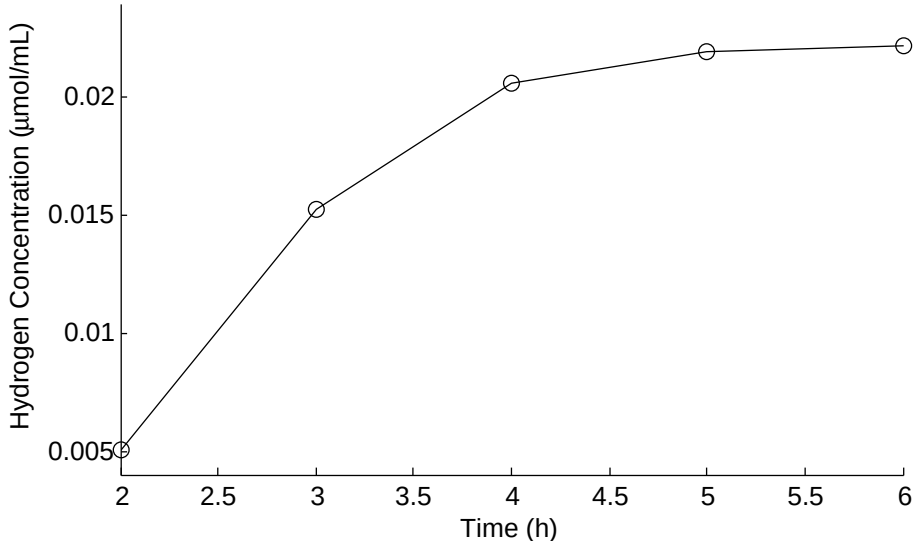

Figure 4.10: Time profile of hydrogen concentration during CO_2 photoreduction experiments using pre-treated control catalyst, prepared as described in Section 2.5.4.a.

the detergent and buffer used in the preparation are also not sufficient to enhance photocatalysis. Furthermore, the hybrid catalyst was shown to convert CO_2 to organic compounds because in the absence of CO_2 no organics were produced.

Different responses to the presence of LHCII were observed on the concentrations of different products. While acetaldehyde, methyl formate and methane productions were greatly enhanced, CO production was not different between hybrid and control experiments after 6 h. This can be explained by the model of the following chapter (Section 5.5), which shows that the more reduced species, such as methane or methanol, needed to form methyl formate, are more strongly affected by the amount of light absorbed relative to the less reduced species. In the case of the model this refers to formic acid. However, the same can be applied to CO, where the C atom has the same oxidation number as HCOOH and which is also produced from CO_2 by one reduction step, as shown in reaction (4.1)

$$CO_2 + 2e^- + 2H^+ \longrightarrow CO + H_2O + 2N_e, \tag{4.1}$$

where e^- and N_e are explained in Section 5.1.3.

Hydrogen experiments (Section 4.2.3) showed that catalysts containing LHCII produced significantly higher amounts of H_2 than catalysts without LHCII. The catalyst treated with glutaraldehyde after LHCII-detergent solution treatment showed the highest H_2 concentration after 3 h reaction. However, because only one experiment was carried out, the significance of the difference of this result compared to the other LHCII-containing catalysts cannot be confirmed. The same applies to differences between the catalysts without LHCII.

Finally, it was shown in Section 4.2.1 that in experiments using UV light, the LHCII hinders photocatalysis. UV light contains higher energy

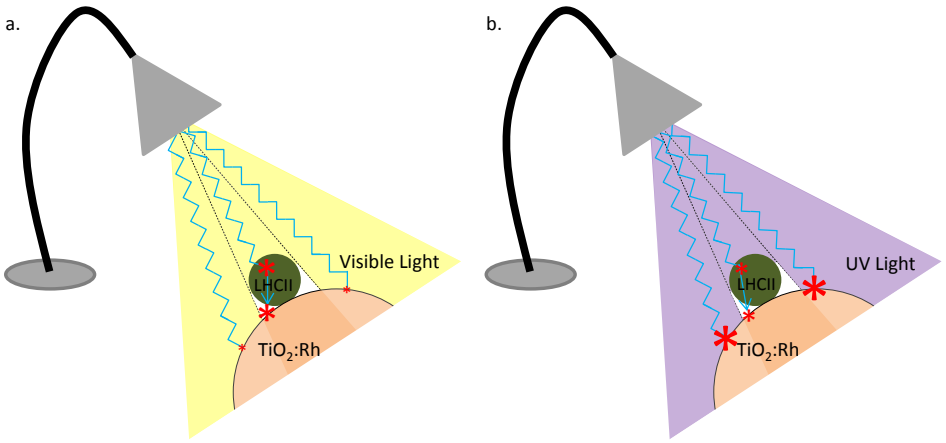

Figure 4.11: Surface shadowing by LHCII and its effect in experiments with visible and UV light. The light energy is represented by the blue lines and causes excitation of electrons (red stars) on the catalyst surface and on the LHCII. The excitation is then transferred from the LHCII to the catalyst. Bigger or smaller stars are used to indicate a larger or smaller amount of excitation. The diagram is not drawn to scale.

photons that are absorbed directly by the catalyst and thus are more effective than indirect energy reaching the catalyst through LHCII (illustrated in figure 4.11), which only absorbs a small amount of UV light (Lichtenthaler et al. 1981). Additionally, from the UV-Vis absorption spectrum of the hybrid catalyst (Section 3.3.1.a, figure 3.4), it is evident that the UV light absorption is much higher than the visible light absorption, even with LHCII. This explains why UV light experiments produce a higher concentration of organics. Furthermore, no absorption increase is observed in the UV light due to LHCII adsorption on the catalyst. In this case, the LHCII may instead be blocking active sites that could otherwise be used for the reaction, by preventing the UV light or the CO_2 from reaching them. On the other hand, in visible light the majority of the excitation comes from LHCII absorption and subsequent transfer to the catalyst (figure 4.11), while direct excitation of the catalyst is minimal. Surface blocking is also expected to occur in this case, but its effect is masked by the overall increase due to LHCII assisting the light harvesting. An understanding of the mechanism of this decrease could be gained by testing different LHCII immobilisation techniques and could lead to its prevention and thus to further increase the organic production of the visible light experiments, as well as the UV light experiments.

For CO_2 photoreduction to be a viable fuel production method in the United Kingdom and northern Europe, and thus avoid further energy costs relating to fuel transport from high light-intensity regions, the hybrid catalyst would have to function efficiently at low intensity light. In plants, LHCII is very efficient at low light conditions and it would be interesting to test if this characteristic is retained in its function with the catalyst. Experiments varying the light intensity could answer this question.

Chapter 5

ODE Models of CO_2 Photoreduction

A lot is unknown about CO_2 photoreduction and a better understanding of the process is necessary for its optimisation. Mathematical models were developed as part of this work to assist the in-depth analysis of the reaction system and identify targets for the optimisation of the experimental process. The LHCII on the catalyst increases the absorption of visible light and therefore, the model is used to test, in particular, the hypothesis that the amount of absorbed light correlates positively with the production of organic compounds.

Section 5.1 describes the system that is modelled in this chapter, together with assumptions made for all the models that will be described in the following sections. Sections 5.2–5.4 describe the simple ODE model developed to simulate artificial photosynthesis. A simplified mechanism will be presented, focusing primarily on the effects of charge in the reactions that CO_2 is involved in. The model description begins by looking at the first steps of the reaction, the conversion of CO_2 to HCOOH, which leads to a model with two variables. This makes it possible to perform phase plane analysis on this system. The adsorption/desorption step is then added to this model. The full mechanism, reactions (5.39), can be separated into repeating units, and the model of Section 5.3 represents the first of these. This separation simplifies the modelling of the full mechanism, based on the analysis of the first unit. Finally, in Section 5.4, the simplified mechanism describing CO_2 to CH_4 conversion is modelled in full.

In sections 5.5–5.6, a more complex reaction mechanism is presented where water splitting is explicitly included and its effects on the reactions of CO_2 photoreduction are investigated. Two models were developed, both of which include water splitting explicitly; the first uses simple mass action kinetics and the second makes use of the Langmuir isotherm. The differences between the two will be presented in detail in the following sections, but it should be noted that the second model was developed in conjunction with the discrete model of Chapter 6 to be compatible with the reactions simulated in that case.

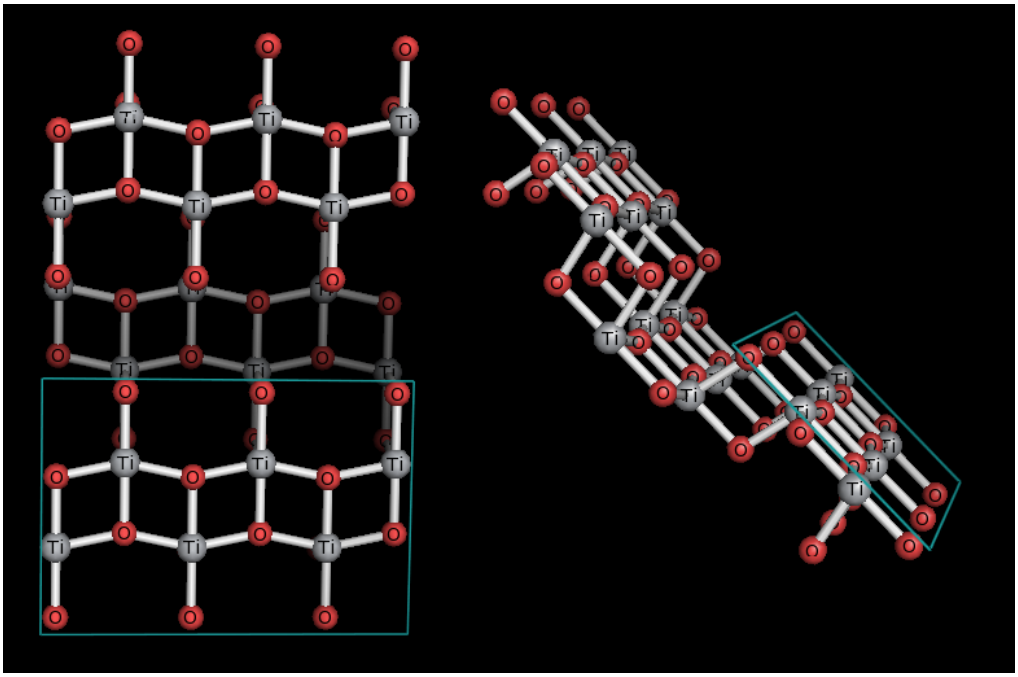

Figure 5.1: The (100) surface of the TiO_2 catalyst.

5.1 Reaction components

5.1.1 The catalyst surface

The surface of TiO_2 is made up of Ti^{4+} and O^{2-} ions (denoted as simply Ti and O respectively in figure 5.1). The bonds formed between the Ti^{4+} and O^{2-} ions have both an ionic and a covalent bonding character (Beltran et al. 2001) and are shown as thick lines connecting the ions in figure 5.1. A photon can be absorbed by an electron associated with an O^{2-}, moving the electron to a Ti^{4+}, leaving a positive hole on the O-ion, now O^{-}, and adding an extra electron to the Ti-ion, now Ti^{3+}. It is these electrons and holes that will react with the carbon species to reduce or oxidise them.

For the reaction to occur, the reagents need to be adsorbed on the surface of the catalyst. The number of sites on the surface (all Ti and O atoms) is constant and can be calculated approximately from measurements of the surface area per gram of the catalyst (Section 3.2.2). It is assumed that the entire surface is made up of the (100) anatase surface, an assumption that will also be used in the discrete spatial model of Chapter 6. "(100)" represents the Miller indices of the surface, used to indicate the orientation of the surface relative to the crystal structure of the material, and the particular surface used here, (100), is shown in figure 5.1.

The (100) surface of the anatase unit cell (indicated by the dashed lines in figure 5.2) has dimensions 3.78 Å×9.51 Å so its surface area is $\sim 3.6 \cdot 10^{-19}$ m^2. Each two dimensional unit cell corresponds to 2 Ti and 4 O surface atoms, as can be seen in figure 5.2. As some of the atoms are shared between unit cells (namely, those at the borders of the unit cell), appropriate corrections need to be made so that these atoms only count toward a fraction of an atom in each unit cell, half or a quarter depending

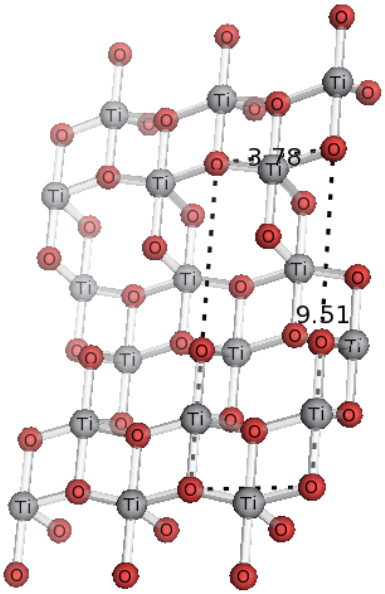

Figure 5.2: The (100) surface of anatase with dashed lines indicating the borders of a unit cell. The dimensions (in Å) of the unit cell are shown.

on their position.

The surface area per gram is ~ 46.2 m^2/g (result from Section 3.2.2) so the number of unit cells per g can be calculated as $\sim 1.28 \cdot 10^{20}$, and from that, the number of sites per g. There are 6 sites per unit cell, therefore there are $7.7 \cdot 10^{20}$ sites per g. For the Nottingham experimental setup (described in Section 4.1.1), 0.5 g catalyst and 200 mL of water were mixed in the reactor. Therefore the concentration of sites is $1.9 \cdot 10^{21}$ sites/L and their molar concentration is $S = 3.2$ mM.

5.1.2 The aqueous solution

There are many different types of reactors in the literature such as those in Ozcan et al. (2007*b*), Wu & Lin (2005), Liou et al. (2011), Tan et al. (2006). The system modelled here is the slurry reactor, described in Chapter 4, where the catalyst is suspended in aqueous solution saturated with carbon dioxide at 1 bar gauge pressure. The molar concentration of carbon dioxide in the solution was calculated to be $6.6 \cdot 10^{-2}$ M and the pH of the solution is ~ 4. From this value, the concentrations of protons and hydroxides in the solution can be estimated as 10^{-4} M and 10^{-10} M respectively. Finally, since the concentrations of all other compounds are small compared to that of water, the water concentration of the suspension can be approximated by the concentration of pure water, 55.5 M. The reactor is sealed during the experiment meaning that the system is closed and therefore mass is conserved. This property is used in the model in the form of carbon conservation. In fact there are more reactions than those modelled in the mechanisms shown, but in each case the assumption is made that the other reactions are negligible relative to those in the model, and therefore the other products are ignored.

5.1.3 Notation

The following notation is used throughout this chapter

- e^- refers to a Ti site with an extra electron (Ti^{3+}).
- N_e refers to a Ti^{4+} site that has the potential to take up an electron and become an e^- site.
- h^+ refers to an O site with a missing electron (a hole, O^-).
- N_h refers to an O^{2-} that can become a h^+ site.
- $[e^-]$, $[N_e]$, $[h^+]$ and $[N_h]$ are the concentrations of the e^-, N_e, h^+ and N_h sites respectively.
- S refers to the concentration of all the sites on the catalyst surface so that
$$[e^-] + [N_e] + [h^+] + [N_h] = S$$
is constant.
- CO_2(aq), HCOOH(aq), HCHO(aq), CH_3OH(aq) and CH_4(aq), refer to the carbon-containing compounds, carbon dioxide, formic acid, formaldehyde, methanol and methane, in the aqueous solution respectively.
- [CO_2(aq)], [HCOOH(aq)], [HCHO(aq)], [CH_3OH(aq)] and [CH_4(aq)] refer to the concentrations of carbon dioxide, formic acid, formaldehyde, methanol and methane in the aqueous solution respectively.
- CO_2(s), HCOOH(s), HCHO(s), CH_3OH(s) and CH_4(s), refer to the carbon-containing compounds, carbon dioxide, formic acid, formaldehyde, methanol and methane respectively, adsorbed on the surface of the catalyst.
- [CO_2(s)], [HCOOH(s)], [HCHO(s)], [CH_3OH(s)] and [CH_4(s)] refer to the concentrations of the carbon dioxide, formic acid, formaldehyde, methanol and methane respectively, adsorbed on the surface of the catalyst.

5.2 Two reaction model

5.2.1 Assumptions

This section introduces the simplified model, which does not describe every step of the reaction but instead has been stripped down to focus only on the e^- and h^+. It is assumed that there will be sufficient quantities of the other compounds available and that the adsorption/desorption rates of these compounds are fast, making the charged sites present on the surface the limiting factor, and therefore the driving force, of the reaction. Instead of adding the other compounds as variables in the model, their effects are included in the reaction rate constants.

This section focuses on the model of CO_2 photoreduction to HCOOH, which is the product with the highest carbon oxidation number. This means that a single reduction step is necessary to convert CO_2 to HCOOH as multielectron reactions are assumed, where the carbon-containing compound reacts simultaneously with two e^- for each reduction step. Similarly a reaction with two h^+ is assumed for the oxidation step.

A compound acting as a source of electrons is necessary to replenish the

electrons of the catalyst that are used in the reduction of carbon dioxide. These electrons will neutralise the holes that would otherwise accumulate on the surface, and so the compound is also referred to as a hole scavenger. The preferred compound for this purpose is water, which also provides the protons needed for the reaction. These protons form the hydrogen atoms in the organic compounds. In parallel to CO_2 reduction, the catalyst also produces oxygen and hydrogen gas by splitting the water. The reactions of water splitting are investigated in sections 5.5 and 5.6.

5.2.2 Reaction mechanism

The first step of the reaction, the photoreduction of CO_2 to HCOOH, is modelled using the reaction mechanism presented below. Reactions (5.1) indicate which reactants are necessary for each of the reactions and the corresponding products. As well as the molecules, the model also describes the charges and neutral sites used and produced by the reactions.
Activation of surface by light:

$$N_e \; + \; N_h \; + \text{light} \xrightarrow{k_0} \text{e}^- + \text{h}^+. \tag{5.1a}$$

Recombination of electron-hole pair:

$$\text{e}^- + \text{h}^+ \xrightarrow{k_{-0}} N_e \; + \; N_h \; + \text{heat}. \tag{5.1b}$$

Reduction of CO_2:

$$\text{CO}_2(\text{aq}) + 2\text{e}^- \xrightarrow{k_1} \text{HCOOH(s)} + 2N_e. \tag{5.1c}$$

Oxidation of HCOOH:

$$\text{HCOOH(s)} + 2\text{h}^+ \xrightarrow{k_{-1}} \text{CO}_2(\text{aq}) + 2N_h. \tag{5.1d}$$

Reactions of hole scavenger:

$$\text{h}^+ + \text{hole scavenger} \underset{k_{-2}}{\overset{k_2}{\rightleftharpoons}} N_h + \text{oxidised hole scavenger} \tag{5.1e}$$

This simple mechanism is an approximation of a more complicated system. The analysis starts from this low level of complexity to gain a better understanding of the system. In fact, the full mechanism is a source of controversy in the literature (Dey 2007). Here, reaction (5.1c) includes the adsorption of CO_2 on the catalyst surface as well as its conversion to HCOOH.

As mentioned in Section 5.2.1, not all reactants are modelled explicitly in this system. In reactions (5.1c)–(5.1d), the hydrogen atoms and the charges are not balanced between reactants and products. The missing compounds are not shown in the mechanism and their concentrations are included in the rate constants.

The hole scavenger and oxidised hole scavenger have been shown explicitly in the mechanism to explain their role in the reactions but their concentrations are also assumed constant and will be incorporated into parameters k_2 and k_{-2} respectively in the ODE system. Furthermore, it is

assumed that the light intensity is constant and therefore it is incorporated into k_0. A change in light intensity, or more accurately the amount of light absorbed by the catalyst, which correlates positively with light intensity, corresponds to a change in the value of k_0.

The heat produced by reaction (5.1b) is not included in the model as it does not fall under the scope of this work. Heat will not affect the other variables because reaction (5.1b) has been assumed irreversible, meaning that energy in the form of light, and not heat, is needed for surface activation (making 5.1a and 5.1b not strictly reverse reactions). The reactor is not isolated and therefore there is heat exchange between the reactor and its surroundings so that the temperature of the reactor is assumed constant. Due to this assumption, heat will also not affect the reaction rate constants.

Using mass action kinetics on system (5.1) leads to the system of ODEs

$$\begin{aligned}
\frac{\mathrm{d}[N_e]}{\mathrm{d}t} &= -k_0[N_e][N_h] + k_{-0}[\mathrm{e}^-][\mathrm{h}^+] + 2k_1[\mathrm{CO_2(aq)}][\mathrm{e}^-]^2, && \text{(5.2a)}\\
\frac{\mathrm{d}[N_h]}{\mathrm{d}t} &= -k_0[N_e][N_h] + k_{-0}[\mathrm{e}^-][\mathrm{h}^+] + 2k_{-1}[\mathrm{HCOOH(s)}][\mathrm{h}^+]^2 \\
&\quad + k_2[\mathrm{h}^+] - k_{-2}[N_h], && \text{(5.2b)}\\
\frac{\mathrm{d}[\mathrm{e}^-]}{\mathrm{d}t} &= k_0[N_e][N_h] - k_{-0}[\mathrm{e}^-][\mathrm{h}^+] - 2k_1[\mathrm{CO_2(aq)}][\mathrm{e}^-]^2, && \text{(5.2c)}\\
\frac{\mathrm{d}[\mathrm{h}^+]}{\mathrm{d}t} &= k_0[N_e][N_h] - k_{-0}[\mathrm{e}^-][\mathrm{h}^+] - 2k_{-1}[\mathrm{HCOOH(s)}][\mathrm{h}^+]^2 \\
&\quad - k_2[\mathrm{h}^+] + k_{-2}[N_h], && \text{(5.2d)}\\
\frac{\mathrm{d}[\mathrm{CO_2(aq)}]}{\mathrm{d}t} &= -k_1[\mathrm{CO_2(aq)}][\mathrm{e}^-]^2 + k_{-1}[\mathrm{HCOOH(s)}][\mathrm{h}^+]^2, && \text{(5.2e)}\\
\frac{\mathrm{d}[\mathrm{HCOOH(s)}]}{\mathrm{d}t} &= k_1[\mathrm{CO_2(aq)}][\mathrm{e}^-]^2 - k_{-1}[\mathrm{HCOOH(s)}][\mathrm{h}^+]^2. && \text{(5.2f)}
\end{aligned}$$

5.2.3 Conservation equations

As discussed earlier, the sites on the surface of the catalyst are conserved. Every Ti site can be an e^- or a N_e so that the sum of the concentrations of the two is equal to the concentration of Ti sites. Similarly, every O site can be a h^+ or a N_h so that the sum of their concentrations is equal to the concentration of the O sites. As there are twice as many O sites relative to the Ti sites, the concentration of O sites is two thirds of the total concentration of sites, while the concentration of Ti sites is one third of the total concentration of sites. Therefore, at any time

$$\begin{aligned}
[N_e] + [\mathrm{e}^-] &= \tfrac{1}{3}S, && \text{(5.3a)}\\
[N_h] + [\mathrm{h}^+] &= \tfrac{2}{3}S. && \text{(5.3b)}
\end{aligned}$$

As well as conservation of surface sites, the reaction also conserves the number of carbon atoms, meaning that

$$[\mathrm{CO_2(aq)}] + [\mathrm{HCOOH(s)}] = C \text{ (constant)}, \qquad \text{(5.4)}$$

where C is the initial total concentration of carbon $C = [\mathrm{CO_2(aq)}]_0 + [\mathrm{HCOOH(s)}]_0$. It is assumed that only $\mathrm{CO_2(aq)}$ is present in the reactor at the start of the simulation so that $[\mathrm{HCOOH(s)}]_0 = 0$. Therefore,

$$C = [\mathrm{CO_2(aq)}]_0, \tag{5.5}$$

where $[\mathrm{CO_2(aq)}]_0$ is $6.6 \cdot 10^{-2}$ M as discussed in Section 5.1.2.

Using these conservation equations, the system can be reduced to 3 equations by replacing

$$\begin{aligned} [N_e] &= \tfrac{1}{3}S - [\mathrm{e^-}], && (5.6a)\\ [N_h] &= \tfrac{2}{3}S - [\mathrm{h^+}], && (5.6b)\\ [\mathrm{CO_2(aq)}] &= C - [\mathrm{HCOOH(s)}]. && (5.6c) \end{aligned}$$

5.2.4 Non-dimensionalisation

Concentrations are nondimensionalised with respect to $\beta = C$ (the units of β being M) and time with respect to $\gamma = k_1\beta^2$ ($\mathrm{s^{-1}}$). The dimensionless parameters are

$$\begin{aligned} \hat{k}_0 &= \frac{k_0\beta}{\gamma}, && (5.7a) & \qquad \hat{k}_2 &= \frac{k_2}{\gamma}, && (5.7d)\\ \hat{k}_{-0} &= \frac{k_{-0}\beta}{\gamma}, && (5.7b) & \qquad \hat{k}_{-2} &= \frac{k_{-2}}{\gamma}, && (5.7e)\\ \hat{k}_{-1} &= \frac{k_{-1}\beta^2}{\gamma}, && (5.7c) & \qquad s &= \frac{S}{\beta}. && (5.7f) \end{aligned}$$

The dimensionless variables are

$$\begin{aligned} \hat{t} &= t\gamma, && (5.8a) & \qquad e &= \frac{[\mathrm{e^-}]}{\beta}, && (5.8c)\\ v_1 &= \frac{[\mathrm{HCOOH(s)}]}{\beta}, && (5.8b) & \qquad h &= \frac{[\mathrm{h^+}]}{\beta}. && (5.8d) \end{aligned}$$

The dimensionless system of ODEs obtained from (5.2), (5.6), (5.7) and (5.8) is

$$\begin{aligned} \frac{\mathrm{d}v_1}{\mathrm{d}t} &= (1-v_1)e^2 - \hat{k}_{-1}v_1h^2, && (5.9a)\\ \frac{\mathrm{d}e}{\mathrm{d}t} &= \hat{k}_0\left(\tfrac{1}{3}s - e\right)\left(\tfrac{2}{3}s - h\right) - \hat{k}_{-0}eh - 2(1-v_1)e^2, && (5.9b)\\ \frac{\mathrm{d}h}{\mathrm{d}t} &= \hat{k}_0\left(\tfrac{1}{3}s - e\right)\left(\tfrac{2}{3}s - h\right) - \hat{k}_{-0}eh - 2\hat{k}_{-1}v_1h^2 \\ &\quad - \hat{k}_2h + \hat{k}_{-2}\left(\tfrac{2}{3}s - h\right), && (5.9c) \end{aligned}$$

with the initial condition $v_1(0) = 0$, and $e(0)$, $h(0)$ being given by input parameters.

5.2.5 Electron-hole pair dynamics

For simplicity, the hats on dimensionless parameters are dropped and, in the rest of this section, all parameters are dimensionless. Electron-hole

pair dynamics are assumed to be faster than carbon and water oxidoreduction and adsorption-desorption dynamics (Indrakanti et al. 2009), therefore $k_0,\, k_{-0} \gg k_{-1},\, k_2,\, k_{-2}$. It is assumed that k_0 and k_{-0} are of order $1/\epsilon$, where $0 < \epsilon \ll 1$, while $k_{-1},\, k_2,\, k_{-2}$ are of order 1. The system of equations becomes

$$\begin{aligned}
\frac{\mathrm{d}v_1}{\mathrm{d}t} &= (1-v_1)e^2 \,-\, k_{-1}v_1h^2, && \text{(5.10a)}\\
\frac{\mathrm{d}e}{\mathrm{d}t} &= \frac{\kappa_0}{\epsilon}(\tfrac{1}{3}s-e)(\tfrac{2}{3}s-h) \,-\, \frac{\kappa_{-0}}{\epsilon}eh \,-\, 2(1-v_1)e^2, && \text{(5.10b)}\\
\frac{\mathrm{d}h}{\mathrm{d}t} &= \frac{\kappa_0}{\epsilon}(\tfrac{1}{3}s-e)(\tfrac{2}{3}s-h) \,-\, \frac{\kappa_{-0}}{\epsilon}eh \,-\, 2k_{-1}v_1h^2 \\
&\quad -k_2h \,+\, k_{-2}(\tfrac{2}{3}s-h), && \text{(5.10c)}
\end{aligned}$$

where $k_0 = \kappa_0/\epsilon$, $k_{-0} = \kappa_{-0}/\epsilon$ and $\kappa_0,\, \kappa_{-0}$ are of order 1. It is assumed that the variables are bounded and of order unity relative to ϵ. In fact, they ought to be bounded for the model to accurately represent the physical system as the concentrations are physically bounded by conservation laws, represented by (5.3)–(5.4), and must be non-negative.

Over a short timescale of order ϵ (meaning $t = \tau\epsilon$ with τ of order 1), to leading order

$$\begin{aligned}
\frac{\mathrm{d}v_1}{\mathrm{d}\tau} &= 0, && \text{(5.11a)}\\
\frac{\mathrm{d}e}{\mathrm{d}\tau} &= \kappa_0\left(\tfrac{1}{3}s-e\right)\left(\tfrac{2}{3}s-h\right) \,-\, \kappa_{-0}eh, && \text{(5.11b)}\\
\frac{\mathrm{d}h}{\mathrm{d}\tau} &= \kappa_0\left(\tfrac{1}{3}s-e\right)\left(\tfrac{2}{3}s-h\right) \,-\, \kappa_{-0}eh. && \text{(5.11c)}
\end{aligned}$$

At steady state this leads to an equation that gives h as a function of e,

$$h \;=\; \frac{2s(s-3e)}{9(K_{eq}-1)e+3s}, \qquad \text{(5.12)}$$

where

$$K_{eq}(\text{constant}) \;\equiv\; \frac{\kappa_{-0}}{\kappa_0} \;=\; \frac{k_{-0}}{k_0}. \qquad \text{(5.13)}$$

So initially, system (5.11) can be expected to evolve rapidly from its initial condition to the state $v_1 = 0$, with h and e satisfying (5.12), before evolving more slowly. Equation (5.12) continues to be satisfied during the slow evolution of the system.

5.2.6 System of 2 ODEs

On a time scale of $t = O(1)$, (5.9c)-(5.9b) gives

$$\frac{\mathrm{d}h}{\mathrm{d}t} \,-\, \frac{\mathrm{d}e}{\mathrm{d}t} \;=\; 2(1-v_1)e^2 \,-\, 2k_{-1}v_1h^2 \,-\, k_2h \,+\, k_{-2}(\tfrac{2}{3}s-h). \qquad \text{(5.14)}$$

However, it was assumed that the much faster reactions (5.1a and 5.1b) will be at steady state at this time scale and therefore, according to (5.12), $h = h(e)$ and so

$$\frac{\mathrm{d}h}{\mathrm{d}t} \,-\, \frac{\mathrm{d}e}{\mathrm{d}t} \;=\; \frac{dh}{de}\frac{\mathrm{d}e}{\mathrm{d}t} \,-\, \frac{\mathrm{d}e}{\mathrm{d}t} \;=\; \left(\frac{dh}{de} \,-\, 1\right)\frac{\mathrm{d}e}{\mathrm{d}t}. \qquad \text{(5.15)}$$

Thus

$$\frac{\mathrm{d}e}{\mathrm{d}t} = \frac{2(1-v_1)e^2 - 2k_{-1}v_1h^2 - k_2h + k_{-2}(\frac{2}{3}s-h)}{\frac{dh}{de}-1}, \tag{5.16}$$

where

$$\frac{\mathrm{d}h}{\mathrm{d}e} = \frac{-2s^2K_{eq}}{(s+3(K_{eq}-1)e)^2}. \tag{5.17}$$

This leads to a system of 2 ODEs for (v_1, e)

$$\frac{\mathrm{d}v_1}{\mathrm{d}t} = (1-v_1)e^2 - k_{-1}v_1h^2, \tag{5.18a}$$

$$\frac{\mathrm{d}e}{\mathrm{d}t} = \frac{2(1-v_1)e^2 - 2k_{-1}v_1h^2 - k_2h + k_{-2}\left(\frac{2}{3}s-h\right)}{\frac{\mathrm{d}h}{\mathrm{d}e}-1}, \tag{5.18b}$$

where h is given by (5.12) and $\mathrm{d}h/\mathrm{d}e$ is given by (5.17). The steady state of this system can be calculated analytically as

$$v_1 = \frac{(k_2(k_2+k_{-2}))^2}{k_2^2(k_2+k_{-2})^2+4k_{-1}k_{-2}^2(k_2+K_{eq}k_{-2})^2}, \tag{5.19a}$$

$$e = s\frac{k_2}{3(k_2+k_{-2}K_{eq})}. \tag{5.19b}$$

5.2.7 Phase Plane Analysis

In order to draw the phase plane of the system (5.18), its Jacobian matrix must be calculated. Functions f and g are defined by $f = \frac{\mathrm{d}v_1}{\mathrm{d}t}$ and $g = \frac{\mathrm{d}e}{\mathrm{d}t}$. The Jacobian matrix in question is $\begin{bmatrix} \frac{\partial f}{\partial v_1} \equiv w & \frac{\partial f}{\partial e} \equiv x \\ \frac{\partial g}{\partial v_1} \equiv y & \frac{\partial g}{\partial e} \equiv z \end{bmatrix}$, where

$$w = -e^2 - k_{-1}h^2, \tag{5.20a}$$

$$x = 2e - 2v_1e - 2k_{-1}v_1h\frac{\mathrm{d}h}{\mathrm{d}e}, \tag{5.20b}$$

$$y = -2\frac{e^2+k_{-1}h^2}{\frac{\mathrm{d}h}{\mathrm{d}e}-1}, \tag{5.20c}$$

$$z = \frac{4e-4v_1e-4k_{-1}v_1h\frac{\mathrm{d}h}{\mathrm{d}e}-(k_2+k_{-2})\frac{\mathrm{d}h}{\mathrm{d}e}}{\frac{\mathrm{d}h}{\mathrm{d}e}-1} - \frac{(2(1-v_1)e^2-2k_{-1}v_1h^2-(k_2+k_{-2})h+\frac{2}{3}k_{-2}s)(\frac{d^2h}{de^2})}{\left(\frac{\mathrm{d}h}{\mathrm{d}e}-1\right)^2}, \tag{5.20d}$$

where h is given by (5.12), $\mathrm{d}h/\mathrm{d}e$ is given by (5.17) and

$$\frac{\mathrm{d}^2h}{\mathrm{d}e^2} = \frac{12s^2K_{eq}(K_{eq}-1)}{(s+3(K_{eq}-1)e)^3}. \tag{5.21}$$

For positive concentrations and rate constants, the signs of the trace and determinant of the Jacobian matrix can be derived at the steady state.

The trace is $\mathrm{Tr}(J) = w + z < 0$, because $w < 0$ and $z < 0$. For w this is obvious from its definition (5.20a). Furthermore, because of (5.12), h and e cannot both be zero, so that the strict inequality is derived. The second fraction of z is zero at the steady state, while the first is strictly negative because the numerator is strictly positive and the denominator negative. The determinant of the Jacobian can be calculated from (5.20) as

$$\det(J) = \frac{(-e^2 - k_{-1}h^2)(-(k_2 + k_{-2})\frac{\mathrm{d}h}{\mathrm{d}e})}{\frac{\mathrm{d}h}{\mathrm{d}e} - 1}. \tag{5.22}$$

The numerator of the determinant (5.22) is strictly negative and so is the denominator, so that $\det(J) > 0$. This result does not depend on the particular parameter values so the steady state is always stable. Furthermore, it can be shown that

$$\mathrm{Tr}(J)^2 > 4\det(J), \tag{5.23}$$

meaning that the steady state is a node. The trace of the Jacobian can be written as

$$\mathrm{Tr}(J) = -e^2 - k_{-1}h^2 + \frac{4e - 4v_1 e - 4k_{-1}v_1 h\frac{\mathrm{d}h}{\mathrm{d}e} - (k_2 + k_{-2})\frac{\mathrm{d}h}{\mathrm{d}e}}{\frac{\mathrm{d}h}{\mathrm{d}e} - 1} \tag{5.24}$$

$$= \frac{A + B + C}{\frac{\mathrm{d}h}{\mathrm{d}e} - 1}, \tag{5.25}$$

where

$$A = \left(\frac{\mathrm{d}h}{\mathrm{d}e} - 1\right)(-e^2 - k_{-1}h^2), \tag{5.26a}$$

$$B = 4e - 4v_1 e - 4k_{-1}v_1 h\frac{\mathrm{d}h}{\mathrm{d}e} \quad \text{and} \tag{5.26b}$$

$$C = -(k_2 + k_{-2})\frac{\mathrm{d}h}{\mathrm{d}e}, \tag{5.26c}$$

with $A > 0$, $B > 0$ and $C > 0$. Additionally, the determinant can be written as

$$\det(J) = \frac{AC}{\left(\frac{\mathrm{d}h}{\mathrm{d}e} - 1\right)^2}, \tag{5.27}$$

so that

$$\mathrm{Tr}(J)^2 - 4\det(J) = \frac{(A - C)^2 + B^2 + 2AB + 2BC}{\left(\frac{\mathrm{d}h}{\mathrm{d}e} - 1\right)^2} \tag{5.28}$$

which is strictly positive, and therefore proves inequality (5.23).

The v_1- and e-isoclines are

$$v_1\text{-isocline: } v_1 = \frac{e^2}{e^2 + k_{-1}\left(\frac{2s(s-3e)}{9(K_{eq}-1)e+3s}\right)^2}, \tag{5.29a}$$

$$e\text{-isocline: } v_1 = \frac{2e^2 - k_2\frac{2s(s-3e)}{9(K_{eq}-1)e+3s} + k_{-2}\left(\frac{2}{3}s - \frac{2s(s-3e)}{9(K_{eq}-1)e+3s}\right)}{2e^2 + 2k_{-1}\left(\frac{2s(s-3e)}{9(K_{eq}-1)e+3s}\right)^2}. \tag{5.29b}$$

Parameter	Value in two equation model (5.18)
$K_{eq} = \frac{k_{-0}}{k_0}$	0.81
k_{-1}	2.7
k_2	$1.9 \cdot 10^{-2}$
k_{-2}	$4.2 \cdot 10^{-2}$
s	$4.8 \cdot 10^{-2}$

Table 5.1: Parameter values used in the two equation model.

The parameter values shown in table 5.1 were used in the calculations below and in figure 5.3. Around the steady state $v_1 = 2.45 \cdot 10^{-2},\ e = 5.7 \cdot 10^{-3}$, the Jacobian matrix is

$$\begin{bmatrix} -1.3 \cdot 10^{-3} & 1.7 \cdot 10^{-2} \\ 9.4 \cdot 10^{-4} & -5.1 \cdot 10^{-2} \end{bmatrix},$$

which has eigenvalues $\lambda_1 = -5.2 \cdot 10^{-2},\ \lambda_2 = -1.0 \cdot 10^{-3}$ and eigenvectors

$$\begin{bmatrix} -0.31 \\ 0.95 \end{bmatrix} \text{ and } \begin{bmatrix} 1 \\ 1.9 \cdot 10^{-2} \end{bmatrix} \text{ respectively.}$$

The isoclines and trajectories in the neighbourhood of the fixed point are shown in figure 5.3. The trajectories follow the arrows shown in the figure. The eigenvectors are also drawn in the same figure.

The eigenvalues are both negative real numbers so the steady state is a stable node, as predicted. Furthermore, because $|\lambda_1| \gg |\lambda_2|$, close to the steady state trajectories move approximately parallel to the first vector much faster than along the second, so they rapidly collapse on to the manifold tangent to the second vector. Because of the slope of the first vector, the steady state value of e is approached faster than that of v_1, in fact, for any change in v_1 there is a change ~ 3 times larger in e, until the variables approach the second vector.

By solving system (5.18) numerically, these concentration changes can be related to the timescales over which they happen. Progression in the direction parallel to the first vector happens over the first ~ 100 dimensionless time units, whereas along the second vector motion is much slower, occurring over ~ 5000 dimensionless time units, or ~ 0.05 s (see figure 5.4 for illustration).

5.2.8 Discussion

This model predicts a unique steady state that will be reached regardless of the initial conditions of v_1 and e, where v_1 corresponds to the concentration of HCOOH, and e to the concentration of the negatively charged sites of the surface. The model also assumes a distinct early timescale for the equilibration of the e and h on the surface as discussed in Section 5.2.5. For the selected parameter values, two more timescales are predicted. The first of these involves a large change in e with a smaller coupled change in v_1. The second sees a large but slow change in v_1, with e gradually following (~ 50 times more slowly) until the system reaches the unique

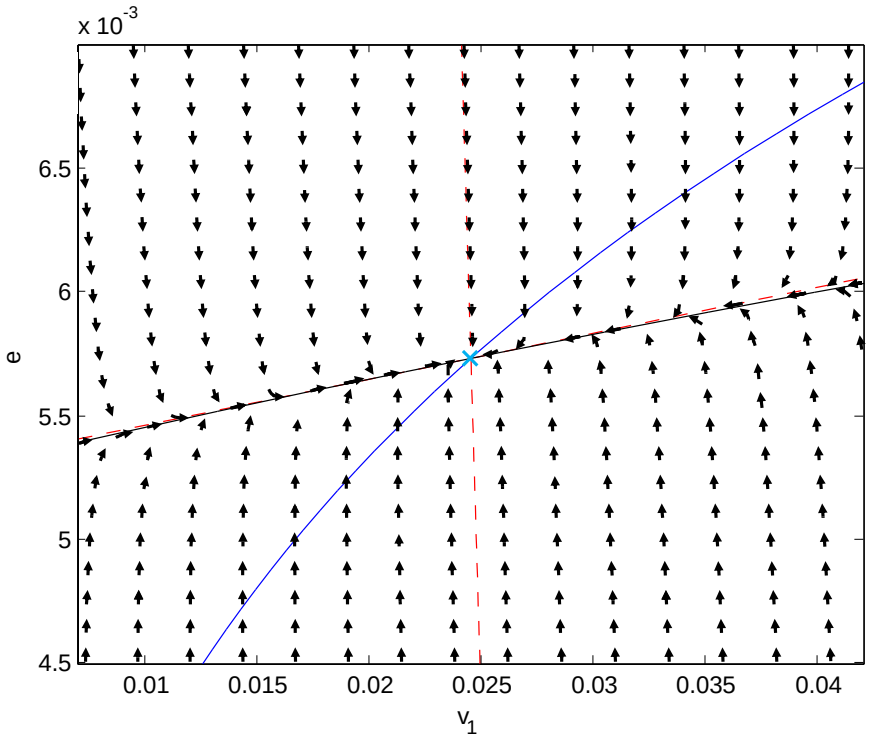

Figure 5.3: Isoclines (solid lines: blue: v_1-isocline, black: e-isocline) and eigenvectors (dashed red lines). The arrows show the direction that the trajectories follow. Note that different scales are used on the horizontal and vertical axes.

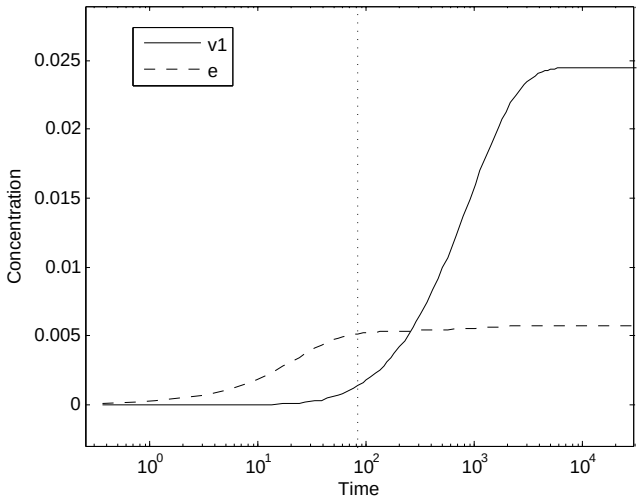

Figure 5.4: Time profiles of v_1 and e. The vertical dotted line shows the time point where the trajectory transitions from approximately parallel to the first vector to approximately along the second vector.

steady state. As v_1 is the product that the experimental work monitors, the third timescale is the most significant one as that is when the majority of the production happens.

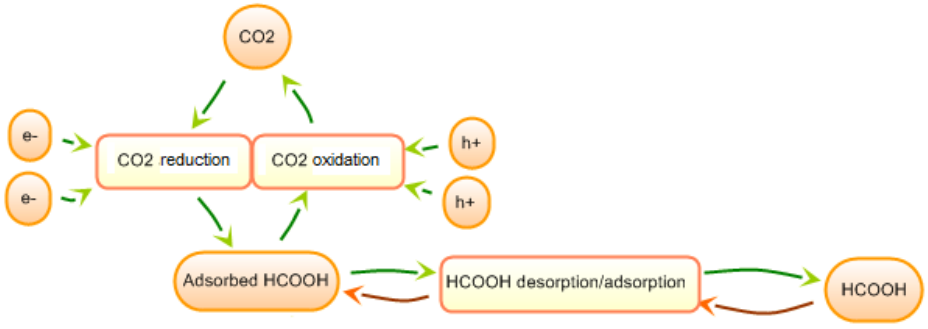

Figure 5.5: Photoreduction of CO_2 to HCOOH.

5.3 Simplified model including adsorption and desorption of products

5.3.1 Adding adsorption and desorption

The following reaction for HCOOH desorption and re-adsorption is now added to the existing mechanism (5.1)

$$\mathrm{HCOOH(s)} \underset{k'_{-1}}{\overset{k'_1}{\rightleftharpoons}} \mathrm{HCOOH(aq)}. \tag{5.30}$$

The resulting system is illustrated in figure 5.5. In the system of ODEs (5.2), (5.2f) is replaced by

$$\begin{aligned} \frac{\mathrm{d[HCOOH(s)]}}{\mathrm{d}t} &= [\mathrm{CO_2(aq)}][\mathrm{e^-}]^2 - k_{-1}[\mathrm{HCOOH(s)}][\mathrm{h^+}]^2 \\ &\quad - k'_1[\mathrm{HCOOH(s)}] + k'_{-1}[\mathrm{HCOOH(aq)}], \qquad (5.31a) \\ \frac{\mathrm{d[HCOOH(aq)]}}{\mathrm{d}t} &= k'_1[\mathrm{HCOOH(s)}] - k'_{-1}[\mathrm{HCOOH(aq)}]. \qquad (5.31b) \end{aligned}$$

Now, conservation of carbon gives

$$[\mathrm{CO_2(aq)}] + [\mathrm{HCOOH(s)}] + [\mathrm{HCOOH(aq)}] = C \text{ (constant)}. \tag{5.32}$$

It is also assumed that $[\mathrm{HCOOH(aq)}]_0 = 0$, so that again $C = [\mathrm{CO_2(aq)}]_0$. This model has the additional dimensionless parameters

$$\hat{k}'_1 = \frac{k'_1}{\gamma}, \quad \hat{k}'_{-1} = \frac{k'_{-1}}{\gamma}$$

and the additional dimensionless variable $v_2 = \dfrac{\mathrm{HCOOH(aq)}}{\beta}$, where β and γ are defined as in Section 5.2.4.

The hats on the dimensionless parameters are dropped for the rest of this section. If it is assumed again that the $\mathrm{e^-}$ and $\mathrm{h^+}$ dynamics are faster

than the other reactions, the number of the variables can be decreased as before. The dimensionless system of ODEs becomes

$$\frac{\mathrm{d}v_1}{\mathrm{d}t} = (1 - v_1 - v_2)e^2 - k_{-1}v_1h^2 - k'_1v_1 + k'_{-1}v_2 \tag{5.33a}$$

$$\frac{\mathrm{d}v_2}{\mathrm{d}t} = k'_1v_1 - k'_{-1}v_2 \tag{5.33b}$$

$$\frac{\mathrm{d}e}{\mathrm{d}t} = \frac{2(1 - v_1 - v_2)e^2 - 2k_{-1}v_1h^2 - k_2h + k_{-2}(\frac{2}{3}s - h)}{\frac{\mathrm{d}h}{\mathrm{d}e} - 1} \tag{5.33c}$$

where h is given by (5.12) and $\mathrm{d}h/\mathrm{d}e$ by (5.17). The initial conditions are $v_1(0) = 0$, $v_2(0) = 0$ and $e(0) = e_0$.

The unique steady state is

$$v_1 = \frac{k'_{-1}(k_2(k_2 + k_{-2}))^2}{(k'_1 + k'_{-1})(k_2(k_2 + k_{-2}))^2 + 4k_{-1}k'_{-1}(k_{-2}(k_2 + K_{eq}k_{-2}))^2}, \tag{5.34a}$$

$$v_2 = \frac{k'_1(k_2(k_2 + k_{-2}))^2}{(k'_1 + k'_{-1})(k_2(k_2 + k_{-2}))^2 + 4k_{-1}k'_{-1}(k_{-2}(k_2 + K_{eq}k_{-2}))^2}, \tag{5.34b}$$

$$e = s\frac{k_2}{3(k_2 + k_{-2}K_{eq})}. \tag{5.34c}$$

This single steady state only depends on the rate constants (including K_{eq}) and the catalyst concentration (s), and not on the initial condition of surface electrons (e). Additionally, from equations (5.34a) and (5.34b) it can be concluded that the final concentration of the organic products is independent of the catalyst concentration in the reactor.

The Jacobian matrix of the ODE system (5.33) was calculated at the steady state using Matlab and it has 3 negative real eigenvalues. Therefore the steady state is a stable node. The parameter values of table 5.1 were again used here, with the addition of parameters k'_1 and k'_{-1} which take values $3.6 \cdot 10^{-6}$ and $4.4 \cdot 10^{-6}$ respectively.

5.3.2 No hole scavenger

If there is no hole scavenger (which, in the model, can be mimicked by setting k_2 and k_{-2} to zero, thus eliminating reaction (5.1e)), the steady state will be different. System (5.33) becomes

$$\frac{\mathrm{d}v_1}{\mathrm{d}t} = (1 - v_1 - v_2)e^2 - k_{-1}v_1h^2 - k'_1v_1 + k'_{-1}v_2, \tag{5.35a}$$

$$\frac{\mathrm{d}v_2}{\mathrm{d}t} = k'_1v_1 - k'_{-1}v_2, \tag{5.35b}$$

$$\frac{\mathrm{d}e}{\mathrm{d}t} = \frac{2(1 - v_1 - v_2)e^2 - 2k_{-1}v_1h^2}{\frac{\mathrm{d}h}{\mathrm{d}e} - 1}, \tag{5.35c}$$

where h is given by (5.12) and $\mathrm{d}h/\mathrm{d}e$ by (5.17). This system has the steady state solution

$$v_1 = \frac{k'_{-1}}{k'_{-1} + k'_1 + k_{-1}k'_{-1}A^2}, \tag{5.36a}$$

$$v_2 = \frac{k'_1}{k'_{-1}}\frac{1}{1 + \frac{k'_1}{k'_{-1}} + k_{-1}A^2}, \tag{5.36b}$$

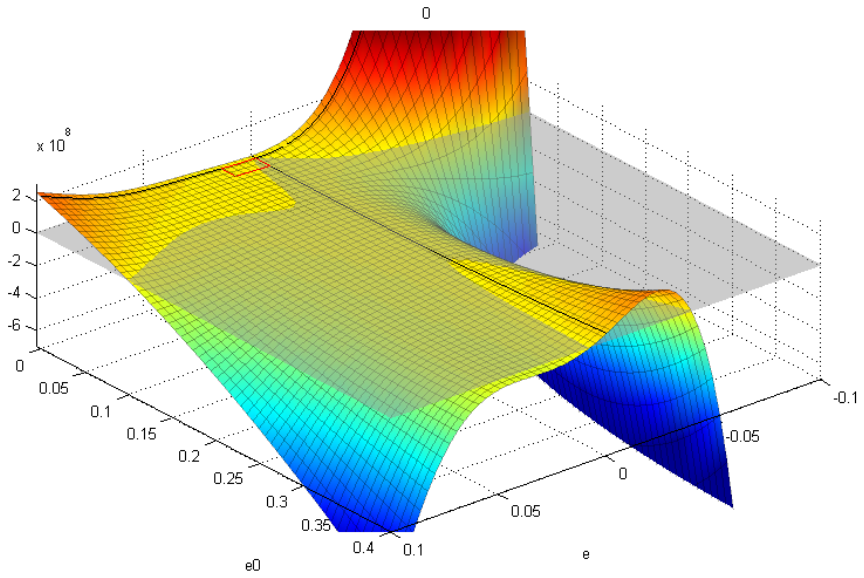

Figure 5.6: Shown in colour is the surface of the sixth order polynomial discussed in Section 5.3.2. In transparent grey is the $z = 0$ plane so that the roots of the polynomial are the intersection of the surface with that plane. Black lines along the surface of the polynomial show its intersection with the e=0 and e_0=0 planes. The red lines surround the range of physically possible values for e and e_0.

where $A = \frac{h}{e}$ and h satisfies (5.12). The steady state value of e can be calculated using equation

$$\frac{\mathrm{d}h}{\mathrm{d}t} - \frac{\mathrm{d}e}{\mathrm{d}t} - 2\frac{\mathrm{d}v_1}{\mathrm{d}t} - 2\frac{\mathrm{d}v_2}{\mathrm{d}t} = 0, \tag{5.37}$$

which is derived from (5.35), and gives

$$h - e - 2v_1 - 2v_2 - h_0 + e_0 = 0, \tag{5.38}$$

where h_0 and e_0 are the initial concentrations of h and e respectively. The initial concentrations of v_1 and v_2 are zero, as discussed earlier.

The steady state value of e is the root of a sixth order polynomial with parameter e_0, the equation of which was derived using the symbolic toolbox of Matlab by replacing into equation (5.38) the steady state formulas of v_1 and v_2 from (5.36) and those of h and h_0 from (5.12). Its general form is very complicated, so it is not shown, but it was drawn in Matlab over e and e_0 and is shown in figure 5.6. The range of e and e_0 used in the figure includes the physically possible range (surrounded by a red line), which is $[0, s/3(= 0.016)]$ for both so that the concentrations are positive and do not exceed the concentration of surface sites that can become negatively charged (Ti). The figure also shows the shape of the surface around this range. For some e_0 values there are multiple real roots of the polynomial (as many as six as will be shown later in figure 5.9). However, in the region of interest there is exactly one root for every value of e_0 that also sits within the acceptable range of e. Figure 5.7 shows e plotted against e_0 in that range.

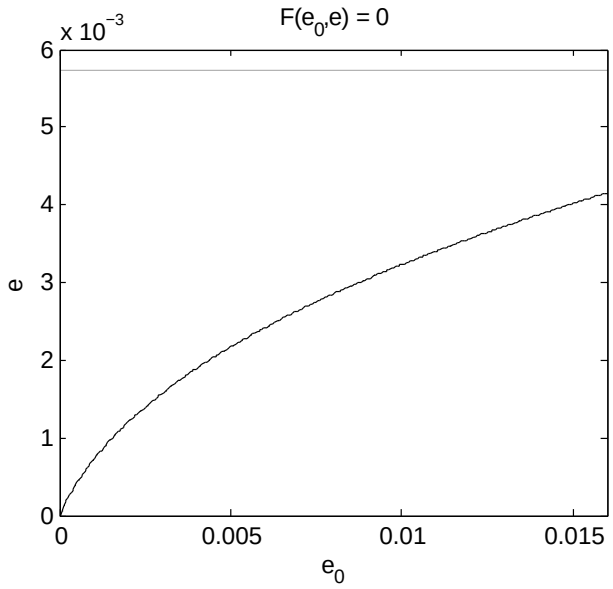

Figure 5.7: Steady state values of e plotted against the equivalent e_0. The black line corresponds to model (5.35) and is calculated from the sixth order polynomial discussed in Section 5.3.2. The grey line corresponds to model (5.33) and shows the value given by equation (5.34c).

5.3.3 Numerical Results

The time profiles of the models of Sections 5.3.1 and 5.3.2 (with and without hole scavenger respectively) are shown in figure 5.8, and they are compared in this section, with a focus on the steady state positions that are reached. Both systems of ODEs, (5.33) and (5.35), were solved numerically using the Matlab solver *ode15s*.

The hole scavenging model (5.33) gives a qualitatively different result to the model without hole scavenger (5.35). In the latter, the final concentrations of the variables depend on the initial condition of e as predicted from solving the system analytically in the previous section. A comparison of the analytic (calculated by solving the sixth order polynomial discussed in Section 5.3.2) and numerical solutions of the steady state values of e against the values of the input parameter e_0 is plotted in figure 5.9 showing a close fit between the solutions of the two methods. The values outside the physically relevant range are also plotted to show the fit between the two. For e_0 close to 1, there are six real solutions but, as mentioned in Section 5.3.2, e and e_0 cannot exceed 0.016 and so these will not be relevant to the modelling of the system.

On the other hand, the model with hole scavenger (5.33) has a steady state that does not depend on the initial condition of e. This steady state is in fact sensitive to the values of parameters k_2 and k_{-2}, which reflect the rates of reactions 5.1e. These parameters determine if the reactor is dominated by CO_2(aq) (which in the model is equal to 1-v_1-v_2) or HCOOH(aq) (v_2) at steady state. The time profiles of v_2 and (1-v_1-v_2) are plotted in figures 5.10, 5.11 for different values of k_2 and k_{-2} to demonstrate that with higher k_2 or lower k_{-2}, the CO_2(aq) will be almost completely re-

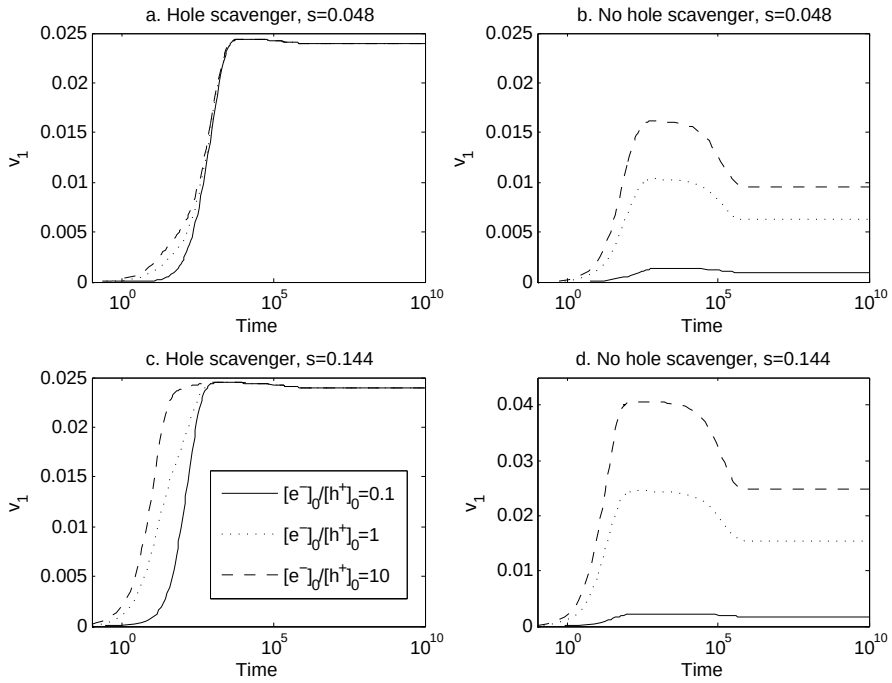

Figure 5.8: v_1 (corresponding to HCOOH(s)) concentration profile with and without hole scavenger varying the initial ratio of e to h and the catalyst concentration (s). Plots a and c show the time profiles of v_1 given by the model (5.33) with $s = 0.048$ and $s = 0.144$ respectively. Three numerical simulations are shown, each with different initial conditions of e, so that e_0/h_0 takes values 0.1, 1 and 10. Plots b and d show equivalent profiles given by model (5.35), again with $s = 0.048$ and $s = 0.144$ respectively.

duced, and the product concentration (v_2 corresponding to HCOOH(aq)) will be greatly increased. For higher k_{-2} or lower k_2, the effect is reversed with very little HCOOH(aq) produced and only a small change to the initial CO_2(aq) condition. Time is represented in dimensionless time units according to equation (5.8a). For reaction rates that are consistent with those used in Section 5.6, 10^{10} dimensionless time units correspond to ~ 28 h.

Furthermore, in the model without hole scavenger (5.35), the steady state will depend on the catalyst concentration (s), unlike the case of the model with hole scavenger as seen in Section 5.3.1. This is also evident in figure 5.8 where a higher value of s is used in plots c and d.

5.3.4 Discussion

Two models have been analysed in this section, one including a hole scavenger to replenish the electrons and drive the reduction of CO_2 forward, and another without. Due to the lack of an external factor driving the relative concentrations of e^- and h^+ in the desirable direction, in the second model the final concentrations of the products depend on the initial ratio of e to h. In this case, the catalyst surface holds some excess charge that is released through the reduction of CO_2. The excess charge together with

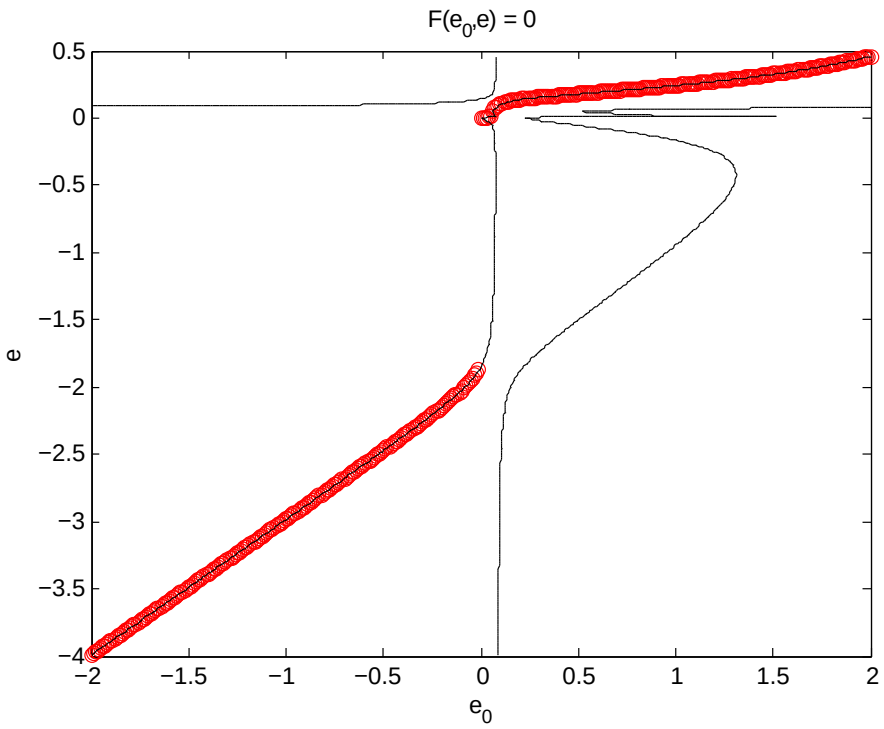

Figure 5.9: The roots of the sixth order polynomial discussed in Section 5.3.2, in black, plotted with numerical solutions of the ODE system, in red, run for a long time so that it has reached equilibrium.

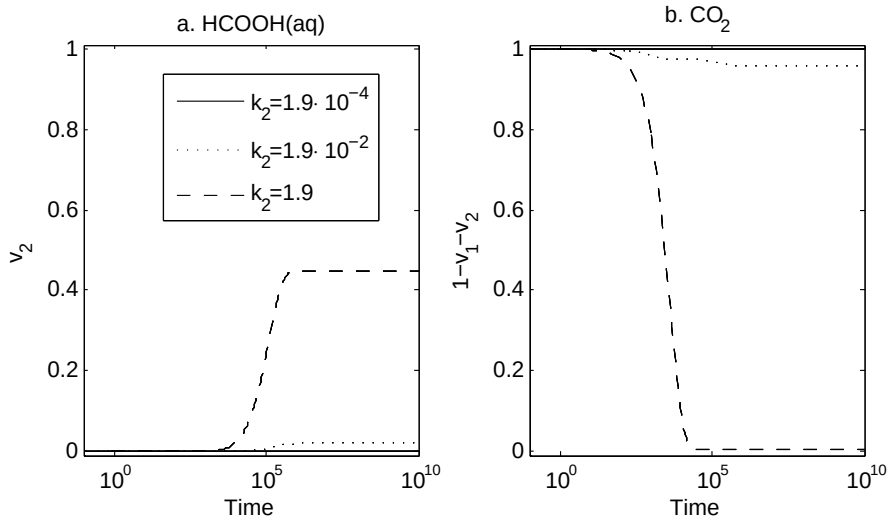

Figure 5.10: The effect of varying parameter k_2 on the dimensionless variables v_2 and $(1 - v_1 - v_2)$, corresponding to [HCOOH(aq)] and [CO_2(aq)] respectively.

the chemical potential of CO_2 drives the reaction forward. The chemical potential of CO_2 is already maximised as no products are present in the reactor at the start of the experiment (or the simulation). To control the ratio of e^- to h^+, negative charge has to be added to the surface from an external source and this will be used up by the reaction. As energy

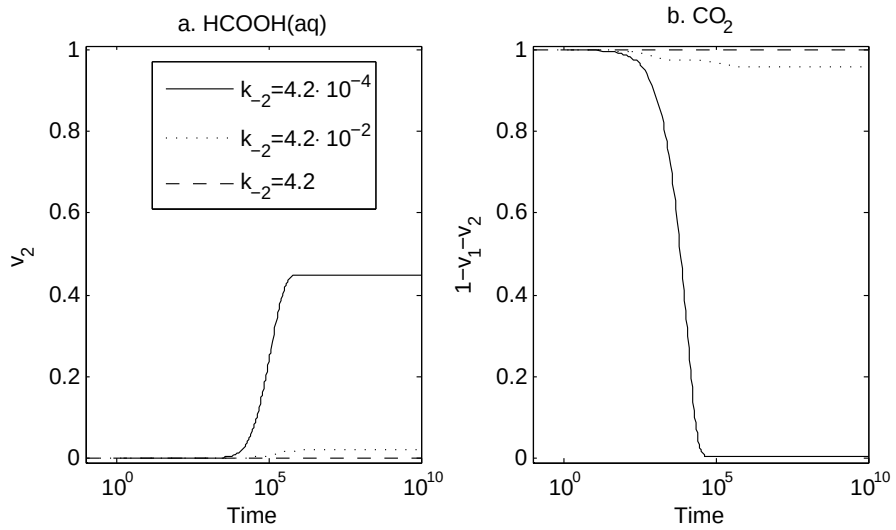

Figure 5.11: The effect of varying parameter k_{-2} on the dimensionless variables v_2 and $(1-v_1-v_2)$, corresponding to [HCOOH(aq)] and [CO_2(aq)] respectively.

is required to provide this initial charge, this is not a preferred method. Indeed, as can be seen from figure 5.8, more product can be obtained by more catalyst with a high e^- to h^+ ratio (plot d) than in the case of the single equilibrium of model (5.33) (plots a,c). However, for more catalyst, more negative charge also needs to be added to this catalyst to achieve that initial ratio of e^- to h^+ and therefore a larger energy input would be needed.

For the model with hole scavenger, the charge is additionally regulated by the hole scavenger which can be controlled by experimental design. As the hole scavenger used in the experiments is water, the fact that some of it may be used up by the reaction is not a concern. Furthermore, in this model, excess initial charge on the surface does not affect the final products and has little effect on the kinetics of the reaction. Therefore, other than light, no energy input is necessary. Instead, the equilibrium amount of products will increase with a more effective hole scavenger (or a higher concentration of it) as shown in figures 5.10 and 5.11.

For the models in this section, the assumption was made that charge is the driving force of the reaction, ignoring other reactants. In practice, a source of protons is needed, as well as the negative charge, to reduce CO_2 to organic compounds. This source of protons may also function as a hole scavenger as in the case of water. The use of water as a hole scavenger is further discussed in Sections 5.5 and 5.6 below.

5.4 Simplified model of CO_2 photoreduction to CH_4

Working in the same way for the full system as for the first step of the photoreduction (producing HCOOH), leads to a system of 9 ODEs and 19 parameters, given in (5.40) below. With the constraint of the carbon

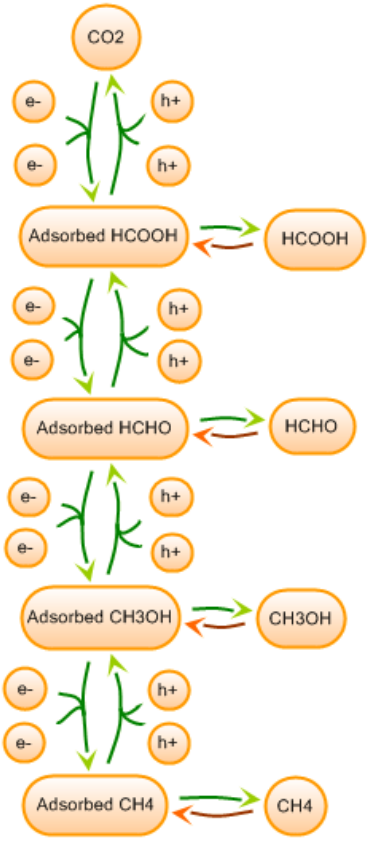

Figure 5.12: The full reaction mechanism of the simplified model, which focuses on the effect of surface charge on the reactions. The species on the right of the diagram are desorbed from the surface into the aqueous solution.

conservation and the assumption of fast e^-- h^+ dynamics, the steady state can be calculated analytically. These calculations and results are described in this section.

5.4.1 The full reaction mechanism

Figure 5.12 is a diagram of the full reaction mechanism that is assumed in this work. System (5.39) consists of the chemical reactions that describe this mechanism.

$$N_e + N_h + \text{light} \xrightarrow{k_0} \text{e}^- + \text{h}^+ \tag{5.39a}$$

$$\text{e}^- + \text{h}^+ \xrightarrow{k_{-0}} N_e + N_h + \text{heat} \tag{5.39b}$$

$$\text{CO}_2(\text{aq}) + 2\text{e}^- \xrightarrow{k_1} \text{HCOOH(s)} + 2N_e \tag{5.39c}$$

$$\text{HCOOH(s)} + 2\text{h}^+ \xrightarrow{k_{-1}} \text{CO}_2(\text{aq}) + 2N_h \tag{5.39d}$$

$$\text{HCOOH(s)} \underset{k'_{-1}}{\overset{k'_1}{\rightleftharpoons}} \text{HCOOH(aq)} \tag{5.39e}$$

$$\text{HCOOH(s)} + 2\text{e}^- \xrightarrow{k_2} \text{HCHO(s)} + 2N_e \tag{5.39f}$$

$$\text{HCHO(s)} + 2\text{h}^+ \xrightarrow{k_{-2}} \text{HCOOH(s)} + 2N_h \tag{5.39g}$$

$$\text{HCHO(s)} \underset{k'_{-2}}{\overset{k'_2}{\rightleftharpoons}} \text{HCHO(aq)} \tag{5.39h}$$

$$\text{HCHO(s)} + 2\text{e}^- \xrightarrow{k_3} \text{CH}_3\text{OH(s)} + 2N_e \tag{5.39i}$$

$$\text{CH}_3\text{OH(s)} + 2\text{h}^+ \xrightarrow{k_{-3}} \text{HCHO(s)} + 2N_h \tag{5.39j}$$

$$\text{CH}_3\text{OH(s)} \underset{k'_{-3}}{\overset{k'_3}{\rightleftharpoons}} \text{CH}_3\text{OH(aq)} \tag{5.39k}$$

$$\text{CH}_3\text{OH(s)} + 2\text{e}^- \xrightarrow{k_4} \text{CH}_4(\text{s}) + 2N_e \tag{5.39l}$$

$$\text{CH}_4(\text{s}) + 2\text{h}^+ \xrightarrow{k_{-4}} \text{CH}_3\text{OH(s)} + 2N_h \tag{5.39m}$$

$$\text{CH}_4(\text{s}) \underset{k'_{-4}}{\overset{k'_4}{\rightleftharpoons}} \text{CH}_4(\text{aq}) \tag{5.39n}$$

$$\text{h}^+ + \text{hole scavenger} \underset{k_{-5}}{\overset{k_5}{\rightleftharpoons}} N_h + \text{oxidised hole scavenger} \tag{5.39o}$$

5.4.2 ODE System

The full reaction mechanism given by equations (5.39) leads to the system of ODEs

$$\frac{\text{d}[\text{CO}_2(\text{aq})]}{\text{d}t} = -k_1[\text{CO}_2(\text{aq})][\text{e}^-]^2 + k_{-1}[\text{HCOOH(s)}][\text{h}^+]^2, \tag{5.40a}$$

$$\begin{aligned}\frac{\text{d}[\text{HCOOH(s)}]}{\text{d}t} = {} & k_1[\text{CO}_2(\text{aq})][\text{e}^-]^2 - k_{-1}[\text{HCOOH(s)}][\text{h}^+]^2 \\ & -k'_1[\text{HCOOH(s)}] + k'_{-1}[\text{HCOOH(aq)}] \\ & -k_2[\text{HCOOH(s)}][\text{e}^-]^2 + k_{-2}[\text{HCHO(s)}][\text{h}^+]^2,\end{aligned} \tag{5.40b}$$

$$\frac{\mathrm{d}[\mathrm{HCOOH(aq)}]}{\mathrm{d}t} = k_1'[\mathrm{HCOOH(s)}] - k_{-1}'[\mathrm{HCOOH(aq)}], \tag{5.40c}$$

$$\begin{aligned}\frac{\mathrm{d}[\mathrm{HCHO(s)}]}{\mathrm{d}t} &= k_2[\mathrm{HCOOH(s)}][\mathrm{e}^-]^2 - k_{-2}[\mathrm{HCHO(s)}][\mathrm{h}^+]^2 \\ &\quad -k_2'[\mathrm{HCHO(s)}] + k_{-2}'[\mathrm{HCHO(aq)}] \\ &\quad -k_3[\mathrm{HCHO(s)}][\mathrm{e}^-]^2 + k_{-3}[\mathrm{CH_3OH(s)}][\mathrm{h}^+]^2,\end{aligned} \tag{5.40d}$$

$$\frac{\mathrm{d}[\mathrm{HCHO(aq)}]}{\mathrm{d}t} = k_2'[\mathrm{HCHO(s)}] - k_{-2}'[\mathrm{HCHO(aq)}], \tag{5.40e}$$

$$\begin{aligned}\frac{\mathrm{d}[\mathrm{CH_3OH(s)}]}{\mathrm{d}t} &= k_3[\mathrm{HCHO(s)}][\mathrm{e}^-]^2 - k_{-3}[\mathrm{CH_3OH(s)}][\mathrm{h}^+]^2 \\ &\quad -k_3'[\mathrm{CH_3OH(s)}] + k_{-3}'[\mathrm{CH_3OH(aq)}] \\ &\quad -k_4[\mathrm{CH_3OH(s)}][\mathrm{e}^-]^2 + k_{-4}[\mathrm{CH_4(s)}][\mathrm{h}^+]^2,\end{aligned} \tag{5.40f}$$

$$\frac{\mathrm{d}[\mathrm{CH_3OH(aq)}]}{\mathrm{d}t} = k_3'[\mathrm{CH_3OH(s)}] - k_{-3}'[\mathrm{CH_3OH(aq)}], \tag{5.40g}$$

$$\begin{aligned}\frac{\mathrm{d}[\mathrm{CH_4(s)}]}{\mathrm{d}t} &= k_4[\mathrm{CH_3OH(s)}][\mathrm{e}^-]^2 - k_{-4}[\mathrm{CH_4(s)}][\mathrm{h}^+]^2 \\ &\quad -k_4'[\mathrm{CH_4(s)}] + k_{-4}'[\mathrm{CH_4(aq)}],\end{aligned} \tag{5.40h}$$

$$\frac{\mathrm{d}[\mathrm{CH_4(aq)}]}{\mathrm{d}t} = k_4'[\mathrm{CH_4(s)}] - k_{-4}'[\mathrm{CH_4(aq)}], \tag{5.40i}$$

$$\begin{aligned}\frac{\mathrm{d}[\mathrm{e}^-]}{\mathrm{d}t} &= \frac{1}{\frac{\mathrm{d}h}{\mathrm{d}e} - 1}\Big(2k_1[\mathrm{CO_2(aq)}][\mathrm{e}^-]^2 - 2k_{-1}[\mathrm{HCOOH(s)}][\mathrm{h}^+]^2 \\ &\quad +2k_2[\mathrm{HCOOH(s)}][\mathrm{e}^-]^2 - 2k_{-2}[\mathrm{HCHO(s)}][\mathrm{h}^+]^2 \\ &\quad +2k_3[\mathrm{HCHO(s)}][\mathrm{e}^-]^2 - 2k_{-3}[\mathrm{CH_3OH(s)}][\mathrm{h}^+]^2 \\ &\quad +2k_4[\mathrm{CH_3OH(s)}][\mathrm{e}^-]^2 - 2k_{-4}[\mathrm{CH_4(s)}][\mathrm{h}^+]^2 \\ &\quad -k_5[\mathrm{h}^+] + k_{-5}(\tfrac{2}{3}S - [\mathrm{h}^+])\Big),\end{aligned} \tag{5.40j}$$

where

$$\frac{\mathrm{d}h}{\mathrm{d}e} = \frac{-2S^2K_{eq}}{(S + 3(K_{eq} - 1)[\mathrm{e}^-])^2}. \tag{5.41}$$

5.4.3 Non-Dimensionalisation

The dimensionless parameters are

$$\hat{k}_0 = \frac{k_0\beta}{\gamma}, \quad (5.42a) \qquad \hat{k}_{-3} = \frac{k_{-3}\beta^2}{\gamma}, \quad (5.42l)$$

$$\hat{k}_{-0} = \frac{k_{-0}\beta}{\gamma}, \quad (5.42b) \qquad \hat{k}'_3 = \frac{k'_3}{\gamma}, \quad (5.42m)$$

$$\hat{k}_1 = \frac{k_1\beta^2}{\gamma} = 1, \quad (5.42c) \qquad \hat{k}'_{-3} = \frac{k'_{-3}}{\gamma}, \quad (5.42n)$$

$$\hat{k}_{-1} = \frac{k_{-1}\beta^2}{\gamma}, \quad (5.42d) \qquad \hat{k}_4 = \frac{k_4\beta^2}{\gamma}, \quad (5.42o)$$

$$\hat{k}'_1 = \frac{k'_1}{\gamma}, \quad (5.42e) \qquad \hat{k}_{-4} = \frac{k_{-4}\beta^2}{\gamma}, \quad (5.42p)$$

$$\hat{k}'_{-1} = \frac{k'_{-1}}{\gamma}, \quad (5.42f) \qquad \hat{k}'_4 = \frac{k'_4}{\gamma}, \quad (5.42q)$$

$$\hat{k}_2 = \frac{k_2\beta^2}{\gamma}, \quad (5.42g) \qquad \hat{k}'_{-4} = \frac{k'_{-4}}{\gamma}, \quad (5.42r)$$

$$\hat{k}_{-2} = \frac{k_{-2}\beta^2}{\gamma}, \quad (5.42h) \qquad \hat{k}_5 = \frac{k_5}{\gamma}, \quad (5.42s)$$

$$\hat{k}'_2 = \frac{k'_2}{\gamma}, \quad (5.42i) \qquad \hat{k}_{-5} = \frac{k_{-5}}{\gamma}, \quad (5.42t)$$

$$\hat{k}'_{-2} = \frac{k'_{-2}}{\gamma}, \quad (5.42j) \qquad s = \frac{S}{\beta}, \quad (5.42u)$$

$$\hat{k}_3 = \frac{k_3\beta^2}{\gamma}, \quad (5.42k) \qquad c = \frac{C}{\beta} = 1. \quad (5.42v)$$

The dimensionless variables are

$$t = t\gamma, \quad (5.43a) \qquad v_5 = \frac{[\mathrm{CH_3OH(s)}]}{\beta}, \quad (5.43g)$$

$$v_0 = \frac{[\mathrm{CO_2(aq)}]}{\beta}, \quad (5.43b) \qquad v_6 = \frac{[\mathrm{CH_3OH(aq)}]}{\beta}, \quad (5.43h)$$

$$v_1 = \frac{[\mathrm{HCOOH(s)}]}{\beta}, \quad (5.43c) \qquad v_7 = \frac{[\mathrm{CH_4(s)}]}{\beta}, \quad (5.43i)$$

$$v_2 = \frac{[\mathrm{HCOOH(aq)}]}{\beta}, \quad (5.43d) \qquad v_8 = \frac{[\mathrm{CH_4(aq)}]}{\beta}, \quad (5.43j)$$

$$v_3 = \frac{[\mathrm{HCHO(s)}]}{\beta}, \quad (5.43e) \qquad e = \frac{[\mathrm{e^-}]}{\beta}, \quad (5.43k)$$

$$v_4 = \frac{[\mathrm{HCOOH(aq)}]}{\beta}, \quad (5.43f) \qquad h = \frac{[\mathrm{h^+}]}{\beta}. \quad (5.43l)$$

The hats on the dimensionless rate constants are dropped and the full

dimensionless system of ODEs is

$$\frac{\mathrm{d}v_0}{\mathrm{d}t} = -k_1 v_0 e^2 + k_{-1} v_1 h^2, \tag{5.44a}$$

$$\frac{\mathrm{d}v_1}{\mathrm{d}t} = k_1 v_0 e^2 - k_{-1} v_1 h^2 - k_1' v_1 + k_1' v_2 - k_2 v_1 e^2 + k_{-2} v_3 h^2, \tag{5.44b}$$

$$\frac{\mathrm{d}v_2}{\mathrm{d}t} = k_1' v_1 - k_1' v_2, \tag{5.44c}$$

$$\frac{\mathrm{d}v_3}{\mathrm{d}t} = k_2 v_1 e^2 - k_{-2} v_3 h^2 - k_2' v_3 + k_{-2}' v_4 - k_3 v_3 e^2 + k_{-3} v_5 h^2, \tag{5.44d}$$

$$\frac{\mathrm{d}v_4}{\mathrm{d}t} = k_2' v_3 - k_{-2}' v_4, \tag{5.44e}$$

$$\frac{\mathrm{d}v_5}{\mathrm{d}t} = k_3 v_3 e^2 - k_{-3} v_5 h^2 - k_3' v_5 + k_{-3}' v_6 - k_4 v_5 e^2 + k_{-4} v_7 h^2, \tag{5.44f}$$

$$\frac{\mathrm{d}v_6}{\mathrm{d}t} = k_3' v_5 - k_{-3}' v_6, \tag{5.44g}$$

$$\frac{\mathrm{d}v_7}{\mathrm{d}t} = k_4 v_5 e^2 - k_{-4} v_7 h^2 - k_4' v_7 + k_4' v_8, \tag{5.44h}$$

$$\frac{\mathrm{d}v_8}{\mathrm{d}t} = k_4' v_7 - k_4' v_8, \tag{5.44i}$$

$$\begin{aligned}\frac{\mathrm{d}e}{\mathrm{d}t} = \frac{1}{\frac{\mathrm{d}h}{\mathrm{d}e} - 1} \big(& 2k_1 v_0 e^2 - 2k_{-1} v_1 h^2 \\ & + 2k_2 v_1 e^2 - 2k_{-2} v_3 h^2 + 2k_3 v_3 e^2 - 2k_{-3} v_5 h^2 \\ & + 2k_4 v_5 e^2 - 2k_{-4} v_7 h^2 - k_5 h + k_{-5}(\tfrac{2}{3} s - h) \big),\end{aligned} \tag{5.44j}$$

where $h = h(e)$ as defined in (5.12) and $\mathrm{d}h/\mathrm{d}e$ is given by (5.17).

At steady state

$$v_1 = \frac{k_1}{k_{-1}} \left(\frac{e}{h}\right)^2 v_0, \tag{5.45a}$$

$$v_2 = \frac{k_1'}{k_{-1}'} v_1, \tag{5.45b}$$

$$v_3 = \frac{k_1 k_2}{k_{-1} k_{-2}} \left(\frac{e}{h}\right)^4 v_0, \tag{5.45c}$$

$$v_4 = \frac{k_2'}{k_{-2}'} v_3, \tag{5.45d}$$

$$v_5 = \frac{k_1 k_2 k_3}{k_{-1} k_{-2} k_{-3}} \left(\frac{e}{h}\right)^6 v_0, \tag{5.45e}$$

$$v_6 = \frac{k'_3}{k_{-3}} v_5, \tag{5.45f}$$

$$v_7 = \frac{k_1 k_2 k_3 k_4}{k_{-1} k_{-2} k_{-3} k_{-4}} \left(\frac{e}{h}\right)^8 v_0, \tag{5.45g}$$

$$v_8 = \frac{k'_4}{k'_{-4}} v_7, \tag{5.45h}$$

$$e = \tfrac{1}{3} s \frac{k_5}{k_5 + k_{-5} K_{eq}}, \tag{5.45i}$$

$$h = \tfrac{2}{3} s \frac{k_{-5}}{k_5 + k_{-5}}, \tag{5.45j}$$

$$\frac{e}{h} = \frac{k_5 (k_5 + k_{-5})}{2 k_{-5} (k_5 + k_{-5} K_{eq})}. \tag{5.45k}$$

Additionally, from carbon conservation

$$c = v_0 + v_1 + v_2 + v_3 + v_4 + v_5 + v_6 + v_7 + v_8, \tag{5.46a}$$

$$\begin{aligned} c = {} & v_0 + \frac{k_1}{k_{-1}} \left(\frac{e}{h}\right)^2 v_0 + \frac{k'_1}{k'_{-1}} \frac{k_1}{k_{-1}} \left(\frac{e}{h}\right)^2 v_0 + \frac{k_1 k_2}{k_{-1} k_{-2}} \left(\frac{e}{h}\right)^4 v_0 \\ & + \frac{k'_2}{k'_{-2}} \frac{k_1 k_2}{k_{-1} k_{-2}} \left(\frac{e}{h}\right)^4 v_0 + \frac{k_1 k_2 k_3}{k_{-1} k_{-2} k_{-3}} \left(\frac{e}{h}\right)^6 v_0 \\ & + \frac{k'_3}{k_{-3}} \frac{k_1 k_2 k_3}{k_{-1} k_{-2} k_{-3}} \left(\frac{e}{h}\right)^6 v_0 + \frac{k_1 k_2 k_3 k_4}{k_{-1} k_{-2} k_{-3} k_{-4}} \left(\frac{e}{h}\right)^8 v_0 \\ & + \frac{k'_4}{k'_{-4}} \frac{k_1 k_2 k_3 k_4}{k_{-1} k_{-2} k_{-3} k_{-4}} \left(\frac{e}{h}\right)^8 v_0, \end{aligned} \tag{5.46b}$$

$$\begin{aligned} v_0 = {} & c \left(1 + \frac{k_1}{k_{-1}} \left(\frac{e}{h}\right)^2 + \frac{k'_1}{k'_{-1}} \frac{k_1}{k_{-1}} \left(\frac{e}{h}\right)^2 + \frac{k_1 k_2}{k_{-1} k_{-2}} \left(\frac{e}{h}\right)^4 + \right. \\ & + \frac{k'_2}{k'_{-2}} \frac{k_1 k_2}{k_{-1} k_{-2}} \left(\frac{e}{h}\right)^4 + \frac{k_1 k_2 k_3}{k_{-1} k_{-2} k_{-3}} \left(\frac{e}{h}\right)^6 + \frac{k'_3}{k_{-3}} \frac{k_1 k_2 k_3}{k_{-1} k_{-2} k_{-3}} \left(\frac{e}{h}\right)^6 + \\ & \left. + \frac{k_1 k_2 k_3 k_4}{k_{-1} k_{-2} k_{-3} k_{-4}} \left(\frac{e}{h}\right)^8 + \frac{k'_4}{k'_{-4}} \frac{k_1 k_2 k_3 k_4}{k_{-1} k_{-2} k_{-3} k_{-4}} \left(\frac{e}{h}\right)^8 \right)^{-1}. \end{aligned} \tag{5.46c}$$

Therefore the values of all the variables at steady state can be calculated from the above equations.

5.4.4 Sensitivity analysis

Sensitivity analysis was carried out to determine those parameters which have the greatest effect on the concentration of products at steady state. This analysis tests the hypothesis that increasing the light absorption will increase methane production. An increase in absorbed light corresponds to a decrease in K_{eq}.

The parameters of the carbon species reduction (k_1, k_2, k_3, k_4) with the carbon species oxidation (k_{-1}, k_{-2}, k_{-3}, k_{-4}), the adsorption of organics (k'_1, k'_2, k'_3, k'_4) with the desorption (k'_{-1}, k'_{-2}, k'_{-3}, k'_{-4}) and the hole scavenger oxidation (k_5) with the equivalent reduction (k_{-5}) were grouped together into three new parameters appearing in the steady state equations of the

variables. These new parameters are

$$K_1 = \frac{k_1}{k_{-1}}, \tag{5.47a}$$

$$K_1' = \frac{k_1'}{k_{-1}'}, \tag{5.47b}$$

$$K_5 = \frac{k_5}{k_{-5}}. \tag{5.47c}$$

It was further assumed that all reduction rates are equal regardless of the carbon compound being reduced and similarly for oxidation rates, adsorption rates and desorption rates. The case of different rates depending on the carbon species was also investigated, but the results are not shown as the conclusions drawn from them are similar to those of the simpler case. As will be shown below, these rates have a relatively small effect compared to K_{eq} and K_5, which correspond to light absorption and reversible hole scavenger oxidation respectively.

The above assumptions led to a 4-dimensional parameter space, spanned by (K_{eq}, K_1, K_1', K_5). As there is little information for the true values of these parameters, they were all sampled from the same log-normal distribution

$$10^{x_i},\ x_i \sim N(0, 16). \tag{5.48}$$

From this distribution, 10^5 sets of parameters were obtained and were used to calculate the corresponding values of the product concentrations at steady state. These values were calculated analytically from the steady state equations (5.45) and (5.46c).

The first-order sensitivity index (SI) (Saltelli et al. 2008) was used as the measure of the sensitivity of a variable j to a parameter k_i. It is defined as

$$SI_{j,k_i} = \frac{V_{k_i}(E_{k_{\sim i}}(Y_j \mid k_i))}{V(Y_j)} \tag{5.49}$$

where i is used to count through the parameters and j is used for the variables (v_j). The quantity k_i represents each of the four parameters (K_{eq}, K_1, K_1', K_5), while $k_{\sim i}$ represents all parameters other than k_i. Every instance of Y_j is the value of variable j at steady state given a set of parameter values. $E_{k_{\sim i}}(Y_j \mid k_i)$ is the expected value of Y_j for a given value of k_i, when all other parameters are free to vary. This was approximated by the mean of Y_j over 500 instances, in an interval around k_i. $V_{k_i}(E_{k_{\sim i}}(Y_j \mid k_i))$ is the variance of these means and $V(Y_j)$ is the variance of Y_j over all possible parameter values k_i. The sensitivity index, SI_{j,k_i}, is always between zero and one as $V_{k_i}(E_{k_{\sim i}}(Y_j \mid k_i)) \leq V(Y_j)$ (Saltelli et al. 2008).

The sensitivity indices were calculated for each parameter-variable pair, and they are shown in table 5.2 and figure 5.13. These suggest that K_{eq} and K_5 are the dominant parameters of this model.

	K_{eq}	K_1	K_1'	K_5
v_0	$2.28 \cdot 10^{-2} \pm 2.02 \cdot 10^{-4}$	$1.48 \cdot 10^{-1} \pm 5.00 \cdot 10^{-4}$	$6.66 \cdot 10^{-3} \pm 9.85 \cdot 10^{-5}$	$7.14 \cdot 10^{-1} \pm 5.40 \cdot 10^{-4}$
v_1	$1.27 \cdot 10^{-2} \pm 1.15 \cdot 10^{-4}$	$8.83 \cdot 10^{-2} \pm 4.54 \cdot 10^{-4}$	$1.24 \cdot 10^{-2} \pm 1.30 \cdot 10^{-4}$	$5.94 \cdot 10^{-1} \pm 7.63 \cdot 10^{-4}$
v_2	$1.23 \cdot 10^{-2} \pm 1.23 \cdot 10^{-4}$	$8.53 \cdot 10^{-2} \pm 4.70 \cdot 10^{-4}$	$4.69 \cdot 10^{-2} \pm 2.59 \cdot 10^{-4}$	$5.73 \cdot 10^{-1} \pm 8.59 \cdot 10^{-4}$
v_3	$1.94 \cdot 10^{-1} \pm 3.78 \cdot 10^{-4}$	$2.69 \cdot 10^{-2} \pm 2.33 \cdot 10^{-4}$	$1.33 \cdot 10^{-2} \pm 1.16 \cdot 10^{-4}$	$3.32 \cdot 10^{-1} \pm 9.06 \cdot 10^{-4}$
v_4	$1.86 \cdot 10^{-1} \pm 4.42 \cdot 10^{-4}$	$2.59 \cdot 10^{-2} \pm 2.25 \cdot 10^{-4}$	$5.06 \cdot 10^{-2} \pm 2.89 \cdot 10^{-4}$	$3.19 \cdot 10^{-1} \pm 9.99 \cdot 10^{-4}$
v_5	$2.77 \cdot 10^{-1} \pm 4.55 \cdot 10^{-4}$	$6.89 \cdot 10^{-2} \pm 3.19 \cdot 10^{-4}$	$7.25 \cdot 10^{-3} \pm 8.40 \cdot 10^{-5}$	$3.63 \cdot 10^{-1} \pm 8.17 \cdot 10^{-4}$
v_6	$2.72 \cdot 10^{-1} \pm 5.06 \cdot 10^{-4}$	$6.77 \cdot 10^{-2} \pm 3.31 \cdot 10^{-4}$	$2.51 \cdot 10^{-2} \pm 2.18 \cdot 10^{-4}$	$3.57 \cdot 10^{-1} \pm 8.53 \cdot 10^{-4}$
v_7	$2.68 \cdot 10^{-1} \pm 5.01 \cdot 10^{-4}$	$1.01 \cdot 10^{-1} \pm 3.62 \cdot 10^{-4}$	$4.47 \cdot 10^{-3} \pm 6.30 \cdot 10^{-5}$	$4.39 \cdot 10^{-1} \pm 6.81 \cdot 10^{-4}$
v_8	$2.66 \cdot 10^{-1} \pm 5.36 \cdot 10^{-4}$	$1.00 \cdot 10^{-1} \pm 3.71 \cdot 10^{-4}$	$1.31 \cdot 10^{-2} \pm 1.53 \cdot 10^{-4}$	$4.36 \cdot 10^{-1} \pm 7.01 \cdot 10^{-4}$

Table 5.2: Sensitivity indices of parameter-variable pairs of model (5.44). The value of the sensitivity index $\pm$ the standard error (SE) is given for each pair. The SE values were calculated from 20 SI values, each corresponding to a sample size of 10^5 parameters sets. The same data is shown in figure 5.13.

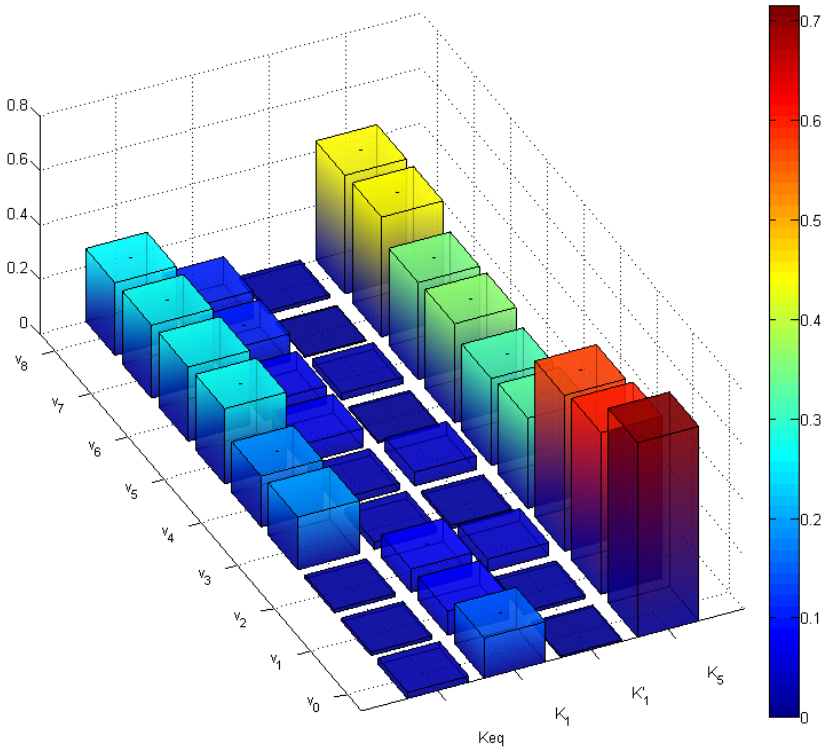

Figure 5.13: Sensitivity indices of parameter-variable pairs of model (5.44). The value of the sensitivity index is shown with the double standard error (SE) bar above and below the mean. The SE for each pair was calculated from 20 SI values, each corresponding to a sample size of 10^5 parameters sets. The data used to draw this figure is given in table 5.2.

In figures 5.14 and 5.15, the calculated steady state concentrations, corresponding to Y_j instances, are plotted against the parameter values (grey points), together with the mean values of the variable over each vertical slice of 500-points (black points). These means correspond to $E_{k_{\sim i}}(Y_j \mid k_i)$ in equation (5.49) and the variance of these over all the slices is approximately $V_{k_i}(E_{k_{\sim i}}(Y_j \mid k_i))$. Figure 5.14 shows the response of the organic products to the parameter K_5. Figure 5.15 shows a selection of variable-parameters pairs. Plots a-d of figure 5.15 show the response of the nondimensionalised variables to parameter K_{eq} and plots e-f show the response of v_8 to K_1 and K_1'. The sensitivity of v_8 to K_5 is not shown in this figure, as it was shown together with the sensitivities of the other products (v_2, v_4 and v_6) in figure 5.14. The sensitivity indices of each variable-parameter pair is shown in both figures in the corresponding plot. Similar plots were made for all combinations of variables and parameters and the ones shown were selected due to their interesting features and to avoid repetition.

5.4.5 Discussion

It was found that the presence and amount of a hole scavenger, which in the model is incorporated in the K_5 parameter, has a strong effect on

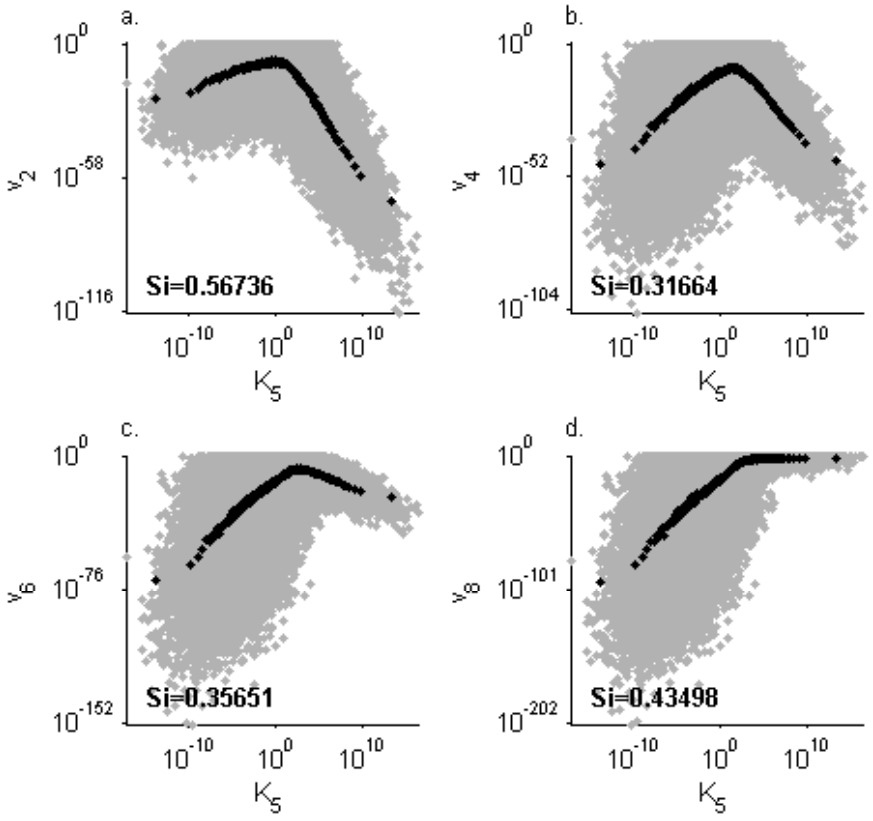

Figure 5.14: Sensitivity of the desorbed organic products to the value of K_5. Plot a shows the sensitivity of v_2 (corresponding to HCOOH(aq)) to K_5. Plots b,c and d show the same for variables v_4 (HCHO(aq)), v_6 (CH_3OH(aq)) and v_8 (CH_4(aq)) respectively. The grey points are the outputs of each parameter set while the black points are the mean values of the variable in the neighbourhood of the parameter value, calculated from 500 points.

the product yield. However, this effect differs depending on the product (figure 5.14). In fact, the direction of the effect changes, so that more oxidised products (such as v_2, corresponding to HCOOH) have a negative correlation with K_5 while this reverses for the more reduced products (such as v_8, corresponding to CH_4).

A similar effect is seen with K_{eq} which relates to the inverse of the light absorbed by the catalyst (figure 5.15). In this case, however, the direction of the relationship does not reverse but instead starts as neutral for v_2 (figure 5.15a), becoming increasingly important with more reduced species, and is maximised for v_8 (figure 5.15d). This observation supports the decision to target the light harvesting capabilities of the catalyst as a way to improve methane production.

Methane production is in fact more sensitive to the hole scavenger efficiency, but because of the chemistry of the reaction, there is a limit to how much K_5 can be increased. The catalyst is suspended in deionised H_2O in the reactor so that the amount of hole scavenger (H_2O) is already

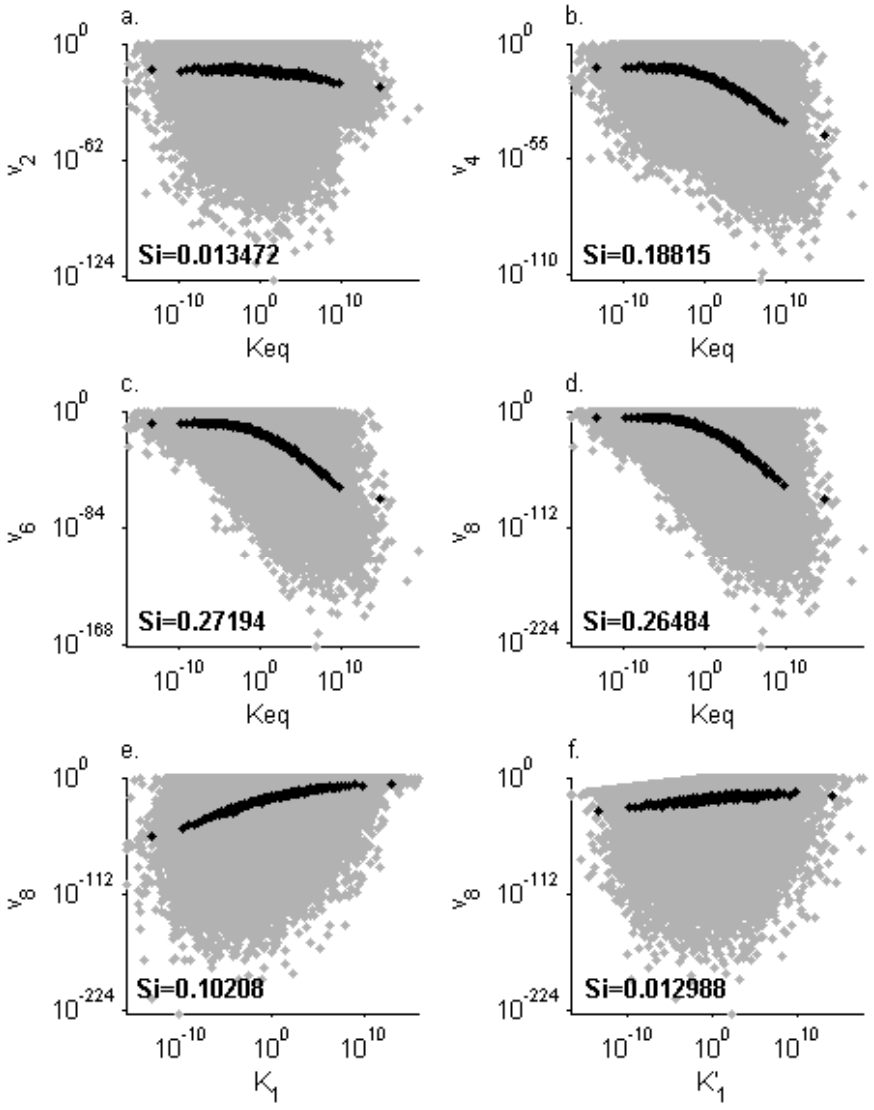

Figure 5.15: Sensitivity of organic products to the value of selected parameters. a–d show variables v_2 (corresponding to HCOOH(aq)), v_4 (HCHO(aq)), v_6 (CH_3OH(aq)) and v_8 (CH_4(aq)) respectively, plotted against parameter K_{eq} while e–f show v_8 plotted against K_1 and K_1'. The grey points are the outputs of each parameter set while the black points are the mean values of the variable in the neighbourhood of the parameter value, calculated from 500 points.

maximised. To change the efficiency of the hole scavenger, a different compound could be used, such as an organic compound that would be oxidised as CO_2 is reduced. However, in that case the hole scavenger would be used up as a fuel for the reactor, reducing the overall efficiency of the system. Therefore, the light harvesting capability of the catalyst is clearly the preferred target for optimisation of the process.

5.5 Mass action model including water oxidation

5.5.1 Reaction Mechanism

The assumptions regarding the catalyst surface are the same in the models that will be presented in this section as those in section 5.1.1. However, while previously it was assumed that all the non-carbon-containing species are abundant and therefore they were not modelled explicitly, in this section the reactions of water splitting will be included in the model. These will replace the hole scavenger oxidation reaction (5.1e), as the hydroxides (OH^-) that are produced from water dissociation will function as the hole scavenger, while the protons (H^+) will function as an electron scavenger, having a similar effect as the oxidised hole scavenger in the previous models. As well as the species introduced in Section 5.1.3, the following species are also involved in this model:

- $H^+(aq)$, $OH^-(aq)$, $H_2O(aq)$, $H_2(aq)$ and $O_2(aq)$, which refer to the protons, hydroxides, water, hydrogen and oxygen in the solution respectively.
- $[H^+(aq)]$ and $[OH^-(aq)]$, which refer to the concentrations of the protons and hydroxides in the solution respectively.

The assumed water splitting mechanism is

$$4h^+ + 2OH^-(aq) \xrightarrow{k_{w1}} O_2(aq) + 4N_h + 2H^+(aq) \tag{5.50a}$$

$$2e^- + 2H^+(aq) \xrightarrow{k_{w2}} 2N_e + H_2(aq) \tag{5.50b}$$

As discussed in Section 5.1.2, the concentrations of $OH^-(aq)$ and $H^+(aq)$ are 10^{-10} M and 10^{-4} M respectively. These are assumed to be constant as they come from a large pool and because the CO_2 acts as a buffer in the solution. This assumption was confirmed experimentally by measuring the pH of the solution throughout the reaction.

Reactions involving e^- and h^+ happen on the surface of the catalyst so all the reacting species need to be adsorbed on to the surface before they can be reduced or oxidised. Here again it is assumed that adsorption and desorption of non-C species are fast and they are included in reactions (5.50).

As well as (5.50), the mechanism used in this model also includes the following reactions

$$N_e + N_h \underset{k_{-0}}{\overset{k_0}{\rightleftharpoons}} \mathrm{e^-} + \mathrm{h^+} \tag{5.51a}$$

$$\mathrm{CO_2(aq)} + 2\mathrm{e^-} + 2\mathrm{H^+(aq)} \xrightarrow{k_1} \mathrm{HCOOH(s)} + 2N_e \tag{5.51b}$$

$$\mathrm{HCOOH(s)} + 2\mathrm{h^+} + 2\mathrm{OH^-(aq)} \xrightarrow{k_{-1}} \mathrm{CO_2(aq)} + 2N_h + 2\mathrm{H_2O(aq)} \tag{5.51c}$$

$$\mathrm{HCOOH(s)} \underset{k'_{-1}}{\overset{k'_1}{\rightleftharpoons}} \mathrm{HCOOH(aq)} \tag{5.51d}$$

$$\mathrm{HCOOH(s)} + 2\mathrm{e^-} + 2\mathrm{H^+(aq)} \xrightarrow{k_2} \mathrm{HCHO(s)} + 2N_e + \mathrm{H_2O(aq)} \tag{5.51e}$$

$$\mathrm{HCHO(s)} + 2\mathrm{h^+} + 2\mathrm{OH^-(aq)} \xrightarrow{k_{-2}} \mathrm{HCOOH(s)} + 2N_h + \mathrm{H_2O(aq)} \tag{5.51f}$$

$$\mathrm{HCHO(s)} \underset{k'_{-2}}{\overset{k'_2}{\rightleftharpoons}} \mathrm{HCHO(aq)} \tag{5.51g}$$

$$\mathrm{HCHO(s)} + 2\mathrm{e^-} + 2\mathrm{H^+(aq)} \xrightarrow{k_3} \mathrm{CH_3OH(s)} + 2N_e \tag{5.51h}$$

$$\mathrm{CH_3OH(s)} + 2\mathrm{h^+} + 2\mathrm{OH^-(aq)} \xrightarrow{k_{-3}} \mathrm{HCHO(s)} + 2N_h + 2\mathrm{H_2O(aq)} \tag{5.51i}$$

$$\mathrm{CH_3OH(s)} \underset{k'_{-3}}{\overset{k'_3}{\rightleftharpoons}} \mathrm{CH_3OH(aq)} \tag{5.51j}$$

$$\mathrm{CH_3OH(s)} + 2\mathrm{e^-} + 2\mathrm{H^+(aq)} \xrightarrow{k_4} \mathrm{CH_4(s)} + 2N_e + \mathrm{H_2O(aq)} \tag{5.51k}$$

$$\mathrm{CH_4(s)} + 2\mathrm{h^+} + 2\mathrm{OH^-(aq)} \xrightarrow{k_{-4}} \mathrm{CH_3OH(s)} + 2N_h + \mathrm{H_2O(aq)} \tag{5.51l}$$

$$\mathrm{CH_4(s)} \underset{k'_{-4}}{\overset{k'_4}{\rightleftharpoons}} \mathrm{CH_4(aq)}. \tag{5.51m}$$

Reaction (5.51a) for the splitting and recombination of electron-hole pairs happens much faster than reactions (5.51b)–(5.51m), (5.50) and so is assumed to be at steady state, as discussed in Section 5.2.5. Energy is required to drive this reaction forward and it is received in the form of light, the intensity of which is incorporated into k_0, while the reverse reaction releases energy in the form of heat. The equilibrium constant of the reaction is again $K_{eq} = \frac{k_{-0}}{k_0}$.

5.5.2 Steady state

The reaction mechanism (5.50)–(5.51) leads to a system of 9 ODEs with 19 parameters. Working in the same way for the resulting equations as for the ODE system of Section 5.4.2, and using the constraint of the carbon conservation and the assumption of fast $\mathrm{e^-}$- $\mathrm{h^+}$ dynamics, gives equations to calculate the steady state analytically as described below, in equations (5.53b)–(5.55).

The system is non-dimensionalised according to (5.42a)–(5.42b), (5.42e)–(5.42f), (5.42i)–(5.42j), (5.42m)–(5.42n), (5.42q)–(5.42r), (5.42u)–(5.43l) and the additional equations

$$\hat{k}_1 = \frac{k_1\beta^4}{\gamma}, \quad (5.52a) \qquad \hat{k}_4 = \frac{k_4\beta^4}{\gamma}, \quad (5.52g)$$

$$\hat{k}_{-1} = \frac{k_{-1}\beta^4}{\gamma}, \quad (5.52b) \qquad \hat{k}_{-4} = \frac{k_{-4}\beta^4}{\gamma}, \quad (5.52h)$$

$$\hat{k}_2 = \frac{k_2\beta^4}{\gamma}, \quad (5.52c) \qquad \hat{k}_{w1} = \frac{k_{w1}\beta^5}{\gamma}, \quad (5.52i)$$

$$\hat{k}_{-2} = \frac{k_{-2}\beta^4}{\gamma}, \quad (5.52d) \qquad \hat{k}_{w2} = \frac{k_{w2}\beta^3}{\gamma}, \quad (5.52j)$$

$$\hat{k}_3 = \frac{k_3\beta^4}{\gamma}, \quad (5.52e) \qquad H_1 = \frac{[\mathrm{H^+(aq)}]}{\beta}, \quad (5.52k)$$

$$\hat{k}_{-3} = \frac{k_{-3}\beta^4}{\gamma}, \quad (5.52f) \qquad H_2 = \frac{[\mathrm{OH^-(aq)}]}{\beta}. \quad (5.52l)$$

The hats on the dimensionless rate constants are dropped, and at steady state

$$\begin{aligned} v_0 = \Bigg(1 &+ \frac{k_1}{k_{-1}}\left(\frac{e}{h}\frac{H_1}{H_2}\right)^2 + \frac{k_1'}{k_{-1}'}\frac{k_1}{k_{-1}}\left(\frac{e}{h}\frac{H_1}{H_2}\right)^2 + \frac{k_1k_2}{k_{-1}k_{-2}}\left(\frac{e}{h}\frac{H_1}{H_2}\right)^4 + \\ &+\frac{k_2'}{k_{-2}'}\frac{k_1k_2}{k_{-1}k_{-2}}\left(\frac{e}{h}\frac{H_1}{H_2}\right)^4 + \frac{k_1k_2k_3}{k_{-1}k_{-2}k_{-3}}\left(\frac{e}{h}\frac{H_1}{H_2}\right)^6 \\ &+\frac{k_3'}{k_{-3}}\frac{k_1k_2k_3}{k_{-1}k_{-2}k_{-3}}\left(\frac{e}{h}\frac{H_1}{H_2}\right)^6 + \frac{k_1k_2k_3k_4}{k_{-1}k_{-2}k_{-3}k_{-4}}\left(\frac{e}{h}\frac{H_1}{H_2}\right)^8 \\ &+\frac{k_4'}{k_{-4}'}\frac{k_1k_2k_3k_4}{k_{-1}k_{-2}k_{-3}k_{-4}}\left(\frac{e}{h}\frac{H_1}{H_2}\right)^8\Bigg)^{-1}, \end{aligned} \quad (5.53a)$$

$$v_1 = \frac{k_1}{k_{-1}}\left(\frac{e}{h}\frac{H_1}{H_2}\right)^2 v_0, \quad (5.53b)$$

$$v_2 = \frac{k_1'}{k_{-1}'}v_1, \quad (5.53c)$$

$$v_3 = \frac{k_1k_2}{k_{-1}k_{-2}}\left(\frac{e}{h}\frac{H_1}{H_2}\right)^4 v_0, \quad (5.53d)$$

$$v_4 = \frac{k_2'}{k_{-2}'}v_3, \quad (5.53e)$$

$$v_5 = \frac{k_1k_2k_3}{k_{-1}k_{-2}k_{-3}}\left(\frac{e}{h}\frac{H_1}{H_2}\right)^6 v_0, \quad (5.53f)$$

$$v_6 = \frac{k_3'}{k_{-3}}v_5, \quad (5.53g)$$

$$v_7 = \frac{k_1k_2k_3k_4}{k_{-1}k_{-2}k_{-3}k_{-4}}\left(\frac{e}{h}\frac{H_1}{H_2}\right)^8 v_0, \quad (5.53h)$$

$$v_8 = \frac{k_4'}{k_{-4}'}v_7, \quad (5.53i)$$

where $H_1 = 1.5 \cdot 10^{-3}$, $H_2 = 1.5 \cdot 10^{-9}$, h satisfies (5.12) and e is the root of the cubic

$$A(K_{eq}-1)^2e^3 + (\tfrac{2}{3}sA(K_{eq}-1) - \tfrac{4}{9}s^2)e^2 + (\tfrac{8}{27}s^3 + \tfrac{1}{9}As^2)e - \tfrac{4}{81}s^4 = 0, \quad (5.54)$$

where

$$A = \sqrt{\frac{k_{w2}}{k_{w1}}}\frac{H_1}{H_2}. \tag{5.55}$$

The signs of the coefficients in 5.54 guarantee at least one real root $e > 0$.

5.5.3 Sensitivity analysis

Sensitivity analysis was carried out on the steady states of the above model as in Section 5.4.4 using the first order sensitivity index as a measure of the sensitivity. The results are compared to those obtained for the simplified model.

In this case, the parameter space is 5-dimensional, spanned by K_{eq}, K_1, K_1' (given by (5.47a) and (5.47b) respectively), H_1 and

$$K_w = \frac{k_{w2}}{k_{w1}}. \tag{5.56}$$

It was again assumed that all parameters in each of the 4 parameter groups (reduction rates, oxidation rates, adsorption rates and desorption rates) took the same value regardless of the carbon compound involved in their reaction.

All parameters were drawn from the same log-normal distribution, (5.48), except for parameter H_1 which was drawn from

$$10^{x_i},\ x_i \sim N(-3, 4). \tag{5.57}$$

This distribution was selected because experimental data gave a good estimate of the value of H_1, which corresponds to the pH of the solution, in the reaction system. However this can be changed experimentally so it was interesting to test the response of the system to changes in its value. 10^5 parameter sets were drawn from these distributions to perform the analysis.

Figure 5.16 shows the sensitivity indices of all the parameter-product pairs. The products are more sensitive to K_1 and K_w than the other parameters, especially the more reduced products, such as v_8 (CH_4(aq)). The same data is shown in table 5.3, which gives the values of the sensitivity indices for the same pairs. The standard error for the measurements is also indicated with the measurements on that table.

Figure 5.17 shows selected pairs of variables and parameters to best illustrate the effect of each parameter. None of the products is strongly sensitive to H_1. K_w, which corresponds to the hole and electron scavenging rates (increasing with electron scavenging and decreasing with hole scavenging), and K_1, which corresponds to the reduction-oxidation rates, have similar sensitivities but with approximately opposite effects (plots c–f of figure 5.17). Variables v_3 and v_4 were selected to show their response to K_1' as they correspond to adsorbed and desorbed HCHO respectively. The effect of K_1' to one of these is the reverse of its effect on the other. This was the case for all adsorbed-desorbed pairs, so only one is shown to avoid repetition.

	K_{eq}	K_1	K_1'	K_w	H_1
v_0	$3.47 \cdot 10^{-3} \pm 5.76 \cdot 10^{-5}$	$4.04 \cdot 10^{-1} \pm 8.52 \cdot 10^{-4}$	$1.99 \cdot 10^{-2} \pm 1.69 \cdot 10^{-4}$	$3.56 \cdot 10^{-1} \pm 8.54 \cdot 10^{-4}$	$4.98 \cdot 10^{-3} \pm 6.97 \cdot 10^{-5}$
v_1	$2.33 \cdot 10^{-3} \pm 4.33 \cdot 10^{-5}$	$2.53 \cdot 10^{-1} \pm 9.65 \cdot 10^{-4}$	$4.18 \cdot 10^{-2} \pm 2.19 \cdot 10^{-4}$	$2.12 \cdot 10^{-1} \pm 8.03 \cdot 10^{-4}$	$2.97 \cdot 10^{-3} \pm 6.14 \cdot 10^{-5}$
v_2	$2.30 \cdot 10^{-3} \pm 4.12 \cdot 10^{-5}$	$2.15 \cdot 10^{-1} \pm 8.07 \cdot 10^{-4}$	$1.88 \cdot 10^{-1} \pm 5.68 \cdot 10^{-4}$	$1.79 \cdot 10^{-1} \pm 6.82 \cdot 10^{-4}$	$2.87 \cdot 10^{-3} \pm 5.30 \cdot 10^{-5}$
v_3	$2.69 \cdot 10^{-3} \pm 5.87 \cdot 10^{-5}$	$2.94 \cdot 10^{-1} \pm 5.53 \cdot 10^{-4}$	$3.38 \cdot 10^{-2} \pm 1.87 \cdot 10^{-4}$	$2.80 \cdot 10^{-1} \pm 5.97 \cdot 10^{-4}$	$2.78 \cdot 10^{-3} \pm 6.49 \cdot 10^{-5}$
v_4	$2.67 \cdot 10^{-3} \pm 5.86 \cdot 10^{-5}$	$2.58 \cdot 10^{-1} \pm 5.49 \cdot 10^{-4}$	$1.56 \cdot 10^{-1} \pm 4.27 \cdot 10^{-4}$	$2.45 \cdot 10^{-1} \pm 6.09 \cdot 10^{-4}$	$2.73 \cdot 10^{-3} \pm 5.68 \cdot 10^{-5}$
v_5	$3.64 \cdot 10^{-3} \pm 8.06 \cdot 10^{-5}$	$4.19 \cdot 10^{-1} \pm 5.16 \cdot 10^{-4}$	$1.53 \cdot 10^{-2} \pm 1.42 \cdot 10^{-4}$	$4.06 \cdot 10^{-1} \pm 6.68 \cdot 10^{-4}$	$4.24 \cdot 10^{-3} \pm 1.07 \cdot 10^{-4}$
v_6	$3.60 \cdot 10^{-3} \pm 7.96 \cdot 10^{-5}$	$3.95 \cdot 10^{-1} \pm 5.01 \cdot 10^{-4}$	$7.19 \cdot 10^{-2} \pm 2.95 \cdot 10^{-4}$	$3.83 \cdot 10^{-1} \pm 6.18 \cdot 10^{-4}$	$4.14 \cdot 10^{-3} \pm 1.07 \cdot 10^{-4}$
v_7	$4.00 \cdot 10^{-3} \pm 8.49 \cdot 10^{-5}$	$4.67 \cdot 10^{-1} \pm 5.01 \cdot 10^{-4}$	$8.36 \cdot 10^{-3} \pm 1.09 \cdot 10^{-4}$	$4.51 \cdot 10^{-1} \pm 6.33 \cdot 10^{-4}$	$4.92 \cdot 10^{-3} \pm 1.21 \cdot 10^{-4}$
v_8	$3.98 \cdot 10^{-3} \pm 8.39 \cdot 10^{-5}$	$4.54 \cdot 10^{-1} \pm 4.85 \cdot 10^{-4}$	$3.68 \cdot 10^{-2} \pm 2.21 \cdot 10^{-4}$	$4.38 \cdot 10^{-1} \pm 5.84 \cdot 10^{-4}$	$4.85 \cdot 10^{-3} \pm 1.22 \cdot 10^{-4}$

Table 5.3: Sensitivity indices of parameter-variable pairs of model (5.51). The value of the sensitivity index $\pm$ the standard error (SE) is given for each pair. The SE values were calculated from 20 SI values, each corresponding to a sample size of 10^5 parameters sets. The same data is shown in figure 5.16.

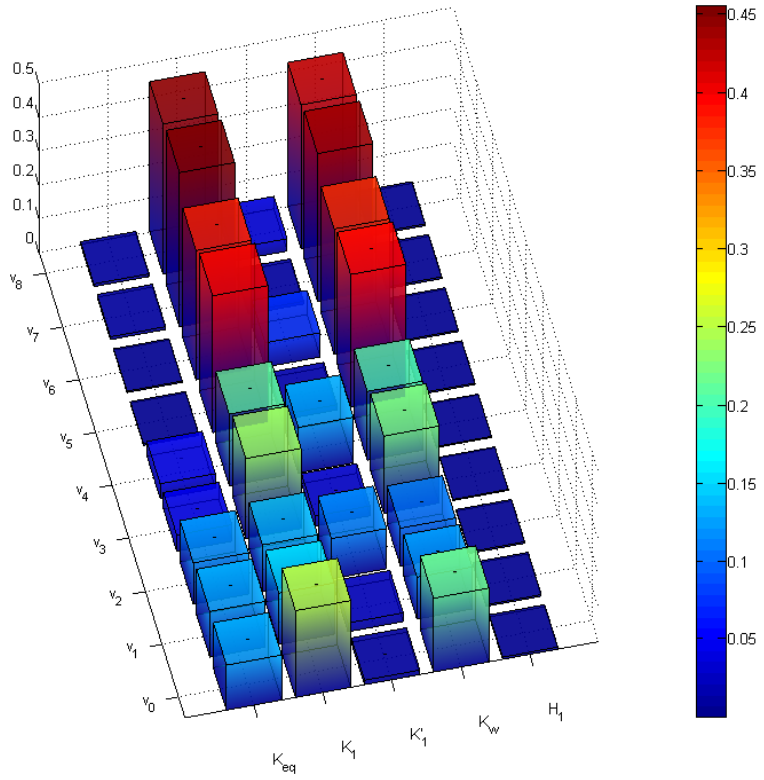

Figure 5.16: Sensitivity indices of parameter-variable pairs of model (5.50)–(5.51). The value of the sensitivity index is shown with the double standard error (SE) bar above and below the mean. The SE for each pair was calculated from 20 SI values, each corresponding to a sample size of 10^5 parameters sets. The data used to draw this figure is given in table 5.3.

For a realistic range of s values (distribution (5.58)), the sensitivity of the products to s is low. However, this is due to the great difference between the ranges tested for s and the other parameters. If an equally small range is tested for the other parameters around the same means but with distribution

$$10^{x_i},\ x_i \sim N(-2, 0.16), \tag{5.58}$$

excluding H_1 which has a separate distribution, then the products are very sensitive to s (figure 5.18).

Figure 5.19 shows the product concentrations given by different sets of parameters plotted against the values of K_{eq}, the parameter which varies depending on light input. It was found that, unlike the simplified model presented in Section 5.4.4, the present model shows a low sensitivity to K_{eq}, and therefore light intensity. In particular these is no change in product concentration in response to changes in K_{eq} for small values of the parameter, but a small decrease in v_8 for larger, increasing K_{eq} values. This pattern suggests that the selection of the parameter range affects the dependency. Indeed, figures 5.20 and 5.21, which test different ranges of the parameter, show that the response changes at different ranges, both quantitatively and

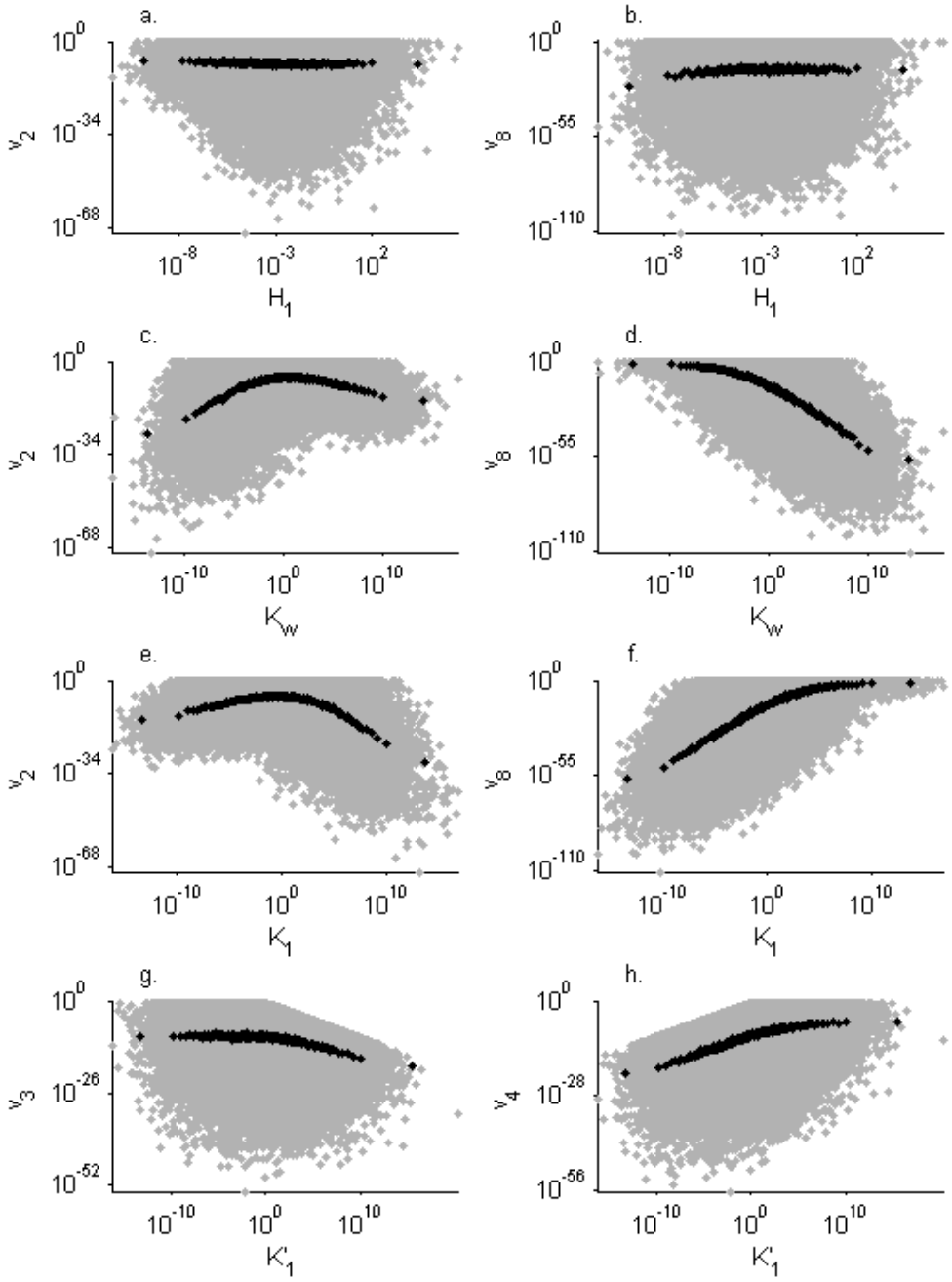

Figure 5.17: Sensitivity of organic products to the value of selected parameters. a–b show variables v_2 (corresponding to HCOOH(aq)) and v_8 (CH_4(aq)) respectively, plotted against parameter H_1, c–d show v_2 and v_8 plotted against K_w, e–f show the same variables against K_1 and g–h show v_3 (HCHO(s)) and v_4 (HCHO(aq)) plotted against K'_1. The grey points are the outputs of each parameter set while the black points are the mean values of the variable in the neighbourhood of the parameter value, calculated from 500 points.

qualitatively. The selected ranges were chosen to be consistent throughout the parameter space.

Figure 5.22 shows how a higher range of K_{eq} affects the sensitivity of the products to H_1. In plots a–b of figure 5.17, the variables did not

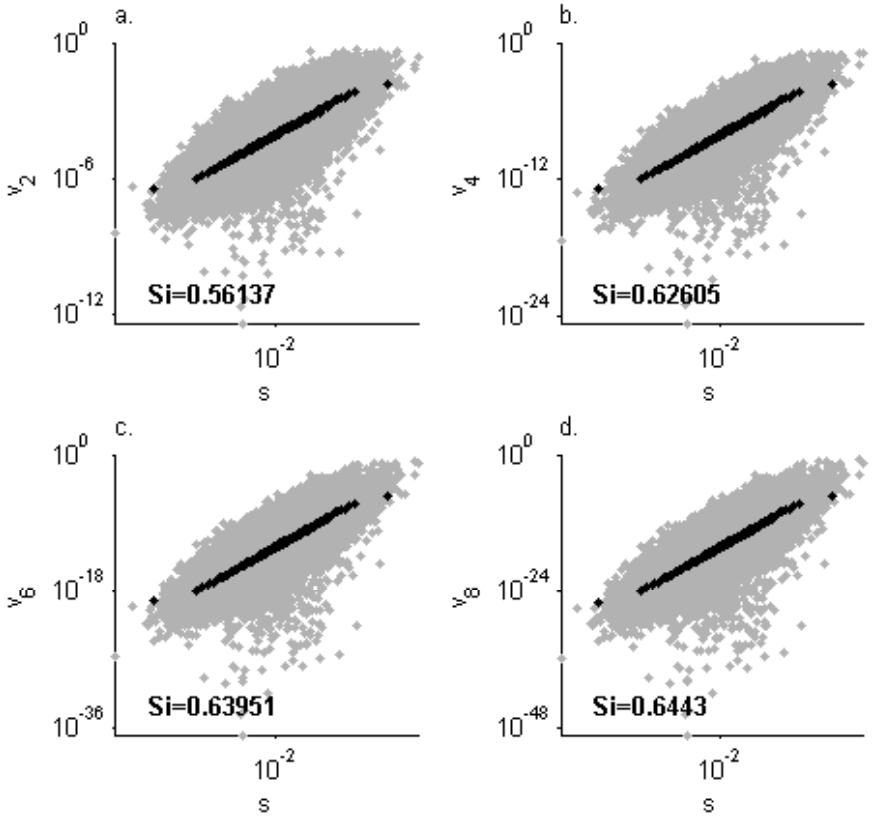

Figure 5.18: Sensitivity of the desorbed organic products, v_2 (HCOOH(aq)), v_4 (HCHO(aq)), v_6 (CH_3OH(aq)) and v_8 (CH_4(aq)), to the value of s, corresponding to the concentration of the catalyst surface sites. The grey points are the outputs of each parameter set while the black points are the mean values of the variable in the neighbourhood of the parameter value, calculated from 500 points.

respond to changes in H_1 whereas in figure 5.22, all variables have a positive relationship with H_1.

5.5.4 Discussion

In this model, the pH of the reactor solution is explicitly included and the effect of its value on the products is tested. The OH^- and H^+ ions, whose concentrations are determined by the pH, are involved in the reactions in two ways, hole scavenging (oxygen and hydrogen production) and as a source of protons. A low pH value means that there is a high concentration of H_1 (therefore H^+) and a low concentration of H_2 (OH^-). OH^- works as a hole scavenger, while H^+ is an electron scavenger. The effect of these concentrations on the hole scavenging leads to a high concentration of h and a low concentration of e, driving CO_2 reduction backwards (oxidising the organic products). Therefore, if the pH was primarily affecting oxidation and reduction through hole scavenging, the concentrations of products should decrease with H_1 and this should be more pronounced in the more reduced species, which need to go through more steps of reduction. However, the

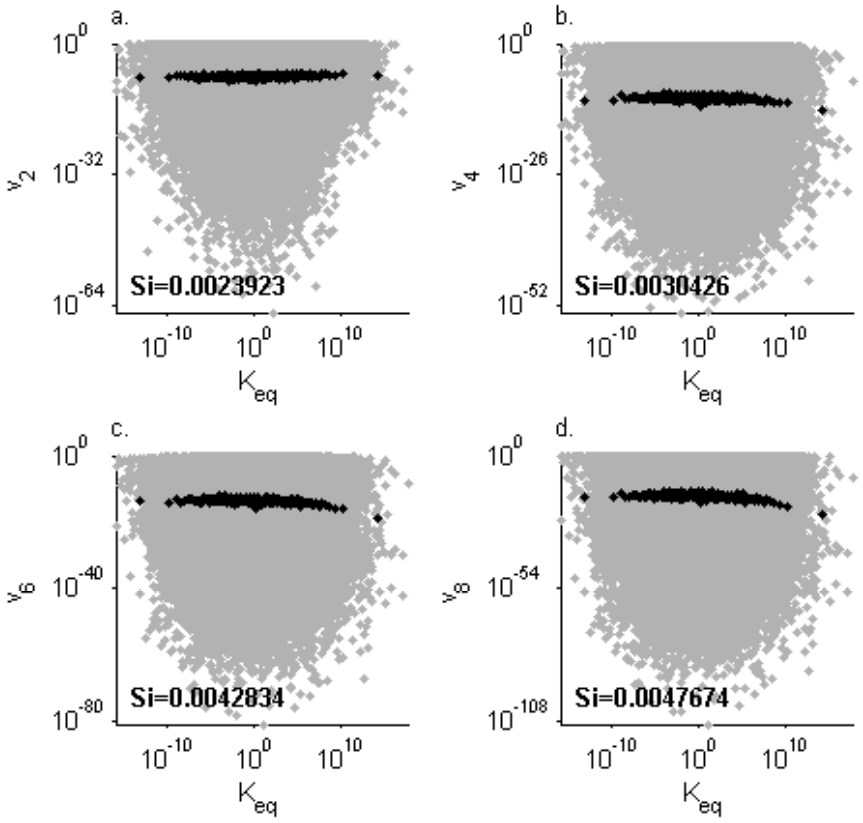

Figure 5.19: Sensitivity of the desorbed organic products, v_2 (HCOOH(aq)), v_4 (HCHO(aq)), v_6 (CH_3OH(aq)) and v_8 (CH_4(aq)), to the value of K_{eq}. The grey points are the outputs of each parameter set while the black points are the mean values of the variable in the neighbourhood of the parameter value, calculated from 500 points.

same ions are also needed for the oxidation and reduction reactions directly; H^+ is the proton source for the reduction of the carbon species, while OH^- is used in their oxidation. These two roles that each ion plays in the system have opposite effects on the reactions that cancel each other out and so it is that in figure 5.17 the pH does not have a net effect on the products.

Parameter K_{eq} (inversely correlated to light intensity) is not as important in the present model as in the simplified model of Section 5.4. The sensitivity of species to K_{eq} depends on the parameter range used for the sensitivity analysis. The products are not strongly sensitive to its value, as seen in figure 5.19, because abundant light was assumed (relative to other factors) and therefore e^- and h^+ are not the limiting factors. Instead, the relative rates of the reduction/oxidation reactions (K_1) and the scavenging reactions (K_w) are the dominant parameters. If, on the other hand, light is assumed to be limiting, a different pattern is observed, as shown in figures 5.20 and 5.21. In the case where K_{eq} takes values around 10^{20}, the same response to K_{eq} is seen as in the previous model (Section 5.4.4), where higher light leads to a higher concentration of products. The response to pH also changes compared to the case of high light intensity, as shown in

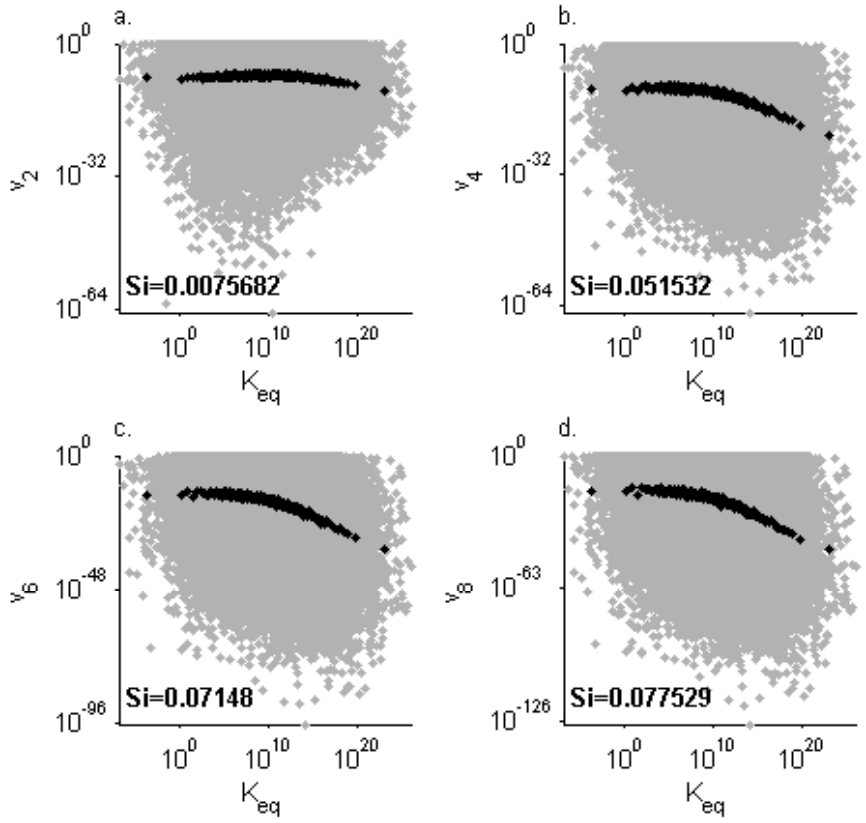

Figure 5.20: Sensitivity of the desorbed organic products, v_2 (HCOOH(aq)), v_4 (HCHO(aq)), v_6 (CH_3OH(aq)) and v_8 (CH_4(aq)), to the value of K_{eq} at intermediate range (drawn from 10^{x_i}, $x_i \sim N(10, 16)$). The grey points are the outputs of each parameter set while the black points are the mean values of the variable in the neighbourhood of the parameter value, calculated from 500 points.

figure 5.22. In this case, where the $[e^-]$ and $[h^+]$ are limited, the direct effect of H_1 and H_2 in the reduction and oxidation reactions outweighs their indirect effect on $[e^-]$ and $[h^+]$.

A wide range of parameters is tested in the sensitivity analysis. In particular, regarding K_{eq}, an even larger parameter range is investigated due to the many factors, such as light intensity and recombination rate, which contribute to its value. In fact, for large values, K_{eq} is approximately proportional to $1/Q^2$, where Q is the number of absorbed photons, so that a modest change in light intensity can lead to a much larger change in its value. Light intensity spans a range of three orders of magnitude between room light conditions, experimental conditions and direct sunlight, as discussed in Sections 3.1, 4.1.1 and 3.4 respectively, so that a difference of 6 orders of magnitude in K_{eq} can be easily justifiable. The ranges used here are more generous due to the uncertainty in their true values.

In the current model, the products are sensitive to s (which corresponds to the concentration of surface sites of the catalyst), suggesting that more catalyst leads to more products, unlike in the case of the model of Section

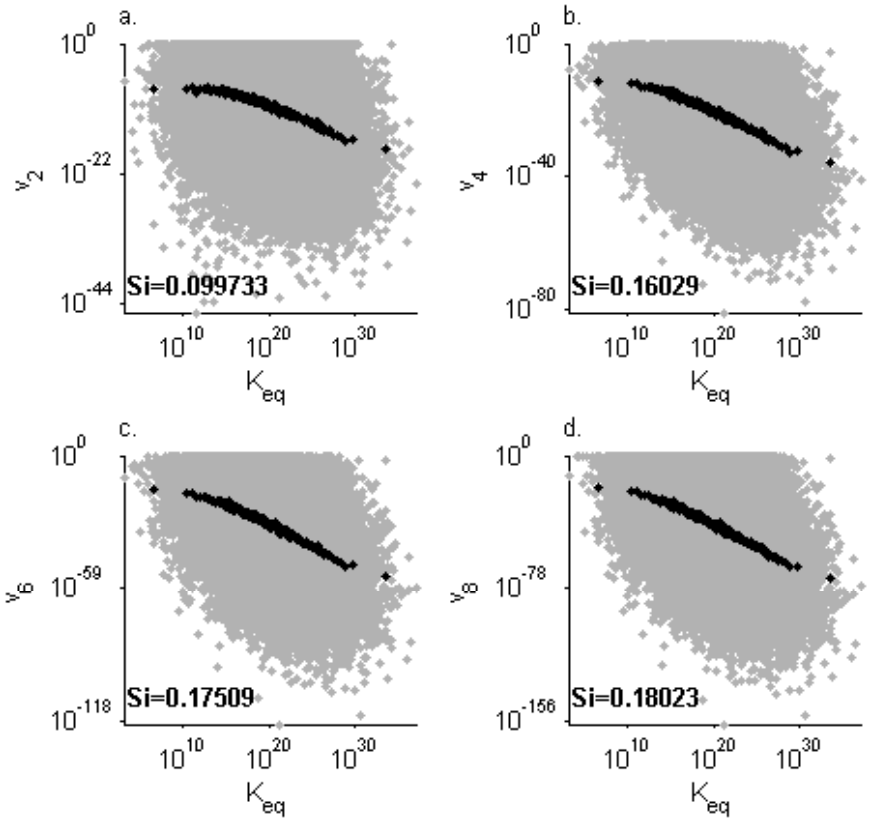

Figure 5.21: Sensitivity of the desorbed organic products, v_2 (HCOOH(aq)), v_4 (HCHO(aq)), v_6 (CH_3OH(aq)) and v_8 (CH_4(aq)), to the value of K_{eq} at high range (drawn from 10^{x_i}, $x_i \sim N(20, 16)$). The grey points are the outputs of each parameter set while the black points are the mean values of the variable in the neighbourhood of the parameter value, calculated from 500 points.

5.4. The sensitivity of the products to s also illustrates that selection of the range of the parameter is important for sensitivity analysis. More information on the parameter values could result in more robust conclusions from the sensitivity analysis performed here.

The assumption that $[H^+(aq)]$ is constant was based on a high concentration of CO_2(aq), which acts as a buffer. In this model, for many parameter sets where light is assumed to be abundant, the steady state is not reached until most of the CO_2 has been used up. In that case the assumption that $[H^+(aq)]$ is constant no longer holds. Experimentally it was observed that methane concentration reaches its maximum value by 3 h Liu (2012), before either H^+ or CO_2 become limiting, as the pH is still 4 at the end of a 3 h experiment. An additional factor is necessary to explain this discrepancy between the model and the experiments. Coverage of the surface sites by intermediates, leading to catalyst deactivation, has been suggested as a cause for the slowing down and eventual ceasing of the production (Tseng et al. 2002).

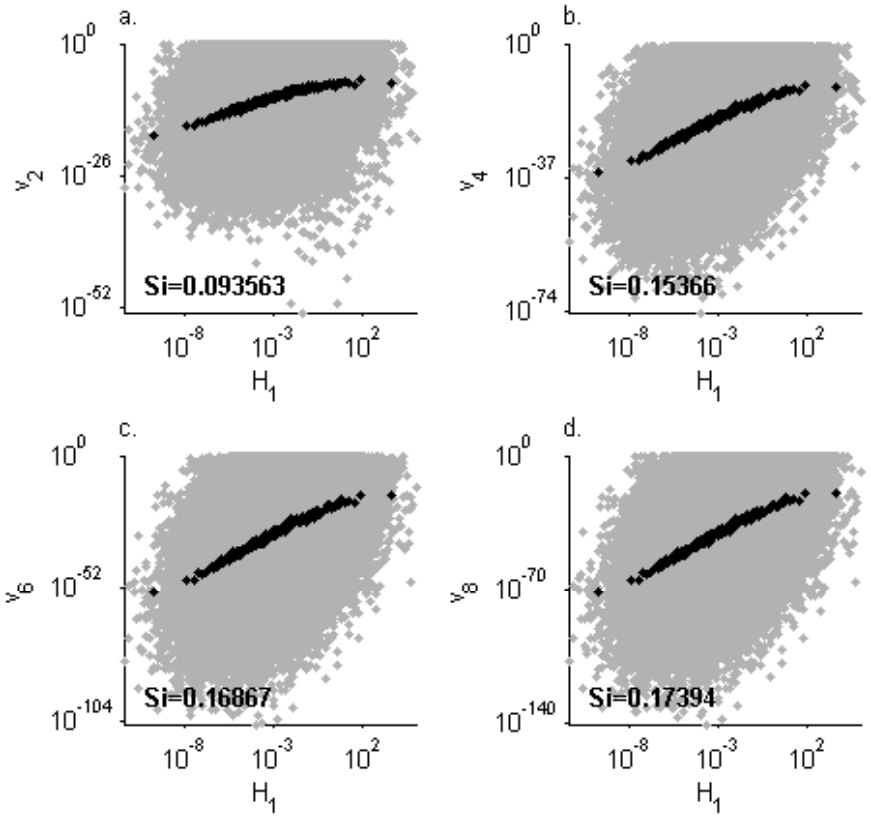

Figure 5.22: Sensitivity of the desorbed organic products, v_2 (HCOOH(aq)), v_4 (HCHO(aq)), v_6 (CH_3OH(aq)) and v_8 (CH_4(aq)), to the value of H_1 at high K_{eq} range (drawn from 10^{x_i}, $x_i \sim N(20, 16)$). The same parameter sets were used as in figure 5.21. The grey points are the outputs of each parameter set while the black points are the mean values of the variable in the neighbourhood of the parameter value, calculated from 500 points.

5.6 ODE model using Langmuir isotherm

5.6.1 Assumptions

In this section it is not assumed that adsorption and desorption of the inorganic species are fast and they are explicitly modelled using the Langmuir isotherm (see section 1.6.2). To do this, the notion of an empty site (E) is introduced, which refers to a site of the surface where nothing is yet adsorbed. This can be any of e^-, N_e, h^+ or N_h as the term "empty" refers to the absence of adsorbates rather than the charge or type of the site. In order for this model to be comparable to the discrete model and also to keep it as simple as possible, the following assumptions were also made.

- The CO_2(aq) concentration is not a variable in this model but instead is assumed constant, as H^+(aq), OH^-(aq) and H_2O(aq) were previously, because it also comes from a very large pool and diffusion is assumed fast.
- Only one atom or one ion can be adsorbed on any site at any time,

regardless of whether this is an e^- site, a N_e site, a h^+ site or a N_h site.

- It has been postulated that the CO_2 adsorption step is assisted by the presence of an electron on the adsorption site which is assumed not to be consumed by the process of adsorption. This e^- causes the CO_2 to bend, thus making it more reactive (Indrakanti et al. 2009).
- CO_2 is assumed to take up both a Ti site (either N_e or e^-) and an O site (either N_h or h^+). Because it is bent, one of its O-atoms will be associated to the Ti while the C will be associated with the O of the surface. All the organic compounds subsequently created on the surface from CO_2 are also assumed to be associated with the same two sites. This is a simplifying assumption as reduced compounds (without oxygens) may not need two sites. Further investigation of this could lead to an improved model but this was not attempted in the scope of this thesis.
- The Langmuir equation is used to model adsorption and desorption (see Section 1.6.2). This is often used to model adsorption/desorption of gases on a surface. In this case molar concentrations are used instead of partial pressures, since the compounds are in a solution. A special case which does not fulfill the assumptions of the Langmuir model is the carbon-containing compounds which have been assumed to take up two sites. The adsorption rate is multiplied by 2 and the desorption rate is divided by 2 in the ODEs to reflect that.
- Because the concentrations of the desorbed organic compounds will be low and diffusion is assumed to be fast, readsorption of the products is ignored. After long reaction times, when the concentrations have increased significantly, this assumption will not hold. In fact, in the literature, photoreduction experiments appear to reach a steady state after a few hours when the product concentration no longer increases (Liu 2012). This is believed to be due to re-adsorption and oxidation of the products (Tseng et al. 2002). However, for the early time of the photoreduction, this assumption will simplify the model without cost.

5.6.2 Reaction Mechanism

The following reaction mechanism is the basis for the model described in this section. It differs from those of the previous sections because it focuses on the early time of the reaction and not the equilibrium, ignoring readsorption of organic products. It also explicitly models adsorption of the reactants, and includes the empty surface sites which are needed for adsorption (e.g. reactions (5.59p), (5.59s)), some redox reactions (if the number of products exceeds the number of reactants, e.g. reaction (5.59w)) and are released ("produced") during desorption (e.g. reactions (5.59f), (5.59i)) and some other redox reactions (e.g. reactions (5.59d), (5.59g)). A simple diagram of the reaction pathway is shown in figure 5.23. It is a simplified version and does not include all the species involved in reactions

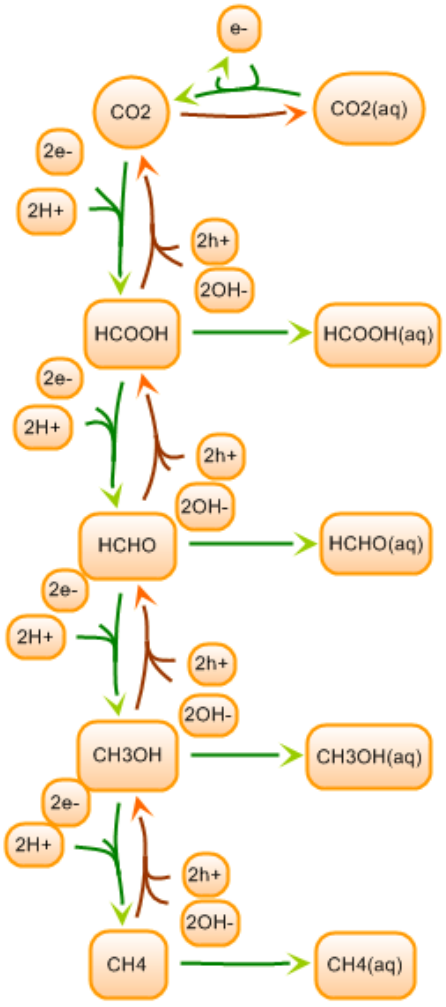

Figure 5.23: Simple pathway of the carbon-compound containing reactions

(5.59), but shows the overall pathway.

$$N_e + N_h \underset{k_{-0}}{\overset{k_0}{\rightleftharpoons}} \mathrm{e^-} + \mathrm{h^+} \tag{5.59a}$$

$$\mathrm{CO_2(aq)} + 2E + \mathrm{e^-} \xrightarrow{k_{a1}} \mathrm{CO_2} + \mathrm{e^-} \tag{5.59b}$$

$$\mathrm{CO_2} \xrightarrow{k_{d1}} \mathrm{CO_2(aq)} + 2E \tag{5.59c}$$

$$\underline{\mathrm{CO_2}} + 2\mathrm{e^-} + 2\mathrm{H^+} \xrightarrow{k_1} \mathrm{HCOOH} + 2N_e + 2E \tag{5.59d}$$

$$\underline{\mathrm{HCOOH}} + 2\mathrm{h^+} + 2\mathrm{OH^-} \xrightarrow{k_{-1}} \mathrm{CO_2} + 2\mathrm{H_2O} + 2N_h \tag{5.59e}$$

$$\mathrm{HCOOH} \xrightarrow{k_{d2}} \mathrm{HCOOH(aq)} + 2E \tag{5.59f}$$

$$\underline{\mathrm{HCOOH}} + 2\mathrm{e^-} + 2\mathrm{H^+} \xrightarrow{k_2} \mathrm{HCHO} + \mathrm{H_2O} + 2N_e + E \tag{5.59g}$$

$$\underline{\mathrm{HCHO}} + 2\mathrm{h^+} + 2\mathrm{OH^-} \xrightarrow{k_{-2}} \mathrm{HCOOH} + \mathrm{H_2O} + 2N_h + E \tag{5.59h}$$

$$\mathrm{HCHO} \xrightarrow{k_{d3}} \mathrm{HCHO(aq)} + 2E \tag{5.59i}$$

$$\underline{\mathrm{HCHO}} + 2\mathrm{e^-} + 2\mathrm{H^+} \xrightarrow{k_3} \mathrm{CH_3OH} + 2N_e + 2E \tag{5.59j}$$

$$\underline{\mathrm{CH_3OH}} + 2\mathrm{h^+} + 2\mathrm{OH^-} \xrightarrow{k_{-3}} \mathrm{HCHO} + 2\mathrm{H_2O} + 2N_h \tag{5.59k}$$

$$\mathrm{CH_3OH} \xrightarrow{k_{d4}} \mathrm{CH_3OH(aq)} + 2E \tag{5.59l}$$

$$\underline{\mathrm{CH_3OH}} + 2\mathrm{e^-} + 2\mathrm{H^+} \xrightarrow{k_4} \mathrm{CH_4} + \mathrm{H_2O} + 2N_e + E \tag{5.59m}$$

$$\underline{\mathrm{CH_4}} + 2\mathrm{h^+} + 2\mathrm{OH^-} \xrightarrow{k_{-4}} \mathrm{CH_3OH} + \mathrm{H_2O} + 2N_h + E \tag{5.59n}$$

$$\mathrm{CH_4} \xrightarrow{k_{d5}} \mathrm{CH_4(aq)} + 2E \tag{5.59o}$$

$$\mathrm{OH^-(aq)} + E \underset{k_{d6}}{\overset{k_{a2}}{\rightleftharpoons}} \mathrm{OH^-} \tag{5.59p}$$

$$\underline{2\mathrm{OH^-}} + 4\mathrm{h^+} + E \xrightarrow{k_5} \mathrm{O_2} + 4N_h + 2\mathrm{H^+} \tag{5.59q}$$

$$\mathrm{O_2} \xrightarrow{k_{d7}} \mathrm{O_2(aq)} + E \tag{5.59r}$$

$$\mathrm{H^+(aq)} + E \underset{k_{d8}}{\overset{k_{a3}}{\rightleftharpoons}} \mathrm{H^+} \tag{5.59s}$$

$$\underline{2\mathrm{H^+}} + 2\mathrm{e^-} \xrightarrow{k_6} 2N_e + \mathrm{H_2} + E \tag{5.59t}$$

$$\mathrm{H_2} \xrightarrow{k_{d9}} \mathrm{H_2(aq)} + E \tag{5.59u}$$

$$\mathrm{H_2O(aq)} + E \underset{k_{d10}}{\overset{k_{a4}}{\rightleftharpoons}} \mathrm{H_2O} \tag{5.59v}$$

$$\underline{\mathrm{H_2O}} + \mathrm{e^-} + \mathrm{h^+} + E \xrightarrow{k_7} \mathrm{H^+} + \mathrm{OH^-} + N_e + N_h \tag{5.59w}$$

5.6.3 Notation of the ODE model

- The coverage of the surface by a species is the fraction of surface sites occupied by molecules/ions/atoms of that species.
  - θ_{H^+}, θ_{OH^-}, θ_{H_2O}, θ_{H_2} and θ_{O_2} refer to the coverages of the surface by the protons, hydroxides, water, hydrogen and oxygen adsorbed on the surface of the catalyst respectively.
  - θ_{CO_2}, θ_{HCOOH}, θ_{HCHO}, θ_{CH_3OH} and θ_{CH_4} refer to the coverages of the surface by the carbon dioxide, formic acid, formaldehyde, methanol and methane adsorbed on the surface of the catalyst

respectively. Each molecule corresponds to two sites therefore the fraction of molecules per total number of sites will be the coverage divided by 2.
  - θ_E refers to the coverage of the remaining empty sites.

  The above coverages add up to 1 ($\sum \theta_x = 1$).
- Θ_{e^-} and Θ_{N_e} are the coverages of the e^- and N_e sites respectively. A different notation is used because only a third of the total number of surface sites is included in the coverage of these species (since only the Ti sites of TiO_2 can become negatively charged). Additionally, the same site can have an adsorbate and an electron and so these coverages are not included in the total coverage of sites. Instead

$$\Theta_{e^-} + \Theta_{N_e} = \tfrac{1}{3}. \tag{5.60}$$

- Similarly for ϑ_{h^+} and ϑ_{N_h}, the coverages of h^+ and N_h, only two thirds of the total number of surface sites can become positively charged (the O sites of TiO_2) and so these are also separate from both the adsorbate coverages and the e^- coverage. In this case

$$\vartheta_{h^+} + \vartheta_{N_h} = \tfrac{2}{3}. \tag{5.61}$$

- $[H^+(aq)]$, $[OH^-(aq)]$, $[H_2O(aq)]$ and $[CO_2(aq)]$, refer to the molar concentration of protons, hydroxides, water and carbon dioxide in the solution respectively, all of which are assumed constant.
- $[HCOOH(aq)]$, $[HCHO(aq)]$, $[CH_3OH(aq)]$, $[CH_4(aq)]$, $[H_2(aq)]$ and $[O_2(aq)]$ refer to the molar concentrations of formic acid, formaldehyde, methanol, methane, hydrogen and oxygen in the solution respectively.

The reaction rates are proportional to the product of the coverages of each of the reactants (mass action kinetics) which corresponds to the probability of all the necessary reactants being on specific sites of the surface. In this case it is assumed sufficient for them to be on adjacent sites to be able to react, as it was assumed that they cannot be on the same site. There are a few different patterns of relative positions of reactants that can lead to a reaction, as will be discussed in the next chapter. This is not important here, as spatial effects are assumed insignificant, but will be necessary for understanding the differences in rate constants between this section and the next chapter.

Additionally, again, it is assumed that reaction (5.59a) for the splitting and recombination of electron-hole pairs happens much faster than reactions (5.59b)–(5.59w) and so is assumed to be at steady state. This will lead to the same equation between h^+ and e^- as found earlier (equation (5.12)) which now takes the form

$$\vartheta_{h^+} = \tfrac{2}{3} \frac{\frac{1}{3} - \Theta_{e^-}}{(K_{eq} - 1)e^- + \frac{1}{3}}. \tag{5.62}$$

5.6.4 ODE System

From the reaction mechanism (5.59b)–(5.59w) and using the rate law according to the Langmuir-Hinselwood model mechanism (described in sec-

tion 1.6.2), the following system of ODEs (5.63) is obtained.

$$\begin{aligned}
\frac{\mathrm{d}\theta_{CO_2}}{\mathrm{d}t} &= 2k'_{a1}\theta_E^2\Theta_{e^-} - \frac{1}{2}k_{d1}\theta_{CO_2} - k_1\theta_{CO_2}\Theta_{e^-}^2\theta_{H^+}^2 \\
&\quad + k_{-1}\theta_{HCOOH}\vartheta_{h^+}^2\theta_{OH^-}^2, && (5.63a)\\
\frac{\mathrm{d}\theta_{HCOOH}}{\mathrm{d}t} &= k_1\theta_{CO_2}\Theta_{e^-}^2\theta_{H^+}^2 - k_{-1}\theta_{HCOOH}\vartheta_{h^+}^2\theta_{OH^-}^2 - \frac{1}{2}k_{d2}\theta_{HCOOH} \\
&\quad - k_2\theta_{HCOOH}\Theta_{e^-}^2\theta_{H^+}^2 + k_{-2}\theta_{HCHO}\vartheta_{h^+}^2\theta_{OH^-}^2, && (5.63b)\\
\frac{\mathrm{d}[\mathrm{HCOOH(aq)}]}{\mathrm{d}t} &= \frac{1}{2}k_{d2}\theta_{HCOOH}S, && (5.63c)\\
\frac{\mathrm{d}\theta_{HCHO}}{\mathrm{d}t} &= k_2\theta_{HCOOH}\Theta_{e^-}^2\theta_{H^+}^2 - k_{-2}\theta_{HCHO}\vartheta_{h^+}^2\theta_{OH^-}^2 - \frac{1}{2}k_{d3}\theta_{HCHO} \\
&\quad - k_3\theta_{HCHO}\Theta_{e^-}^2\theta_{H^+}^2 + k_{-3}\theta_{CH_3OH}\vartheta_{h^+}^2\theta_{OH^-}^2, && (5.63d)\\
\frac{\mathrm{d}[\mathrm{HCHO(aq)}]}{\mathrm{d}t} &= \frac{1}{2}k_{d3}\theta_{HCHO}S, && (5.63e)\\
\frac{\mathrm{d}\theta_{CH_3OH}}{\mathrm{d}t} &= k_3\theta_{HCHO}\Theta_{e^-}^2\theta_{H^+}^2 - k_{-3}\theta_{CH_3OH}\vartheta_{h^+}^2\theta_{OH^-}^2 - \frac{1}{2}k_{d4}\theta_{CH_3OH} \\
&\quad - k_4\theta_{CH_3OH}\Theta_{e^-}^2\theta_{H^+}^2 + k_{-4}\theta_{CH_4}\vartheta_{h^+}^2\theta_{OH^-}^2, && (5.63f)\\
\frac{\mathrm{d}[\mathrm{CH_3OH(aq)}]}{\mathrm{d}t} &= \frac{1}{2}k_{d4}\theta_{CH_3OH}S, && (5.63g)\\
\frac{\mathrm{d}\theta_{CH_4}}{\mathrm{d}t} &= k_4\theta_{CH_3OH}\Theta_{e^-}^2\theta_{H^+}^2 - k_{-4}\theta_{CH_4}\vartheta_{h^+}^2\theta_{OH^-}^2 \\
&\quad - \frac{1}{2}k_{d5}\theta_{CH_4}, && (5.63h)\\
\frac{\mathrm{d}[\mathrm{CH_4(aq)}]}{\mathrm{d}t} &= \frac{1}{2}k_{d5}\theta_{CH_4}S, && (5.63i)\\
\frac{\mathrm{d}\theta_{H_2O}}{\mathrm{d}t} &= 2k_{-1}\theta_{HCOOH}\vartheta_{h^+}^2\theta_{OH^-}^2 + k_2\theta_{HCOOH}\Theta_{e^-}^2\theta_{H^+}^2 \\
&\quad + k_{-2}\theta_{HCHO}\vartheta_{h^+}^2\theta_{OH^-}^2 + 2k_{-3}\theta_{CH_3OH}\vartheta_{h^+}^2\theta_{OH^-}^2 \\
&\quad + k_4\theta_{CH_3OH}\Theta_{e^-}^2\theta_{H^+}^2 + k_{-4}\theta_{CH_4}\vartheta_{h^+}^2\theta_{OH^-}^2 \\
&\quad + k'_{a4}\theta_E - k_{d10}\theta_{H_2O} - k_7\theta_{H_2O}\Theta_{e^-}\vartheta_{h^+}\theta_E, && (5.63j)\\
\frac{\mathrm{d}\theta_{OH^-}}{\mathrm{d}t} &= -2k_{-1}\theta_{HCOOH}\vartheta_{h^+}^2\theta_{OH^-}^2 - 2k_{-2}\theta_{HCHO}\vartheta_{h^+}^2\theta_{OH^-}^2 \\
&\quad - 2k_{-3}\theta_{CH_3OH}\vartheta_{h^+}^2\theta_{OH^-}^2 - 2k_{-4}\theta_{CH_4}\vartheta_{h^+}^2\theta_{OH^-}^2 \\
&\quad + k'_{a2}\theta_E - k_{d6}\theta_{OH^-} - 2k_5\vartheta_{h^+}^4\theta_{OH^-}^2\theta_E \\
&\quad + k_7\theta_{H_2O}\Theta_{e^-}\vartheta_{h^+}\theta_E, && (5.63k)
\end{aligned}$$

$$\frac{\mathrm{d}\theta_{O_2}}{\mathrm{d}t} = k_5\vartheta_{h^+}^4\theta_{OH^-}^2\theta_E - k_{d7}\theta_{O_2}, \tag{5.63l}$$

$$\frac{\mathrm{d}[\mathrm{O_2(aq)}]}{\mathrm{d}t} = k_{d7}\theta_{O_2}S, \tag{5.63m}$$

$$\begin{aligned}\frac{\mathrm{d}\theta_{H^+}}{\mathrm{d}t} = &-2k_1\theta_{CO_2}\Theta_{e^-}^2\theta_{H^+}^2 - 2k_2\theta_{HCOOH}\Theta_{e^-}^2\theta_{H^+}^2 \\ &-2k_3\theta_{HCHO}\Theta_{e^-}^2\theta_{H^+}^2 - 2k_4\theta_{CH_3OH}\Theta_{e^-}^2\theta_{H^+}^2 + 2k_5\vartheta_{h^+}^4\theta_{OH^-}^2\theta_E \\ &+k'_{a3}\theta_E - k_{d8}\theta_{H^+} - 2k_6\Theta_{e^-}^2\theta_{H^+}^2 + k_7\theta_{H_2O}\Theta_{e^-}\vartheta_{h^+}\theta_E,\end{aligned} \tag{5.63n}$$

$$\frac{\mathrm{d}\theta_{H_2}}{\mathrm{d}t} = k_6\Theta_{e^-}^2\theta_{H^+}^2 - k_{d9}\theta_{H_2}, \tag{5.63o}$$

$$\frac{\mathrm{d}[\mathrm{H_2(aq)}]}{\mathrm{d}t} = k_{d9}\theta_{H_2}S. \tag{5.63p}$$

In the above system of equations S is the concentration of all sites on the catalyst surface,

$$\begin{aligned} k'_{a1} &= k_{a1}\cdot[\mathrm{CO_2(aq)}] = k_{a1}\cdot(6.6\cdot10^{-2}M), && (5.64a)\\ k'_{a2} &= k_{a2}\cdot[\mathrm{OH^-(aq)}] = k_{a2}\cdot(10^{-10}M), && (5.64b)\\ k'_{a3} &= k_{a3}\cdot[\mathrm{H^+(aq)}] = k_{a3}\cdot(10^{-4}M) \text{ and} && (5.64c)\\ k'_{a4} &= k_{a4}\cdot[\mathrm{H_2O(aq)}] = k_{a4}\cdot(55.5M). && (5.64d)\end{aligned}$$

Additionally for Θ_{e^-} and ϑ_{h^+}

$$\begin{aligned}\frac{\mathrm{d}\Theta_{e^-}}{\mathrm{d}t} = &\ k_0\Theta_{N_e}\vartheta_{N_h} - k_{-0}\Theta_{e^-}\vartheta_{h^+} - 2k_1\theta_{CO_2}\Theta_{e^-}^2\theta_{H^+}^2 \\ &-2k_2\theta_{HCOOH}\Theta_{e^-}^2\theta_{H^+}^2 - 2k_3\theta_{HCHO}\Theta_{e^-}^2\theta_{H^+}^2 \\ &-2k_4\theta_{CH_3OH}\Theta_{e^-}^2\theta_{H^+}^2 - 2k_6\Theta_{e^-}^2\theta_{H^+}^2 \\ &-k_7\theta_{H_2O}\Theta_{e^-}\vartheta_{h^+}\theta_E,\end{aligned} \tag{5.65}$$

$$\begin{aligned}\frac{\mathrm{d}\vartheta_{h^+}}{\mathrm{d}t} = &\ k_0\Theta_{N_e}\vartheta_{N_h} - k_{-0}\Theta_{e^-}\vartheta_{h^+} - 2k_{-1}\theta_{HCOOH}\vartheta_{h^+}^2\theta_{OH^-}^2 \\ &-2k_{-2}\theta_{HCHO}\vartheta_{h^+}^2\theta_{OH^-}^2 - 2k_{-3}\theta_{CH_3OH}\vartheta_{h^+}^2\theta_{OH^-}^2 \\ &-2k_{-4}\theta_{CH_4}\vartheta_{h^+}^2\theta_{OH^-}^2 - 4k_5\vartheta_{h^+}^4\theta_{OH^-}^2\theta_E \\ &-k_7\theta_{H_2O}\Theta_{e^-}\vartheta_{h^+}\theta_E,\end{aligned} \tag{5.66}$$

and

$$\begin{aligned}\frac{\mathrm{d}\vartheta_{h^+}}{\mathrm{d}t} - \frac{\mathrm{d}\Theta_{e^-}}{\mathrm{d}t} &= \frac{\mathrm{d}\vartheta_{h^+}}{\mathrm{d}\Theta_{e^-}}\frac{\mathrm{d}\Theta_{e^-}}{\mathrm{d}t} - \frac{\mathrm{d}\Theta_{e^-}}{\mathrm{d}t} \\ &= \left(\frac{\mathrm{d}\vartheta_{h^+}}{\mathrm{d}\Theta_{e^-}} - 1\right)\frac{\mathrm{d}\Theta_{e^-}}{\mathrm{d}t}.\end{aligned} \tag{5.67}$$

Thus

$$\begin{aligned}\frac{\mathrm{d}\Theta_{e^-}}{\mathrm{d}t} &= \frac{1}{\left(\frac{d\vartheta_{h^+}}{d\Theta_{e^-}} - 1\right)}\Big(k_0\Theta_{N_e}\vartheta_{N_h} - k_{-0}\Theta_{e^-}\vartheta_{h^+} \\ &\quad -2k_{-1}\theta_{HCOOH}\vartheta_{h^+}^2\theta_{OH^-}^2 - 2k_{-2}\theta_{HCHO}\vartheta_{h^+}^2\theta_{OH^-}^2 \\ &\quad -2k_{-3}\theta_{CH_3OH}\vartheta_{h^+}^2\theta_{OH^-}^2 - 2k_{-4}\theta_{CH_4}\vartheta_{h^+}^2\theta_{OH^-}^2 \\ &\quad -4k_5\vartheta_{h^+}^4\theta_{OH^-}^2\theta_E - k_7\theta_{H_2O}\Theta_{e^-}\vartheta_{h^+}\theta_E \\ &\quad -\big(k_0\Theta_{N_e}\vartheta_{N_h} - k_{-0}\Theta_{e^-}\vartheta_{h^+} - 2k_1\theta_{CO_2}\Theta_{e^-}^2\theta_{H^+}^2 \\ &\quad -2k_2\theta_{HCOOH}\Theta_{e^-}^2\theta_{H^+}^2 - 2k_3\theta_{HCHO}\Theta_{e^-}^2\theta_{H^+}^2 \\ &\quad -2k_4\theta_{CH_3OH}\Theta_{e^-}^2\theta_{H^+}^2 - 2k_6\Theta_{e^-}^2\theta_{H^+}^2 \\ &\quad -k_7\theta_{H_2O}\Theta_{e^-}\vartheta_{h^+}\theta_E)\Big). \end{aligned} \tag{5.68}$$

From equation (5.62), it is deduced that

$$\frac{\mathrm{d}\vartheta_{h^+}}{\mathrm{d}\Theta_{e^-}} = -\frac{\frac{1}{3}\frac{2}{3}K_{eq}}{(\frac{1}{3} + (K_{eq} - 1)\Theta_{e^-})^2}. \tag{5.69}$$

Therefore

$$\begin{aligned}\frac{\mathrm{d}\Theta_{e^-}}{\mathrm{d}t} &= \frac{(\frac{1}{3} + (K_{eq} - 1)\Theta_{e^-})^2}{(\frac{1}{3} + (K_{eq} - 1)\Theta_{e^-})^2 + \frac{2}{9}K_{eq}}\big(-2k_1\theta_{CO_2}\Theta_{e^-}^2\theta_{H^+}^2 \\ &\quad +2k_{-1}\theta_{HCOOH}\vartheta_{h^+}^2\theta_{OH^-}^2 - 2k_2\theta_{HCOOH}\Theta_{e^-}^2\theta_{H^+}^2 \\ &\quad +2k_{-2}\theta_{HCHO}\vartheta_{h^+}^2\theta_{OH^-}^2 - 2k_3\theta_{HCHO}\Theta_{e^-}^2\theta_{H^+}^2 \\ &\quad +2k_{-3}\theta_{CH_3OH}\vartheta_{h^+}^2\theta_{OH^-}^2 - 2k_4\theta_{CH_3OH}\Theta_{e^-}^2\theta_{H^+}^2 \\ &\quad +2k_{-4}\theta_{CH_4}\vartheta_{h^+}^2\theta_{OH^-}^2 + 4k_5\vartheta_{h^+}^4\theta_{OH^-}^2\theta_E - 2k_6\Theta_{e^-}^2\theta_{H^+}^2\big), \end{aligned} \tag{5.70}$$

where ϑ_{h^+} is calculated from equation (5.62).

Finally, because of the conservation of sites on the surface, the following equation is obtained.

$$\begin{aligned}\theta_E &= 1 - \theta_{CO_2} - \theta_{HCOOH} - \theta_{HCHO} - \theta_{CH_3OH} - \theta_{CH_4} \\ &\quad -\theta_{H^+} - \theta_{OH^-} - \theta_{H_2O} - \theta_{H_2} - \theta_{O_2}. \end{aligned} \tag{5.71}$$

In this case, because it was assumed that the $[CO_2(aq)]$ is a constant source of carbon, carbon conservation cannot be used. This assumption is valid because, at early time, the other carbon-compounds have relatively negligible concentrations so that the change to $[CO_2(aq)]$ is not significant relative to its value.

5.6.5 Parameter Values

The equilibrium constant for adsorption/desorption of carbon dioxide on to the catalyst surface from gas phase was found in the literature (Wu et al. 2005). The equivalent was not found for aqueous suspension which is used here, so the gas value was used. For the values of each of the parameters (k_{a1} and k_{d1}), the fraction of which is the equilibrium constant, values were chosen so as to allow simulation with the discrete model, which will

Parameter	Value
$K_{eq} = \frac{k_{-0}}{k_0}$	0.81 (dimensionless)
k_0	10^5 s^{-1}
k_{-0}	$8.1 \cdot 10^4$ s^{-1}
k_1, k_2, k_3, k_4	$2.25 \cdot 10^7$ s^{-1}
k_{-1}, k_{-2}, k_{-3}, k_{-4}	$6 \cdot 10^7$ s^{-1}
k_5	$1.33 \cdot 10^6$ s^{-1}
k_6	$3 \cdot 10^6$ s^{-1}
k_7	$8.67 \cdot 10^6$ s^{-1}
k_{d1}, k_{d2}, k_{d3}, k_{d4}	100 s^{-1}
k_{d6}, k_{d8}	10^4 s^{-1}
k_{d7}, k_{d9}	10^5 s^{-1}
k_{d10}	0.1 s^{-1}
k_{a1}	$2.5 \cdot 10^3$ $s^{-1}M^{-1}$
k_{a2}, k_{a3}	$2.5 \cdot 10^4$ $s^{-1}M^{-1}$
k_{a4}	2.3 $s^{-1}M^{-1}$

Table 5.4: Parameter values used in the model of Section 5.6.

be presented in the next chapter. This reaction does not appear in the earlier models. The redox reaction rates (k_1, k_2, k_3, k_4, k_{-1}, k_{-2}, k_{-3}, k_{-4}) match the values of the earlier models (of sections 5.2 and 5.3) but are given here in their dimensional forms. They are not based on literature values but were also selected for the successful simulation of the discrete model.

5.6.6 Numerical results of ODE model

The ODE system (5.63), (5.70) was run in Matlab using the ode15s solver with initial conditions corresponding to no adsorbed species present on the surface ($\theta = 0$ for all species), no organic compounds in the solution ([HCOOH(aq)], [HCHO(aq)], [CH_3OH(aq)] and [CH_4(aq)] are all equal to 0), no oxygen or hydrogen in the solution ([O_2(aq)], [H_2(aq)] =0) and equal amounts of Θ_{e^-} and ϑ_{h^+} (23.25%) selected so that they satisfy equation (5.62). The parameter values used are shown in table 5.4 and the results are shown in figure 5.24 (solid lines). The catalyst surface reaches a steady state condition within the first 1 s of the reaction and after that the coverages of all the adsorbed species remain constant. The desorption of products continues at a constant rate after 1 s (linear functions of time).

5.6.7 Validation of e^--h^+ assumption

To test whether the assumption relating to the steady state of e^--h^+ pair formation and recombination (reactions (5.59a)) was a reasonable one, the model was also simulated with equations for the rate of change of Θ_{e^-} (equation (5.65)) and ϑ_{h^+} (equation (5.66)) separately, not assuming the two reactions to be at steady state. For the same K_{eq}, when the reaction rate constants were large ($\sim$ 3 orders of magnitude larger than the next largest rate constant), the time profiles of all the variables were exactly the

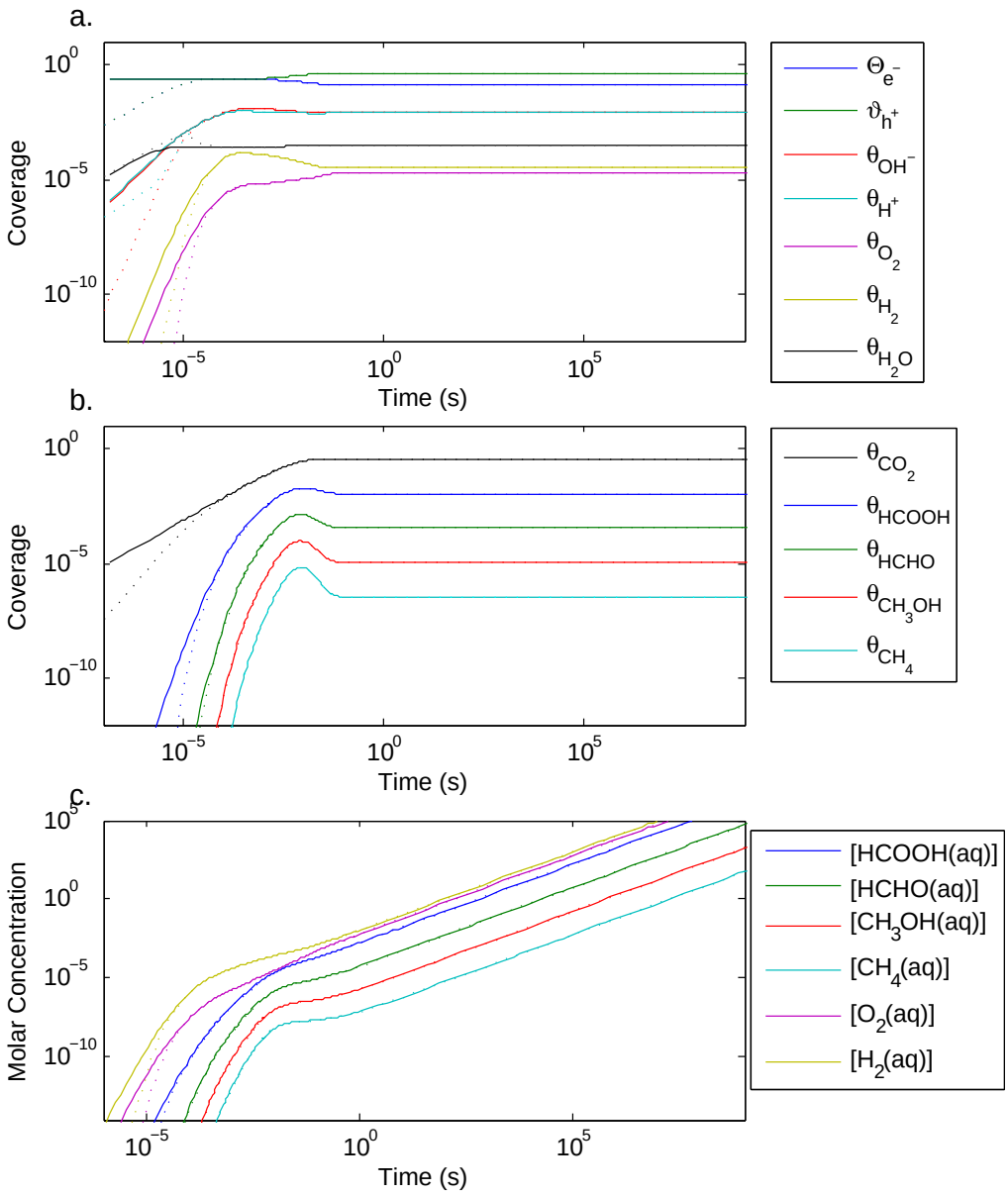

Figure 5.24: Numerical simulations of the ODE model (5.63), (5.70) (solid lines) and of ODE model (5.63), (5.65),(5.66) (dotted lines). a. Time profiles of variables Θ_{e^-}, ϑ_{h^+}, θ_{OH^-}, θ_{H^+}, θ_{O_2} and θ_{H_2}. b. Time profiles of variables θ_{CO_2}, θ_{HCOOH}, θ_{HCHO}, θ_{CH_3OH} and θ_{CH_4}. c. Time profiles of variables [HCOOH(aq)], [HCHO(aq)], [CH_3OH(aq)], [CH_4(aq)], [O_2(aq)] and [H_2(aq)].

same as in the model where steady state is assumed. Even when the rate constants took values similar to many of the other parameters (k_0 and k_{-0} in table 5.4), the time profiles were only different before 10^{-3} s and reached the same linear growth and steady state conditions for all variables (figure 5.24, dotted lines).

5.6.8 Discussion

Using the assumptions of Section 5.6.1, a more detailed and realistic photoreduction mechanism has been investigated while keeping the model simple. The analysis of this model leads to predictions about the maximum production rate for each of the investigated organic compounds, as well as the hydrogen and the oxygen produced by the reaction (as opposed to steady state values predicted by the models of the previous sections). These rates could be compared with experimental data, and parameter estimation could be used to fit the outputs of this model to the results of the experiments and find a credible range for the parameter values. Unfortunately, as discussed in Chapter 4, the quality and quantity of the experimental results is insufficient to allow for this analysis here. Using this model it was also confirmed that the assumption regarding fast e^--h^+ dynamics, which led to a simplification of this and previous models, does not change the profile of the products other than at a very early timescale. The results of this model are further discussed in Section 6.2 with relation to the results of a discrete model based on the same reaction mechanism.

5.7 Conclusions

A few different ODE models of CO_2 photoreduction were developed and investigated in this chapter, starting from a simple, two-variable model of CO_2 to HCOOH conversion and adding complexity gradually, to reach more complicated models simulating redox reactions of organic models, adsorption/desorption and water splitting reactions. Predictions were made using each model, some of which were in agreement with the other models, while others contradicted those of other models. By comparing these to each other and experimental data, the most appropriate model can be selected for future use. However, all are presented here to show the progression through them and to better explain the system.

Experimentally, the concentration of organics shows a saturating effect, with the rate of production slowing down and stopping after a few hours (Liu 2012). The time it takes for production to stop depends on the experimental conditions and varies greatly. The models presented in this chapter also show this pattern, with the exception of the model of Section 5.6 which focuses on the early stages of the reaction and shows a constant production rate. All other models predict that the product concentrations in the reactor will reach a steady state. Indeed, the model of Section 5.2 predicts that this steady state is a stable node. An explicit equation is given for all the product concentrations at steady state in relation to the parameters (equations (5.45) and (5.46c)).

In the simplified model of CO_2 photoreduction to CH_4 (Section 5.4), sensitivity analysis showed that the parameters corresponding to light and the hole scavenger have the strongest effect on the organic product concentrations at steady state. Additionally, because each reduction step is affected by these parameters, more reduced products are more sensitive to them as the effect builds up with each step. Between hole scavenger and light, the latter is the preferred target for the experimental enhancement of

the catalyst, because increasing its light absorption efficiency, for example by attaching the LHCII to its surface, would lead to increased production without additional consumption of energy (light of the same or lower intensity could lead to more photons being absorbed). To improve the hole scavenger efficiency, a fuel would have to replace water as the scavenger and this would be consumed by the reaction. It should further be noted that K_{eq}, the parameter that relates to light absorption, also incorporates e^--h^+ pair recombination rate, another important factor that has been targeted to optimise photoreduction (Indrakanti et al. 2009).

The effect of pH was investigated using the model of Section 5.5. Its effect only on the redox reactions was considered and it was shown that, for abundant light (or low recombination of e^- and h^+), the product concentrations were not sensitive to it. This changed for low light where the pH effect on the product concentrations was stronger.

Similarly the effect of K_{eq} was only evident for limiting light/fast recombination conditions. Further work on the model and experimental data for parameter estimation are needed to determine the light intensity at which the catalyst becomes saturated. Whether light saturation is also observed for the early time production rate, and if this happens at the same intensity, could be tested using the model of Section 5.6, again following parameter estimation.

Another prediction relates to the effect of the amount of catalyst added to the reactor on the final concentration of products. In the literature, product concentration results are often reported in units of product per g of catalyst used, indicating the widely held belief that there is a linear relationship between catalyst amount and final product concentration. The specific surface area of catalysts is also usually reported (the surface area per g), because that is the part of the catalysts that interacts with the reactants. In the models of section 5.2–5.4, the catalyst surface sites concentration has no effect on the equilibrium concentrations. On the other hand, in the model of Section 5.5, the product concentrations are sensitive to the surface sites concentration but the relationship is not linear. In fact, regression on the data in plot d of figure 5.18 gives the equation

$$v_8 = 0.17 s^{7.7}, \tag{5.72}$$

where v_8 corresponds to CH_4(aq) and s to the concentration of catalyst surface sites. In the model of Section 5.6, the rate of product desorption, equations (5.63c), (5.63e), (5.63g) and (5.63i), depends linearly on the concentration of the surface sites. Together, these results suggest that the steady state of the system, as predicted by the earlier models, is not reached, and a different factor is necessary to explain the slowing down and cessation of the production. Catalyst deactivation, which was discussed in Section 5.5.4, can explain this effect as it would cause the s to gradually decrease until the whole surface was blocked. In this case, the rate of production would be more important for the final concentration than the steady state of the system.

The results of the model of Section 5.6 give a constant production rate (corresponding to the maximum production rate) rather than constant con-

centrations. This model can make predictions for the early time of the reaction, before the increase of the product concentrations allows significant back-reaction (oxidation of organic products back to CO_2) and before deactivation has decreased the number of active sites. It was also used to compare with the discrete model of the next chapter and its results in this capacity will be discussed later (Section 6.2).

Chapter 6

Discrete Space Stochastic Model of CO_2 Photoreduction

In the previous chapter, spatial effects were ignored when modelling the reactions of CO_2 photoreduction. A spatial model was developed to test how its results differ from the ODE models of Chapter 5, in order to examine the importance of these spatial effects. Because the structure of the catalyst surface consists of discrete Ti and O sites, the model used a discrete space approach. A stochastic model was used to simulate the reactions occurring on a lattice representing the surface, the same as those presented in the mechanism of Section 5.6. The Gillespie algorithm was used to model photoreduction as a continuous time process with one action per time step and time steps of variable length.

6.1 Description of the discrete model

6.1.1 The Lattice

The model considers a 2-dimensional surface, part of the (100) surface of anatase TiO_2, which consists of a repeated pattern as shown in figure 5.1. Grooves in the surface separate it into long thin strips. It is assumed that the compounds cannot diffuse across the groove while adsorbed on the surface, and so the strips are treated as isolated from one another. A segment of the lattice representing the surface in the model is shown in figure 6.1; this indicates the simplified positions of the Ti and O sites assumed by the model.

The state of the lattice is represented by three matrices, one representing the adsorbates (**A**), one for the charge (**C**) and a third (**D**) for the relative position of the "other" C-species-containing site. As mentioned earlier, it is assumed that carbon species occupy two sites instead of one. Since it is possible that two C-species will adsorb on adjacent sites, and these sites will have the same label in **A**, a way is needed to distinguish between sites occupied by the same molecule and sites occupied by adjacent molecules. This third matrix serves this purpose by providing the direction of the other site occupied by the same molecule.

The indices of each matrix, represented by subscripts i, j, correspond to the coordinates on the lattice of the model, so that i is the index transverse

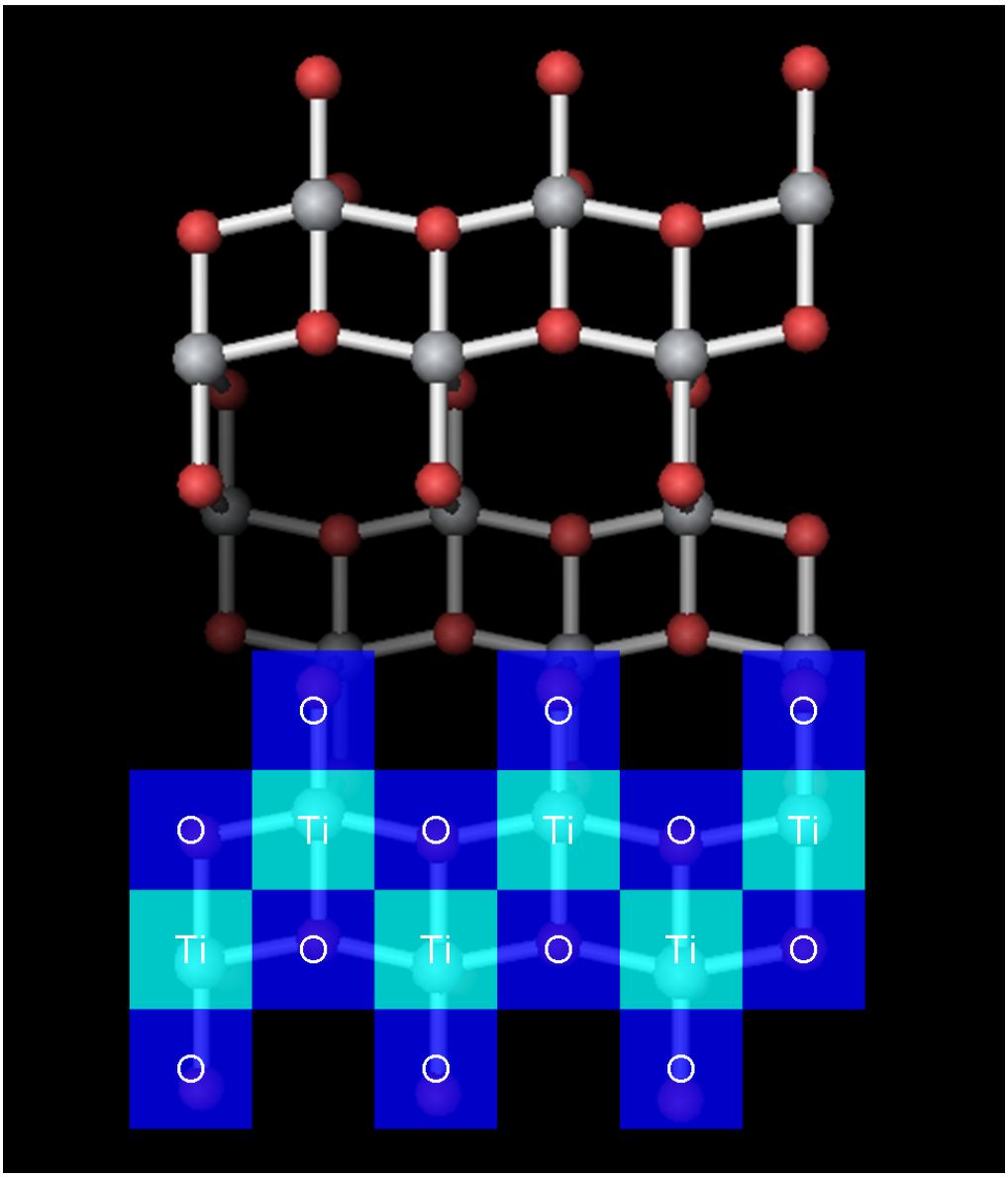

Figure 6.1: The surface of the TiO_2 catalyst with the diagram of the lattice used in the model superimposed on to it.

to the strip and j indicates position along it. Therefore, $i \in \{1,\ 2,\ 3,\ 4\}$ and $j \in \{1,\ 2,\ \ldots\ ,\ L\}$, where L is the length of the lattice.

The identity of the sites on the lattice (whether they are O, Ti or out-of-plane sites) are given from their i and j coordinates by

- O site if $(i + j) = 0 (\mathrm{mod}\ 2)$,
- Ti site if $(i + j) = 1 (\mathrm{mod}\ 2)$ and $1 < i < 4$,
- out-of-plane site otherwise.

A represents the chemical species adsorbed on each site which can be one of CO_2, HCOOH, HCHO, CH_3OH, CH_4, H^+, OH^-, H_2, O_2, H_2O or an empty site (E). Therefore each element $A_{i,j}$ shows the chemical on site (i, j). This is represented in the model by integers from 0 to 10 with 0

corresponding to an empty site and 1–10 corresponding to the chemical species in the order shown, so that $A_{i,j} \in \{0,\ 1,\ 2,\ \ldots,\ 10\}$.

C represents the charge on each site. Each element $C_{i,j} \in \{-1,\ 0,\ 1\}$, corresponds respectively to negatively charged (e^-), neutral (N_e, N_h) and positively charged (h^+) sites.

D represents the direction in which the other site occupied by the same molecule is. Each element

$$D_{i,j} \in \begin{cases} \{(0,\ 0)\} & \text{, if } A_{i,j} = 0 \text{ or } A_{i,j} > 5, \\ \{(0,1),(0,-1),(1,0),(-1,0)\} & \text{, if } 0 < A_{i,j} < 6. \end{cases} \tag{6.1}$$

In the case of C-species ($0 < A_{i,j} < 6$), these encode the relative position of the other site that is occupied by the same C-species, so that $(i,j) + D_{i,j}$ will give the position on the lattice of that other site. In the case of non-C-species (which only take up one site), $(i,j) + D_{i,j}$ is the position of the site itself.

6.1.2 Diffusion and migration along the surface

All adsorbed carbon species are assumed to be immobile and do not diffuse along the surface. The other adsorbates may diffuse to an adjacent site regardless of its charge, provided it is not an out-of-plane site. Periodic boundary conditions are assumed on the (left and right) sides of the lattice (i.e. $A_{i,0} \equiv A_{i,L}$, $A_{i,L+1} \equiv A_{i,1}$ and same for **C**, **D**).

Migration of adsorbates is represented by $A_{i,j} \leftrightarrow A_{(i,j)+\mathbf{d}}$, where

$$\mathbf{d} \in \left\{ \begin{array}{l} \{(1,0)\},\ \text{if } i = 1,\ j \text{ is odd} \\ \{(0,1),(0,-1),(1,0),(-1,0)\},\ \text{if } 1 < i < 4 \text{ and } (i+j) \text{ is odd}, \\ \{(0,1),(0,-1),(1,0)\},\ \text{if } i = 2 \text{ and } j \text{ is even}, \\ \{(0,1),(0,-1),(-1,0)\},\ \text{if } i = 3 \text{ and } j \text{ is odd}, \\ \{(-1,0)\},\ \text{if } i = 4,\ j \text{ is even}. \end{array} \right\} \tag{6.2}$$

If $A_{(i,j)+\mathbf{d}}$ is empty ($A_{(i,j)+\mathbf{d}}(t) = 0$) and $A_{i,j}(t)$ contains a non-C adsorbate ($A_{i,j}(t) > 5$), then migration can occur, in which an exchange occurs between the species so that at time $t + dt$, when the migration has taken place, $A_{i,j}(t+dt) = 0$ and $A_{(i,j)+\mathbf{d}}(t+dt) = A_{i,j}(t)$.

Electrons and holes also migrate on the surface and can only be associated with a Ti or an O site respectively. They cannot migrate to adjacent sites as these are always of the opposite identity. Instead they migrate to diagonally adjacent neutral sites of matching identity. For example, in figure 6.2 the h^+ on site (3, 3) can migrate to sites (2, 2), (2, 4), (4, 4) or (4, 2), while the e^- on site (3, 4) can only migrate to site (2, 5), since its other diagonally adjacent Ti site is already charged.

Migration of charge is represented as $C_{i,j} \leftrightarrow C_{(i,j)+\mathbf{d}'}$, so that $C_{(i,j)+\mathbf{d}'}(t+dt) = C_{i,j}(t)$ and $C_{i,j}(t+dt) = C_{(i,j)+\mathbf{d}'}(t)$, where $C_{i,j}(t) \neq 0$, $C_{(i,j)+\mathbf{d}'}(t) = 0$ and

$$\mathbf{d}' \in \left\{ \begin{array}{l} \{(1,1),(1,-1),(-1,1),(-1,-1)\},\ \text{if } 1 < i < 4 \text{ and } C_{i,j}(t) = 1, \\ \{(1,1),(1,-1)\},\ \text{if } i = 1 \text{ or } (i = 2 \text{ and } C_{i,j}(t) = -1), \\ \{(-1,1),(-1,-1)\},\ \text{if } i = 4 \text{ or } (i = 3 \text{ and } C_{i,j}(t) = -1). \end{array} \right\}$$

The selected migration rate constants for adsorbates and charge are shown in table 6.1.

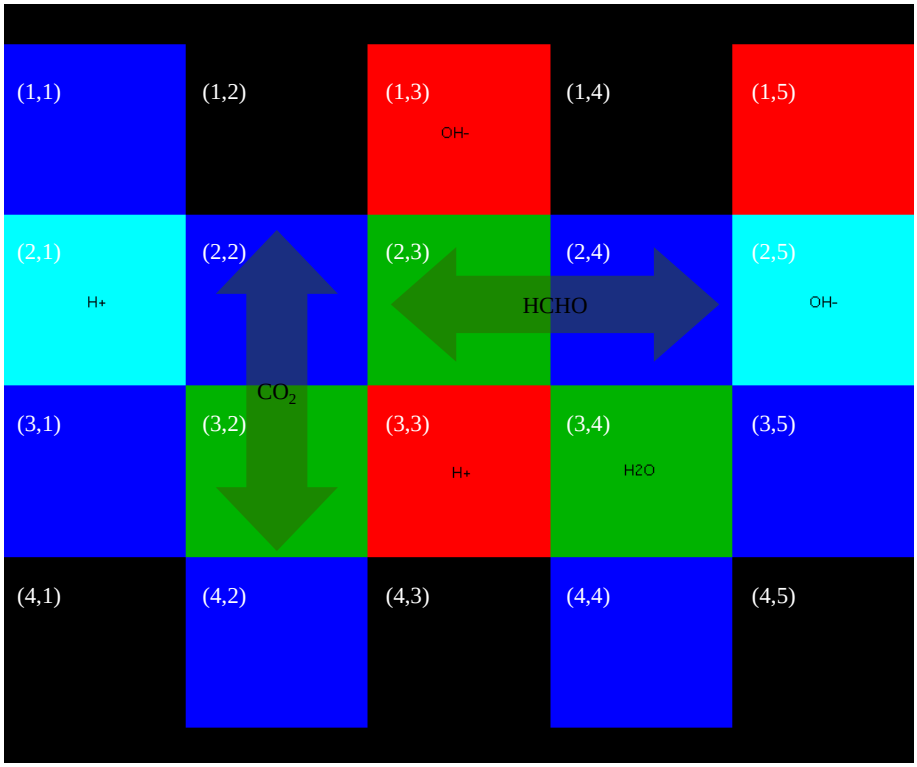

Figure 6.2: An example of a small lattice is shown where three reactions are possible, CO_2 reduction (5.59d), HCHO oxidation (5.59h) and water splitting (5.59w). The sites are coloured to indicate the type of site, green for e^-, red for h^+, cyan for N_e, blue for N_h and black for no site (out-of-plane site). The adsorbates are shown on the associated sites and in particular carbon-containing compounds, which take up two sites, are shown as arrows spread over the two sites.

6.1.3 Reactions simulated by the model

6.1.3.a Adsorption/Desorption

Adsorption changes E sites ($A_{i,j}(t) = 0$) to sites with adsorbate ($A_{i,j}(t + dt) > 0$) and desorption does the opposite, following the adsorption and desorption reactions of mechanism (5.59). In the case of CO_2 adsorption, a pair of adjacent empty sites, one of which must be negatively charged, are changed to CO_2 sites, and the relative positions of the sites are indicated in **D**. Similarly, **A** and **D** are changed back to empty sites during C-species desorption. The charge of the sites is not affected in any of the adsorption/desorption reactions.

6.1.3.b Redox reactions

The reactions modelled here are the same as those of (5.59). Each surface site can be occupied by only one molecule/ion of adsorbate and by only one e^-/h^+. However, an e^- or a h^+ can be present on the same site as an adsorbate. Because of this, for multielectron reactions and for reactions involving more than one molecule/ion, the reaction may occur when the necessary species are on the same and adjacent sites. In particular, a "core"

was selected for each reaction, which can consist of a molecule or a pair of ions. This includes one type of reactant in each reaction and is used as the centre of that reaction (it is assumed that all other reactants need to interact with it directly). The core species are the underlined reactants in chemical reactions (5.59). For the reaction to occur, all reactants need to be in the "neighbourhood" of the core. The "neighbourhood" of a site (i, j), $N_{i,j}$, is defined as the site itself and up to four nearest neighbours, that is, $N_{i,j} = \{(\ (i,j) + \mathbf{d})\}$ where

$$\mathbf{d} \in \left\{ \begin{array}{l} \{(0,0),(0,1),(0,-1),(1,0),(-1,0)\}, \text{ if } 1 < i < 4, \\ \{(0,0),(0,1),(0,-1),(-1,0)\}, \text{ if } i = 4, \\ \{(0,0),(0,1),(0,-1),(1,0)\}, \text{ if } i = 1. \end{array} \right\}$$

If the core consists of more than one site, which is true in all cases other than reaction (5.59w), then the neighbourhood of the core is the union of the neighbourhoods of each of its sites. For example in the case of a C-species the neighbourhood of the core (which is the C-species) is given by $N_{i,j} \cup N_{(i,j)+D_{i,j}}$.

An example lattice is shown in figure 6.2 where different reactions are possible, discussed in the following paragraphs. In this figure, green represents the e^- sites, red represents the h^+ sites, blue represents the N_h sites and cyan the N_e sites. Black is shown for out-of-plane sites. The adsorbates are also shown on the site(s) they are associated with.

The neighbourhood of the CO_2 represented by the vertical arrow (sites (2,2) and (3,2)) consists of sites (2, 1), (3, 1), (1, 2), (2, 2), (3, 2), (4, 2), (2, 3) and (3, 3). Note that this includes the core sites themselves and the adjacent out-of-plane sites. The core sites need to be included as the charge necessary for the reactions may be present on one of those. The out-of-plane sites will not affect the result as no charge or species is ever present on them (as far as the model is concerned). For efficiency, in the implementation of the model, a further condition excludes these sites from the neighbourhood. Additionally, the core sites are excluded during the search of the neighbourhood for other adsorbates and only sites of matching identity are searched for the necessary charge. This, however, does not affect the results of the model, only the implementation time.

In the example of figure 6.2, the CO_2 can be chemically reduced by reaction (5.59d), as all the reactants are present in its neighbourhood. The two e^- are on sites (3, 2) and (2, 3) and the two H^+ are on sites (2, 1) and (3, 3). Sites (2, 1) and (3, 3) will become empty (E) but will retain any charge they had as this was not used in the reaction. The e^- sites will be converted to N_e sites, but retain any adsorbates.

Similarly, the HCHO on sites (2, 3) and (2, 4) can be oxidised using the h^+ on sites (1, 3) and (3, 3) and the OH^- on sites (1, 3) and (2, 5) by reaction (5.59h). The organic compound produced (HCOOH) will remain on the same sites as the HCHO, the h^+ will again be consumed but in this case a H_2O molecule is also produced. This will be deposited on to one of the sites (randomly selected out of the two) which previously had OH^-.

The third reaction which is possible on this lattice is water splitting (5.59w) on site (3, 4). For this reaction, the empty site needed can be

found on (4, 4) or (3, 5), the e^- on site (3, 4) and the h^+ on (3, 3). The OH^- will be produced on the H_2O site (3, 4) and the H^+ will be made on the selected empty site. The charges will be neutralised.

It is worth noting that the third reaction is counted by the simulation as two different "possible reactions" that can be performed on this lattice, one for each of the empty sites. The number of "possible reactions" is important for the algorithm, as shown in Section 6.1.4, and so this has to be considered when selecting and interpreting the parameters used for this simulation.

6.1.3.c Excitation/Recombination

For two adjacent sites, which are not out-of-plane, such that $C_{i,j}(t) = 0$ and $C_{(i,j)+\mathbf{d}}(t) = 0$, where $\mathbf{d}$ is defined by (6.2), an excitation can occur so that the Ti (N_e) will become an e^- ($C_{i,j} = -1$) and the O (N_h) will become a h^+ ($C_{(i,j)+\mathbf{d}} = +1$), i.e. the forward (5.59a) reaction. A recombination will cause the opposite change so that if $C_{i,j}(t) = 1$ and $C_{(i,j)+\mathbf{d}}(t) = -1$, after the recombination event the sites will be $C_{i,j}(t + dt) = 0$ and $C_{(i,j)+\mathbf{d}}(t + dt) = 0$, i.e. the backward (5.59a) reaction.

6.1.4 The simulation

The general form of the Gillespie algorithm, as given in Erban et al. (2007), consists of 4 steps.

1. Generate two random numbers r_1, r_2 from a (0, 1) uniform distribution.

2. For each reaction calculate its propensity, $\alpha_i(t)$, and then calculate

$$\alpha_0 = \sum_{i=1}^{q} \alpha_i(t).$$

3. Calculate

$$\tau = \frac{1}{\alpha_0} \ln \left[\frac{1}{r_1} \right].$$

   The time when the next chemical reaction takes place is $t + \tau$.

4. Determine which reaction occurs at time $t + \tau$ by finding j such that

$$r_2 \geq \frac{1}{\alpha_0} \sum_{i=1}^{j-1} \alpha_i$$

   and

$$r_2 < \frac{1}{\alpha_0} \sum_{i=1}^{j} \alpha_i.$$

   Simulate the j-th reaction. Continue with step 1 for time $t + \tau$.

Parameter	Value in ODE model	Value in Discrete model
$K_{eq} = \frac{k_{-0}}{k_0}$	0.81 (dimensionless)	-
k_0	10^5 s^{-1}	10^5 s^{-1}
k_{-0}	$8.1 \cdot 10^4$ s^{-1}	$8.1 \cdot 10^4$ s^{-1}
k_1, k_2, k_3, k_4	$2.25 \cdot 10^7$ s^{-1}	10^6 s^{-1}
k_{-1}, k_{-2}, k_{-3}, k_{-4}	$6 \cdot 10^7$ s^{-1}	10^6 s^{-1}
k_5	$1.33 \cdot 10^6$ s^{-1}	10^6 s^{-1}
k_6	$3 \cdot 10^6$ s^{-1}	10^6 s^{-1}
k_7	$8.67 \cdot 10^6$ s^{-1}	10^6 s^{-1}
k_{d1}, k_{d2}, k_{d3}, k_{d4}	100 s^{-1}	100 s^{-1}
k_{d6}, k_{d8}	10^4 s^{-1}	10^4 s^{-1}
k_{d7}, k_{d9}	10^5 s^{-1}	10^5 s^{-1}
k_{d10}	0.1 s^{-1}	0.1 s^{-1}
k_{a1}	$2.5 \cdot 10^3$ s^{-1}M^{-1}	$2.5 \cdot 10^3$ s^{-1}M^{-1}
k_{a2}, k_{a3}	$2.5 \cdot 10^4$ s^{-1}M^{-1}	$2.5 \cdot 10^4$ s^{-1}M^{-1}
k_{a4}	2.3 s^{-1}M^{-1}	2.3 s^{-1}M^{-1}
$k_m(\mathrm{e}^-)$	-	$3.33 \cdot 10^5$ s^{-1}
$k_m(\mathrm{h}^+)$	-	$2 \cdot 10^5$ s^{-1}
k_m(Ads)	-	$2 \cdot 10^5$ s^{-1}

Table 6.1: Parameter values used in the two models. K_{eq}–k_{a4} are from reaction mechanism (5.59), k_m parameters correspond to the migration rates of e^-, h^+ and non-C containing adsorbates accordingly.

In this case a reaction refers to all of the reactions of the ODE model described in Section 5.6 (reactions (5.59)), including excitation, recombination, adsorption, desorption and redox reactions, and also all possible migration events, which are treated in the same way as reactions. A propensity is calculated for each reaction using the list of all possible reactions,

$$\alpha_i(t) = k_i N_i, \tag{6.3}$$

where k_i is the rate constant of reaction i and N_i is the number of reactions of type i that can be performed on the lattice at time t. After every reaction, as well as the matrices, the list of all possible reactions is also updated so that the propensities (α_i) can be calculated easily. For efficiency, only changes that apply to the particular reaction are made rather than recalculating the entire list.

6.1.5 Parameter Values

The same or equivalent parameter values were used for the reaction rates in the ODE model of section 5.6 and the discrete model described here (table 6.1). As mentioned in section 5.6.5, the CO_2 adsorption/desorption equilibrium constant was found in the literature. For each of the rate constants involved in the reactions, values were chosen so as to avoid immediate blocking of all surface sites, an effect here called "lattice locking". This phenomenon is discussed later, in Section 6.2.1, with the investigation of the case where the lattice becomes completely covered in water molecules,

preventing C-compounds from being adsorbed. Depending on the parameters, there could instead be a case where the lattice becomes completely covered in carbon dioxide, preventing water from being adsorbed. Either of these cases make it impossible for any reaction to occur.

In the discrete model the rate constants are the propensity of a reaction being successful, given that all the necessary components are present in one of the correct arrangements. However, the necessary components can be present in a few different arrangements (as is clear from figure 6.2) and it is important to include this information in each rate constant in order to have equivalent values for the discrete and ODE models. The rates in the ODE model are proportional to the probability of a species occupying a specific site. In the translation of the rates from the ODE to the discrete model, where a compound can occupy one of a few sites with equivalent effect for the reaction, the number of different possible arrangements of reactants needs to be incorporated into the rate constant.

6.2 Results of discrete model simulation and comparison with ODE model

The results of almost 500 runs of the discrete model with varying sizes of lattice were averaged and are shown in figure 6.3. The results of the discrete simulations are plotted together with the solution of the ODE model (of Section 5.6) with equivalent parameters. For most compounds, the profiles predicted by the two models are similar. However, the adsorbed water surface concentration is much lower in the ODE model compared to the discrete model, due to indirect spatial effects, as discussed later, in Section 6.3.

As well as the coverages and concentrations of the species involved, the frequency of the reactions was assessed for both models. Table 6.2 shows the frequency of selected reactions for the two models. In the ODE model, the numbers of reductions and oxidations per site are much greater than in the discrete model. However, there is a smaller number of net reductions per site (57.96) relative to the discrete model (113.11). Furthermore, while the water desorption frequency is significantly higher in the discrete model, consistent with the higher water coverage, water splitting is more frequent in the ODE model. Finally, the difference in water adsorption frequency between the two models cannot account for the difference in the water coverages.

6.2.1 Lattice lock

It was observed that for small lattice sizes, after a certain time, the lattice will fill with water and lock up (no further reaction was then possible). In those cases, the lattice was either totally neutral (no charges present) or totally positively charged (h^+ on all O-sites, no e^-). The size of the lattice was plotted against the time at which the lock occurred and is shown in figure 6.4. The red points correspond to positively charged locked states while the blue points correspond to neutral locked states. This phenomenon was observed in lattice sizes of less than 42 sites ('x' in figure) It was

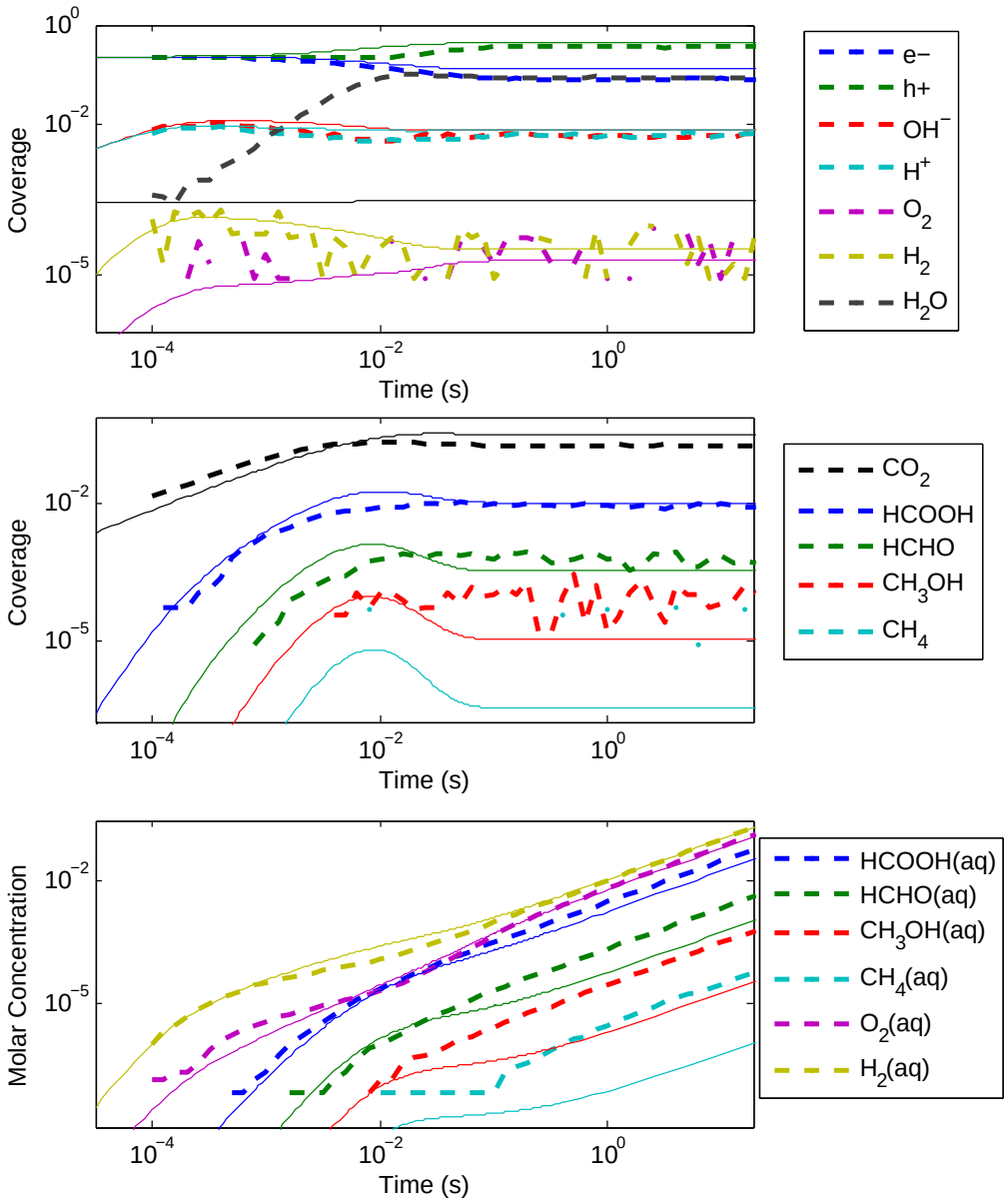

Figure 6.3: Log-log plot of surface coverage and molar product concentration predictions by the discrete model for different lattice sizes (dashed lines). The predictions of the ODE model of Section 5.6 are shown in thin solid lines, for comparison.

predicted that the 42-site lattice would lock at $\sim 10^4 s$ and a longer run of the simulation was performed which confirmed this ('+' in figure 6.4). The H_2O coverage of the simulations of the 42-site lattice are shown in figure 6.5 against time. The H_2O coverage does not rise gradually, but appears to jump to a full coverage between two measurements. This feature was not present in the ODE model, which represents averages over a large number of lattice sites but was also run for much longer times.

Reaction	ODE model	Discrete model
Carbon reduction	860.71	176.50 (4.30)
Carbon oxidation	802.75	63.39 (2.25)
Water splitting	9872.3	6549.9 (8.10)
Water desorption	0.0031	0.9143 (0.17)
Water adsorption	8264.9	6416.0 (9.16)

Table 6.2: Number of occurrences of a reaction per site in the two models. A mean of five simulations of the discrete model is shown with the equivalent standard deviation in brackets.

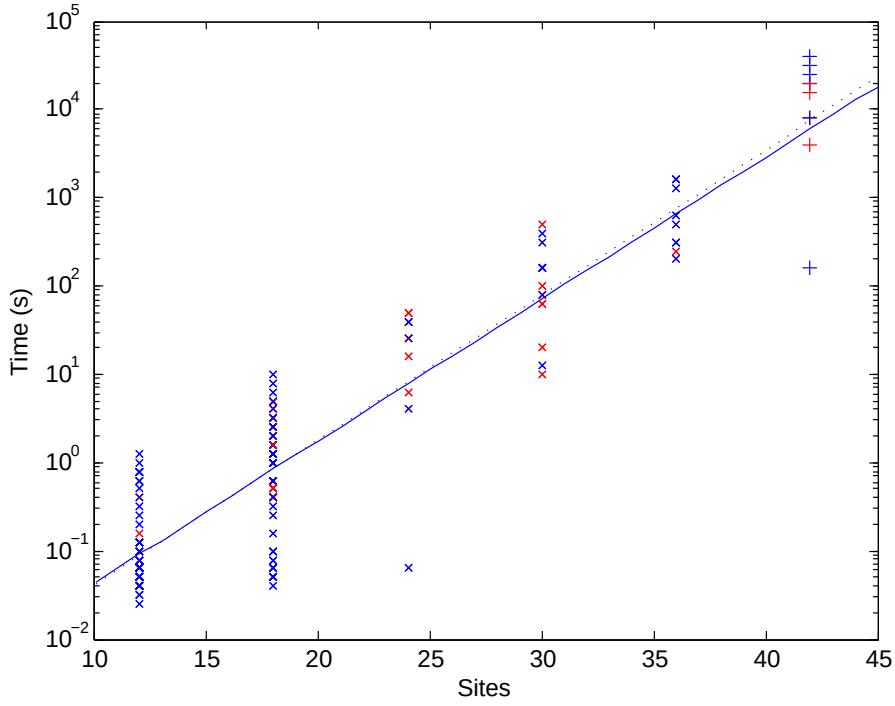

Figure 6.4: The size of the lattice plotted against the time at which it filled with water. The red points correspond to positively charged locked states while the blue correspond to neutral locked states. Linear regression was performed on the lattice sizes < 42 (solid line) and on all the points (dashed line).

6.3 Discussion

The current modelling approach, as well as that of Section 5.6, focused on the early time of the reaction where product concentrations increase approximately linearly. A higher water coverage of the surface is predicted by the discrete model relative to the ODE model. As can be seen from table 6.2, the number of water adsorptions is close to the number of water splitting reactions, with the latter being higher. The difference is due to water coming from the carbon oxidation and reduction reactions, while the water desorption is low, so it does not have a significant effect. The water being

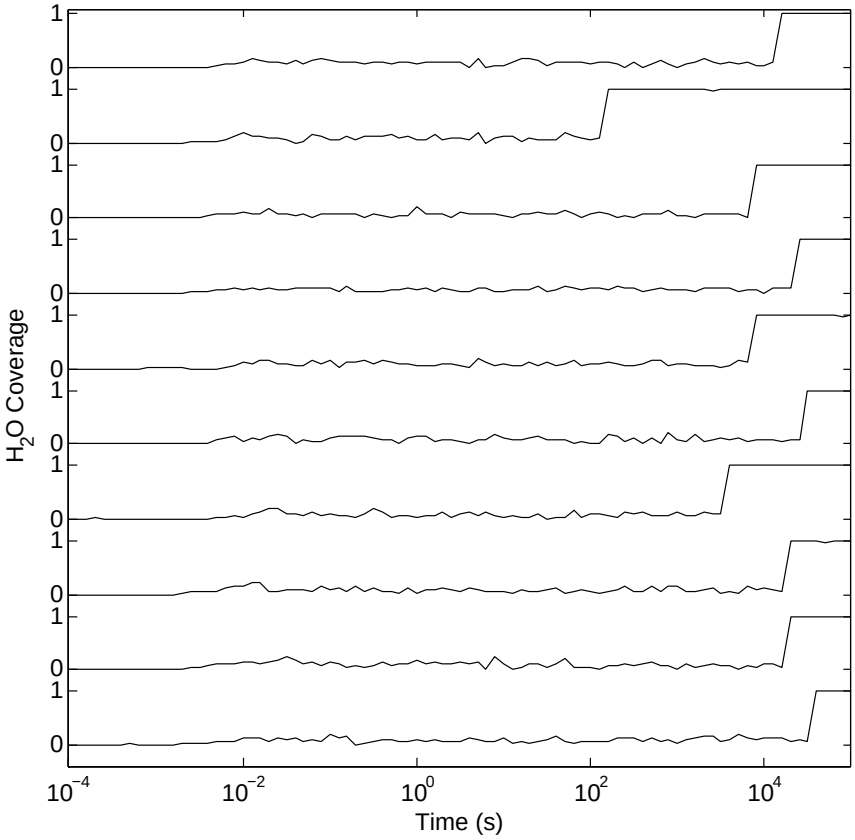

Figure 6.5: The time profile of H_2O coverage of a 42-site lattice. Different simulations are shown with a vertical distance of 1.4 to clearly distinguish each run and the vertical axis is labelled accordingly.

produced by oxidation and reduction of C-species in the discrete model has a lower probability of reacting due to local depletion of charge and crowding of neighbouring sites (by the C-species and other H_2O molecules produced from the reaction). Therefore the removal of water by water splitting is delayed, giving a higher surface concentration.

In the ODE model, the oxidation frequency is almost equal to that of reduction. However, in the discrete model, oxidation is only $\sim 1/3$ of the reduction frequency, explaining the higher concentration of organic products in this model. Again, this is likely to be due to spatial effects. Reduction is the only source of the species HCOOH, HCHO, CH_3OH and CH_4, which are necessary for oxidation reactions. In the ODE model, the production of reduced species immediately increases the rate of oxidation, whereas in the discrete model this is not the case. Following the reduction, the neighbourhood of the involved C-species contain empty sites or water where previously there were H^+ ions. Therefore, fewer sites are available for the presence of the OH^- ions necessary for oxidation, and so the probability is lower for an oxidation immediately following a reduction, giving time for the product to be desorbed. The structure of the lattice may further assist these spatial effects, by restricting the movement of the reactants, and

further delaying reactions. This may account for the much lower overall frequency of oxidations and reductions in the discrete model.

The total coverage of the lattice sites by water was observed after a long reaction time, which led to the lattice "locking" in an almost irreversible state. Only desorption and re-adsorption of water was observed once this state was reached. This configuration is not a steady state of the system and it will not be reached by the ODE model. Furthermore, if this state is used as initial conditions for the ODE model, the solution appears to move away from it towards the steady state, but does so only very slowly. For the discrete model this condition was reached due to stochastic, spatial and discrete effects, and once there, the probability of returning to the steady state was very low. This was supported by the fact that there was no gradual increase in the water coverage, but a sudden increase due to a stochastic fluctuation that crossed some threshold and became locked in this state. This observation could explain the decrease of the reaction rates observed experimentally with time, see figures 4.8 and 4.10 in this thesis and the results of Liu (2012), which was also discussed in Section 5.5.4. The sudden locking of particles at different times would appear as a gradual decrease of the production rate in experiments, due to the averaging over many particles, and would lead to the eventual stalling of the reaction.

The early time model predictions cannot be compared to experimental results because the product concentrations at this early time are below the detection limit of the equipment used. However, the projected concentration assuming a continued linear increase can be compared to the concentrations from the results of Chapter 4. These are found to be four orders of magnitude higher than the experimental values but also, at time 1 s, the value is already one order of magnitude higher than the final, experimentally measured methane concentration. This overestimation is due to the parameter values used in the early time models (Section 5.6 and Chapter 6) which correspond to high light and low recombination rates assumed by the model to speed up the stochastic simulation. Parameter fitting could give a more accurate model but more data is required for this to be possible.

LHCII was not included in this simulation. Further work on the model could investigate the effect of localised energy/electron injection from LHCII, leading to localised excitation events or excess negative charge on the surface respectively. This could be used to simulate the different possible mechanisms of the functional relationship between LHCII and catalyst, discussed later in Section 7.3, and help to distinguish between them.

Chapter 7

Discussion

The ideal catalyst system for CO_2 photoreduction should be highly selective for CO_2 as a substrate to use CO_2 from the atmosphere. It should also selectively produce an organic compound that can be used as a fuel and as a feedstock for industry, and the CO_2 conversion rate and light-to-chemical energy conversion efficiency must be high. The system would need to absorb visible light over the full range of the solar spectrum and be efficient at variable light intensities. Light absorption should be followed by rapid separation of the electron and the hole to avoid recombination. The material used would need to be cheap and abundant to allow for extensive use. It must also be stable in response to the different light conditions. Furthermore, photoreduction should be possible without a sacrificial electron donor (i.e. hole scavenger) with only water and CO_2 used to produce oxygen and the organic compound. Finally, re-oxidation of products must be avoided, perhaps by separation and rapid removal of the organic compounds from the CO_2.

7.1 Comparing a theoretically optimal system with the natural photosynthetic machinery

Such an ideal system is still very far from the artificial photocatalysts available today, but, in nature, a system has evolved and is used by plants to perform photosynthesis that is in many ways close to this optimal system. Plants capture CO_2 from the atmosphere using the enzyme Rubisco. Though this enzyme also captures O_2, considering that the concentrations of O_2 and CO_2 in the atmosphere are 20% and 0.04% respectively, its specificity would be the envy of artificial catalysts. The product of natural photosynthesis is glucose, which is not a high energy compound compared to conventional fuels. However, the need of plants for a "fuel" is not as important as that for a building block for other organics (feedstock in industrial terms), which glucose serves in plants.

The theoretical maximum energy to biomass conversion efficiency of C3 plants (those that perform photorespiration) is 4.6% while that of C4 plants (which inhibit photorespiration by biochemically concentrating CO_2 before the Rubisco reaction (Horton & Murchie 2000)) is 6% (Zhu et al.

2008). In fact, $\sim 50\%$ of the efficiency is lost because of solar radiation that is outside the photosynthetically active range (mostly infrared light). Even within the photosynthetically active range, plant photosynthesis primarily uses red and blue light, and the blue photons are converted to red before utilisation with the excess energy dissipated as heat. Green light, which is at the peak of solar radiation, is not used.

On the other hand, plants are especially good at adapting to rapidly changing light conditions by strongly regulating their photosynthetic machinery. One tightly organised cascade of chromophores leads to very efficient light harvesting and another, one of electron acceptors, leads to rapid separation of the electron and the hole. Furthermore, photosynthesis evolved having access only to materials abundant on the Earth's surface, and therefore only these are used in the photosynthetic machinery. Additionally, water is the electron donor in natural photosynthesis, so that H_2O and CO_2 are combined to produce O_2 and sugars. Due to all of these features, the natural photosynthesis system has been studied as a model for water splitting and CO_2 photoreduction and a lot of work is currently focused on biomimetic artificial systems (Nocera 2012, Limburg et al. 2001, Jiang et al. 2013) and hybrid systems directly incorporating parts of the photosynthetic machinery or other enzymes into the artificial system (Woolerton et al. 2010, Wenk et al. 2002, Kato et al. 2013, Das et al. 2004).

Finally, carbohydrates are exported from chloroplasts as GAP (in exchange for phosphate influx), or react to form starch inside the chloroplast, during the day, and are exported as glucose or maltose during the night (Schleucher et al. 1998). This is similar to the suggested mechanism to avoid re-oxidation of products in the ideal artificial system. However, in the case of natural photosynthesis, the high regulation of metabolic processes is likely to be the true reason for its prevention.

7.2 Comparing existing artificial systems with the theoretically optimal system

7.2.1 Substrate and product selectivity

Currently, even the best artificial catalysts work only under concentrated pure CO_2 atmospheres, to make use of a high chemical potential of CO_2. Therefore, it is recommended to initially use gas from power plants' emissions for the conversion of CO_2 back into fuel, which will allow for the recycling of CO_2 at the power plants. This would allow the storage of solar energy in organic fuels and the prevention of CO_2 emissions. A challenge of using power plant emissions is that they contain impurities such as SO_x, a known issue for CCS which may impair stability of transport and storage of CO_2 streams (IEAGHG 2011/04, June, 2011), and which have been shown to poison TiO_2 (Shang et al. (2002) showed this effect for SO_3). High purity CO_2 streams would be necessary, adding to the cost of the CO_2 recycling. Alternatively, a catalyst that is more resilient to impurities could be selected for this process. However, immediate photoreduction of the emissions from power plants would increase the energy yield of the power

plants and could be used in an intermediate stage, prior to atmospheric CO_2 photoreduction. Research into these systems could then assist in the scaling up of the process through interaction with industry.

As discussed in the introduction, a large market for fuel is the transport sector. Capture of CO_2 from fuel used for transport is unlikely to be a viable option and the use of H_2 as a fuel is likely to become the preferred option. However, until H_2 can be safely stored and used efficiently for transport, fuel from CO_2 recycling may help bridge the gap between the increasing energy demands and decreasing reserves of fossil fuels. Instead of avoiding emissions, use of fuel, produced from CO_2 recycling at power plants, would lead to delayed emissions and it could almost double the energy produced per CO_2 molecule released into the atmosphere, depending on the energy value of the CO_2 photoreduction product. When technology has moved from capture at power plants, to capture from the atmosphere, CO_2 photoreduction (even with transport CO_2 emissions) will truly recycle CO_2, similarly to the natural carbon cycle. Furthermore, LHCII has been shown to help both CO_2 photoreduction and water splitting so it could be used for H_2 production if this becomes the preferred fuel.

An organic compound that can be used as a fuel must have a high energy density (energy per unit volume) and high specific energy (energy per unit mass), be easy to store and relatively safe to handle. Methane (CH_4) is commonly used as a household fuel for cooking and heating (it is the main constituent of natural gas). It has a higher specific energy but a lower energy density than methanol. Methanol is also more useful for industrial purposes. Ethanol has an even higher energy density than methanol and is already commonly used together with gasoline or alone as a fuel for transport in Brazil (Goldemberg 2006). Butanol is better still as a fuel but photocatalysis to larger compounds (more than two carbons) is likely to be difficult. Ethanol has been reported as a CO_2 photoreduction product (Rajalakshmi et al. 2012) and, in the current work, acetaldehyde production was reported. Organic compounds with three carbon atoms have also been reported (Subrahmanyam et al. 1999) but no report of larger CO_2 photoreduction products was found in the literature. Methane was also detected in this work in the gas phase, and together with methanol, which has been reported in the literature as a product (Wu & Lin 2005), they are believed to be the source of the methyl-formate detected in the liquid phase of the reactor here. A single compound (or an appropriate mix that can be used together) would be the preferable product of CO_2 photoreduction. Alternatively, an inexpensive purification method could allow the use of a catalyst that is less selective.

7.2.2 Production rates and efficiency of different artificial systems

The efficiencies of dye-sensitised CO_2 photoreduction systems were discussed in Section 1.5. Furthermore, the comparison between the deterministic, spatially homogeneous ODE model of Section 5.6 and the stochastic, spatially discrete model of Chapter 6 outlined the importance of spatial effects for the production rates. Different surface structures may result in

different photoactivities simply due to the restrictions placed on the reactants due to the site positions, even without considering their reactivity using complex computational chemistry. Therefore, the selection of the catalyst crystal face is of key importance.

Very efficient and selective catalysts for CO_2 photoreduction to CO have been discovered using Ru and Re, two of the rarest elements in the Earth's crust. A recent report by Tamaki et al. (2012) found a Ru-Re supramolecular complex with a high turnover number ($TN_{CO} = 207$) and frequency ($TF_{CO} = 281\ h^{-1}$). A sacrificial electron donor (1-benzyl-1,4-dihydronicotinamide) was used to reduce the excited Ru photosensitiser which then passed on the electron to the Re catalyst. Visible CO bubble formation was shown at high light intensity ($>$ 420 nm light from 500 W high pressure mercury lamp). H_2 production is also reported for this system, at a much lower rate. The CO concentration increases rapidly at first and then levels off after $\sim$ 10 h.

A different approach with a hybrid system was reported by Amao et al. (2012) who used the enzyme formate dehydrogenase (FDH), with a chlorin-e_6 photosensitiser, a viologen electron carrier and NADPH as a sacrificial electron donor, to convert CO_2 to HCOOH under visible light (100 mW cm^{-2}). Approximately 20 mmol HCOOH were produced after 3 h of irradiation and the increase of the HCOOH concentration was linear for the first 2 h and slightly slower for the third.

These production rates are very high compared to studies from a few years earlier. However, they rely on sacrificial electron donors for regeneration and not water splitting. This issue is discussed further in Section 7.2.7.

7.2.3 Optimal use of visible light

Intuitively, the rate of the reaction should increase with light intensity, but it is interesting that the steady state concentration is also affected, as seen in the predictions of the models of sections 5.4 and 5.5. The product concentrations reported in Section 4.2.1 are believed to be steady state values of the model according to experiments carried out in UV light (Liu 2012), though this may not be the case due to the fact that visible light is used in the work reported here. Higher light absorption is expected in the case of the hybrid catalyst, and higher methane concentration is observed at the steady state, which agrees with the predicted results. Furthermore, low sensitivity to light is predicted for HCOOH concentration (and for [CO], as they are equivalent in terms of the modelling because they are both created from a two electron - two proton reduction reaction from CO_2), in agreement with the experimental work of Section 4.2.2 where the CO concentration is the same between control and hybrid catalyst.

The absorption spectra of the hybrid catalyst prepared in this work show small LHCII-specific peaks, suggesting that only a small amount of LHCII covers the surface. This is because only a small amount of LHCII is added to the preparation mixture, and not due to the adsorption technique which is $\sim$ 95% effective. This is confirmed by TGA which showed that the weight of LHCII is only $0.9wt\%$ of the weight of TiO_2:Rh-LHCII.

However, a large increase in visible light production of reduced C-species and H_2 was shown, in response to even this small addition of LHCII to the TiO_2:Rh catalyst surface. A higher concentration of LHCII could lead to a further increase in photocatalytic activity, but it is necessary to have a balance between the blocking of active sites and increasing light absorption as suggested by the UV light experiments.

To maximise the efficiency of light harvesting, more dyes could be combined to cover the entire visible light spectrum. Various chromophores were combined for this purpose by Terazono et al. (2009). However, due to the preparation procedure of the system, excess electron acceptor was present in the solution together with the synthetic complex, which led to energy dissipation as heat. It was concluded that "very strong, specific binding" is necessary for such a system. The LHCII, which has specific binding sites for its chromophores and interacts with PSII in a highly regulated way, is a good example of such a system.

7.2.4 Charge separation

A common problem that limits photocatalysis efficiency is charge recombination. Following the electron and hole separation caused by the absorption of a photon, the two will rapidly recombine leading to the loss of the absorbed energy as heat. Delaying the recombination increases the probability of a reaction occurring as it increases the time available for the e^- and h^+ to react. A long-lived charge-separated state in a supramolecular system was recently reported in D'Souza et al. (2011) using an antenna-reaction centre mimic leading to the positive charge on a zinc porphyrin and the negative charge on a fullerene with a boron dipyrrin antenna between them. A further difficulty is the separation of multiple electrons to produce a multiply charged donor and acceptor pair. This is necessary for the multi-electron reactions of water splitting and CO_2 photoreduction. Karlsson et al. (2012) recently reported a two-electron charge-separated state forming by subsequent photon absorption without the use of sacrificial electron donors/acceptors, in a molecular system coupled to TiO_2. A short time is necessary between the two photons for this state to occur. LHCII could assist such a system by providing the concentrated excitation energy.

A buried junction photoelectrochemical cell has been developed using cheap and abundant materials (Reece et al. 2011, Cox et al. 2013), in which a semiconductor is used for light absorption and the charge is separated to the anode (for O_2 production) and the cathode (for H_2 production). This allows separate optimisation of the components for light absorption, charge transfer and the two catalysts for the oxygen and hydrogen reactions. An alternative to charge separation is the suppression of recombination, which was shown for hematite electrodes by Peter et al. (2012) following treatment with cobalt nitrate solution. In the TiO_2:Rh-LHCII system described here, depending on the mechanism by which LHCII assists photocatalysis (discussed later in Section 7.3), charge separation could be assisted by transfer of e^- to the catalyst while the h^+ remain on the LHCII.

7.2.5 Cheap and abundant materials

Materials that are often used for photocatalysis, such as ruthenium, rhodium and platinum among others, are known as precious metals due to their rarity and high price. Both of these properties make these materials bad candidates for a commercial device. LHCII is made from abundant materials and in fact is the most common membrane protein complex on earth (Wientjes et al. 2013). On the other hand, the TiO_2:Rh catalyst used here contains small amounts of Rh, one of the rarest and most expensive of precious metals. An alternative catalyst could be used in conjunction with LHCII as an antenna, such as the TiO_2:Cu prepared in this work (but not tested for photoactivity), and it is predicted that the effect would be similar.

7.2.6 Stability of artificial systems

For a sustainable method of artificial photosynthesis, stability of the photocatalytic material is a central issue. Lack of stability, and therefore a low turnover number (moles converted by a mole of catalyst before it becomes inactive), would mean that new material would constantly have to be prepared, adding to the cost of the process both in terms of financial cost and environmental cost. Highly reactive conditions are present in the reactor during water splitting. Hydroxyl radicals are known to be formed during TiO_2 illumination (Peral & Ollis 1992) which are useful in applications of water treatment to degrade organic and inorganic pollutants (Carp et al. 2004). Unfortunately, these could also cause damage to the photocatalytic system.

Before photocatalysis, the LHCII is intact on the catalyst surface in the hybrid system presented in this work, demonstrated by the fact that the chlorophylls inside the LHCII are coupled, as can be seen from figure 3.7b where excitation of chlorophyll *b* leads to chlorophyll *a* fluorescence. A year-old sample was also analysed by absorption and fluorescence spectroscopy. Its LHCII-specific absorption is decreased only a little and fluorescence at 680 nm is still high. However, increased chlorophyll *b* fluorescence suggests that the chlorophylls are no longer fully coupled and so the integrity of the LHCII is not confirmed. Additionally, following the photoreduction of CO_2 with TiO_2:Rh-LHCII, the LHCII signal is lost from both the absorption and fluorescence spectra (figure 3.17) and is decreased in TGA, as shown in figure 3.18. These results show that LHCII is not stable on the catalyst during photoreduction conditions. The methods of stabilising the LHCII on the catalyst which were tested in this work, were not sufficient to protect the material from photodamage. In other work, silica encapsulation has been shown to increase the stability of proteins (Ellerby et al. 1992) and to allow enzyme activity in that state (Liu & Chen 1999).

Cardoso et al. (2011) report on the use of LHCII in a synthetic self-assembled membrane which, in conjunction with Pt nanoparticles (catalyst) and NADPH (electron donor), can produce H_2 in response to light irradiation. This system was tested with light-dark cycles (2 h light and 2 h dark) and it continues to produce H_2 during irradiation after 100 h of

cycles. The stability of LHCII was also assessed using circular dichroism and was shown to be stable after 48 h in the polymer (not in reaction conditions).

Another hybrid system in the literature used phycocyanin, the cyanobacterial light-harvesting complex equivalent, on hematite (Fe_2O_3), and showed a two-fold increase in photocurrent (Bora et al. 2012), similar to the two-fold increase seen in the current work for methane production. This system was stable after 1 h of light irradiation, showing no decrease in the photocurrent produced. Water oxidation is believed to be the source of the electrons in this system, as opposed to oxidation of the phycocyanin, and this is supported by the stability of the materials.

In the plant, reactive oxygen species are formed which damage PSII. Rather than using stable components in the photosynthetic machinery, a different approach is followed by plants. PSII is repaired by disassembly and the replacement of the D1 subunit, which is the primary target of photodamage (Komenda et al. 2012). Kanan & Nocera (2008) developed a self-assembled system for water splitting with Co and phosphate that is a structural analogue of the PSII-OEC (Nocera 2012). This was shown to produce O_2 with high efficiency. This system can undergo repair (self-healing) in response to an applied potential of 1.3 V (Lutterman et al. 2009). This means that, for this system, stability is not a relevant issue and instead cycles of catalysis and repair are performed.

7.2.7 Sustainable photocatalysis without a sacrificial electron donor

Water splitting and CO_2 photoreduction have as a purpose the production of fuel. If a photocatalytic system relies on consumption of a fuel for the scavenging of holes, the net fuel production will be zero. Therefore, water splitting needs to be the only electron donor. However, as shown in the modelling work of sections 5.3–5.4, the quality of the hole scavenger has a strong effect on the steady state concentration of products so these are often used in the literature. Sacrificial electron donors could be helpful for research into effective CO_2 catalysts that can then be used in systems where a water splitting catalyst replaces the sacrificial donor.

In the work described here, high purity water was used for CO_2 photoreduction without the addition of a sacrificial electron donor. Esswein et al. (2011) have reported the use of natural water from a river and from the sea with the cobalt catalyst mentioned above (Kanan & Nocera 2008) and a nickel catalyst (Dincă et al. 2010) for water splitting. They compared the action of the two catalysts in these two waters to that in purified water and found that the Co catalyst can function in natural waters as well as pure water, while the Ni catalyst is degraded in natural waters.

7.2.8 Product re-oxidation and the steady state

It has been shown experimentally in many studies, including this one, that the product concentration initially increases and then reaches a plateau, which is believed to be a steady state between CO_2 reduction and product re-oxidation (Tseng et al. 2002). This steady state was calculated,

using this assumption, in terms of parameter values by different models in Chapter 5, first focusing only on the surface charge and then also including the effects of protons and hydroxides. The steady state was found to be stable for all parameter values in Section 5.2 and stable for the selected parameters in Section 5.3.1.

On the other hand, the early-time model did not allow for readsorption of organic products, assuming that their low concentration early in the reaction made the process negligible. Therefore, no steady state is predicted for this model. However, in the discrete-space, stochastic simulation, a state is reached, that, though not theoretically a steady state, gives a very low probability of escape due to the surface competition between water oxidation and CO_2 reduction. This may be an alternative explanation to the observed photoreduction stalling. Changing the hydrophilicity of the TiO_2 surface could decrease H_2O adsorption and therefore help CO_2 adsorption and through it, reaction. Alternatively, a gas phase reactor can be used, such as the optical fibre reactor described in (Wu & Lin 2005), where the partial pressure of moisture can be adjusted to give an optimum CO_2 to H_2O ratio.

7.3 LHCII-catalyst functional relationship

From the enhanced photoreduction of TiO_2:Rh-LHCII in visible light, it is evident that there is a functional relationship between the catalyst and the LHCII adsorbed on its surface. Both parts are needed because LHCII cannot function as a catalyst without TiO_2 to photoreduce CO_2, as shown by the results of Control 2, table 4.1. This functional relationship raised the question of how LHCII functions as a light antenna to assist photocatalysis in the artificial system, namely whether energy transfer or charge transfer occurs. There have been accounts of charge transfer through the pigment matrix in dried chloroplasts, as mentioned by Lawlor (2001). In fact, it was initially thought that the chloroplast may function as a semiconductor (Arnold & Sherwood 1957) but this idea was later abandoned. This could support the charge transfer hypothesis, especially since the preparation of TiO_2:Rh-LHCII involves a drying step. Furthermore, the fluorescence spectrum of LHCII (figure 3.7) includes a peak that may be evidence of charge transfer. On the other hand, it has been shown, using reaction-centreless mutants, that in vivo charge separation occurs in the reaction centres and not in the LHCII (Bogomolni & Klein 1975), supporting the energy transfer hypothesis. However, it is unknown how the interaction with the catalyst surface affects the properties of LHCII and this could potentially make charge separation possible.

Regarding the energy transfer hypothesis, fluorescence resonance energy transfer (FRET) works by radiationless excitation transfer between chromophores with overlapping absorption and emission bands. This has been shown between LHCII and type II core-shell CdTe/CdSe/ZnS quantum dots (QD) (Werwie et al. 2012) where it was confirmed that the LHCII passed light energy to the QD via FRET. For the same process to be occurring in the hybrid catalyst (energy transfer from LHCII to the TiO_2), the absorption spectrum of TiO_2 would have to overlap with the fluorescence

spectrum of LHCII, which is not the case (figures 3.4 and 3.7).

The simultaneous absorption by one molecule of two-photons can lead to excitation using their combined energy (So et al. 2000), so that, during fluorescence, a photon of energy higher than each of the exciting photons will be formed. This property is used in two-photon fluorescence microscopy, where enhanced green fluorescent proteins are detected, allowing the visualisation of single molecules in live cells with increased sensitivity and signal to noise ratio (Hou & Cheng 2012). It has also been used to convert infra-red light to blue and UV light with the purpose of exciting materials with a large band-gap using solar radiation (Méndez-Ramos et al. 2013).

The combination of two photons to make one higher energy photon has also been shown to occur for certain organic chromophores via triplet-triplet annihilation (TTA), the combination of two triplet states to produce one higher energy singlet state, resulting in UV emission from visible light excitation (Singh-Rachford & Castellano 2009). TTA upconversion has also been used experimentally to enhance solar energy storage (Borjesson et al. 2013) and to produce photocurrent in a photoelectrochemical cell (Khnayzer et al. 2012).

Upconversion to UV light by either of these methods could create an overlap between the absorption and emission spectra of the catalyst and LHCII respectively, and may allow energy transfer by FRET from the LHCII to the catalyst. Additionally, resonance transfer only works at distances of 1–10 nm. Further work is needed to confirm if this is possible in the system described here, by spectroscopy, to test the upconversion hypothesis, and by imaging of the LHCII on the catalyst, to visualise their relative positions.

In the work on LHCII in synthetic membrane structures (Cardoso et al. 2011), discussed in Section 7.2.6, the mechanism is reported as charge transfer. However, this is not shown directly, but is given as an explanation to the photoinduced H_2 production of the LHCII- Pt system. This hypothesis is supported in the paper, by the fact that one of the chlorophyll *a* pairs in the LHCII, Chl 611–612, has a similar arrangement as the reaction centre pair, and this LHCII pair is suggested as the site of the charge separation event in their system. This explanation could also be valid for the system in the current thesis.

In the case of charge transfer, the electrons that are removed from the LHCII have to be replenished by an electron donor (or hole scavenger as it was called in Chapter 5). Otherwise the LHCII becomes a sacrificial electron donor and the system is not sustainable. In the case of energy transfer, the LHCII is not used up by the reaction in the absence of an electron donor, but one is still necessary, because, following charge separation using energy from the LHCII, holes will accumulate on the catalyst if a hole scavenger is not present. Hydrogen production was demonstrated in this work (Section 4.2.3), suggesting that water splitting is occurring simultaneously with CO_2 reduction. Therefore, the production of oxygen will use the excess holes if these are on the catalyst surface or it may regenerate the LHCII, depending on the mechanism of the functional relationship. A difference between the system in (Cardoso et al. 2011) and that presented

here is the presence of a sacrificial electron donor in the synthetic membrane system, which would make the regeneration of LHCII possible without the need for water splitting, and explain the continued H_2 production that they report.

Whether by energy or charge transfer, the light being absorbed and used by the hybrid catalyst is believed to be the blue light at the 435 nm absorption peak. This is because of the lower signal at that wavelength in the excitation spectra of hybrid catalysts which does not match the absorption spectra (figure 3.13). This may suggest that light at that wavelength is photochemically quenched. The photoactivity of light of different colour regions could be measured (using filters) to test this hypothesis.

It would be interesting to see how visible light catalysts interact with the antenna. In those cases, an overlap between the bands is expected to occur and therefore upconversion of photons would not be needed for energy transfer by FRET. However, if significant visible light is absorbed without the LHCII, an effect similar to the UV light experiment could be observed with the LHCII hindering photoreduction. If that is the case, it would suggest that the light absorption and energy/charge transfer mechanism by LHCII is not as effective as direct excitation.

Experiments with visible light catalysts would most likely not give conclusive evidence to support either the energy or the charge transfer hypothesis. Lower photoactivity of the catalyst containing LHCII would give support to the energy transfer mechanism as charge transfer also results in charge separation which is expected to assist photoreduction further (delay recombination). On the other hand, if the photoactivity is higher for the hybrid catalyst, it could also support the energy transfer mechanism with increased FRET giving increased photoactivity, or it could be due solely to the catalyst itself having increased photoactivity in the visible region. Highly accurate measurements could help distinguish between these two cases. If the increase in visible light catalyst - LHCII systems is more than in TiO_2:Rh-LHCII, then the increase is unlikely to be due to charge transfer, which should not be affected by the absorption spectrum of the catalyst. Furthermore, differential catalyst absorption in the red and blue regions could give further insights into the mechanism of the functional relationship.

7.4 Comparing natural and artificial photosynthesis and their mathematical models

There are many natural photosynthesis models which focus on different processes of photosynthesis. This is clear from the different chapters in Laisk et al. (2009), such as van Grondelle et al. (2009), who model LHCII and the photosystems, Rubin & Riznichenko (2009), who focus on the ETC, von Caemmerer et al. (2009), who model the integrated "light"-"dark" reactions, and many more, even moving from leaves to whole canopies and the globe. In the last few years, there has been an effort to make a complete model of photosynthesis by bringing together the many models that exist

in the literature for each part (Šafránek et al. 2011). There are difficulties with this endeavour, due to timescale differences between the various processes that happen in photosynthesis, but it is important to connect these despite their different timescales because there are interactions between them, especially through the regulation of each.

As with natural photosynthesis, there are models of artificial photosynthesis which also focus on different parts of the process. Quantum chemical modelling is used by Indrakanti et al. (2008) to model CO_2 adsorption on different anatase crystal faces, while there is well established theory on excitation of semiconductor surfaces by light, and the recombination of the e^--h^+ pairs (Panda 2009). The e^- transport in TiO_2 is modelled by a random walk by Nelson (1999). This model may be useful to incorporate into the discrete model presented in this work to give more realistic e^- behaviour. The adsorption and redox reactions on the surface of TiO_2 are modelled by Tan et al. (2008) starting with the Langmuir-Hinshelwood mechanism and making simplifying assumptions to lead to a single equation for the kinetics of the production with three parameters that can be fitted to the model. Re-oxidation of the products is included in this model, as it was in the early, mass action models presented in the current work (sections 5.2–5.4). Another model which uses the Langmuir-Hinshelwood mechanism is presented by Wu et al. (2005) but, in this model, re-oxidation of products is assumed to be negligible, as in the models presented in Section 5.6 and Chapter 6. This model assumes that methanol production is rate-limiting and consists of one simple equation, relating methanol, water and CO_2 partial pressures and light intensity, with three parameters.

The greatest difference between the natural and artificial systems is that regulation is a key aspect of the natural system while that is not the case for artificial photosynthesis. That is seen in many of the natural photosynthesis models, such as Zhu et al. (2013) where regulatory steps are included explicitly and von Caemmerer (2013) where the conclusions from the model consider the regulatory steps that were not included. On the other hand, in artificial photosynthesis, there is not such a high level of control, even in complex molecular systems. An interesting question is whether regulation will be a necessary aspect also for artificial photosynthesis to maximise efficiency at different environments and protect the photosynthetic machinery. With stable or self-healing systems that can work in high light, this may not be a problem in terms of damage to the photocatalyst. However, for a system that can work well under different conditions, a mechanism to switch between them, such as dye-sensitization for low light and direct excitation for high light, may be preferable. Alternatively, different materials may work best under different climates, or even seasons within the year, depending on sunlight intensity.

7.5 Solar fuel and biofuel

Most renewable sources produce electricity, which, like solar energy from photovoltaics, will have to be stored in order to provide a secure energy future. The exception is biofuel. Land competition is often discussed in terms of biofuels due to an increasing population requiring an increase in food

supply. From projections for 2050, Doornbosch & Steenblik (2007) found that this is not a problem for all continents. This study assumed a 1.1% yearly increase in agricultural food productivity (research into increasing crop production and optimisation targets are discussed in (Murchie et al. 2009, Murchie & Niyogi 2011)). Doornbosch & Steenblik (2007) predict that Europe, U.S. and Asia will not have spare land once the available land needed for food is considered. On the other hand, South America and Africa will have surplus cultivable land that can be used for biofuel, even after the increased population is fed. This suggests that, in certain areas, biofuel might be a viable energy source. In fact, these regions are expected to show a high increase in energy needs in the following decades. However, this solution is not enough to cover the worlds energy needs and local solutions may be preferable, as discussed also in terms of different solar devices in the previous section.

An alternative to biofuels, is solar fuels, in particular hydrogen from water splitting, and small organics or CO from CO_2 photoreduction. A different route for solar fuel production is the electrochemical CO_2 conversion. This is an indirect method, which could use electricity from other renewable sources to convert CO_2 to energy-rich compounds. There are many challenges with this method, as well as direct CO_2 photoreduction, related to efficiency due to the difficulty in the reduction of CO_2, stability of catalysts and the selective production of a single compound. Chen et al. (2012) recently reported on a selective CO_2 to CO electrocatalyst that was stable for 8 h.

7.6 Conclusions

From the experimental work in this thesis, it was shown that LHCII adsorbs onto the surface of the catalyst and increases its visible light absorption. It is concluded that LHCII can enhance CO_2 photoreduction with TiO_2:Rh catalyst, if issues with LHCII stability and maximising light absorption without interfering with catalysis are dealt with. It can possibly also be used with other catalysts to find an optimum combination of materials for photoactivity in visible light.

From the mathematical modelling work it was found that the steady state concentrations of CO_2 photoreduction products are sensitive to light and, in fact, sensitivity increases with decreasing oxidation number of the carbon atom of the product. However, there is a light saturation effect so that at high intensities the system is not sensitive to changes in light. The pH of the solution in the reactor is also important for the steady state concentrations under limiting light. The rate of the reaction was shown to depend on the spatial arrangement of the surface sites. Experiments with measurements of the product concentration at different times early in the reaction could be used to estimate parameter values and then the model could be used to make predictions such as the ideal hydrophilicity of the catalyst and the light saturation intensity to find the optimal experimental conditions.

The experimental and theoretical approaches together suggest that the photocatalysis stalling, which is often observed in CO_2 photoreduction ex-

periments, is not due to a steady state between products and reactants. In the model, $[CO_2(aq)]$ and $[H^+(aq)]$ are predicted to be limiting at steady state and this was not observed experimentally. Therefore, another mechanism must be responsible for the inactivity of the photocatalyst, such as the one suggested by the discrete model where the water coverage overwhelmed the catalyst.

A novel hybrid photocatalyst was presented in this work that can perform CO_2 photoreduction. As the material is now, it cannot be used commercially, due to the very low concentration of organics produced, the low selectivity for products and its instability. These are problems present to some extent with all CO_2 photoreduction systems and intense research is still underway in this field to overcome them. An improved system may be able to work to convert the emissions of power plants in the near future, while atmospheric CO_2 photoreduction will require research into substrate-selective catalysts which are also efficient photocatalysts, or the development of a more complex system that combines different materials for each purpose.

Bibliography

Amao, Y., Shuto, N., Furuno, K., Obata, A., Fuchino, Y., Uemura, K., Kajino, T., Sekito, T., Iwai, S., Miyamoto, Y. & Matsuda, M. (2012), 'Artificial leaf device for solar fuel production', *Faraday Discuss.* **155**, 289–296.

Anpo, M., Yamashita, H., Ichihashi, Y. & Ehara, S. (1995), 'Photocatalytic reduction of CO_2 with H_2O on various titanium oxide catalysts.', *Journal of Electroanalytical Chemistry* **396**, 21–26.

Arnold, W. & Sherwood, H. (1957), 'Are chloroplasts semiconductors?', *Proceedings of the National Academy of Sciences* **43**, 105–114.

Beddard, G. & Porter, G. (1976), 'Concentration quenching in chlorophyll', *Nature* **260**, 366–367.

Beltran, A., Sambrano, J., Calatayud, M., Sensato, F. & Andres, J. (2001), 'Static simulation of bulk and selected surfaces of anatase TiO_2', *Surface Science* **490**(1), 116–124.

Bogomolni, R. & Klein, M. (1975), 'Mobile charge carriers in photosynthesis.', *Nature* **258**, 88–89.

Bora, D. K., Rozhkova, E. A., Schrantz, K., Wyss, P. P., Braun, A., Graule, T. & Constable, E. C. (2012), 'Functionalization of nanostructured hematite thin-film electrodes with the light-harvesting membrane protein c-phycocyanin yields an enhanced photocurrent', *Advanced Functional Materials* **22**(3), 490–502.

Borjesson, K., Dzebo, D., Albinsson, B. & Moth-Poulsen, K. (2013), 'Photon upconversion facilitated molecular solar energy storage', *J. Mater. Chem. A* **1**, 8521–8524.

Boutin, A., Coasne, B., Fuchs, A. H., Galarneau, A. & Di Renzo, F. (2012), 'Experiment and theory of low-pressure nitrogen adsorption in organic layers supported or grafted on inorganic adsorbents: Toward a tool to characterize surfaces of hybrid organic/inorganic systems', *Langmuir* **28**(25), 9526–9534.

Cardoso, M. B., Smolensky, D., Heller, W. T., Hong, K. & O'Neill, H. (2011), 'Supramolecular assembly of biohybrid photoconversion systems', *Energy Environ. Sci.* **4**, 181–188.

Carp, O., Huisman, C. & Reller, A. (2004), 'Photoinduced reactivity of titanium dioxide', *Progress in Solid State Chemistry* **32**(12), 33 – 177.

Chen, Y., Li, C. W. & Kanan, M. W. (2012), 'Aqueous CO_2 reduction at very low overpotential on oxide-derived Au nanoparticles', *Journal of the American Chemical Society* **134**(49), 19969–19972.

Chiou, Y.-C., Kumar, U. & Wu, J. (2009), 'Photocatalytic splitting of water on $NiO/InTaO_4$ catalysts prepared by an innovative sol-gel method.', *Applied Catalysis A: General* **357**, 73–78.

Conti, J., Holtberg, P., Beamon, J. A., Napolitano, S., Schaal, A. M., Turnure, J. T., Westfall, L., Doman, L. E., Arora, V., Metelitsa, A., Leahy, M., Barden, J. L., Ford, M., Mellish, M. L., Jones, A., Murphy, B. T., Lillis, K., Slater-Thompson, N., Hojjati, B., Peterson, D., Gross, P., Zaretskaya, V. V., Chase, N., Morris, M. & Lindstrom, P. (2013), International energy outlook 2013, Technical report, U.S. Energy Information Administration.

Cox, C. R., Winkler, M. T., Pijpers, J. J. H., Buonassisi, T. & Nocera, D. G. (2013), 'Interfaces between water splitting catalysts and buried silicon junctions', *Energy Environ. Sci.* **6**, 532–538.

Das, R., Kiley, P. J., Segal, M., Norville, J., Yu, A. A., Wang, L., Trammell, S. A., Reddick, L. E., Kumar, R., Stellacci, F., Lebedev, N., Schnur, J., Bruce, B. D., Zhang, S. & Baldo, M. (2004), 'Integration of photosynthetic protein molecular complexes in solid-state electronic devices', *Nano Letters* **4**(6), 1079–1083.

Dey, G. R. (2007), 'Chemical reduction of CO_2 to different products during photo catalytic reaction on TiO_2 under diverse conditions: an overview', *Journal of Natural Gas Chemistry* **16**, 217–226.

Dincă, M., Surendranath, Y. & Nocera, D. G. (2010), 'Nickel-borate oxygen-evolving catalyst that functions under benign conditions', *Proceedings of the National Academy of Sciences* **107**(23), 10337–10341.

Doornbosch, R. & Steenblik, R. (2007), *Biofuels: Is the Cure Worse Than the Disease?*, Organisation for Economic Co-operation and Development.

D'Souza, F., Wijesinghe, C. A., El-Khouly, M. E., Hudson, J., Niemi, M., Lemmetyinen, H., Tkachenko, N. V., Zandler, M. E. & Fukuzumi, S. (2011), 'Ultrafast excitation transfer and charge stabilization in a newly assembled photosynthetic antenna-reaction center mimic composed of boron dipyrrin, zinc porphyrin and fullerene', *Phys. Chem. Chem. Phys.* **13**, 18168–18178.

Ellerby, L., Nishida, C., Nishida, F., Yamanaka, S., Dunn, B., Valentine, J. & Zink, J. (1992), 'Encapsulation of proteins in transparent porous silicate glasses prepared by the sol-gel method', *Science* **255**(5048), 1113–1115.

Erban, R., Chapman, J. & Maini, P. (2007), 'A practical guide to stochastic simulations of reaction-diffusion processes', *arXiv preprint arXiv:0704.1908* .

Esswein, A. J., Surendranath, Y., Reece, S. Y. & Nocera, D. G. (2011), 'Highly active cobalt phosphate and borate based oxygen evolving catalysts operating in neutral and natural waters', *Energy Environ. Sci.* **4**, 499–504.

Farquhar, G., von Caemmerer, S. & Berry, J. (1980), 'A biochemical model of photosynthetic CO_2 assimilation in leaves of C3 species', *Planta* **149**(1), 78–90.

Fujishima, A. & Honda, K. (1972), 'Electrochemical photolysis of water at a semiconductor electrode.', *Nature* **238**, 37–38.

Fujishima, A., Rao, T. & Tryk, D. (2000), 'Titanium dioxide photocatalysis.', *Journal of Photochemistry and Photobiology C: Photochemistry Reviews* **1**, 1–21.

Goldemberg, J. (2006), 'The ethanol program in Brazil', *Environmental Research Letters* **1**(1), 014008.

Grätzel, M. (2005), 'Solar energy conversion by dye-sensitized photovoltaic cells.', *Inorganic chemistry* **44**(20), 6841–6851.

Hahn, B. (1991), 'Photosynthesis and photorespiration: Modelling the essentials', *Journal of Theoretical Biology* **151**(1), 123 – 139.

Heinz Walz GmbH (1999), *Photosynthesis Yield Analyzer Mini-PAM, Portable Chlorophyll Fluorometer, Handbook of Operation*, Heinz Walz GmbH, Germany.

Hench, L. L. & West, J. K. (1990), 'The sol-gel process', *Chemical Reviews* **90**(1), 33–72.

Horton, P. & Murchie, E. (2000), C4 photosynthesis in rice: some lessons from studies of C3 photosynthesis in field-grown rice, *in* P. M. J.E. Sheehy & B. Hardy, eds, 'Redesigning Rice Photosynthesis to Increase Yield Proceedings of the Workshop on the Quest to Reduce Hunger:Redesigning Rice Photosynthesis', Vol. 7 of *Studies in Plant Science*, Elsevier, pp. 127 – 144.

Horton, P., Wentworth, M. & Ruban, A. (2005), 'Control of the light harvesting function of chloroplast membranes: the LHCII-aggregation model for non-photochemical quenching.', *FEBS Letters* **579**, 4201–4206.

Hou, X. & Cheng, W. (2012), 'Detection of single fluorescent proteins inside eukaryotic cells using two-photon fluorescence', *Biomed. Opt. Express* **3**(2), 340–353.

Huld, T. & Dunlop, E. D. (2013), Photovoltaic geographical information system, Technical report, European Commission, Joint Research Centre, Institute for Environment and Sustainability, Renewable Energies Unit. **URL:** *http://re.jrc.ec.europa.eu/pvgis/apps4/pvest.php*

IEAGHG (2011/04, June, 2011), Effects of impurities on geological storage of CO_2, Technical report, Global CCS Institute.
URL: *http://www.globalccsinstitute.com/publications/effects-impurities-geological-storage-co2*

Indrakanti, V. P., Kubicki, J. D. & Schobert, H. H. (2008), 'Quantum chemical modeling of ground states of CO_2 chemisorbed on anatase (001), (101), and (010) TiO_2 surfaces', *Energy & Fuels* **22**(4), 2611–2618.

Indrakanti, V. P., Kubicki, J. D. & Schobert, H. H. (2009), 'Photoinduced activation of CO_2 on Ti-based heterogeneous catalysts: Current state, chemical physics-based insights and outlook', *Energy Environ. Sci.* **2**, 745–758.

Inoue, T., Fujishima, A., Konishi, S. & Honda, K. (1979), 'Photoelectrocatalytic reduction of carbon dioxide in aqueous suspensions of semiconductor powders.', *Nature* **277**, 637–638.

Jiang, Y., Li, F., Huang, F., Zhang, B. & Sun, L. (2013), 'Chemical and photocatalytic water oxidation by mononuclear Ru catalysts', *Chinese Journal of Catalysis* **34**(8), 1489 – 1495.

Kanan, M. W. & Nocera, D. G. (2008), 'In situ formation of an oxygen-evolving catalyst in neutral water containing phosphate and Co^{2+}', *Science* **321**(5892), 1072–1075.

Kaneco, S., Shimizu, Y., Ohta, K. & Mizuno, T. (1998), 'Photocatalytic reduction of high pressure carbon dioxide using TiO_2 powders with a positive hole scavenger.', *Journal of Photochemistry and Photobiology A: Chemistry* **115**, 223–226.

Karlsson, S., Boixel, J., Pellegrin, Y., Blart, E., Becker, H.-C., Odobel, F. & Hammarström, L. (2012), 'Accumulative electron transfer: Multiple charge separation in artificial photosynthesis', *Faraday Discuss.* **155**, 233–252.

Kato, M., Cardona, T., Rutherford, A. W. & Reisner, E. (2013), 'Covalent immobilization of oriented photosystem II on a nanostructured electrode for solar water oxidation', *Journal of the American Chemical Society* **135**(29), 10610–10613.

Khnayzer, R. S., Blumhoff, J., Harrington, J. A., Haefele, A., Deng, F. & Castellano, F. N. (2012), 'Upconversion-powered photoelectrochemistry', *Chem. Commun.* **48**, 209–211.

Komenda, J., Sobotka, R. & Nixon, P. J. (2012), 'Assembling and maintaining the photosystem II complex in chloroplasts and cyanobacteria', *Current Opinion in Plant Biology* **15**(3), 245 – 251.

Krüger, T. P. J., Ilioaia, C., Valkunas, L. & van Grondelle, R. (2011), 'Fluorescence intermittency from the main plant light-harvesting complex: Sensitivity to the local environment', *The Journal of Physical Chemistry B* **115**(18), 5083–5095.

Krüger, T. P. J., Novoderezhkin, V. I., Ilioaia, C. & van Grondelle, R. (2010), 'Fluorescence spectral dynamics of single LHCII trimers', *Biophysical Journal* **98**(12), 3093–3101.

Kühlbrandt, W. & Wang, D. N. (1991), 'Three-dimensional structure of plant light-harvesting complex determined by electron crystallography', *Nature* **350**, 130–134.

Laisk, A., Nebdal, L. & Govindjee, eds (2009), *Photosynthesis in Silico: Understanding Complexity from Molecules to Ecosystems*, Springer, The Netherlands.

Lawlor, D. (2001), *Photosynthesis 3rd ed*, BIOS Scientific Publishers Ltd, Oxford.

Lee, C.-W., Antoniou Kourounioti, R., Wu, J. C. S., Murchie, E., Maroto-Valer, M., Jensen, O. E., Huang, C.-W. & Ruban, A. (2014), 'Photocatalytic conversion of CO_2 to hydrocarbons by light-harvesting complex assisted Rh-doped TiO_2 photocatalyst', *Journal of CO_2 Utilization* **5**(0), 33 – 40.

Lichtenthaler, H., Burkard, G., Kuhn, G. & Prenzel, U. (1981), 'Light-induced accumulation and stability of chlorophylls and chlorophyll-proteins during chloroplast development in radish seedlings', *Zeitschrift für Narurforschung C* **36c**, 421–430.

Limburg, J., Vrettos, J. S., Chen, H., de Paula, J. C., Crabtree, R. H. & Brudvig, G. W. (2001), 'Characterization of the O_2-evolving reaction catalyzed by $[(terpy)(H_2O)Mn^{III}(O)_2Mn^{IV}(OH_2)(terpy)](NO_3)_3$ (terpy = 2,2:6,2-Terpyridine)', *Journal of the American Chemical Society* **123**(3), 423–430.

Liou, P.-Y., Chen, S.-C., Wu, J. C. S., Liu, D., Mackintosh, S., Maroto-Valer, M. & Linforth, R. (2011), 'Photocatalytic CO_2 reduction using an internally illuminated monolith photoreactor', *Energy Environ. Sci.* **4**, 1487–1494.

Liu, D. (2012), Effects of Metal Modification on Titanium Dioxide for Photocatalytic Reduction of Carbon Dioxide., PhD thesis, University of Nottingham: U.K.

Liu, D.-M. & Chen, I.-W. (1999), 'Encapsulation of protein molecules in transparent porous silica matrices via an aqueous colloidal sol-gel process', *Acta Materialia* **47**(18), 4535 – 4544.

Liu, J., Lauterbach, R., Paulsen, H. & Knoll, W. (2008), 'Immobilization of light-harvesting chlorophyll a/b complex (LHCIIb) studied by surface plasmon field-enhanced fluorescence spectroscopy.', *Langmuir* **24**, 9661–9667.

Liu, S., Zhao, Z. & Wang, Z. (2007), 'Photocatalytic reduction of carbon dioxide using sol-gel derived titania-supported CoPc catalysts', *Photochemical & photobiological sciences: Official journal of the European Photochemistry Association and the European Society for Photobiology* **6**, 695–700.

Liu, Z., Yan, H., Wang, K., Kuang, T., Zhang, J., Gui, L., An, X. & Chang, W. (2004), 'Crystal structure of spinach major light-harvesting complex at 2.72Å resolution.', *Nature* **428**, 287–292.

Logan, S. R. (1996), *Fundamentals of Chemical Kinetics*, Addison Wesley Longman Limited.

Lutterman, D. A., Surendranath, Y. & Nocera, D. G. (2009), 'A self-healing oxygen-evolving catalyst', *Journal of the American Chemical Society* **131**(11), 3838–3839.

Marin, G. B. & Yablonsky, G. S. (2011), *Kinetics of Chemical Reactions, Decoding Complexity*, Wiley-VCH Verlag & Co.

Méndez-Ramos, J., Ruiz-Morales, J., Acosta-Mora, P., del Castillo, J. & Yanes, A. (2013), 'Rare-earth doped nano-glass-ceramics for extending spectral response of water-splitting semiconductor electrodes by high intense UV-blue up-conversion: Turning the sun into blue', *Journal of Power Sources* **238**(0), 313 – 317.

Mitchell, M. J., Jensen, O. E., Cliffe, K. A. & Maroto-Valer, M. M. (2010), 'A model of carbon dioxide dissolution and mineral carbonation kinetics', *Proceedings of the Royal Society A: Mathematical, Physical and Engineering Science* **466**(2117), 1265–1290.

Murchie, E. H. & Niyogi, K. K. (2011), 'Manipulation of photoprotection to improve plant photosynthesis', *Plant Physiology* **155**(1), 86–92.

Murchie, E. H., Pinto, M. & Horton, P. (2009), 'Agriculture and the new challenges for photosynthesis research', *New Phytologist* **181**(3), 532–552.

Nelson, J. (1999), 'Continuous-time random-walk model of electron transport in nanocrystalline tio$_2$ electrodes', *Phys. Rev. B* **59**, 15374–15380.

Nguyen, T.-V., Wu, J. C. S. & Chiou, C.-H. (2008), 'Photoreduction of CO_2 over ruthenium dye-sensitized TiO_2-based catalysts under concentrated natural sunlight.', *Catalysis Communications* **9**, 2073–2076.

Nocera, D. G. (2012), 'The artificial leaf', *Accounts of Chemical Research* **45**(5), 767–776.

Oliver, M., Velten, J. & Mischler, B. (2005), 'Desiccation tolerance in bryophytes: a reflection of a primitive strategy for plant survival in dehydrating habitats.', *Integr. Comp. Biol.* **45**, 788–799.

Ozcan, O., Yukruk, F., Akkaya, E. & Uner, D. (2007*a*), 'Dye sensitized artificial photosynthesis in the gas phase over thin and thick TiO_2 films under UV and visible light irradiation.', *Applied Catalysis B: Environmental* **71**, 291297.

Ozcan, O., Yukruk, F., Akkaya, E. & Uner, D. (2007*b*), 'Dye sensitized CO_2 reduction over pure and platinized TiO_2.', *Topics in Catalysis* **44**(4), 523–528.

Panda, S. (2009), *Microelectronics and Optoelectronics Technology*, Laxmi Publications Pvt Limited, New Delhi.

Parkhurst, D. F. (1977), 'A three-dimensional model for CO_2 uptake by continuously distributed mesophyll in leaves', *Journal of Theoretical Biology* **67**(3), 471 – 488.

Pascal, A., Liu, Z., Broess, K., van Oort, B., van Amerongen, H., Wang, C., Horton, P., Robert, B., Chang, W. & Ruban, A. (2005), 'Molecular basis of photoprotection and control of photosynthetic light-harvesting.', *Nature* **436**, 134–137.

Peral, J. & Ollis, D. F. (1992), 'Heterogeneous photocatalytic oxidation of gas-phase organics for air purification: Acetone, 1-butanol, butyraldehyde, formaldehyde, and m-xylene oxidation', *Journal of Catalysis* **136**(2), 554 – 565.

Peter, L. M., Wijayantha, K. G. U. & Tahir, A. A. (2012), 'Kinetics of light-driven oxygen evolution at α-Fe_2O_3 electrodes', *Faraday Discuss.* **155**, 309–322.

Porra, R., Thompson, W. & Kriedemann, P. (1989), 'Determination of accurate extinction coefficients and simultaneous equations for assaying chlorophylls a and b extracted with four different solvents: verification of the concentration of chlorophyll standards by atomic absorption spectroscopy', *Biochimica et Biophysica Acta* **975**, 384–394.

Proctor, M., R., L. & Duckett, J. (2007), 'Desiccation tolerance in the moss polytrichum formosum: physiological and fine-structural changes during desiccation and recovery.', *Ann. Bot.* **99**, 75–93.

Rajalakshmi, K., Jeyalakshmi, V., Krishnamurthy, K. R. & Viswanathan, B. (2012), 'Photocatalytic reduction of carbon dioxide by water on titania: Role of photophysical and structural properties', *Indian Journal of Chemistry* **51A**, 411–419.

Reece, S. Y., Hamel, J. A., Sung, K., Jarvi, T. D., Esswein, A. J., Pijpers, J. J. H. & Nocera, D. G. (2011), 'Wireless solar water splitting using silicon-based semiconductors and earth-abundant catalysts', *Science* **334**(6056), 645–648.

Rohacek, K. & Bartak, M. (1999), 'Technique of the modulated chlorophyll fluorescence: basic concepts, usual parameters, and some applications', *Photosynthetica* **37(3)**, 339–363.

Ruban, A., Solovieva, S., Lee, P., Ilioaia, C., Wentworth, M., Ganeteg, U., Klimmek, F., Chow, W., Anderson, J., Jansson, S. & Horton, P. (2006), 'Plasticity in the composition of the light harvesting antenna of higher plants preserves structural integrity and biological function.', *Journal of Biological Chemistry* **281**, 14981–14990.

Ruban, A. V., Johnson, M. P. & Duffy, C. D. (2012), 'The photoprotective molecular switch in the photosystem II antenna', *Biochimica et Biophysica Acta (BBA) - Bioenergetics* **1817**(1), 167 – 181.

Ruban, A. V., Johnson, M. P. & Duffy, C. D. P. (2011), 'Natural light harvesting: principles and environmental trends', *Energy Environ. Sci.* **4**, 1643–1650.

Ruban, A. V., Lee, P. J., Wentworth, M., Young, A. J. & Horton, P. (1999), 'Determination of the stoichiometry and strength of binding of xanthophylls to the photosystem II light harvesting complexes', *Journal of Biological Chemistry* **274**(15), 10458–10465.

Ruban, A. V. & Murchie, E. H. (2012), 'Assessing the photoprotective effectiveness of non-photochemical chlorophyll fluorescence quenching: A new approach', *Biochimica et Biophysica Acta (BBA) - Bioenergetics* **1817**(7), 977 – 982.

Ruban, A. V., Young, A. J., Pascal, A. A. & Horton, P. (1994), 'The effects of illumination on the xanthophyll composition of the photosystem II light-harvesting complexes of spinach thylakoid membranes.', *Plant Physiology* **104**, 227–234.

Ruban, A., Wentworth, M., Yakushevska, A., Andersson, J., Lee, P., Keegstra, W., Dekker, J., Boekema, E., Jansson, S. & Horton, P. (2003), 'Plants lacking the main light-harvesting complex retain photosystem II macro-organization.', *Nature* **421**, 648–652.

Rubin, A. & Riznichenko, G. (2009), Modeling of the primary processes in a photosynthetic membrane, *in* A. Laisk, L. Nebdal & Govindjee, eds, 'Photosynthesis in Silico: Understanding Complexity from Molecules to Ecosystems', Springer, The Netherlands, pp. 151–176.

Šafránek, D., Červený, J., Klement, M., Pospíšilová, J., Brim, L., Lazár, D. & Nedbal, L. (2011), 'E-photosynthesis: Web-based platform for modeling of complex photosynthetic processes', *Biosystems* **103**(2), 115 – 124.

Saltelli, A., Ratto, M., Andres, T., Campolongo, F., Cariboni, J., Gatelli, D., Saisana, M. & Tarantola, S. (2008), *Global Sensitivity Analysis: The Primer*, John Wiley, Chichester, UK.

Schindler, J., Wurster, R., Zerta, M., Blandow, V. & Zittel, W. (2006), Where will the energy for hydrogen production come from?, Technical report, European Hydrogen Association.

Schleucher, J., Vanderveer, P. & Sharkey, T. (1998), 'Export of carbon from chloroplasts at night', *Plant Physiol.* **118**, 1439–1445.

Schrödinger, LLC (2010), The PyMOL molecular graphics system, version 1.3r1. http://www.pymol.org.

Shang, J., Zhu, Y., Du, Y. & Xu, Z. (2002), 'Comparative studies on the deactivation and regeneration of TiO_2 nanoparticles in three photocatalytic oxidation systems: C_7H_{16}, SO_2, and $C_7H_{16}SO_2$', *Journal of Solid State Chemistry* **166**(2), 395 – 399.

Shiraishi, Y. & Hirai, T. (2008), 'Selective organic transformations on titanium oxide-based photocatalysts.', *Journal of Photochemistry and Photobiology C: Photochemistry Reviews* **9**, 157–170.

Singh-Rachford, T. & Castellano, F. (2009), 'Low power visible-to-UV upconversion', *The Journal of Physical Chemistry A* **113**, 5912–5917.

So, P. T. C., Dong, C. Y., Masters, B. R. & Berland, K. M. (2000), 'Two-photon excitation fluorescence microscopy', *Annual Review of Biomedical Engineering* **2**(1), 399–429.

Stark, M.-B. & Holmberg, K. (1989), 'Covalent immobilisation of lipase in organic solvents.', *Biotechnology and Bioengineering* **34**, 942–950.

Subrahmanyam, M., Kaneco, S. & Alonso-Vante, N. (1999), 'A screening for the photo reduction of carbon dioxide supported on metal oxide catalysts for C1-C3 selectivity', *Applied Catalysis B: Environmental* **23**(23), 169 – 174.

Tamaki, Y., Watanabe, K., Koike, K., Inoue, H., Morimoto, T. & Ishitani, O. (2012), 'Development of highly efficient supramolecular CO_2 reduction photocatalysts with high turnover frequency and durability', *Faraday Discuss.* **155**, 115–127.

Tan, S., Zou, L. & Hu, E. (2006), 'Photocatalytic reduction of carbon dioxide into gaseous hydrocarbon using TiO_2 pellets.', *Catalysis Today* **115**, 269–273.

Tan, S., Zou, L. & Hu, E. (2008), 'Kinetic modelling for photosynthesis of hydrogen and methane through catalytic reduction of carbon dioxide with water vapour.', *Catalysis Today* **131**, 125–129.

Tans, P. & Keeling, R. (2013), Monthly mean atmospheric carbon dioxide at Mauna Loa Observatory, Hawaii, Technical report, NOAA/ESRL (www.esrl.noaa.gov/gmd/ccgg/trends/) and Scripps Institution of Oceanography (scrippsco2.ucsd.edu/).

Taylor, R., Fournier, S., Simons, B., Kaplan, H. & Hefford, M. (2005), 'Covalent protein immobilization on glass surfaces: Application to alkaline phosphatase.', *Journal of Biotechnology* **118**, 265–269.

Terazono, Y., Kodis, G., Liddell, P. A., Garg, V., Moore, T. A., Moore, A. L. & Gust, D. (2009), 'Multiantenna artificial photosynthetic reaction center complex', *The Journal of Physical Chemistry B* **113**(20), 7147–7155.

Tiwari, J. L., Hobbie, J. E., Reed, J. P., Stanley, D. W. & Miller, M. C. (1978), 'Some stochastic differential equation models of an aquatic ecosystem', *Ecological Modelling* **4**(1), 3 – 27.

Tseng, I.-H., Chang, W.-C. & Wu, J. (2002), 'Photoreduction of CO_2 using sol-gel derived titania and titania-supported copper catalysts.', *Applied Catalysis B: Environmental* **37**, 37–48.

van Grondelle, R., Novoderezhkin, V. & Dekker, J. (2009), Modeling light harvesting and primary charge separation in photosystem I and photosystem II, *in* A. Laisk, L. Nebdal & Govindjee, eds, 'Photosynthesis in Silico: Understanding Complexity from Molecules to Ecosystems', Springer, The Netherlands, pp. 33–53.

Varghese, O., Paulose, M., LaTempa, T. & Grimes, C. (2009), 'High-rate solar photocatalytic conversion of CO_2 and water vapor to hydrocarbon fuels.', *Nano Letters* **9**, 731–737.

von Caemmerer, S. (2013), 'Steady-state models of photosynthesis', *Plant, Cell & Environment* **36**(9), 1617–1630.

von Caemmerer, S., Farquhar, G. & Berry, J. (2009), Biochemical model of C_3 photosynthesis, *in* A. Laisk, L. Nebdal & Govindjee, eds, 'Photosynthesis in Silico: Understanding Complexity from Molecules to Ecosystems', Springer, The Netherlands, pp. 209–230.

Wang, C., Thompson, R., Baltrus, J. & Matranga, C. (2010), 'Visible light photoreduction of CO_2 using $CdSe/Pt/TiO_2$ heterostructured catalysts.', *The Journal of Physical Chemistry Letters* **1**, 48–53.

Waseda, Y., Matsubara, E. & Shinoda, K. (2011), *X-Ray Diffraction Crystallography: Introduction, Examples and Solved Problems*, Springer.

Weetall, H. (1969), 'Alkaline phosphatase insolubilized by covalent linkage to porous glass', *Nature* **223(5209)**, 959–960.

Wenk, S.-O.-O., Qian, D.-J., Wakayama, T., Nakamura, C., Zorin, N., Rgner, M. & Miyake, J. (2002), 'Biomolecular device for photoinduced hydrogen production', *International Journal of Hydrogen Energy* **27**(1112), 1489 – 1493.

Wentworth, M., Ruban, A. & Horton, P. (2004), 'The functional significance of the monomeric and trimeric states of the photosystem II light harvesting complexes.', *Biochemistry* **43**, 501–509.

Werwie, M., Xu, X., Haase, M., Basché, T. & Paulsen, H. (2012), 'Bio serves nano: Biological light-harvesting complex as energy donor for semiconductor quantum dots', *Langmuir* **28**(13), 5810–5818.

Wientjes, E., van Amerongen, H. & Croce, R. (2013), 'LHCII is an antenna of both photosystems after long-term acclimation', *Biochimica et Biophysica Acta (BBA) - Bioenergetics* **1827**(3), 420 – 426.

Woolerton, T., Sheard, S., Reisner, E., Pierce, E., Ragsdale, S. & Armstrong, F. (2010), 'Efficient and clean photoreduction of CO_2 to CO by enzyme-modified TiO_2 nanoparticles using visible light.', *J. Am. Chem. Soc.* **132**, 2132–2133.

Wu, J. (2009), 'Photocatalytic reduction of greenhouse gas CO_2 to fuel.', *Catal Surv Asia* **13**, 30–40.

Wu, J. C., Lin, H.-M. & Lai, C.-L. (2005), 'Photo reduction of CO_2 to methanol using optical-fiber photoreactor', *Applied Catalysis A: General* **296**, 194–200.

Wu, J. & Lin, H.-M. (2005), 'Photo reduction of CO_2 to methanol via TiO_2 photocatalyst', *International Journal of Photoenergy* **7**(3), 115–119.

Wu, J., Tseng, I.-H. & Chang, W.-C. (2001), 'Synthesis of titania-supported copper nanoparticles via refined alkoxide sol-gel process.', *Journal of Nanoparticle Research* **3**, 113–118.

Xue, Y., Smith, T. M. & Reynolds, R. W. (2003), 'Interdecadal changes of 30-yr SST normals during 1871-2000.', *J. Climate* **16**, 1601–1612.

Yamashita, H., Nishiguchi, H., Kamada, N., M., A., Teraoka, Y., Hatano, H., Ehara, S., Kikui, K., Palmisano, L., Sclafani, A., Schiavello, M. & Fox, M. A. (1994), 'Photocatalytic reduction of CO_2 with H_2O on TiO_2 and Cu/TiO_2 catalysts.', *Res. Chem. Intermed.* **20**, 815–823.

Yang, C., Boggasch, S., Haase, W. & Paulsen, H. (2006), 'Thermal stability of trimeric light-harvesting chlorophyll a/b complex (LHCIIb) in liposomes of thylakoid lipids.', *Biochimica et Biophysica Acta* **1757**, 1642–1648.

Zhao, Z., Fan, J., Xie, M. & Wang, Z. (2009), 'Photo-catalytic reduction of carbon dioxide with in-situ synthesized $CoPc/TiO_2$ under visible light irradiation', *Journal of Cleaner Production* **17**, 1025–1029.

Zhao, Z.-H., Fan, J.-M. & Wang, Z.-Z. (2007), 'Photo-catalytic CO_2 reduction using solgel derived titania-supported zinc-phthalocyanine.', *Journal of Cleaner Production* **15**(18), 1894–1897.

Zhu, X.-G., Long, S. P. & Ort, D. R. (2008), 'What is the maximum efficiency with which photosynthesis can convert solar energy into biomass?', *Current Opinion in Biotechnology* **19**(2), 153 – 159.

Zhu, X.-G., Wang, Y., Ort, D. R. & Long, S. P. (2013), 'e-photosynthesis: a comprehensive dynamic mechanistic model of C3 photosynthesis: from light capture to sucrose synthesis', *Plant, Cell & Environment* **36**(9), 1711–1727.